

Droplet wetting on chemically and mechanically structured surfaces

Zur Erlangung des akademischen Grades
Doktor der Ingenieurwissenschaften
von der KIT-Fakultät für Maschinenbau
des Karlsruher Instituts für Technologie (KIT)

genehmigte **Dissertation**

von

M.Sc. Yanchen Wu

Tag der mündlichen Prüfung : 21.09.2021

Hauptreferentin: Prof. Dr. rer. nat. Britta Nestler

Korreferent: Prof. Dr. rer. nat. Pavel Levkin

Abstract

In this thesis, the droplet wetting behaviors on chemically patterned and mechanically structured surfaces are investigated. Here, the equilibrium shapes and the quasi-equilibrium movements of droplets on chemically patterned surfaces, the wetting behaviors of multiphase droplets on chemically heterogeneous surfaces, and the droplet permeation behaviors in a single pore structure are addressed. Last but not least, the phase-field model is validated to investigate the droplet dynamics on solid heterogeneous surfaces and the validated model is utilized to study the controllable satellite droplet formation during the thin liquid film dewetting process on chemically patterned surfaces.

For droplets on chemically patterned surfaces, firstly the equilibrium shape of droplets and the contact line movement on chemically stripe-patterned surfaces are studied. The phase-field model is shown to be highly robust when simulating the equilibrium shape, the spreading of the contact line, and phase change of droplets on chemically patterned surfaces. A morphological diagram is obtained which reveals that the droplet aspect ratio and the number of equilibrium shapes are closely related to the scaled stripe width. Through the comparisons between condensing and evaporating droplets, a hysteresis phenomenon is observed, proving that the different droplet shapes can be obtained via distinct moving paths. Furthermore, a mathematical-physical model is proposed to describe the droplet configurations on three typically programmable, chemically patterned surfaces. This analytical model is based on the calculation of surface energy landscape and has been successfully validated through phase-field simulations and experiments. It can serve as guidance for experiments and simulations to find different equilibrium shapes without blind attempts. Particularly, this analytical model is valid for the situation where the chemical heterogeneity size is comparable to the droplet size. Besides, a modified Cassie-Baxter model is proposed to address the anisotropic wetting configurations. Additionally, the multiphase phase-field model is used to study the multiphase droplet wetting behaviors on chemically patterned surfaces. The interaction of liquid-liquid interface, influenced by different values of interfacial tensions, is discussed.

The phase-field model is further validated to study the droplet wetting states in a pore structure. Thereafter, the droplet wetting behavior in a pore structure is theoretically and numerically explored, so as to find the criterion for droplet permeation. It is proved that the open angle and hydrophobicity of the substrate both have a great impact on the droplet permeation behavior.

Finally, the Cahn-Hilliard model is coupled with Navier-Stokes equations to study the droplet dynamics on chemically patterned surfaces. A new strategy was found to control the formation of satellite droplets through a deliberate design of the chemical patterns.

Kurzfassung

In dieser Arbeit wird das Benetzungsverhalten von Tröpfchen auf chemisch und mechanisch strukturierten Oberflächen untersucht. Dabei werden die Gleichgewichtsformen und die Quasi-Gleichgewichtsbewegungen von Tröpfchen auf chemisch strukturierten Oberflächen, das Benetzungsverhalten von mehrphasigen Tröpfchen auf chemisch heterogenen Oberflächen und das Tröpfchenpermeationsverhalten in einer einzelnen Porenstruktur behandelt. Zu guter Letzt wird das Phasenfeldmodell validiert, um die Tropfendynamik auf festen heterogenen Oberflächen zu untersuchen. Das validierte Modell wird verwendet, um die kontrollierbare Bildung von Satellitentröpfchen während des Entnetzungsprozesses eines dünnen Flüssigkeitsfilms auf chemisch strukturierten Oberflächen zu untersuchen.

Für Tröpfchen auf chemisch strukturierten Oberflächen werden zunächst die Gleichgewichtsform von Tröpfchen und die Kontaktlinienbewegung auf chemisch streifengemusterten Oberflächen untersucht. Das Phasenfeldmodell erweist sich bei der Simulation der Gleichgewichtsform, der Ausbreitung der Kontaktlinie und des Phasenwechsels von Tröpfchen auf chemisch strukturierten Oberflächen als sehr sicher und resistent. Das Ergebnis ist ein morphologisches Diagramm, das zeigt, dass das Tröpfchen-Seitenverhältnis und die Anzahl der Gleichgewichtsformen eng mit der skalierten Streifenbreite zusammenhängen. Durch den Vergleich zwischen kondensierenden und verdampfenden Tröpfchen wird ein Hysteresephänomen beobachtet, das beweist, dass die verschiedenen Tröpfchenformen über unterschiedliche Bewegungspfade gewonnen werden können. Darüber hinaus wird ein mathematisch-physikalisches Modell vorgeschlagen, um die Tröpfchenkonfigurationen auf drei typischerweise programmierbaren, chemisch strukturierten Oberflächen zu beschreiben. Dieses analytische Modell basiert auf der Berechnung der Oberflächenenergielandschaft und wurde erfolgreich mit Phasenfeldsimulationen und Experimenten validiert. Es kann als Anleitung für Experimente und Simulationen dienen, um verschiedene Gleichgewichtsformen ohne Blindversuche zu finden. Insbesondere ist dieses analytische Modell für die Situation gültig, in der die Größe der chemischen Heterogenität mit der Tröpfchengröße vergleichbar ist. Außerdem wird ein modifiziertes Cassie-Baxter-Modell vorgeschlagen, in dem die anisotropen Benetzungskonfigurationen berücksichtigt werden. Zusätzlich wird das Mehrphasen-Phasenfeldmodell verwendet, um das Benetzungsverhalten von mehrphasigen Tröpfchen auf chemisch strukturierten Oberflächen zu untersuchen. Dabei wird die Interaktion der Flüssig-Flüssig-Grenzfläche, die durch die unterschiedlichen Werte der Grenzflächenspannungen beeinflusst wird, diskutiert.

Um die Tröpfchenbenetzungszustände in einer Porenstruktur zu untersuchen, wird das Phasenfeldmodell weiter validiert. Anschließend wird das Benetzungsverhalten von Tröpfchen in einer

Porenstruktur theoretisch und numerisch untersucht, um das Kriterium für die Permeation der Tröpfchen zu finden. Es wird nachgewiesen, dass der offene Winkel und die Hydrophobizität des Substrats einen großen Einfluss auf das Permeationsverhalten der Tröpfchen haben.

Schließlich wird das Cahn-Hilliard-Modell mit Navier-Stokes-Gleichungen gekoppelt, um die Tröpfchendynamik auf chemisch strukturierten Oberflächen zu untersuchen. Es wurde eine neue Strategie gefunden, die es ermöglicht, die Bildung von Satellitentröpfchen durch ein bewusstes Design der chemischen Muster zu steuern.

Acknowledgement

The present dissertation was finished during my work as a research assistant at the Institute of Applied Materials-Computational Materials Science (IAM-CMS) in Karlsruhe Institute of Technology (KIT) supervised by Prof. Dr. rer. nat. Britta Nestler. I was so lucky to be part of this active and dynamic research group with people of different backgrounds. This thesis becomes reality with the kind support from many individuals. I would like to take this opportunity to extend my sincere thanks to all of them.

First and foremost, I acknowledge my deepest gratitude to my supervisor Prof. Dr. rer. nat. Britta Nestler for her insightful guidance, constant encouragement, and invaluable scientific suggestions. I also appreciate her providing me the freedom to explore the most interesting phenomena in the field of droplet wetting and fluid dynamics. Many thanks to her for providing me the chance to supervise several excellent bachelor and master students from KIT, who have tremendously supported my work. Many thanks to Britta for letting me establish cooperation with researchers from several institutes especially with Prof. Pavel Levkin. I am grateful to Pavel for his instructive insights that have inspired me a lot. I also admire him for his capability of making connections with researchers from different disciplines.

In addition, I would like to thank my group leaders Dr. Michael Selzer and Dr. Fei Wang for their helpful discussions and our cooperation in cosupervising of students. Especially, I really appreciate Dr. Fei Wang for his overwhelming enthusiasm, brilliance, and immense knowledge. I really enjoy the intensive discussions with Fei and Haodong, which inspires me a lot. Many thanks to Haodong Zhang for our cooperation work on the topic of multiple emulsions and phase separation and many thanks for our daily jokes and many pleasures sharing with Fei Wang, Yuhan Cai, Yinghan Zhao, Nico Brandt during lunchtime.

I am also thankful to my collaborators Mariia Kuzina and Prof. Markus Reischl for providing experimental support and image analysis in the project of droplet shape analysis. I am grateful to my collaborators Mariia Kuzina and Johannes Scheiger for the cooperation of the water-ring project, and many thanks to Prof. Steffen Hardt and Dr. Michael Eigenbrod for the feedback on the phase-field modeling of the water-ring project.

I also thank the secretariat, many thanks to Ms. Inken Heise, Ms. Birgitt Hardt, and Ms. Michelle Ritzinger for helping with all the paper works. Many thanks to Mr. Leon Geisen for the organization of seminars and conference information. Many thanks to Leon for helping me correct the Abstract in German. Many thanks to Mr. Christof Ratz, Mr. Domenic Frank, Ms. Roxanne Hohl for the technical support of computers and systems. Also many thanks to the Hiwi students Weidong Huang, Nico Luksch, Fabian Epp, Xiuzhen Li, the bachelor students Henning Kloos, Julian Leutz, Nam Luong,

Björn Nembach, Marvin Rüdert, and master students Shaoping Ma, Weidong Huang, Tianxi Wang, Sai Zheng.

I am very grateful to my parents and my brother for their unconditional support and encouragement. Especially, I would like to express my love and gratitude to my girlfriend for her understanding and patience.

Finally, I acknowledge funding of the research through the Gottfried-Wilhelm Leibniz prize NE 822/31-1 of the German Research Foundation (DFG).

Preface

This dissertation investigates droplet wetting behaviors on heterogeneous substrates via phase-field simulations. It mainly addresses the equilibrium shapes and quasi-equilibrium morphological transition for droplets on chemically patterned surfaces. Based on the assumption of the geometry for equilibrated droplets and surface energy minimization, the energy landscape method and modified Cassie-Baxter model are proposed. The two models describe the equilibrium shapes of droplets on chemically patterned surfaces where the droplet size is comparable to the surface heterogeneity, which are confirmed by phase-field simulations. Besides, the droplet permeation behavior in pore structures and the droplet dynamics on different substrates are also discussed. The introduction for the motivations, physical fundamentals, the state of research, and numerical methods are presented in the first three chapters. Chapters 4-9 contain 5 published and 2 unpublished articles, which are slightly adjusted without changing the original contents. The 7 articles are listed as follows:

- **Article 1:** Y. Wu, F. Wang, M. Selzer, and B. Nestler. Investigation of equilibrium droplet-shapes on chemically striped patterned surfaces using phase-field method. *Langmuir*, 2019, **35**, 8500–8516.
- **Article 2:** Y. Wu, F. Wang, M. Selzer, and B. Nestler. Droplets on chemically patterned surface: A local free energy minima analysis. *Physical Review E Rapid Communications*, 2019, **100**, 041102.
- **Article 3:** Y. Wu, F. Wang, S. Ma, M. Selzer, and B. Nestler. How do chemical patterns affect equilibrium droplet shapes? *Soft Matter*, 2020, **16**, 6115-6127.
- **Article 4:** J. M. Scheiger, M. A. Kuzina, M. Eigenbrod, Y. Wu, F. Wang, S. Heissler, S. Hardt, B. Nestler, P. A. Levkin. Liquid wells as self-healing, functional analogues to solid vessels. *Advanced Materials*, 2021, **33**, 2100117.
- **Article 5:** Y. Wu[†], M. Kuzina[†] (co-first author), F. Wang, M. Reischl, M. Selzer, B. Nestler, P. A. Levkin. Equilibrium droplet shapes on chemically patterned surfaces: theoretical calculation, phase-field simulation, and experiments. *Journal of Colloid and Interface Science*, 2022, **606**, 1077–1086.
- **Article 6:** Y. Wu, F. Wang, W. Huang, M. Selzer, and B. Nestler. Capillary adsorption of water droplets into a beak-shaped tube structure. *Under review in Physical Review Letters*.

-
- **Article 7: Y. Wu**, F. Wang, T. Wang, M. Selzer, and B. Nestler. Phase-field investigation of thin liquid film dewetting on chemically patterned surfaces. *In preparation*.

In the last chapter, summaries and future directions are given.

The following two works that published during the PhD study, are not included in the present dissertation.

- H. Zhang, † **Y. Wu** † (co-first author), F. Wang, F. Guo, and B. Nestler. Phase-field modeling of multiple emulsions via spinodal decomposition. *Langmuir*, 2021, **37**(17), 5275–5281.
- M. Wörner, N. Samkhaniani, X. Cai, **Y. Wu**, A. Majumdar, H. Marschall, B. Frohnäpfel, O. Deutschmann. Spreading and rebound dynamics of sub-millimeter urea-water-solution droplets impinging on substrates of varying wettability. *Applied Mathematical Modeling*, 2021, **95**, 53–73.

The permission to use the figures from literature has been granted by the corresponding publishers.

Author's contribution

The supervisor for the whole project is Prof. Dr. rer. nat. Britta Nestler.

- **Article 1:** Y. Wu performed the simulations, analyzed the data, discussed with F. Wang and wrote the draft with the feedback from F. Wang, M. Selzer, and B. Nestler.
- **Article 2:** Y. Wu proposed the analytical model and discussed with F. Wang. Y. Wu performed the simulations, analyzed the data, and wrote the draft with the feedback from F. Wang, M. Selzer, and B. Nestler.
- **Article 3:** Y. Wu extended the analytical model and discussed with F. Wang. Y. Wu and S. Ma (master student) performed the simulations. Y. Wu analyzed the data, and wrote the draft with the feedback from F. Wang, S. Ma, M. Selzer, and B. Nestler.
- **Article 4:** J. M. Scheiger, P. A. Levkin, and M. A. Kuzina designed the experiments. J. M. Scheiger and P. A. Levkin proposed the original idea. M. A. Kuzina conducted the experiments. Y. Wu, F. Wang, B. Nestler, S. Hardt, M. Eigenbrod conducted and analyzed the simulations. S. Heissler helped with Raman experiments. My contribution to the project (simulations) with a brief description of the concept is presented in chapter 7.
- **Article 5:** Y. Wu and M. Kuzina proposed the idea and discussed with F. Wang, P. A. Levkin, M. Selzer, and B. Nestler. Y. Wu performed simulations and theoretical calculations. M. Kuzina conducted experiments. M. Reischl helped with picture analysis. Y. Wu wrote the draft with feedback from M. Kuzina, F. Wang, M. Reischl, M. Selzer, B. Nestler, and P. A. Levkin.
- **Article 6:** Y. Wu proposed the original idea and discussed with F. Wang and M. Selzer. Y. Wu and W. Huang (student assistant) performed simulations, Y. Wu wrote the draft with feedback from F. Wang, W. Huang, M. Selzer, and B. Nestler.
- **Article 7:** Y. Wu proposed the original idea and discussed with F. Wang. Y. Wu and T. Wang (master student) performed simulations. Y. Wu wrote the draft with feedback from F. Wang, T. Wang, M. Selzer, and B. Nestler.

君子终日乾乾，夕惕若厉，无咎。

**All day long the superior man is creatively active. At
nightfall his mind is still beset with cares. In this
case, there will be no mistake.**

Contents

Abstract	i
Kurzfassung	iv
I. Introduction and literature review	1
1. Introduction	3
1.1. Motivation	3
1.2. Synopsis	6
2. Physical fundamentals and literature review	7
2.1. Surface tension and Young-Laplace equation	7
2.2. Contact angle and the Young's law	8
2.3. The Wenzel and Cassie-Baxter's model	9
2.4. Multiphase-droplet-system	10
2.5. Droplet spreading and thin-film dewetting on solid substrates	11
2.6. Evaporation and condensation of sessile droplets	13
II. Methods	15
3. Phase-field method	17
3.1. Allen-Cahn model for multiphase system	17
3.2. Allen-Cahn model for two-phase system	19
3.3. Cahn-Hilliard model for multiphase system	20
3.4. Cahn-Hilliard model for two-phase system	21
3.4.1. Non-dimensional calculation	22
3.4.2. Calculation of surface tension	23
3.4.3. Derivation of the natural boundary condition	24

III. Results and discussion: Static or quasi-static problems	27
4. Single droplet on chemically striped surfaces: A phase-field investigation	29
4.1. Simulation setups	29
4.2. Validation of the numerical model	29
4.3. Droplet shape analysis	37
4.3.1. Droplet deposition and condensation in quasi-equilibrium state	37
4.3.2. Droplet evaporation in quasi-equilibrium state and hysteresis phenomenon	41
4.3.3. Influence of perturbations on the morphological transition	45
4.3.4. Droplet phase change in non-equilibrium states	47
4.4. Summary	48
5. Single droplet on chemically patterned surfaces: A combined study through theoretical and numerical methods	53
5.1. Simplified analytical model and simulation setups	54
5.1.1. The calculation of the total interfacial energy	54
5.1.2. Simulation setups	56
5.1.3. Validation of the high symmetry property of equilibrated droplets	57
5.2. Droplet shape analysis by using the simplified model	59
5.2.1. Striped patterned surfaces	59
5.2.2. Chocolate patterned surfaces	59
5.2.3. Chessboard patterned surfaces	63
5.2.4. Summary and conclusion	63
5.3. Generalized analytical model and modified CB model	65
5.4. Droplet shape analysis by using the generalized model	68
5.4.1. Droplet size	68
5.4.2. Contact angle	72
5.4.3. The ratio of the hydrophilic area to the hydrophobic area	76
5.4.4. Summary and Conclusions	77
6. Single droplet on chemically patterned surfaces: theoretical calculation, phase-field simulation, and experiments	79
6.1. Methods	79
6.2. Droplet shape analysis	80
6.2.1. Analysis of top views	80
6.2.2. Analysis of side views	85
6.2.3. Analysis of droplet height and surface energy	85
6.2.4. Analysis of droplet evaporation	87
6.3. Conclusion	89

7. Multiphase droplets on chemically heterogeneous surfaces	91
7.1. Liquid-liquid confinement	91
7.2. Multiphase droplets manipulation on solid substrate	93
7.3. Summary and remarks	94
8. Droplet on mechanically heterogeneous surfaces	95
8.1. Validation of the numerical model for droplet in a pore structure	95
8.2. Analysis of the criterion for droplet permeation in a pore structure	97
8.2.1. Analytical model	97
8.2.2. Analysis of the droplet penetration behavior	99
8.3. Summaries and conclusions	103
IV. Results and discussion: Dynamic problems	105
9. Droplet dynamics on solid heterogeneous surfaces	107
9.1. Validation of the CHNS model for fast spreading on homogeneous surfaces	107
9.2. Validation of the CHNS model for droplet dynamics on mechanically heterogeneous surfaces	108
9.3. Validation of the CHNS model for droplet dynamics on chemically patterned surface	109
9.4. Analysis of thin liquid film dewetting on chemically patterned surfaces	110
9.5. Summary	113
V. Conclusion and outlook	117
10. Conclusion and outlook	119
10.1. Conclusion and remarks	119
10.2. Future directions	121
VI. Appendices	123
A. Calculation of double-well function	125
B. Prediction of droplet shapes	127
B.1. Droplet size	127
B.2. Contact angle	130
B.3. The ratio of the hydrophilic area to the hydrophobic area	133
B.4. Code for the energy landscape model	135
C. Supplemental information to chapter 6	139
C.1. Discussion of the controlling parameters for chemical patterns	139

C.2. Pattern information	141
C.3. Shape comparison	142
C.4. Calculation of Bond number	143
D. List of Symbols	145
E. List of Abbreviations	149
Bibliography	167

Part I.

Introduction and literature review

1. Introduction

1.1. Motivation

The wetting phenomena are ubiquitous in nature and our daily lives. For instance, the dewdrops exhibited on leaves make the plants more resilient in hot and dry conditions (see Fig. 1.1 [1]). Some birds have evolved themselves to possess feathers with superhydrophobic structures, which could partially prevent heat loss from impacting rain droplets [2, 3]. In daily lives, the annoying trickle of water along the outside of a receptacle as pouring, is called “teapot effect”, where surface wettability of the receptacle takes an important role [4, 5]. The deposition of coffee particles at the edge of the evaporating coffee contained droplets, known as the “coffee ring effect”, is caused by a capillary flow [6].

Apart from explaining the underlying mechanisms for the common interesting wetting phenomena in nature and daily lives, I am willing to harness the wetting properties for practical use. Nowadays, wetting is indeed of great significance for the cutting-edge technical applications. Various applications are based on the control of the droplet wetting behaviors. These include inkjet printing [7, 8], droplet splitting and sampling (Fig. 1.2) [9, 10], microfluidics [11] and so on. Taking inkjet printing, for example, the static wetting morphology is very crucial to improve the printing quality. The inkjet printing technology has been applied to the fabrication of OLED displays, where precise control of droplet size and position is essential. Arias et al. [12] stated that the size, position, and resolution in the fabrication of thin-film-transistor array is affected by the balance between pinning



Figure 1.1.: Morning dews on a leaf [1].

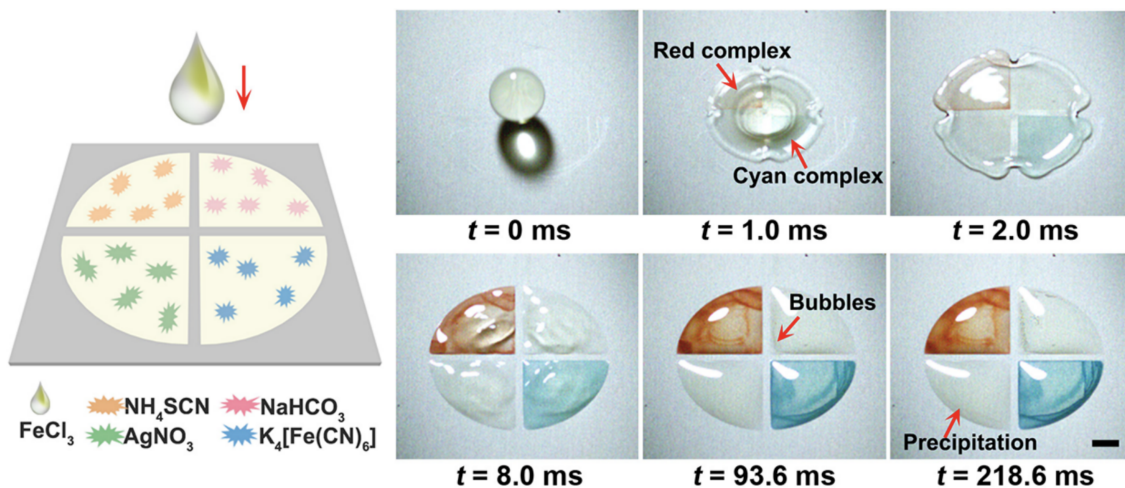


Figure 1.2.: Droplet splitting and simultaneous arrayed reactions on a hydrophobic surface with hydrophilic areas. Different chemicals predeposited on the hydrophilic areas independently reacts with the splitted droplets simultaneously after splitting [9].

and overspreading of the printed ink on the solid substrate. As shown in Fig. 1.2, chemical patterns are introduced for the self-splitting method, making the simultaneous multireactions possible. A typical novel application of controlling droplet dynamics in microfluidics is the so-called hotspot cooling technology [13]. As illustrated in Fig. 1.3, in the sealed vapor chamber, the working fluid vaporizes around the hotspots and condenses on the bottom plate beneath the hotspots. The condensate droplets coalesce and then jump from the superhydrophobic bottom plate to the hotspots. This process allows handling of mobile hotspots, and thus provides a smart way of heat management in microelectronics. For more discussions about the fundamentals and applications of wetting, readers are referred to the book of Law and Zhao [14].

When a droplet contacts a solid surface, it will eventually arrive at the thermodynamic equilibrium state. If the solid surface is ideally homogeneous, the equilibrium shape of the droplet can be

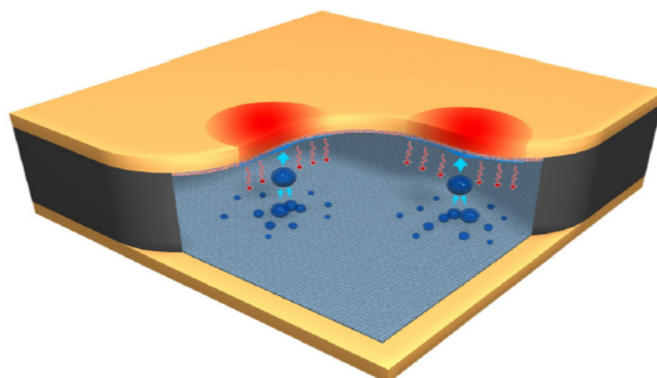


Figure 1.3.: Schematic of the hotspot cooling technique in a sealed vapor chamber. The top (bottom) plate is the superhydrophilic evaporator (superhydrophobic condenser) [13].

accurately described by the Young's law. However, there are always mechanical and chemical inhomogeneities on real surfaces. These inhomogeneities may lead to anisotropic wetting morphologies of the droplets, making it difficult to theoretically describe the equilibrium shapes. Although Wenzel [15] and Cassie [16] have devoted themselves to the wetting droplet on heterogeneous surfaces, their models are restricted to the situation where droplet size is much larger than the inhomogeneities. Understanding the droplet wetting behavior on heterogeneous surfaces has a fundamental meaning for real-world applications. It is thus of vital significance to establish a theoretical framework to address the wetting behavior on heterogeneous surfaces.

The present dissertation mainly focuses on the static states and quasi-static movements of droplets on chemically patterned surfaces and mechanically structured surfaces. However, further exploration of the droplet dynamics on solid heterogeneous is provided in the last part of the work. When we consider the droplet dynamics on a solid surface, the moving contact line dynamics must be involved. This leads to a multi-scale problem, since the large-scale dynamics are governed by hydrodynamics, while the moving contact line dynamics is determined by the physics on around molecular length scales [17]. In hydrodynamics, the classic no-slip boundary condition at solid wall leads to stress singularity. An alternative method to handle this problem is the phase-field (PF) method. As a diffuse interface method, the PF method introduces diffusive fluxes and allows for the contact line motion [18].

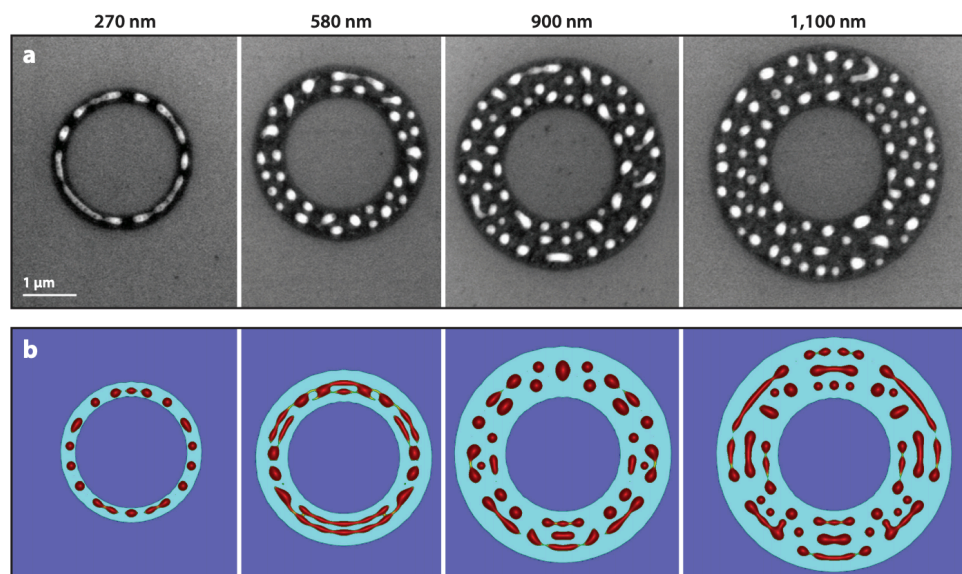


Figure 1.4.: (a) Scanning electron micrographs of 7.8-nm-thick copper rings with various widths following pulsed laser exposure. (b) Simulation results via thin-film model (Similar to Cahn-Hilliard model [19]). Here, the light blue background indicates the original ring. As the width of the ring increases, the ring transitions from a purely Rayleigh-Plateau-type instability to a situation where both thin-film instability and Rayleigh-Plateau-type instability coexist [20].

The present thesis adopts two types of PF models (the Allen-Cahn model and Cahn-Hilliard model) combined with a thermodynamics consistent wetting boundary condition to simulate the droplet wetting behaviors. Both of the two types of PF models can be considered as the gradient flow of the Lyapunov energy functional and the total free energy decreases with time. The two models thus have the same equilibrium solutions. However, the Allen-Cahn model is a gradient descent method, which shows a different kinetic path as the Cahn-Hilliard type model. The advantage of the Allen-Cahn model over the Cahn-Hilliard model is that it is more numerically efficient. Thus the Allen-Cahn model is adopted to address the static and quasi-static problems in this work. As a naturally conserved model, the Cahn-Hilliard model is appropriate to describe the dynamic process. For instance, it has been applied to analyze interfacial instability phenomena such as Rayleigh-Plateau-type instability, spinodal dewetting, droplet breakup, droplet impact, and splash, etc [21]. In this thesis, Cahn-Hilliard model is utilized to analyze the droplet dynamics. Fig. 1.4 illustrates a typical example for the interfacial instability phenomena, where the simulations show good agreement with experiments.

1.2. Synopsis

The outline of this dissertation is as follows. In chapter 2, physical fundamentals and a literature review of droplet wetting on heterogeneous surfaces are given. Subsequently, the phase-field models including the Allen-Cahn (AC) model and Cahn-Hilliard (CH) model utilized for simulating the droplet wetting behavior is formulated in chapter 3. In chapter 4, the AC model is validated and applied to investigate the equilibrium morphologies of droplets on chemically striped surfaces. In addition, the morphology transitions for evaporating and condensing droplets in quasi-equilibrium are contemplated. In the following chapters 5 and 6, an analytical model is proposed to delineate the droplet patterns on chemically patterned surfaces. PF simulations are conducted to confirm the analytical model. Moreover, a modified Cassie-Baxter (CB) model is established. The analytical model, PF simulations and experiments are used to quantitatively analyze the anisotropic wetting morphologies. In chapter 7, the multiphase AC model is utilized to simulate the confinement of low surface tension liquid in a water ring placed on a chemically patterned surface. The model is further tested for the studying of multiphase droplets movements driven by the wettability gradient on the substrate. From chapter 4 to chapter 7, the droplet wetting behaviors on chemically patterned surfaces are concerned. Chapter 8 moves on to discuss the mechanically or geometrically heterogeneous substrate. This chapter presents the numerical and theoretical study of droplet penetration behavior in a pore structure. Chapter 9 focuses on the dynamics of droplets on solid heterogeneous surfaces. The CH model coupled with Navier-Stokes (NS) equations or CHNS model is validated against the data from the literature. Thereafter, the thin-film dewetting on chemically patterned surfaces is explored by using CHNS model. Finally, in chapter 10, the whole work is summarized and important achievements, findings are highlighted. The outlook and possible topics for future research are provided.

2. Physical fundamentals and literature review

Wetting is usually termed as the ability of a liquid to maintain contact with a solid surface. Wetting phenomena are where the disciplines chemistry, physics, material science, and engineering meet. Surface chemistry determines the contact energy of the surface with liquids and vapors and it is related to short-ranged interactions. However, surface forces like van der Waals forces are long ranged, which influence the way droplet spreading over a solid surface [22]. Indeed, wetting is involved in a wide range of applications, for instance, from wetting of viruses at the nanoscale to oil recovery at a large scale. In the following, a literature review for the physical fundamentals of wetting, droplet wetting on chemically and mechanically heterogeneous surfaces are conducted.

2.1. Surface tension and Young-Laplace equation

Surface tension is an important factor for wetting phenomena. I could understand it from mechanical and thermodynamic points of view, respectively. It has thus the dimension of force per unit length or energy per unit area. For the former view, the cohesive forces for a molecule within the liquid are equal in every direction, which results in a net force of zero. However, due to the lack of cohesive forces outside of the liquid, the molecules at the surface are pulled inward of the liquid. Besides, there is also tangential force parallel to the liquid surface. The net force causes the liquid surface to form a minimum area. For the latter one, to minimize the energy of the liquid, the number of molecules at the surface, which is of higher energy, must be minimized and this leads to a minimal surface area. Actually the idea that surface tension can only be fully understood if the liquid-gas interface is not considered as sharp but diffuse dates back to Poisson [23]. In the diffuse interface methods, the surface tension of a flat interface is equal to the surface density of the excess grand thermodynamic potential [24].

If the interface is curved, surface tension causes a pressure difference across the liquid-vapor interface. The relationship between the pressure difference Δp and the curvature of the interface is revealed by the Young-Laplace equation, formulating as [25, 26, 27]:

$$\Delta p = \gamma \left(\frac{1}{R_1} + \frac{1}{R_2} \right), \quad (2.1)$$

where γ is surface tension and R_1, R_2 depict the principal radii of curvature. Specially, for a spherical droplet, I have:

$$\Delta p = \frac{2\gamma}{R}, \quad (2.2)$$

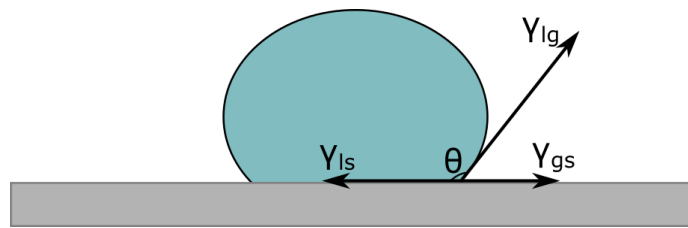


Figure 2.1.: Schematic of Young's equation, which describes a mechanical force balance on the three-phase contact line.

with R denoting the droplet radius and Δp is called Laplace pressure. The equation also explains the creation of emulsions and emulsion coarsening via Ostwald ripening [28]. Moreover, Laplace pressure gradient reveals the mechanism of directional transport of water drops in natural systems [29, 30, 31, 32], and most recently this mechanism is further applied to design droplet transport structures and surfaces [33, 34, 35].

2.2. Contact angle and the Young's law

When a droplet contacts with an ideally smooth, rigid, and solid substrate, it will form a contact line where liquid, gas, and solid substrate meet. As illustrated in Fig. 2.1, the Young's equation [25] relates the surface tensions for liquid-solid γ_{ls} , liquid-gas γ_{lg} , and gas-solid γ_{gs} and the equilibrium contact angle θ through force balance as

$$\gamma_{ls} = \gamma_{gs} - \gamma_{lg} \cos \theta. \quad (2.3)$$

It is noted that the Young's equation describes the droplet at an equilibrium state. The equilibrium contact angle θ is measured macroscopically and its value quantifies the wettability of the surface. For instance, when $\theta < 90^\circ$, the solid surface is considered as hydrophilic while it is called hydrophobic surface when $\theta > 90^\circ$. Especially, when $\theta > 150^\circ$, the surface becomes superhydrophobic, and the droplet on it approaches a spherical shape.

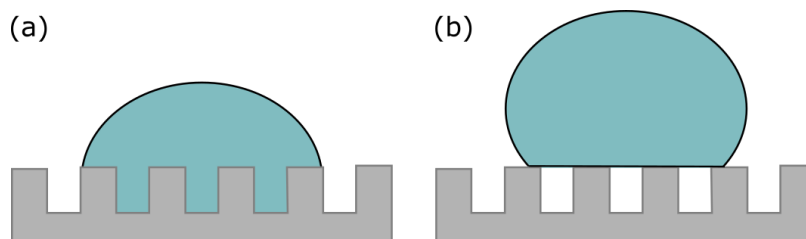


Figure 2.2.: Droplet on rough surfaces. (a) Wenzel state. (b) Cassie-Baxter state.

2.3. The Wenzel and Cassie-Baxter's model

In reality, there are always roughness and defects on a real surface. The chemical and physical properties of the solid surfaces enormously affect the wetting behavior of droplets. It has been shown that if the heterogeneity is three orders of magnitudes smaller than the sessile droplet, it will have little influence on the optical profile of the droplet [14, 36]. In this condition, I could still use the contact angle to characterize the wetting state. The pioneers Wenzel, Cassie, and Baxter have laid the foundations for describing wetting on rough and chemically heterogeneous surfaces since the 1940s [15, 37, 38]. There are two wetting states when droplets are deposited on rough surfaces, namely, the Wenzel state and the Cassie-Baxter state, as shown in Fig. 2.2(a) and (b), respectively. In Wenzel state, the droplet fully wets the rough surface and when the substrate is hydrophilic in chemistry, the roughness facilitates the Wenzel state. However, in Cassie-Baxter state, the droplet stays over the rough structure with pockets of air trapped beneath the droplet. In this state, the droplet indicates a large apparent contact angle and has a small sliding angle. A typical example of this kind of superhydrophobic surface is the Lotus leaf exhibiting a self-cleaning property. The apparent contact angle for Wenzel state is described by the Wenzel equation

$$\cos \theta_w = r \cos \theta, \quad (2.4)$$

where θ_w denotes the Wenzel angle, θ depicts the contact angle for the smooth surface with the same material. r is defined as the ratio of the real to the projected area covered by the drop. Cassie and Baxter extended the formulation of the apparent contact angles for the wetting of porous surfaces. It is assumed that the apparent contact angle is determined by the energies of the contact area under the droplet, which has two components: components 1 and 2. The apparent contact angle is expressed as

$$\cos \theta_{app} = f_1 \cos \theta_1 + f_2 \cos \theta_2, \quad (2.5)$$

where f_1 and f_2 are the area fractions for the two components and θ_1 and θ_2 are the corresponding contact angles, respectively. Indeed Eq. 2.5 can be used to describe droplet wetting state on chemically heterogeneous surfaces with two chemical components. For porous surfaces, one of the component (f_2) is air ($\theta_2 = 180^\circ$), Eq. 2.5 becomes

$$\cos \theta_{CB} = f_1 \cos \theta_1 + f_1 - 1, \quad (2.6)$$

which is the Cassie-Baxter equation and θ_{CB} is Cassie-Baxter angle. It should be noted that the Wenzel and Cassie-Baxter models are valid only if the droplet size is much larger than that of the surface structure. The expressed apparent contact angle of the droplet reveals the average wetting properties of the substrate.

The chemical and geometric heterogeneity of the surfaces, however, can be large and delicately modified to achieve controlled wettability, which is widely applied to printing techniques and microfluidic devices. These chemically heterogeneous and topographically structured surfaces have been studied for decades [39, 40, 41, 42, 43, 44, 45, 46, 19, 47]. Due to the existence of the contact pinning effect and contact angle hysteresis, there may exist multiple equilibrium states so that a unique apparent contact angle is not sufficient to describe the wetting states. A theoretical description of the

wetting behavior of droplets on these surfaces is very challenging. The multiple equilibrium states of droplets correspond to different local free energy minima between which there are energy barriers. The transition between different equilibrium states needs to overcome the energy barriers and thus needs external disturbing forces such as vibration, gravity, and electrical force, etc. The present thesis deals with the problems for wetting morphologies of droplets on chemically patterned surfaces where the pattern size is comparable to the droplet size. A concise theoretical model is established to address this problem and based on this framework the classic Cassie-Baxter model is extended. For more details, please refer to chapter 5.

2.4. Multiphase-droplet-system

Multiphase flow especially ternary fluid flow is omnipresent in the applications of microfluidics, pharmacology, combustion engines, oil recovery, and so on. In the past years, several numerical models addressing the multiphase flow such as PF methods [49, 50, 51, 52, 53], lattice Boltzmann (LB) method [54, 55, 56, 57], level-set model [58, 59, 60] have been proposed. Some of these papers are also involved

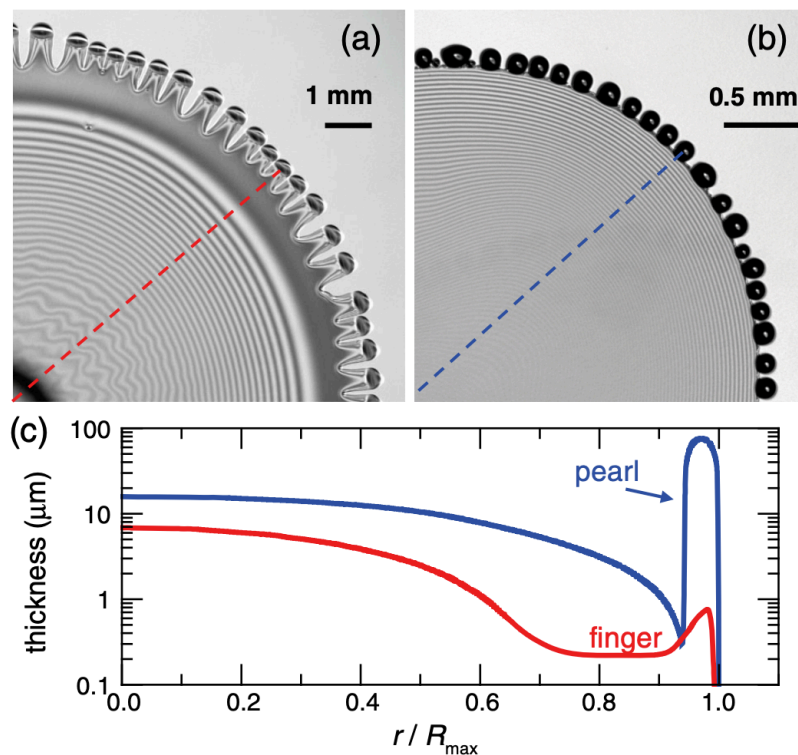


Figure 2.3.: Partial image of an isopropanol drop with (a) ethylene glycol (volume fraction $\phi_v = 0.1$) and (b) dodecane ($\phi_v = 0.1$) spreading on a silicon wafer. The surface tension gradient between isopropanol and ethylene glycol is around 10 times greater than for dodecane. (c) The thickness profiles of the drop in (a) and (b) are highlighted in red and blue colors, corresponding to the red and blue dashed lines in (a) and (b) [48].

with the wetting phenomena. In reality, the different phases can be miscible or immiscible, in/out of chemical equilibrium (chemical potential matching for each component in the system [22]), where many physical phenomena come into play. Typical examples for an immiscible multi-droplet system at chemical equilibrium is the colliding of binary droplets in the air without substrate [61] or with a substrate [62]. While for multiphase-droplet system out of chemical equilibrium, the interesting phenomena include the concentration gradients induced Marangoni flow [6], selective evaporation of droplets [63], fingering instability on substrates (see Fig. 2.3 [48]), and so on. For more examples and comments, readers are referred to the review paper of Lohse and Zhang [64]. The present dissertation utilizes a multiphase Allen-Cahn model to simulate the equilibrium states of immiscible multiphase droplets on a chemically patterned surface (see chapter 7).

2.5. Droplet spreading and thin-film dewetting on solid substrates

When I initially release a droplet onto a solid surface, it will spread and evolve towards its equilibrium shape. The spreading rate of the droplet is of vital importance for many practical applications such as painting, coating, printing, lubrication, to name a few. There are two different descriptions of droplet spreading: (i) Hydrodynamic model; (ii) Molecular kinetic model. The former one describes that the dominant dissipation comes from the viscous flows in the bulk of the droplet. Based on this concept, a scaling law determining the time evolution of the droplet base radius $R_b(t)$ is obtained, which is formulated as $R_b(t) \sim t^{1/10}$. This scaling law is known as Tanner's law and has been widely corroborated by numerous theoretical and experimental works [65, 66, 67, 68, 69, 70, 71, 72, 73, 74]. The latter one emphasizes the dissipation that occurs in the vicinity of the moving contact line caused by the interaction between fluid and solid. This approach describes a scaling law of $R_b(t) \sim t^{1/7}$ [75, 76, 77]. The above analysis is based on the assumption of a small droplet, namely, the droplet radius is smaller than the capillary length. However, if the droplet is large, gravity will take an important role. In this condition, the power in the scaling law becomes 1/8 or 1/7 [22, 78]. If the spreading drops are of low viscosity, and I consider the interplay between inertia and surface tension and regardless of viscous dissipation, the power law in the early stage of spreading becomes $R_b(t) \sim t^{1/2}$ [79]. Bird et al. [80] have shown that the exponent of the scaling law for initial wetting depends on the equilibrium contact angle. In chapter 9, the CHNS model is validated against the experiments in the work of Bird et al. [80].

When the substrate is not homogeneous, the spreading dynamics can be changed. The droplet contact line could be pinned at the local structure or be guided to a preferred direction. Periodically distributed inhomogeneities may cause a stick-slip behavior of the contact line (see Fig. 2.4). In past years, numerous studies have been devoted to this topic theoretically [82, 83, 84, 85], numerically [86, 87, 88] and experimentally [89, 90, 91, 92, 93]. Since the spreading process is enormously influenced by surface properties, researchers are devoted to designing functional surfaces to control the spreading process of droplets. For instance, most recently, Miao et al. [94] found that the microchannel and

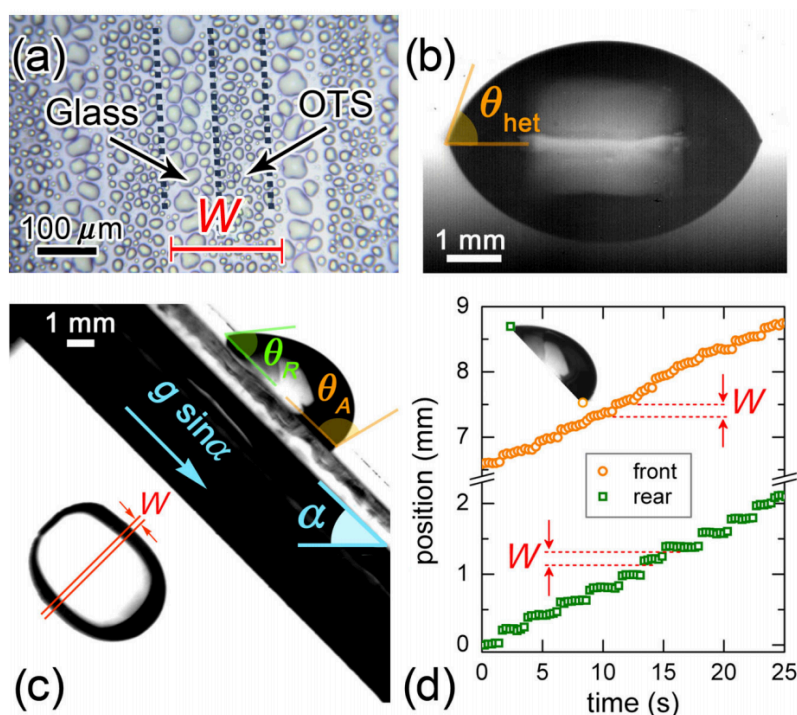


Figure 2.4.: (a) Condensation on a strip patterned surface. The hydrophilic glass and hydrophobic OTS can be recognized by the condensed droplet size: small (large) droplets correspond to hydrophobic OTS (hydrophilic glass). (b) Static water drop on the strip patterned surface. (c) Sliding drop on an inclined substrate. Top right: Lateral view. Bottom left: Contact line view. (d) Stick-slip moving behaviors of the droplet front and rear contact points [81].

nanofiber array morphology facilitates the rapid superspreading on animals' corneas, which provides a guideline for accelerating the spreading speeds of droplets.

Thin-film dewetting phenomena have been exploited in liquids [95, 96, 97, 98, 99], polymers [100, 101, 102, 103, 104, 105] and solids [106, 107, 108]. The study of thin-film dates back to Reynolds [109] who created the so-called "lubrication theory", which is a simplification of the NS equations and denotes a single nonlinear partial differential equation for the film thickness. The film evolution equation has the same form as the CH equation [19, 110]. In recent years, not only the film thickness but other scalar fields have been considered in the coupled evolution equations to address the thin film flows [99]. Various interesting physical phenomena are coming into play in thin-film dynamics. For instance, in the dewetting process, rupture and hole formation usually happen, which leads to different droplet patterns. The thin-film dewetting processes may also cause the fingering of viscous flows, appearing in a wide range of areas. In nature, thin-films are present as tear film in eyes [111], as liquid lining in lungs [112], or even as lava on earth [113]. The applications in which thin-films are involved include microfluidics, lubricating coatings, solar cells, sensors, and others [99, 114]. Fig. 2.5 shows an example of a dewetting polymer thin-film with the pinch-off of a small droplet from the rim. In this community, ruptures, the growth of holes, the stability of liquid fronts have been concerned

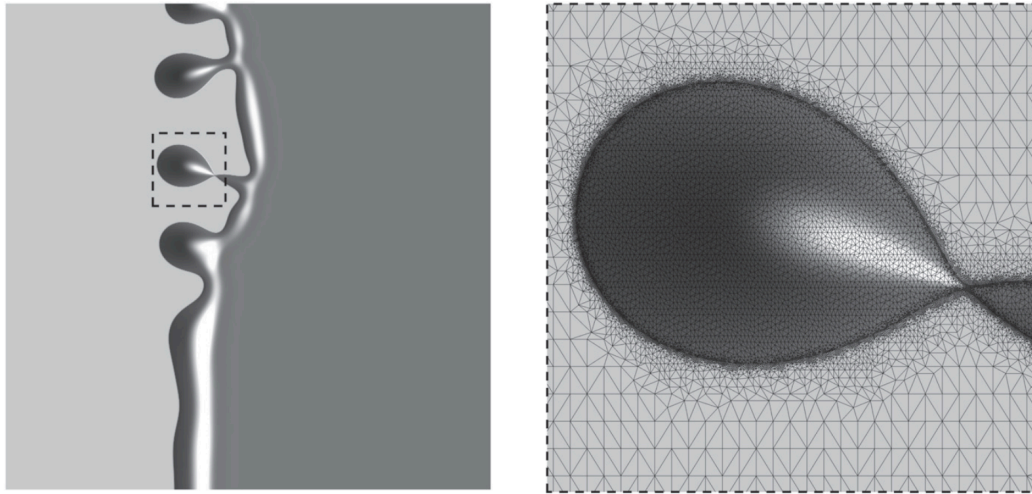


Figure 2.5.: Left: Simulation of a dewetting polymer rim and pinch-off of a single droplet highlighted with dashed lines. Right: Magnification of the highlighted droplet [105].

in the past years. To control the breakup of thin-films, structured or patterned substrates, heat and electric fields, surfactant, and so on have been utilized, making this topic even more fascinating. In chapter 9, thin-film dewetting on the chemically patterned surface is studied using the CHNS model, and the aim is to explore a potential way to break the thin films in a controlled manner.

2.6. Evaporation and condensation of sessile droplets

Evaporation and condensation of sessile droplets on substrates are very common in daily lives and applications like painting, coating, ink-jet printing, DNA chip manufacturing, and so on. Condensation or evaporation takes place when the ambient atmosphere is supersaturated or unsaturated. In the presence of contact angle hysteresis, there are three modes of evaporation or condensation for droplets on a surface, namely, the constant contact angle (CCA) mode, the constant contact radius (CCR) mode and a mixed mode (both contact angle and radius change). In the case of diffusion-controlled evaporation, for a CCA mode, the evaporation rate is directly proportional to the radius of the droplet base or the perimeter [115, 116, 117]. Semenov et al. [118] showed the total evaporation flux has nothing to do

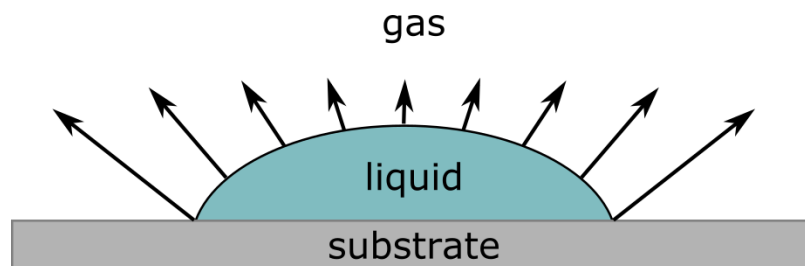


Figure 2.6.: Evaporating sessile droplet on a substrate with locally non-uniform evaporation flux.

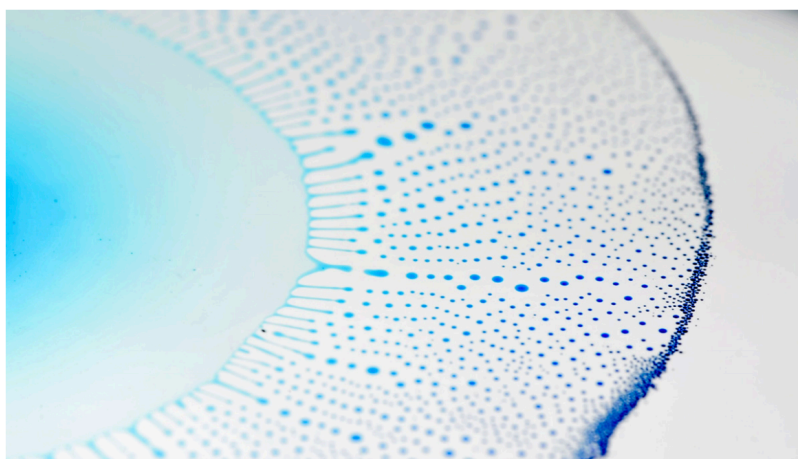


Figure 2.7.: A binary drop of alcohol and water on a bath of sunflower oil. The binary drop spreads and fragments into a myriad of tiny droplets [121].

with the distribution of the local evaporation flux over the droplet surface, but it is proportional to the droplet perimeter. Researches have pointed out that when the contact angle $\theta < 90^\circ$, the evaporation happens more intensively in the vicinity of the three-phase contact line (see Fig. 2.6). The alternative explanations are as follows [117]: (i) The existence of disjoining pressure at the three-phase contact line; (ii) Non-uniform distribution of vapor flux over the droplet; (iii) Non-uniform distribution of the temperature field.

In the evaporation process, Marangoni flow is generated due to a surface tension gradient caused by temperature difference. The effect of Marangoni flow on evaporation rates of heated water drops has been studied by Girard et al. [116]. They concluded that the contribution of the Marangoni flow to the evaporation process can be neglected in comparison with the heat conduction inside the water droplets. Semenov et al. [118] reported that the Marangoni convection introduces nonlinearity in the proportionality of the evaporation rate to the radius of the droplet base. Hu and Larson [119] reported that in particles contained droplet the Marangoni flow prohibits the formation of ring-like stains during the drying process. There are a lot of interesting phenomena related to the Marangoni flow, such as “tears of wine” [120], Marangoni bursting [121, 122] (see Fig. 2.7), and so on.

The investigation of the above-mentioned topics including droplet wetting, droplet dynamics, phase transition, interfacial instability, and others has narrowed the gap from fluid dynamics to chemical engineering, chemistry, and material science. These developments address the challenges in various areas like energy, environment, agriculture, medical, food, industrial production, and so on. To have a quantitative understanding of such physicochemical hydrodynamics systems, numeric modeling is of great significance. In this dissertation, the phase-field models are utilized to address these problems. In the next chapter, the phase-field models will be introduced.

Part II.

Methods

3. Phase-field method

The phase-field method has become a popular and powerful numerical approach for modeling the mesoscale morphological and microstructure evolution in materials appearing in a wide range of areas including metallurgy, hydrodynamics, chemical reactions, phase transformations, and biology [123]. This method describes different phases by using a set of order parameters that rapidly and continuously change across the interfacial regions but maintain constant values in the bulk phases. The diffuseness of the interface between two phases is the most important characteristic of the phase-field model. The concept of “diffuse interface” dates back to van der Waals [124] who considered capillary phenomena based on thermodynamics. The advantage of the diffuse interface is that there is no need to explicitly track the positions of interfaces. This property facilitates the numerical treatment of topological changes and makes it possible to model near-singular interfacial phenomena such as droplet breakup and coalescence, moving contact line [21, 125]. The temporal and spatial evolution of the order parameters is governed by the Cahn-Hilliard (nonlinear diffusion equation) [126, 127] or the Allen-Cahn equation (time-dependent Ginzburg-Landau) [128], both of which reduce the total free energy, obeying the second law of thermodynamics. The main purpose of this chapter is to give a brief introduction of the Allen-Cahn type and Cahn-Hilliard type phase-field models which are adopted in the present dissertation.

3.1. Allen-Cahn model for multiphase system

The Allen–Cahn (AC) model is a reaction–diffusion model which has been utilized to study the motion of anti-phase boundaries in crystalline solids [129], mixture of incompressible fluids [130], nucleation of solids [131], the geometric evolution by mean curvature [132] and so on. The AC model involves a second-order spatial derivative and thus is numerically efficient. However, it is not a mass conservative method, and several researchers have been devoted to developing a volume-preserved type Allen–Cahn model [133, 134, 135, 136, 137, 138, 139, 140], where time-dependent or space and time dependent Lagrange multipliers have been applied to address this issue.

The present dissertation adopts a volume-preserved Allen-Cahn-type phase-field (PF) model which introduces an antiferroic free energy density to counterbalance phase changes [141, 142, 52]. The model is used to simulate the wetting behaviors of (multi-) droplets on chemically patterned surfaces surrounded by air. In this model, a space and time dependent vector-valued variable $\vec{\phi}(\vec{x}, t) = (\phi_1(\vec{x}, t), \dots, \phi_N(\vec{x}, t))$ is introduced to characterize the state of N-phase system. Here, each component $\phi_\alpha(x, t)$, $\alpha \in 1, \dots, N$, describes the state of the phase α . Particularly, in the bulk of each

liquid phase ($\alpha \in 1, \dots, N-1$), I have $\phi_\alpha(\vec{x}, t) = 1$; along the liquid-gas interface, the value of $\phi_\alpha(\vec{x}, t)$ changes from 0 to 1; in the gas phase ($\alpha = N$), $\phi_\alpha(\vec{x}, t) = 0$. Obviously, the constraint $\sum_{\alpha=1}^N \phi_\alpha(\vec{x}, t) = 1$ must be satisfied. Based on the Ginzburg-Landau energy density functional, the free energy functional with volume preservation is formulated as:

$$\mathcal{F} = \int_{\Omega} [(1/\epsilon)w(\vec{\phi}) + \epsilon a(\vec{\phi}, \nabla \vec{\phi}) + f_0(\vec{\phi})] d\Omega, \quad (3.1)$$

where Ω is the spatial domain and ϵ determines the interface width.

The multi-obstacle potential $w(\vec{\phi})$ reads:

$$w(\vec{\phi}) = \frac{16}{\pi^2} \sum_{\alpha < \beta} \gamma_{\alpha\beta} \phi_\alpha \phi_\beta + \sum_{\alpha < \beta < \delta} \gamma_{\alpha\beta\delta} \phi_\alpha \phi_\beta \phi_\delta, \quad (3.2)$$

with $\gamma_{\alpha\beta}$ denoting the surface/interfacial energy density of the α - β phase boundary. The higher order term $\sum_{\alpha < \beta < \delta} \gamma_{\alpha\beta\delta} \phi_\alpha \phi_\beta \phi_\delta$ suppresses the artificial third phase contributions along binary phase boundaries [143]. The multi-obstacle potential can be also substituted by a multi-well type potential [144], but the multi-obstacle potential showed advantageous in terms of the calibration of surface energy densities [141].

The term $a(\vec{\phi}, \nabla \vec{\phi})$ is the gradient energy density and is expressed as

$$a(\vec{\phi}, \nabla \vec{\phi}) = \sum_{\alpha < \beta} \gamma_{\alpha\beta} (\phi_\alpha \nabla \phi_\beta - \phi_\beta \nabla \phi_\alpha)^2, \quad (3.3)$$

with $\vec{q} = (\phi_\alpha \nabla \phi_\beta - \phi_\beta \nabla \phi_\alpha)$ indicating a generalized gradient vector.

The bulk free energy density $f_0(\phi)$ is introduced to ensure the volume preservation:

$$f_0(\vec{\phi}) = \sum_{\alpha=1}^N \chi_\alpha h(\phi_\alpha). \quad (3.4)$$

Here, χ_α is a weight function discussed in literature [141]. $h(\phi_\alpha) = \phi_\alpha^3(6\phi_\alpha^2 - 15\phi_\alpha + 10)$ depicts an interpolation function and its first derivative equals zero in the bulk phase.

To model the liquid-solid interaction, a wall free energy f_w is added to the original free energy functional, thus:

$$\mathcal{F} = \int_{\Omega} [(1/\epsilon)w(\vec{\phi}) + \epsilon a(\vec{\phi}, \nabla \vec{\phi}) + f_0(\vec{\phi})] d\Omega + \int_{A_{ls}} f_w(\phi) dA, \quad (3.5)$$

with A_{ls} indicating the solid-fluid boundary. f_w is given as

$$f_w = \sum_{\alpha < \beta} \gamma_{\alpha s} h(\phi_\alpha) + m \sum_{\alpha < \beta < \delta} \gamma_{\alpha\beta\delta} \phi_\alpha \phi_\beta \phi_\delta. \quad (3.6)$$

Here, $\gamma_{\alpha s}$ represents the surface tension between the phase α and solid substrate.

The equilibrium state of the system meets with the condition for $\delta\mathcal{F}/\delta\phi = 0$ (δ -variational derivative). A time relaxation coefficient τ is introduced to describe the free energy evolution following the gradient descent path (the so-called model A dynamics [145, 146]): $\tau\epsilon\partial_t\phi = -\delta\mathcal{F}/\delta\phi$, which is further formulated as

$$\tau\epsilon\partial_t\phi_\alpha = -(1/\epsilon)w_{,\phi_\alpha}(\vec{\phi}) + \epsilon(\nabla \cdot a_{,\nabla\phi_\alpha}(\vec{\phi}, \nabla \vec{\phi}) - a_{,\phi_\alpha}(\vec{\phi}, \nabla \vec{\phi})) - f_{0,\phi_\alpha}(\vec{\phi}) - \lambda_1, \quad (3.7)$$

in Ω and the natural boundary condition on A_{ls} :

$$-\epsilon a_{,\nabla\phi_\alpha}(\vec{\phi}, \nabla\vec{\phi}) \cdot \vec{n} - f_{w,\phi_\alpha}(\vec{\phi}) - \lambda_2 = 0. \quad (3.8)$$

Here, \vec{n} is the normal vector of the substrate. It is worth noting that Eq. 3.8 relates the interfacial/surface tensions between liquid-gas, liquid-liquid, liquid-solid, and gas-solid, and ensures the right equilibrium contact angles on the substrate. The partial derivatives $\partial/\partial_{\phi_\alpha}$ and $\partial/\partial_{\nabla\phi_\alpha}$ of the functions are indicated by the subscript $_{,\phi_\alpha}$ and $_{,\nabla\phi_\alpha}$, respectively. The Lagrange multipliers λ_1 and λ_2 ensure the constraint $\sum_{\alpha=1}^N \phi_\alpha(\vec{x}, t) = 1$ in the domain Ω and on the substrate A_{ls} , respectively, which are given as follows:

$$\lambda_1 = \frac{1}{N} \sum_{\alpha=1}^N \left(-(1/\epsilon)w_{,\phi_\alpha}(\vec{\phi}) + \epsilon(\nabla \cdot a_{,\nabla\phi_\alpha}(\vec{\phi}, \nabla\vec{\phi}) - a_{,\phi_\alpha}(\vec{\phi}, \nabla\vec{\phi})) - f_{0,\phi_\alpha}(\vec{\phi}) \right), \quad (3.9)$$

$$\lambda_2 = \frac{1}{N} \sum_{\alpha=1}^N \left(-\epsilon a_{,\nabla\phi_\alpha}(\vec{\phi}, \nabla\vec{\phi}) \cdot \vec{n} - f_{w,\phi_\alpha}(\vec{\phi}) \right). \quad (3.10)$$

For a sufficiently long time, the functional derivative $\delta\mathcal{F}/\delta\phi$ approaches zero, and the energy minimum state or equilibrium state is achieved.

3.2. Allen-Cahn model for two-phase system

For a liquid-gas system $N = 2$, I have then $\phi_l(\vec{x}, t) + \phi_g(\vec{x}, t) = 1$ with the symbol l and g standing for liquid and gas phases, respectively. In this case, by defining the local volume fraction of the liquid phase $\phi_l(\vec{x}, t) := \phi$ and then I obtain the local volume fraction of the liquid phase $\phi_g(\vec{x}, t) = 1 - \phi$. The total free energy functional becomes

$$\mathcal{F} = \int_{\Omega} [(1/\epsilon)w(\phi) + \epsilon\gamma_{lg}(\nabla\phi)^2 + f_0(\phi)]d\Omega + \int_{A_{ls}} f_w(\phi)dA, \quad (3.11)$$

with the obstacle potential: $w(\phi) = (16/\pi^2)\gamma_{lg}\phi(1 - \phi)$, if $0 \leq \phi \leq 1$; and $w(\phi) = \infty$, if $\phi < 0$ or $\phi > 1$. γ_{lg} is the liquid-gas surface tension. The term $\epsilon\gamma_{lg}(\nabla\phi)^2$ indicates a gradient energy density and $f_0(\phi)$ ensures the volume preservation. The wall free energy density is simplified as

$$f_w(\phi) = \gamma_{ls}h(\phi) + \gamma_{gs}[1 - h(\phi)], \quad (3.12)$$

without the higher order term. The evolution of ϕ is:

$$\tau\epsilon\partial_t\phi = -(16/\pi^2)\gamma_{lg}(1 - 2\phi)/\epsilon + 2\epsilon\gamma_{lg}\Delta\phi - f'_0(\phi) - kh'(\phi) - g'(\phi), \quad (3.13)$$

in Ω and

$$-2\epsilon\gamma_{lg}\nabla\phi \cdot \vec{n} + (\gamma_{gs} - \gamma_{ls})h'(\phi) = 0. \quad (3.14)$$

on A_{ls} . γ_{ls} and γ_{gs} are liquid-solid and gas-solid interfacial tensions, respectively. Eq. 3.14 describes an equilibrium relationship between γ_{lg} , γ_{ls} and γ_{gs} , which leads to the classic Young's law. This

boundary condition can be also modified as a dynamic type by introducing a phenomenological parameter τ_w determining the deviation of the dynamic contact angle from the equilibrium one. It is formulated as [21]:

$$\tau_w \partial_t \phi = 2\epsilon \gamma_{lg} \nabla \phi \cdot \vec{n} - (\gamma_{gs} - \gamma_{ls}) h'(\phi). \quad (3.15)$$

The parameter τ_w is related to the physical properties such as density and viscosity. For smaller τ_w the contribution from the term $\tau_w \partial_t \phi$ can be neglected and the contact angle immediately approaches the equilibrium contact angle as the liquid contact with the substrate. However, for greater τ_w , the dynamic contact angle deviates significantly from the static equilibrium one and the fast interfacial dynamics or the states out of equilibrium can be captured. The study of moving contact lines by using diffuse-interface approach has become popular in past decades [147, 148, 44, 149, 17, 150, 151, 152, 153], and this diffuse-interface model has been proved to agree remarkably well with the molecular dynamics simulations and experiments.

According to the studied system, the total free energy may also include elastic strain energy, magnetic energy, electrostatic energy, and/or under applied external fields such as electrical, temperature, and magnetic fields [123]. The present dissertation takes the influence of evaporation/condensation and gravity into consideration. The total free energy can be extended as:

$$\mathcal{F} = \int_{\Omega} [(1/\epsilon)w(\phi) + \epsilon \gamma_{lg} (\nabla \phi)^2 + f_0(\phi) + f_{driv}(\phi) + g(\phi)] d\Omega + \int_{A_{ls}} f_w(\phi) dA. \quad (3.16)$$

Here, $f_{driv}(\phi)$ describes the driving force for evaporation/condensation and is formulated as

$$f_{driv}(\phi) = kh(\phi), \quad (3.17)$$

where k is a constant determining the phase change rate. The term $g(\phi)$ models the gravitational effect, which is expressed as

$$g(\phi) = \rho_l \vec{g} \cdot \vec{x} h(\phi) - \rho_g \vec{g} \cdot \vec{x} [1 - h(\phi)]. \quad (3.18)$$

Here, ρ_l and ρ_g are liquid and gas densities, respectively, and \vec{g} is the gravity vector.

The evolution of ϕ in Ω is

$$\tau \epsilon \partial_t \phi = -(16/\pi^2) \gamma_{lg} (1 - 2\phi)/\epsilon + 2\epsilon \gamma_{lg} \Delta \phi - f'_0(\phi) - kh'(\phi) - g'(\phi). \quad (3.19)$$

The evolution of ϕ on A_{ls} is also controlled by Eq. 3.14 or Eq. 3.15.

3.3. Cahn-Hilliard model for multiphase system

In this section, Cahn-Hilliard (CH) model is introduced. The CH model is a fourth-order PDE and becomes more and more popular in simulating complex and evolving interface topologies and interfacial instability for multi-phase flow due to its conservative nature. For a multi-phase system, to distinguish from the Allen-Cahn model, the order parameter is indicated by the vector-valued variable $\vec{c}(\vec{x}, t) = (c_1(\vec{x}, t), c_2(\vec{x}, t), \dots, c_N(\vec{x}, t))$ with the component c_i denoting the state of the phase

i. Concerning the constraint $\sum_{i=1}^N c_i = 1$, there is only $N - 1$ independent component(s). The time evolution of the compositions for each component follows the so-called model H dynamics [145, 146]:

$$\frac{\partial c_i}{\partial t} + \vec{u} \cdot \nabla c_i = \nabla \cdot \left[\sum_{j=1}^N (M_{ij} \nabla \frac{\delta \mathcal{F}}{\delta c_j}) \right], \quad i = 1, 2, \dots, N. \quad (3.20)$$

Here, \vec{u} is the velocity of convection and the Onsager mobility coefficient M_{ij} is expressed as

$$M_{ij} = \begin{cases} M_0 c_i (1 - c_i) & \text{if } i = j; \\ -M_0 c_i c_j & \text{else,} \end{cases} \quad (3.21)$$

with $M_0 = \epsilon D / \sigma$. σ is a parameter related to the surface energy density and D is the diffusion coefficient. The generalized free energy functional for an N -component mixture can be formulated as [126, 154, 145, 155]:

$$\mathcal{F} = \int_{\Omega} \left[f(c) - 2\sigma \epsilon \sum_{i,j=1}^N K_{ij} \nabla c_i \nabla c_j \right] d\Omega, \quad (3.22)$$

where K_{ij} is gradient energy matrix related to the surface tension between domains with composition differences. The bulk free energy density f reads

$$f = \frac{\sigma}{\epsilon} \left(\sum_{i=1}^N c_i \ln c_i + \sum_{i,j=1}^N \chi_{ij} c_i c_j \right). \quad (3.23)$$

Here, χ_{ij} indicates the interaction parameter between components i and j . When $i = j$, $\chi_{ij} = 0$. To solve the solution for velocity and order parameter the Navier–Stokes equations must be coupled. The Navier-Stokes equation reads

$$\rho \left(\frac{\partial \vec{u}}{\partial t} + \vec{u} \cdot \nabla \vec{u} \right) = -\nabla p - \nabla \cdot \bar{\bar{\Theta}} + \nabla \cdot \mu (\nabla \vec{u} + \nabla \vec{u}^T). \quad (3.24)$$

Note that the contribution of capillary forces in this equation is given by the term $-\nabla \cdot \bar{\bar{\Theta}}$ with the Korteweg stress tensor $\bar{\bar{\Theta}} = \sum_{i=1}^N c_i \nabla \frac{\delta \mathcal{F}}{\delta c_i}$ [147, 156, 157, 145, 158]. p , ρ and μ indicate pressure, density and dynamic viscosity, respectively. ρ and μ can be linearly interpolated by the order parameter [159]. Together with the incompressibility constraint:

$$\nabla \cdot \vec{u} = 0, \quad (3.25)$$

and given boundary and initial conditions, the whole system (\vec{u}, p, c_i) can be solved [159].

However, in the diffusive regime with smaller velocity, model H reduces to model B (without hydrodynamic flow) behavior and the second term in Eq. 3.20 vanishes and there is no need to solve NS equations. Most recently, Mao et al. have adopted model B to investigate the equilibrium phase behavior and morphology of N -component ($N > 3$) liquid mixtures [155, 160].

3.4. Cahn-Hilliard model for two-phase system

For a two-phase system with $N = 2$ and $c_1 + c_2 = 1$ I obtain the Cahn-Hilliard equation for c_1 :

$$\frac{\partial c_1}{\partial t} + \vec{u} \cdot \nabla c_1 = \nabla \cdot \left(\frac{\epsilon}{\sigma} D c_1 (1 - c_1) \nabla \frac{\delta \mathcal{F}}{\delta c_1} \right) + \nabla \cdot \left(-\frac{\epsilon}{\sigma} D c_1 c_2 \nabla \frac{\delta \mathcal{F}}{\delta c_2} \right), \quad (3.26)$$

By defining $c =: c_1$ and substituting c_2 with $1 - c$, I have:

$$\frac{\partial c}{\partial t} + \vec{u} \cdot \nabla c = \nabla \cdot \left(\frac{\epsilon}{\sigma} Dc(1 - c) \nabla \frac{\delta \mathcal{F}}{\delta c} \right), \quad (3.27)$$

The free energy functional of the system \mathcal{F} is written as

$$\mathcal{F} = \int_{\Omega} \left[f(c) + 2\sigma\epsilon(\nabla c)^2 \right] d\Omega. \quad (3.28)$$

The free energy density f reads [161]

$$f(c) = \frac{\sigma}{\epsilon} [c \ln c + (1 - c) \ln(1 - c) + \chi c(1 - c)]. \quad (3.29)$$

χ indicates an interaction coefficient between the two components. This is a double-well function with energy minima $(c_{e1}, f(c_{e1}))$ and $(c_{e2}, f(c_{e2}))$. The concentrations c_{e1} and c_{e2} denote the two equilibrium concentrations with $f'(c_{e1}) = f'(c_{e2}) = 0$. The advantage of choosing a double-well potential is that the spinodal decomposition can be captured. While this is not possible by using a obstacle potential, since there is no inflection point in the obstacle function [162].

Substituting the above two equations into Eq. 3.27, the following equation is obtained:

$$\frac{\partial c}{\partial t} + \vec{u} \cdot \nabla c = \nabla \cdot \left[\frac{\epsilon}{\sigma} Dc(1 - c) \nabla \left(\frac{\partial f}{\partial c} - 4\sigma\epsilon \nabla^2 c \right) \right], \quad (3.30)$$

The Navier-Stokes equation reads

$$\rho \left(\frac{\partial \vec{u}}{\partial t} + \vec{u} \cdot \nabla \vec{u} \right) = -\nabla p - \nabla \cdot \bar{\bar{\Theta}} + \nabla \cdot \mu(\nabla \vec{u} + \nabla \vec{u}^T) + \rho \vec{g}. \quad (3.31)$$

The capillary force is described by the term $-\nabla \cdot \bar{\bar{\Theta}}$ with the stress tensor $\bar{\bar{\Theta}} = 4\sigma\epsilon \nabla c \otimes \nabla c - (2\sigma\epsilon \nabla c \cdot \nabla c + f) \bar{\bar{I}}$ [163, 161]. $\bar{\bar{I}}$ is the unit tensor. The formulation of the potential form of the surface tension forcing can be written as $\frac{\partial f}{\partial c} \nabla c$ or $-c \nabla \frac{\partial f}{\partial c}$, as discussed in the literature [21]. Bonart et al. have found that nonlinear relation between density and order parameter leads to the loss of total mass [164]. In this work, ρ and μ have linear functional relationship with the order parameter c :

$$\rho(c) = \rho_g + \frac{\rho_w - \rho_g}{c_{e2} - c_{e1}} (c - c_{e1}), \quad (3.32)$$

$$\mu(c) = \mu_g + \frac{\mu_w - \mu_g}{c_{e2} - c_{e1}} (c - c_{e1}). \quad (3.33)$$

ρ_g and ρ_w are densities for gas and liquid phases. μ_g and μ_w are dynamic viscosities for gas and liquid phases. For an incompressible system, the densities for gas and liquid don't change and I obtain

$$\nabla \cdot \vec{u} = 0. \quad (3.34)$$

For small density ratio, usually the Boussinesq approximation is used to handle the densities [159].

3.4.1. Non-dimensional calculation

By choosing three parameters namely surface tension of water ($\sigma = 7.28 \times 10^{-2}$ N/m), and viscosity of water ($\mu_w = 1.0 \times 10^{-3}$ kg/ms) and characteristic length ($x^* = 1 \times 10^{-5}$ m) as characteristic

parameters, the related physical variables can be non-dimensionilzed. The scaling factors is as follows: velocity $u^* = \sigma/\mu_w$, time $t^* = \mu_w x^*/\sigma$, and pressure $p^* = \mu_w u^*/x^*$. The dimensionless variables are calculated by these scaling factors such that I obtain $\tilde{u} = u/u^*$, $\tilde{t} = t/t^*$, $\tilde{p} = p/p^*$, $\tilde{x} = x/x^*$, $\tilde{\mu} = \mu/\mu_w$ and so on. The variables labeled with tilde are dimensionless variables. The dimensionless CH equation reads

$$\frac{\partial c}{\partial \tilde{t}} + \tilde{u} \cdot \tilde{\nabla} c = (1/Pe) \tilde{\nabla} \cdot \left[c(1-c) \tilde{\nabla} \left(\frac{\partial \tilde{f}}{\partial c} - 4Cn^2 \tilde{\nabla}^2 c \right) \right], \quad (3.35)$$

where $Pe = u^* x^*/D$ and $Cn = \epsilon/x^*$ are Peclet number and Cahn number, respectively. The dimensionless NS equation is

$$(\rho/\rho_w) \left(\frac{\partial \tilde{u}}{\partial \tilde{t}} + \tilde{u} \cdot \tilde{\nabla} \tilde{u} \right) = -(1/Re) \tilde{\nabla} \tilde{p} \quad (3.36)$$

$$+ [1/(WeCn)] \tilde{\nabla} \cdot [(Cn^2 \tilde{\nabla} c \cdot \tilde{\nabla} c + \tilde{f})I - 4Cn^2 \tilde{\nabla} c \otimes \tilde{\nabla} c] \quad (3.37)$$

$$+ (1/Re) \tilde{\nabla} \cdot (\mu/\mu_w) (\tilde{\nabla} \tilde{u} + \tilde{\nabla} \tilde{u}^T) + (Bo/We) (\rho/\Delta\rho) \vec{e}_z, \quad (3.38)$$

where $Re = \rho_w x^* u^*/\mu_w$, $Bo = \Delta\rho g(x^*)^2/\sigma$, $We = \rho_w (u^*)^2 x^*/\sigma$ are Reynolds number, Bond number, and Weber number respectively. The Reynolds number Re describes the ratio between the inertial and viscous force. The Bond number Bo expresses the ratio between the buoyancy and the surface tension force. \vec{e}_z is the unit vector in the z -direction. The Weber number We expresses the ratio between the inertia and surface tension force. The incompressible constraint:

$$\nabla \cdot \tilde{u} = 0. \quad (3.39)$$

3.4.2. Calculation of surface tension

The surface energy (surface tension between liquid and gas) can be considered as the total grand chemical potential excess at the interface

$$\gamma_{lg} = \int_{-\infty}^{+\infty} (\Delta f + 2\sigma\epsilon(\partial c/\partial x)^2) dx, \quad (3.40)$$

where $\Delta f = f(c) - f(c_{e1})$ or $\Delta f = f(c) - f(c_{e2})$. The concentrations c_{e1} and c_{e2} are the two equilibrium concentrations with $f'(c_{e1}) = f'(c_{e2}) = 0$. At equilibrium, $\Delta f = 2\sigma\epsilon(\partial c/\partial x)^2$ and I obtain

$$\gamma_{lg} = \int_{-\infty}^{+\infty} 4\sigma\epsilon(\partial c/\partial x)^2 dx = \int_{c_{e1}}^{c_{e2}} 4\sigma\epsilon(\partial c/\partial x) dc \quad (3.41)$$

By changing dx as dc :

$$\gamma_{lg} = \int_{c_{e1}}^{c_{e2}} 2\sqrt{2\sigma\epsilon\Delta f} dc = \sigma * I \quad (3.42)$$

where

$$I = 2 \int_{c_{e1}}^{c_{e2}} \sqrt{2\Delta f} dc, \quad (3.43)$$

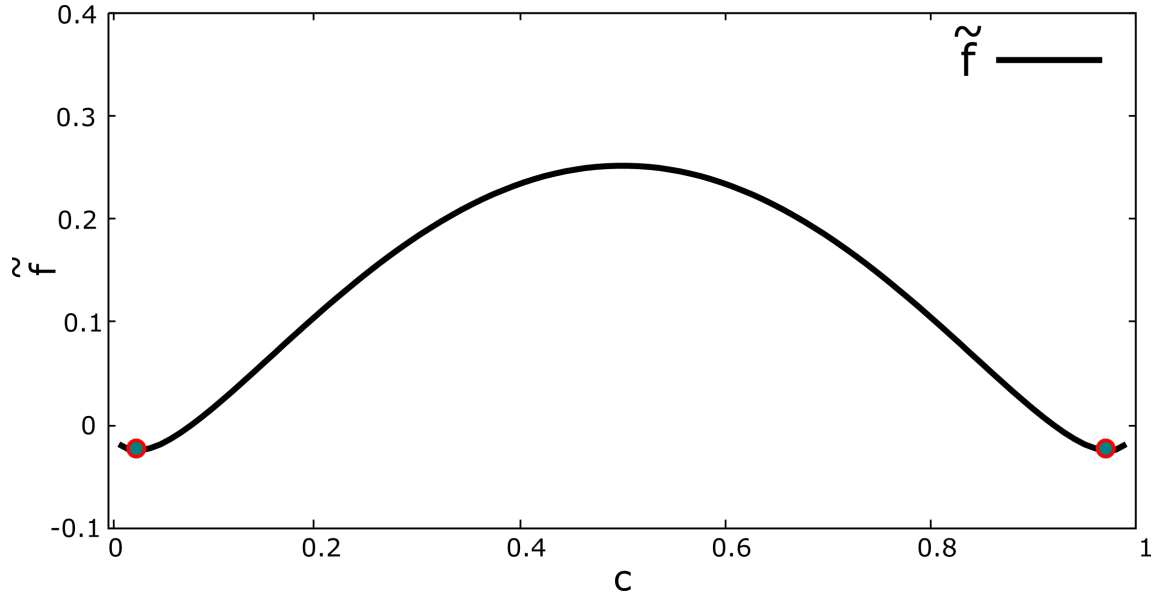


Figure 3.1.: The free energy \tilde{f} as a function of concentration c : $\tilde{f}(c) = c \ln c + (1 - c) \ln(1 - c) + 3.78c(1 - c)$. The two points $(0.0273, -0.0249)$ and $(0.9727, -0.0249)$ are the free energy minimum states, corresponding to the gas and liquid bulk phases, respectively.

with $\Delta\tilde{f} = \epsilon\Delta f/\sigma$. Let the integration $I = 1$, then I have $\gamma_{lg} = \sigma$. One alternative double-well function $f(c)$ is given:

$$\tilde{f}(c) = c \ln c + (1 - c) \ln(1 - c) + \chi c(1 - c), \quad (3.44)$$

with $\chi = 3.78$, $c_{e1} = 0.0273$ and $c_{e2} = 0.9727$. Fig. 3.1 displays the double-well function with two local minima.

3.4.3. Derivation of the natural boundary condition

At the substrate, the free energy functional reads

$$\mathcal{F}_s = \int_{\Omega} 2\sigma\epsilon(\nabla c)^2 d\Omega + \int_{A_{ls}} f_w(c) dA. \quad (3.45)$$

Here, $f_w(c) = \gamma_{ls}l(c) + \gamma_{gs}(1 - l(c))$ with $l(c) = -4.73c^3 + 7.10c^2 - 0.38c$ denoting an interpolation function with $l(c_{e1}) = 0$, $l(c_{e2}) = 1$, and $l'(c_{e1}) = l'(c_{e2}) = 0$. The variational calculation

$$\frac{\delta\mathcal{F}_s}{\delta c} = 0, \quad (3.46)$$

together with the divergence theorem transforming the volume integration to the surface integral lead to the following boundary condition at the fluid-substrate interface:

$$4\sigma\epsilon\nabla c \cdot \vec{n} - (\gamma_{gs} - \gamma_{ls})l'(c) = 0. \quad (3.47)$$

With $\gamma_{lg} = \sigma$, the dimensionless equation reads

$$4Cn\tilde{\nabla}c \cdot \vec{n} - \frac{(\gamma_{gs} - \gamma_{ls})}{\gamma_{lg}}l'(c) = 0 \quad (3.48)$$

For the dynamic boundary:

$$\tau_w \frac{\partial c}{\partial t} = 4\gamma_{lg} \epsilon \nabla c \cdot \vec{n} - (\gamma_{gs} - \gamma_{ls}) l'(c) \quad (3.49)$$

Here, the parameter τ_w is phenomenological parameter. The dimensionless dynamic boundary:

$$Ag \tilde{\tau}_w \frac{\partial c}{\partial \tilde{t}} = 4Cn \tilde{\nabla} c \cdot \vec{n} - \frac{(\gamma_{gs} - \gamma_{ls})}{\gamma_{lg}} l'(c) \quad (3.50)$$

$Ag = \mu_w u^* / \sigma$ is a dimensionless number expressing the ratio between the work done by the viscous force and the energy needed for a molecular site interchange [17].

Part III.

Results and discussion: Static or quasi-static problems

4. Single droplet on chemically striped surfaces: A phase-field investigation

In this chapter, the AC model is used to simulate the equilibrium shape of a single droplet with different sizes deposited on chemically striped patterned surfaces. Additionally, the movements of evaporating and condensing droplets in quasi-equilibrium and far from equilibrium states are analyzed. The outline of this chapter is as follows. Firstly, simulation setups are introduced. Next, numerical validations are carried out to show the validity of the AC model. Thereafter, the numerical results along with a detailed analysis of the droplet shapes are presented. At last, the whole work in this chapter is summarized and the vision for future work is given. This chapter was published in Ref. [165].

4.1. Simulation setups

The evolution equations for the order parameter are discretized by the finite difference method with an explicit Euler time marching scheme. The simulations are performed in 3D geometries by using an equidistant mesh with a spacing of $\Delta x = \Delta y = \Delta z$. The effect of the mesh resolution on the simulation results is investigated in the following section. The numerical stability of the simulations is guaranteed by choosing a fine time step $\Delta t < \tau(\Delta x)^2 / (2 \cdot \text{dimension} \cdot 2\gamma_{lg})$ according to the von Neumann stability analysis [161].

In the simulations, I set the relaxation parameter $\tau = 1$. The length x , time t , and energy E are nondimensionalized by the characteristic length $x^* = 1 \times 10^{-6}$ m, the characteristic time $t^* = 1 \times 10^{-9}$ s, and the characteristic energy $E^* = 1 \times 10^{-11}$ J, respectively. In the following, transformed dimensionless parameters are used.

4.2. Validation of the numerical model

Numerical simulations are performed to show the validity of the phase-field model for simulating droplet wetting on surfaces with certain equilibrium contact angles. Firstly, the sensitivity study of the mesh resolution is conducted. Droplets with different values of the Cahn number Cn , which is defined as the ratio of the interface width ε to the droplet diameter D , are simulated. Our simulations are carried out in a 3D domain with a size of $200 \times 200 \times 120$. The number of cells across the droplet-gas interface is kept as 10 in all of the simulations. At the beginning, a droplet with a radius of 40 is placed on the top of the surface and the distance between the mass point of the droplet and the

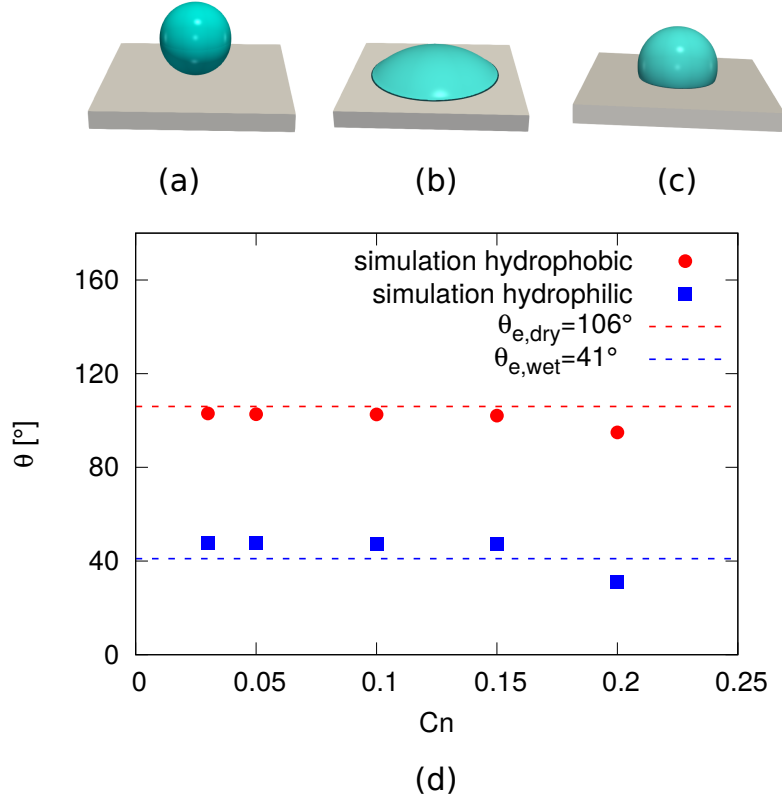


Figure 4.1.: Snapshots of droplets and sensitivity study depending on the Cahn number: (a) droplet at initial time, (b) and (c) droplets at equilibrium on two different surfaces, (d) simulation results on two different surfaces for different values of Cn . The red circles and blue squares show the simulation results on surfaces with equilibrium contact angles $\theta_{e,wet} = 41^\circ$ and $\theta_{e,dry} = 106^\circ$ respectively. The red and blue dashed lines correspond to the two equilibrium contact angles $\theta_{e,wet} = 41^\circ$ and $\theta_{e,dry} = 106^\circ$.

surface is the same as its radius. The initial setup is shown in Figure 4.1(a). In Figure 4.1(b) and (c), the equilibrium states of a droplet on surfaces with equilibrium contact angles $\theta_{e,wet} = 41^\circ$ and $\theta_{e,dry} = 106^\circ$ are presented, respectively. The contact angles of droplets at the final state on the two surfaces are measured by using a modified marching square algorithm [166, 167] Figure 4.1(d) shows the simulation results for droplets with Cahn number Cn varying from 0.03 to 0.2, which is achieved by varying the resolution Δx from 0.6 to 4. The red circles and blue squares represent the simulation results on surfaces with equilibrium contact angles $\theta_{e,wet} = 41^\circ$ and $\theta_{e,dry} = 106^\circ$, respectively. The red and blue dashed lines correspond to the two equilibrium contact angles $\theta_{e,wet} = 41^\circ$ and $\theta_{e,dry} = 106^\circ$ according to the Young's law. It is observed from Figure 4.1(d) that the simulation results on the two surfaces are convergent to the equilibrium contact angles as the Cahn number Cn decreases. When $Cn < 0.15$, the variation of the results is very small, while for $Cn = 0.2$, a relatively big deviation

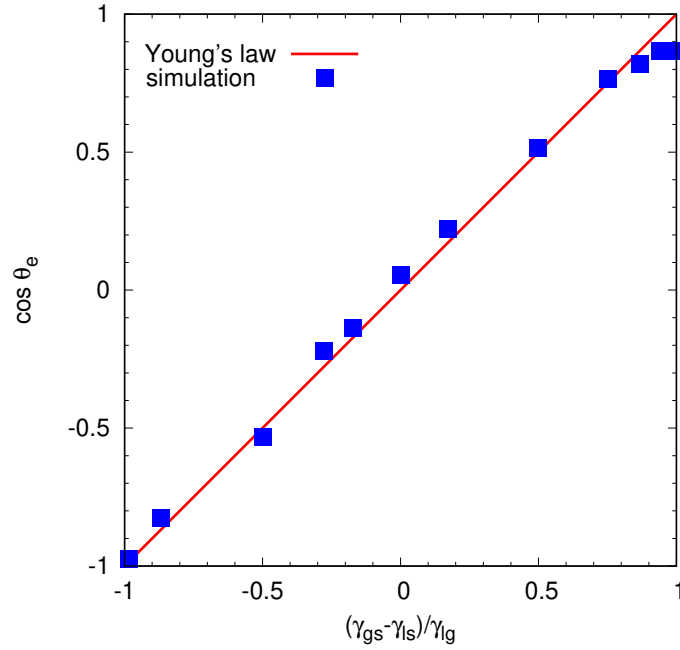


Figure 4.2.: The cosine of the equilibrium contact angle versus $(\gamma_{gs} - \gamma_{ls})/\gamma_{lg}$. Blue squares show the simulation results and the contact angles of droplets at final states are measured by using a modified marching square algorithm [166, 167]. The red line corresponds to the theoretical prediction of Young's law.

appears. As a compromise of the simulation precise and computational efforts, the Cahn number Cn is constrained in the range of $Cn \in [0.05, 0.15]$ for the simulations in this work.

After the sensitivity study of the mesh resolution, the approach capturing contact angle is validated. Droplets deposited on homogeneous surfaces with equilibrium contact angles ranging from 10° to 170° are simulated. At equilibrium, the contact angles are measured through a modified marching square algorithm [166, 167]. The cosine of measured data versus $(\gamma_{gs} - \gamma_{ls})/\gamma_{lg}$ is plotted in Figure 4.2. The simulation results are shown by the blue squares and the red line depicts the theoretical prediction of Young's law. The simulations match the Young's law very well except when the contact angle is less than 20° , i.e., $(\gamma_{gs} - \gamma_{ls})/\gamma_{lg} > 0.94$, which is due to the limited numerical resolution of small contact angles.

Next, the phase-field model for simulating spreading dynamics of a partially wetting droplet on a flat surface is validated against an exponential power law proposed by Lavi and Marmur [168]. The main purpose is to show the validity of the dynamical contact angle boundary condition and to study the influence of the phenomenological parameter τ_w . The exponential power law of Lavi and Marmur [168] was empirically derived from experimental data reading

$$\frac{A}{A_f} = 1 - \exp(-\lambda t^m) \quad (4.1)$$

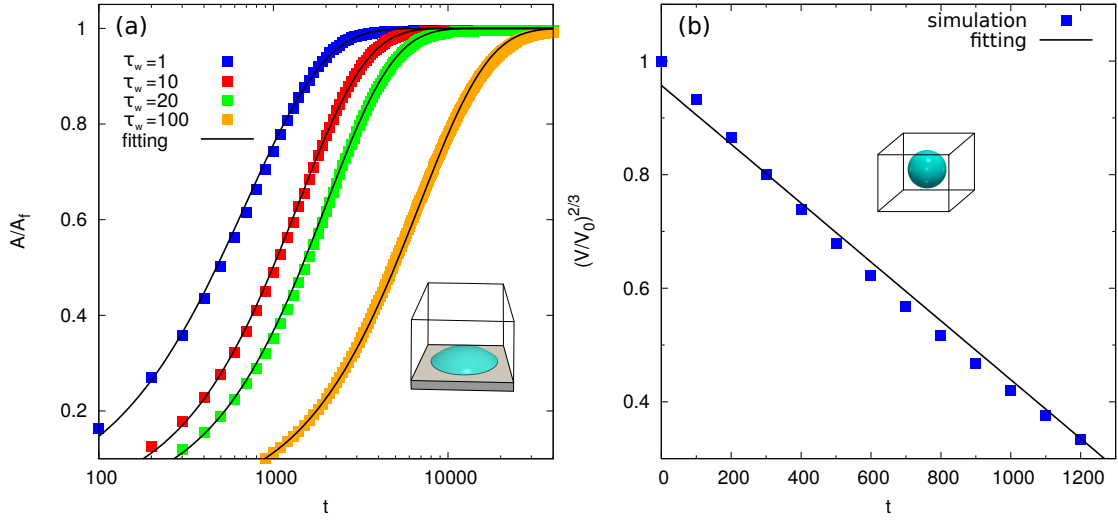


Figure 4.3.: Validation of the numerical model through comparison with analytical power laws. (a) Temporal evolution of the dimensionless wetted area of droplets spreading on a surface ($\theta_e = 41^\circ$). A_f and A are final and temporal wetted areas of the droplet, respectively. Different colored squares indicate the simulation results for different τ_w values. The solid curves correspond to the fitting curves of the exponential power law proposed by Lavi and Marmur [168]. (b) Temporal evolution of the dimensionless volume of an evaporating droplet suspended in vapor without wetting. V_0 and V are initial and temporal volumes of the droplet, respectively. The blue squares show the simulation results and the solid line indicates the fitting line in accordance with the well-known D^2 -law [169]. The insets in (a) and (b) are the snapshots showing the simulation scenes.

where A_f and A are the final and temporal wetted areas of the droplet, respectively. λ and m denote non-negative parameters, which are determined by fitting through experimental data. To make a qualitative comparison with the exponential power law, simulations for droplets spreading on a flat surface with equilibrium contact angle $\theta_e = 41^\circ$ are conducted. The droplet with radius $r = 40$ and Cahn number $Cn = 0.05$ is considered. The droplet is initially released on the top of the surface and the distance between the center of mass of the droplet and the surface is the same as its radius. The evolutions of A/A_f versus t for $\tau_w = 1, 10, 20,$ and 100 are plotted in Figure 4.3(a) with different colored squares. The solid curves are the fitting curves according to the exponential power law and the fitting parameter m ranges from 0.95 to 1.12. It can be seen that the agreement between the simulation results and the exponential power law Equation (4.1) is excellent. Additionally, it is found that the increase of τ_w slows down the kinetics of the contact line movements. This is reasonable, since large viscosities or strong wall bonds of liquid lead to a slow kinetics.

Afterwards, simulation of the evaporation of a static drop suspended in vapor without wetting is performed to show the validity of the phase-field model for simulating liquid-vapor phase change. The result is compared to the well-known D^2 -law for the droplet evaporation. According to this law, the

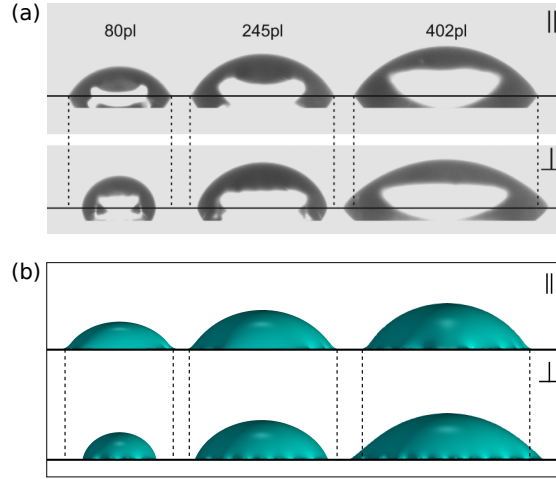


Figure 4.4.: Snapshots of droplets deposited on striped patterned surface for different liquid volumes. (a) Experimental results. Reprinted with permission from Ref. [170]. Copyright 2012 American Chemical Society. (b) Present simulation results. The top rows in (a) and (b) illustrate the droplet shapes in the direction parallel to the stripes and the bottom rows depict the droplet shapes in the perpendicular direction. The hydrophilic and hydrophobic stripes in (a) are 12 and 6 in dimensionless width, respectively. The dimensionless width of the 80 pL (initial dimensionless diameter 53) droplet in the perpendicular direction is 65. The solid lines are baselines of the surface and dashed lines show the droplet width in the parallel direction.

square of the evaporating drop diameter decreases linearly with the time, as $D^2/D_0^2 = 1 - kt$. Here D_0 and D are initial and temporal diameters of the droplet, respectively, and k is a rate constant [169]. The simulations are carried out in a 3D domain ($200 \times 200 \times 120$) with a droplet (radius $r = 40$) located in the domain center. In Figure 4.3(b), $V^{2/3}$ (effectively D^2) as a function of time is plotted for the simulated evolution as square data points and the solid line refers to the fitting line of the D^2 -law. A good agreement between the numerical results and the D^2 -law is obtained.

Simulations of droplets on chemically striped surface are also validated. Firstly, the final droplet shape on the chemically striped surface is considered. Icompare our simulation results with the experimental results from Jansen et al. [170], who used droplets with three different sizes (80, 245, and 402 pL in volume or 53, 78, and 92 in dimensionless diameter) to study the effect of volume to the anisotropic wetting on chemically striped surface. The hydrophilic (SiO_2 , $\theta_{e,\text{wet}} = 27^\circ$) and hydrophobic (PFDTs, $\theta_{e,\text{dry}} = 106^\circ$) stripes of the surface are 12 and 6 in dimensionless width, respectively. In the present simulations, the droplet sizes are the same as that in the work of Jansen et al. [170]. The dimensionless widths of the hydrophilic and hydrophobic stripes are also 12 and 6, respectively. The equilibrium shapes of droplets for experimental and simulation results are illustrated in Figure 4.4(a) and (b), respectively. The top rows in (a) and (b) show the droplet shapes in the direction parallel to the stripes, while the second rows indicate the droplet shapes in the perpendicular direction. As

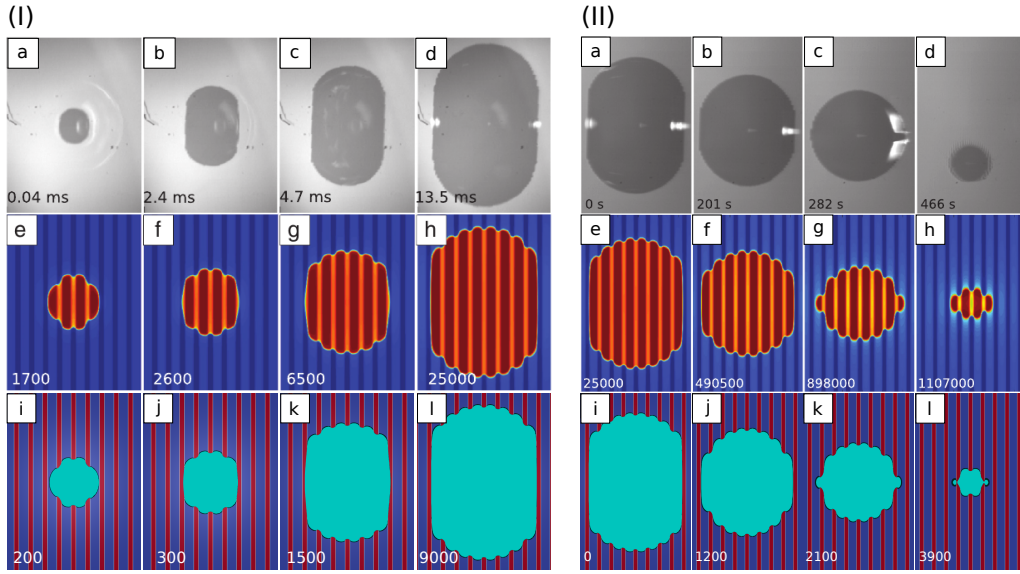


Figure 4.5.: Temporal evolution of droplet shape for spreading and evaporation processes: (I) bottom view of a droplet with constant volume spreading on striped patterned surface, (II) bottom view of a droplet evaporating on striped patterned surface. (a)-(h): Experimental and LB simulation results. Reprinted with permission from Ref. [171]. Copyright 2013 American Physical Society. (i)-(l): Present simulation results. The hydrophilic and hydrophobic stripes ($\theta_{e,wet} = 40^\circ$ and $\theta_{e,dry} = 110^\circ$) are indicated by blue and red stripes in the present simulations, respectively.

the volume rises, the droplet base radius in both directions increases as well. The elongation for the 80 pL droplet is the largest and becomes less profound for the 245 pL droplet, while for the 402 pL case, the base radius in the perpendicular direction is larger than the one in the parallel direction. On the one hand, the contact angle in the perpendicular direction changes because of the contact line pinning and depinning effect, as shown in the second rows in Figure 4.4(a) and (b). On the other hand, the contact angle in the parallel direction changes only slightly, as indicated in the first rows in Figure 4.4(a) and (b). The droplet-shapes in the present simulations show a very good agreement with the experimental results and the simulation can also reproduce the effect of volume to the anisotropic wetting properties on chemically striped surface.

In order to validate the simulation of droplet-spreading and evaporation processes on chemically striped surface, simulations are conducted to make a comparison with the work of Jansen et al. [171]. They investigated this phenomenon through lattice Boltzmann (LB) method and experiments. In their experiments, water droplets are used. The surface is made up of hydrophilic (SiO_2 , $\theta_{e,wet} = 40^\circ$) and hydrophobic (PFDTs, $\theta_{e,dry} = 110^\circ$) stripes with the stripe width ratio $w_{PFDTs}/w_{SiO_2} = 0.5$. In the LB simulations, a static contact angle boundary condition is adopted. The dimensionless droplet radius is 99 and the dimensionless stripe widths are 10 and 20 for the hydrophobic and hydrophilic stripes. The present simulations use a dynamic contact angle model as the boundary condition. Given that the

water droplet viscosity is relatively small, $\tau_w = 1$ is chosen in our simulations. The initial droplet radii and the widths for hydrophobic and hydrophilic stripes are the same as those in the LB simulations of Jansen et al. [171]. Figure 4.5(I) and (II) show the bottom view of the evolution of the droplet shape for droplet-spreading and evaporation processes. (a)-(d), (e)-(h), and (i)-(l) are the experimental results, LB simulations, and the present simulations, respectively. In droplet-spreading process, the droplet firstly touches the surface and then spreads over it. Because the droplet spreads preferably parallel to the stripes, the droplet is eventually elongated in this direction. In the case of evaporation process, the contact line firstly recedes in the direction parallel to the stripes, while it is pinned perpendicular to the stripes. The details of the contact line advancing and receding motions and droplet shapes show significant similarities between the present results and the results of Jansen et al. [171].

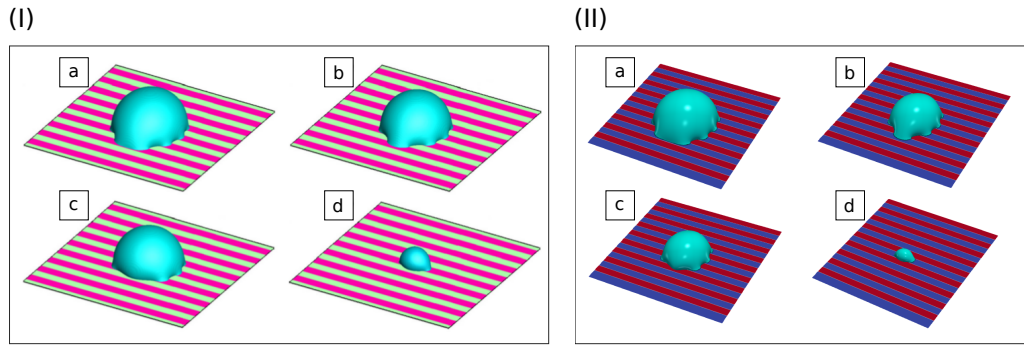


Figure 4.6.: Snapshots of droplet evaporation on striped patterned surface: (I) LB simulation from Yu et al. Reprinted with permission from Ref. [172]. Copyright 2017 Elsevier. (a) $t = 10^5 \delta_t$, (b) $t = 1.35 \times 10^5 \delta_t$, (c) $t = 1.4 \times 10^5 \delta_t$ and (d) $t = 3.05 \times 10^5 \delta_t$. δ_t is the time step. (II) Present simulation. (a) $t = 0.4 \times 10^3$, (b) $t = 1 \times 10^3$, (c) $t = 1.2 \times 10^3$ and (d) $t = 2.6 \times 10^3$. The equilibrium contact angles for hydrophilic and hydrophobic stripes are $\theta_{e,wet} = 60^\circ$ and $\theta_{e,dry} = 120^\circ$, respectively.

To validate the capability of the phase-field model to investigate the contact line pinning-depinning mechanism, a further simulation is done to compare with the LB simulation of Yu et al. [172]. In their study, the evaporation of a droplet with radius $r = 40$ on chemically striped surface is simulated and the movements of the contact line and contact angle are discussed. The hydrophilic and hydrophobic stripes of the surface are of the same width 11, and the corresponding static equilibrium contact angles are $\theta_{e,wet} = 60^\circ$ and $\theta_{e,dry} = 120^\circ$, respectively. By setting the same conditions with the study of Yu et al. [172], a phase-field simulation is conducted in this work. Figure 4.6 illustrate the snapshots of droplet evaporation for different time steps. (I) and (II) show the results of Yu et al. [172] and the present phase-field simulation, respectively. In Figure 4.7, the variations of the contact angle and contact radius (or base radius) in the perpendicular and parallel directions are plotted. (a)-(d) are the results of Yu et al. [172] and (e)-(h) correspond to the present simulation. R_e denotes the contact radius when evaporation begins and δ_t is the time step. From Figure 4.6 and Figure 4.7, I can see that the droplet evaporates in a different way in the directions parallel and perpendicular to the stripes. In the

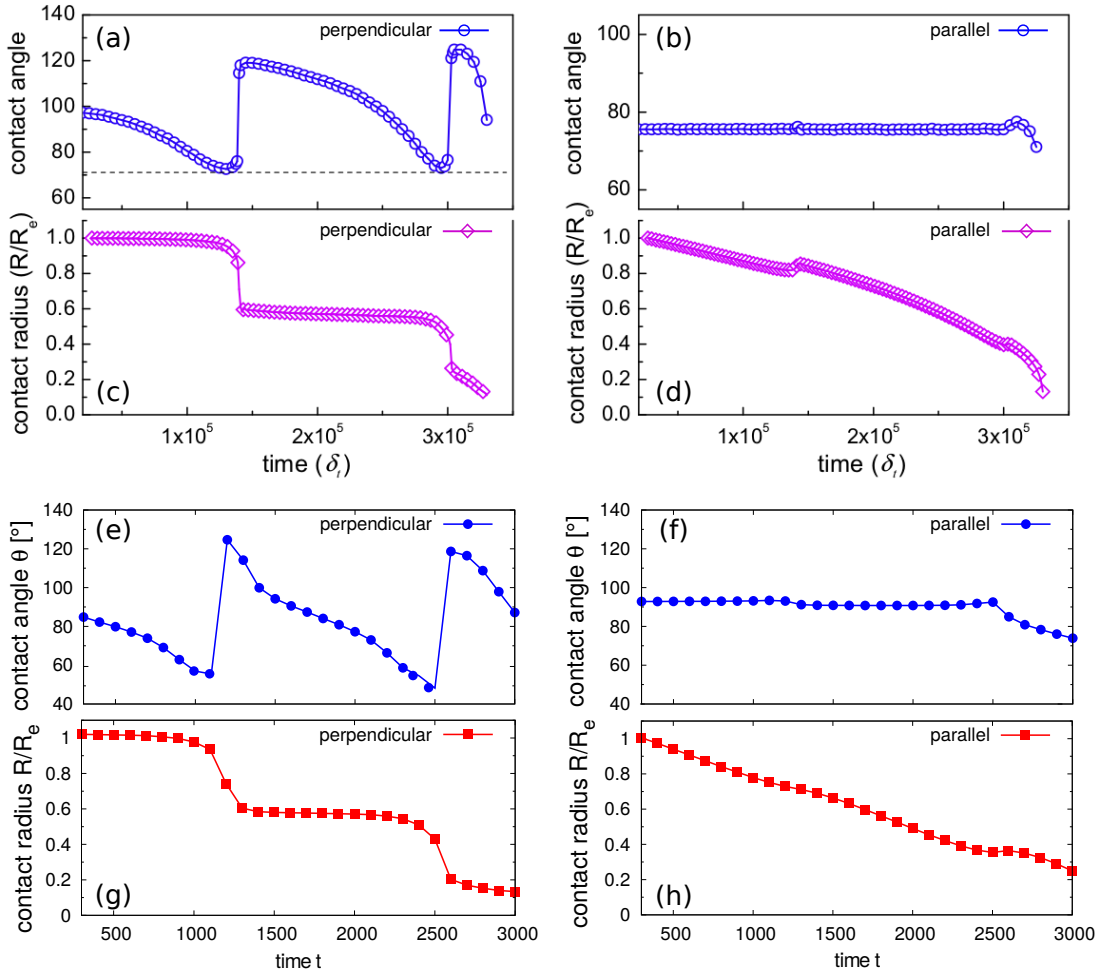


Figure 4.7.: Contact angle and non-dimensional base radius of an evaporating droplet as a function of time in the perpendicular direction (left) and the parallel direction (right) on striped patterned surface. δ_t is the time step. (a)-(d) LB simulation from Yu et al. Reproduced with permission from Ref. [172]. Copyright 2017 Elsevier. The legends are added by the present authors. (e)-(h) Present simulation.

perpendicular direction, the droplet initially evaporates in the CCR mode. The contact line is pinned on the stripe boundary while the contact angle decreases, as can be seen in Figure 4.7(a) and (c) from $t = 2 \times 10^4 \delta_t$ to $t = 1.2 \times 10^5 \delta_t$ (or in (e) and (g) from $t = 0$ to $t = 1000$). The droplet then jumps two times in the following process. In the parallel direction, however, the droplet evaporates almost in the CCA mode. The contact angle remains unchanged and the contact radius decreases with time, as shown in Figure 4.7(b) and (d) (or (f) and (h)). The droplet shapes as well as the movements of contact line and contact angle exhibit pronounced similarities between the present phase-field simulation and the LB simulation of Yu et al. [172].

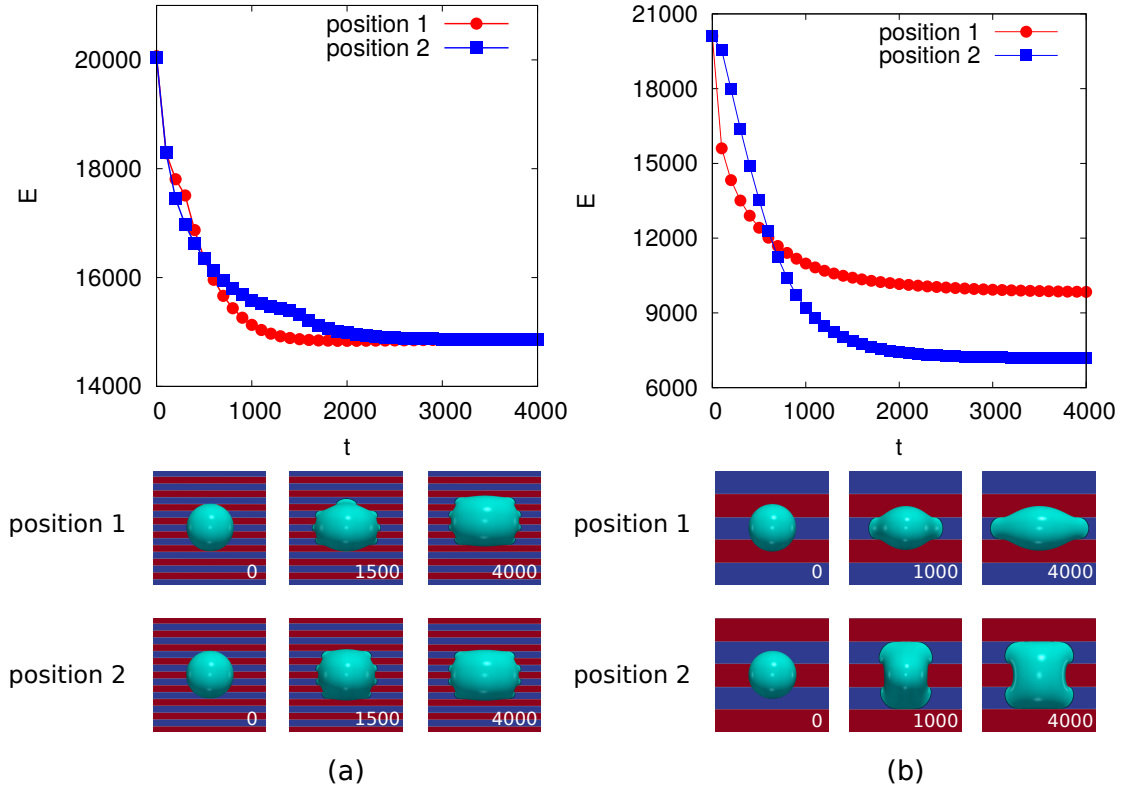


Figure 4.8.: Surface energy evolution and snapshots of droplet spreading. Position 1 is above the center line of a blue stripe and position 2 is above the center line of a red stripe. The numbers at the bottom right corner in the snapshots indicate the dimensionless time. (a) $d/V^{1/3} = 0.19$. (b) $d/V^{1/3} = 0.62$.

4.3. Droplet shape analysis

4.3.1. Droplet deposition and condensation in quasi-equilibrium state

In this section, the equilibrium shapes of droplets on chemically striped patterned surfaces, on which the equilibrium contact angle alternates $\theta_{e,\text{wet}} = 41^\circ$ and $\theta_{e,\text{dry}} = 106^\circ$, are investigated. In the following, the blue and red stripes indicate the hydrophilic ($\theta_{e,\text{wet}}$) and hydrophobic ($\theta_{e,\text{dry}}$) ones, respectively. Initially, two droplets with radius $r = 40$ are released on two different positions on the striped patterned surface. The first position is above the center line of a blue stripe, while the second position is above the center line of a red one. The former and the latter ones are named as position 1 and 2, respectively.

Driven by the surface energy minimization, the shapes of the droplets evolve with time. The surface energies as a function of time and snapshots of the droplets spreading are illustrated in Figure 4.8. Two distinct stripe widths $d = 12, 40$ are considered in (a) and (b). In Figure 4.8(a) ($d = 12$, i.e. $d/V^{1/3} = 0.19$), despite different initial positions, the final shapes of the droplets are the same, as shown by the snapshots at the time $t = 4000$. This is clearly evidenced by the fact that the surface

energies of the two droplets converge to the same value, as can be seen by the red and the blue curves in Figure 4.8(a). As far as I am aware, this phenomenon has not yet been reported in literature. Contrarily, in Figure 4.8(b) ($d = 40$, i.e., $d/V^{1/3} = 0.62$), the final shapes of the droplets are not identical when droplets are deposited on the positions 1 and 2 (see snapshots at the time $t = 4000$ in (b)). These two distinct equilibrium shapes correspond to two surface energy minima, as displayed by the curves in Figure 4.8(b). It is noteworthy that in (a), the final shape of the droplet is the same as the one in Figure 4.8(a) at $t = 4000$ when a droplet is initially placed between the positions 1 and 2. Whereas, in (b), two different equilibrium shapes appear when I release a droplet somewhere between the positions 1 and 2. The equilibrium states depend on the distance to the position 1 and 2 (see refs [173, 174] for more details). Thus, I conclude that the final shape of the droplet is dependent on two significant factors, (i) the relative size of the droplet compared with the stripe width and (ii) the initial position of the droplet, from which the droplet is released.

In order to systematically study the vital factors (i) and (ii), I vary the ratio $d/V^{1/3}$ and release the droplets on the positions 1 and 2 to scrutinize the final shapes of the droplets. Because of the computational effort, I here constrain to the consideration that the droplet size is comparable to the stripe width. The droplet radius is fixed as $r = 40$ and the stripe width varies from 7 to 160. The droplet aspect ratio ξ (defined as R_1/R_2 with R_1 and R_2 representing the base radii parallel and perpendicular to the stripes, respectively) as a function of $d/V^{1/3}$ is depicted in Figure 4.9(a).

At equilibrium, the droplets cover different number of hydrophilic (blue) stripes, which is indicated by the symbols with varying colors, e.g. blue squares–1 stripe, red circles–2 stripes (the other colored symbols are interpreted in the legend). According to the number of covered hydrophilic stripes, the diagram is divided into 6 areas: (I) $0.9 < d/V^{1/3} < 3$. For a droplet released on the position 1, only one hydrophilic stripe is wetted, as pictured in the left part of Figure 4.9(c) for $d/V^{1/3} = 2.5, 1.4, 1.1$. This scenario is described by the blue squares in the area I and it is observed that as the ratio $d/V^{1/3}$ increases, the aspect ratio ξ decreases. It is noticed that when $d/V^{1/3}$ is large enough, i.e., stripe width is large compared with the droplet base diameter, the droplet deposits in the same way as on a homogeneous surface and the aspect ratio $\xi = 1$ keeps constant. When the droplet is released on the position 2, the droplet will stay on the red stripe (e.g. $d/V^{1/3} = 2.5$) or break up (e.g. $d/V^{1/3} = 1.1, 1.4$) into two small droplets with the same size, sited respectively on two blue stripes (see the right part of (c)). This kind of breakup is out of the scope of the present study and will not be discussed in detail. (II) $0.42 < d/V^{1/3} \leq 0.9$. In this area, for a fixed ratio, e.g. $d/V^{1/3} = 0.9, 0.7, 0.5$ (see Figure 4.9(d)), there are two significantly different patterns where one or two blue stripes are wetted. The former and the latter cases correspond to the droplets initially placed on the positions 1 and 2 and are depicted by the blue squares and the red circles in the area II, respectively. (III) $0.25 < d/V^{1/3} < 0.42$. The relative droplet size is bigger than the one in the areas I and II and either two or three blue stripes are wetted. Typical equilibrium shapes are displayed in Figure 4.9(e) and the results are demonstrated by the red circles and the green triangles in the area III in Figure 4.9(a). (IV)–(VI) $0.1 < d/V^{1/3} < 0.25$. With a further decrease in the ratio of $d/V^{1/3}$, more hydrophilic stripes are wetted due to the relatively large volume of the droplet. It should be noticed, that on the boundary between two areas,

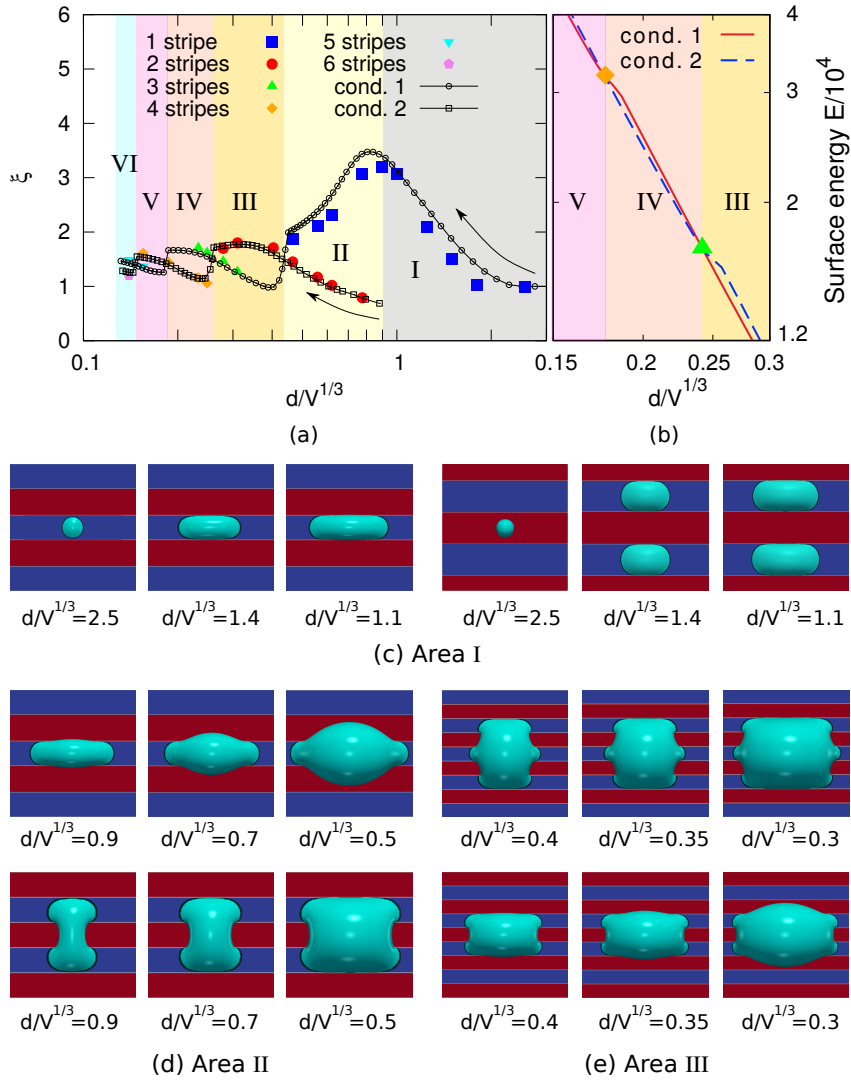


Figure 4.9.: Morphological diagram: (a) Droplet aspect ratio ξ as a function of $d/V^{1/3}$. Symbols show the results of droplet deposition from a series of independent simulations with different ratios of $d/V^{1/3}$. Different colored symbols indicate the equilibrium shapes covering different number of hydrophilic stripes. The black solid lines with circles and with squares are the first and second condensation lines, respectively, corresponding to the droplets initially deposited on the positions 1 and 2. The diagram is divided into 6 areas according to the number n of the wetted hydrophilic stripe(s). I: $n = 1$, II: $n = 1$ and 2, III: $n = 2$ and 3, IV: $n = 3$ and 4, V: $n = 4$ and 5, VI: $n = 5$ and 6. (b) Surface energy evolution as a function of $d/V^{1/3}$ in the area $d/V^{1/3} \in [0.15, 0.4]$. The red solid line and the blue dashed line correspond to the first and second condensations, respectively. The orange rhombus and green triangle denote the intersections. (c), (d) and (e) Equilibrium droplet-shapes in the areas I, II and III, respectively. In the left and right three images of (c), droplets are released on the positions 1 and 2, respectively. At the top and the bottom pictures in (d) and (e), droplets are deposited on the positions 1 and 2, respectively.

e.g. $d/V^{1/3}=0.19$, which is denoted by the orange rhombus in Figure 4.9(a), a unique equilibrium shape appears in spite of different release positions and this phenomenon has never been reported in literature.

The contact line movement of a depositing droplet is similar to the one of a condensing droplet, when the phase transition rate is extremely low, such that at every time step, the droplet obeys the principle of surface energy minimization. In order to further explore the underlying mechanism of the relationship between the droplet aspect ratio ξ and the relative size of the droplet, two individual simulations for the condensations of a droplets on the positions 1 and 2 are performed. The stripe width of the surface is 30 and $\tau_w = 1$. The results of these two simulations are presented in Figure 4.9(a) by the black lines with circles (position 1) and squares (position 2). The arrows denote the volume-increase direction. I observe that all the colored symbols in the areas I-VI perfectly lie in the two condensation lines. For the first condensation line, the small droplet initially lies in the center of a hydrophilic stripe and grows through condensation following the direction of the arrow. The increase in the volume gives rise to a jump from one wetted hydrophilic stripe to three, then five stripes. Each jump leads to a rapid decrease of the droplet aspect ratio ξ and the reason is discussed in the following. Similarly, when a droplet is originally placed on a hydrophobic stripe (the second condensation line), it jumps from two hydrophilic stripes to four and then six stripes. Both condensation lines exhibit a typical “stick-slip-jump” behavior that has been discussed in literature [175]. The intersections of the two condensation lines exactly locate on the boundaries of different areas, as shown in Figure 4.9(a). These intersections correspond to the situation where there is a unique equilibrium state irrespective of the initially released positions, which has been exemplarily illustrated in Figure 4.8(a). Within each area excluding I, two equilibrium states exist for a certain ratio of $d/V^{1/3}$, corresponding to two different surface energy minima, as aforementioned in Figure 4.8(b). The number of equilibrium states is corroborated through the following surface energy analysis. Figure 4.9(b) shows the surface energy evolution for the first and second condensations in the range $d/V^{1/3} \in [0.15, 0.4]$, which is in the areas III, IV and V. The red solid line and the blue dashed line correspond to the first and second condensations, respectively. These two lines diverge from each other within the three areas and intersect on the left and right boundaries of the area IV. The intersections are denoted by the orange rhombus and the green triangle, which exactly coincide with the two intersections on the two boundaries of the area IV in Figure 4.9(a). Therefore, I conclude that there are either one or two minima in the surface energy landscape with regard to the droplet deposition on a chemically striped patterned surface. This finding is also consistent with the analysis of Gea Jódar et al. [176].

It is noteworthy that from I to VI, the droplet aspect ratio ξ demonstrates a periodic oscillation with a decreasing amplitude. When the ratio of $d/V^{1/3}$ is beyond the area VI, i.e., the droplet size is much greater than the stripe width, the aspect ratio ξ converges to a certain value. The droplet behavior in the area beyond I-VI has been studied by Bliznyuk et al. [177] and Jansen et al. [178]. The periodic oscillation behavior of the droplet aspect ratio ξ has been also observed by David et al. [179], but due to the narrow varying range of the stripe width in their study, an asymptotic analysis to obtain the value of the droplet aspect ratio ξ for $d/V^{1/3} \ll 1$ is not possible.

The underlying mechanism for the morphological transition shown in Figure 4.9 is elucidated by analyzing the contact angles parallel and perpendicular to the stripes (θ_1 and θ_2). The contact angle θ_1 is described by Cassie-Baxter equation [38]:

$$\theta_1 = \arccos(f_1 \cos \theta_{e,\text{wet}} + f_2 \cos \theta_{e,\text{dry}}) \quad (4.2)$$

where f_1 and f_2 are the area fractions of the hydrophilic and hydrophobic stripes, respectively. The angle θ_2 is measured along the line perpendicular to the stripes and passing through the droplet center. The variation of θ_1 and θ_2 during the condensation 1 is represented in Figure 4.10(a). According to the varying behavior of θ_2 , the diagram is partitioned into three phases 1-3 and is read from the right to the left. The morphological evolution in these three phases is shown in Figure 4.10(e). In the phase 1, the droplet contact line sticks to the boundary between the blue and the red stripes, engendering an increase of θ_2 till the maximum value $\theta_{e,\text{dry}}$ is reached. This phenomenon is known as contact line pinning effect [180]. However, the contact line spreads easily in the direction parallel to the stripes and θ_1 is slightly increased, which is caused by a subtle increase in the hydrophobic area fraction f_1 . As a result, the droplet is elongated parallel to the stripes and the corresponding aspect ratio ξ , which is illustrated by the blue line in Figure 4.10(c), keeps rising. In the phase 2, the contact line slips over the red stripe and θ_2 retains unchanged with the maximum value. Because of the slip movement perpendicular to the stripes in this phase instead of the stick behavior as in the phase 1, the elongation effect of the droplet is less pronounced. Thus, the aspect ratio ξ decreases. Moreover, since more hydrophobic area is wetted, θ_1 rises. In the phase 3, the droplet jumps to a new blue stripe with a prompt decrease in θ_2 , which gives rise to a decline of the droplet aspect ratio ξ . This stick-slip-jump behavior repeats periodically as the droplet gets even larger (small value of $d/V^{1/3}$) and spreads over more stripes due to the condensation. In Figure 4.10(b), (d) and (f) which are for the condensation 2, a similar stick-slip-jump phenomenon is observed as well.

In Figure 4.10(c) and (d), our simulation results are compared with the model of Jansen et al. [178] (red lines), which describes the aspect ratio ξ by using θ_1 and θ_2 :

$$\xi = \left[\frac{\sin \theta_1}{1 - \cos \theta_1} \right] \left[\frac{1 - \cos \theta_2}{\sin \theta_2} \right] \quad (4.3)$$

It is observed that there is a good agreement between our simulation results and the model except in the situation where only one hydrophilic stripe is wetted (phases 1-3 in Figure 4.10(c)). The deviation is primarily due to the approximation of the model that the droplet profile is fitted with a part of a circle. This approximation is apparently not accurate when only one hydrophilic stripe is wetted.

4.3.2. Droplet evaporation in quasi-equilibrium state and hysteresis phenomenon

In order to further examine the similarities of droplet deposition and condensation, both of which can be regarded as advancing contact line dynamics, a receding contact line dynamics, i.e., droplet evaporation, is now considered. Similar to the simulations of condensation, two individual simulations for a droplet evaporation on the positions 1 and 2 are conducted. The stripe width of the surface is still 30 and $\tau_w = 1$. Here, I postulate that the phase transition rate is extraordinarily low and the droplet is

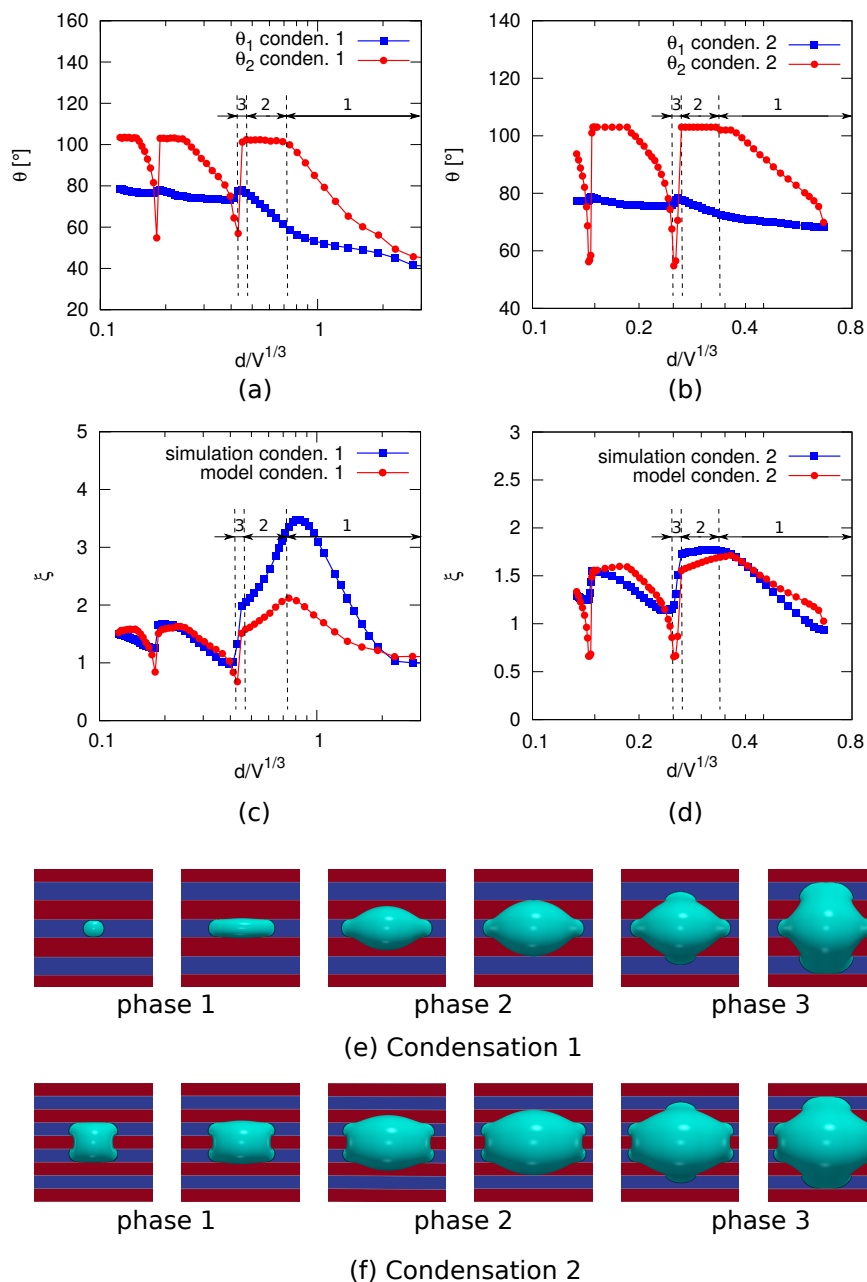


Figure 4.10.: (a) and (b) Directional contact angles θ_1 and θ_2 as a function of $d/V^{1/3}$ for the first and second condensation. θ_1 is described by Cassie-Baxter equation and θ_2 is measured along the line perpendicular to the stripes and passing through the droplet center. (c) and (d) Droplet aspect ratio ξ as a function of $d/V^{1/3}$ for the first and second condensation, obtained from simulations (blue lines with squares) and the model of Jansen et al. [178] (red line with circle points). (e) and (f) Droplet morphological transitions in phases 1-3 for the first and second condensation.

in a state of equilibrium at each time step. The first and second evaporation lines, which correspond to the simulations with droplets initially on the positions 1 and 2, are illustrated in Figure 4.11(a) and (b), respectively. The colored symbols and the two condensation lines are directly taken from Figure 4.9(a). I read the evaporation lines (red lines) from the left to the right sides ($d/V^{1/3}$ increases or V decreases) in the diagram and the condensation lines (black lines) in the opposite direction ($d/V^{1/3}$ decreases or V increases). A typical hysteresis phenomenon is perceived: Different droplet aspect ratios ξ are observed in the condensation and the evaporation lines for a fixed value of $d/V^{1/3}$. In Figure 4.11(a), the evaporation line 1 significantly diverges from the condensation line 1 in the ranges: $0.18 < d/V^{1/3} < 0.3$ and $0.4 < d/V^{1/3} < 1$. Distinguishable divergences between the evaporation line 2 and the condensation line 2 also appear in the ranges: $0.14 < d/V^{1/3} < 0.21$ and $0.24 < d/V^{1/3} < 0.45$, as can be seen in Figure 4.11(b). In other areas, the evaporation lines coincide with the condensation lines. The difference between the two curves in the range of $1 < d/V^{1/3} < 3$ in Figure 4.11(a) is owing to the small Cahn number Cn of the droplet, because the droplet diameter is relatively small in this region.

As a typical example, I analyze the evolution of the equilibrium droplet-shapes in the range $d/V^{1/3} \in [0.23, 0.5]$ in Figure 4.11(b), which is highlighted between the two vertical dashed lines. The black and the red arrows indicate the evolution directions for the condensation and the evaporation, respectively. The corresponding morphological transitions of the droplets in this range are displayed in Figure 4.11(d) and (e). In the condensation process, initially, the contact line sticks to the boundary of the red-blue stripes and stretches outwards parallel to the stripes, leading to an elongation of the droplet ($d/V^{1/3} = 0.5$ and 0.4 in Figure 4.11(d)). Thereafter, the contact line slips over the red stripe outwards ($d/V^{1/3} = 0.3$ in Figure 4.11(d)) and jumps to a new red-blue boundary ($d/V^{1/3} = 0.25$ in Figure 4.11(d)). As a consequence, the elongation effect declines and the aspect ratio ξ decreases. On the contrary, in the evaporation process, at the beginning, the contact line sticks to a red-blue boundary and retreats parallel to the stripes, as shown in Figure 4.11(e), $d/V^{1/3} = 0.23, 0.25$ and 0.3 . The stick and retreating behavior gives rise to the decrease in the aspect ratio ξ . Afterwards, the contact line slips over the blue stripe inwards then jumps to a new red-blue boundary, resulting in an increase of ξ ($d/V^{1/3} = 0.4$ and 0.5 in Figure 4.11(e)). Similar morphological transitions for droplet condensation and evaporation have also been found on surfaces with linear grooves [181, 182]. In summary, the pinning-depinning effect at the red-blue stripe boundary and different moving directions of the contact line parallel to the stripes contribute to the distinct morphological transitions for the condensation and the evaporation processes and thus a hysteresis phenomenon is present.

It is noticed that in the hysteresis area, two different droplet-morphologies appear for a fixed value of $d/V^{1/3}$, as annotated by the red stars in Figure 4.11(d) and (e). While in the regions out of the hysteresis area, only one equilibrium droplet-shape exists, as shown in Figure 4.11(d) and (e) for $d/V^{1/3} = 0.23$ and 0.5 . Figure 4.11(c) illustrates the surface energy evolution of a condensing (black solid line) and an evaporating droplet (red dashed line) in the range $d/V^{1/3} \in [0.22, 0.6]$. The hysteresis area is highlighted with the green color and in this area the black and the red lines diverge from each other, whereas the two lines overlap perfectly out of the hysteresis area, which is excellently

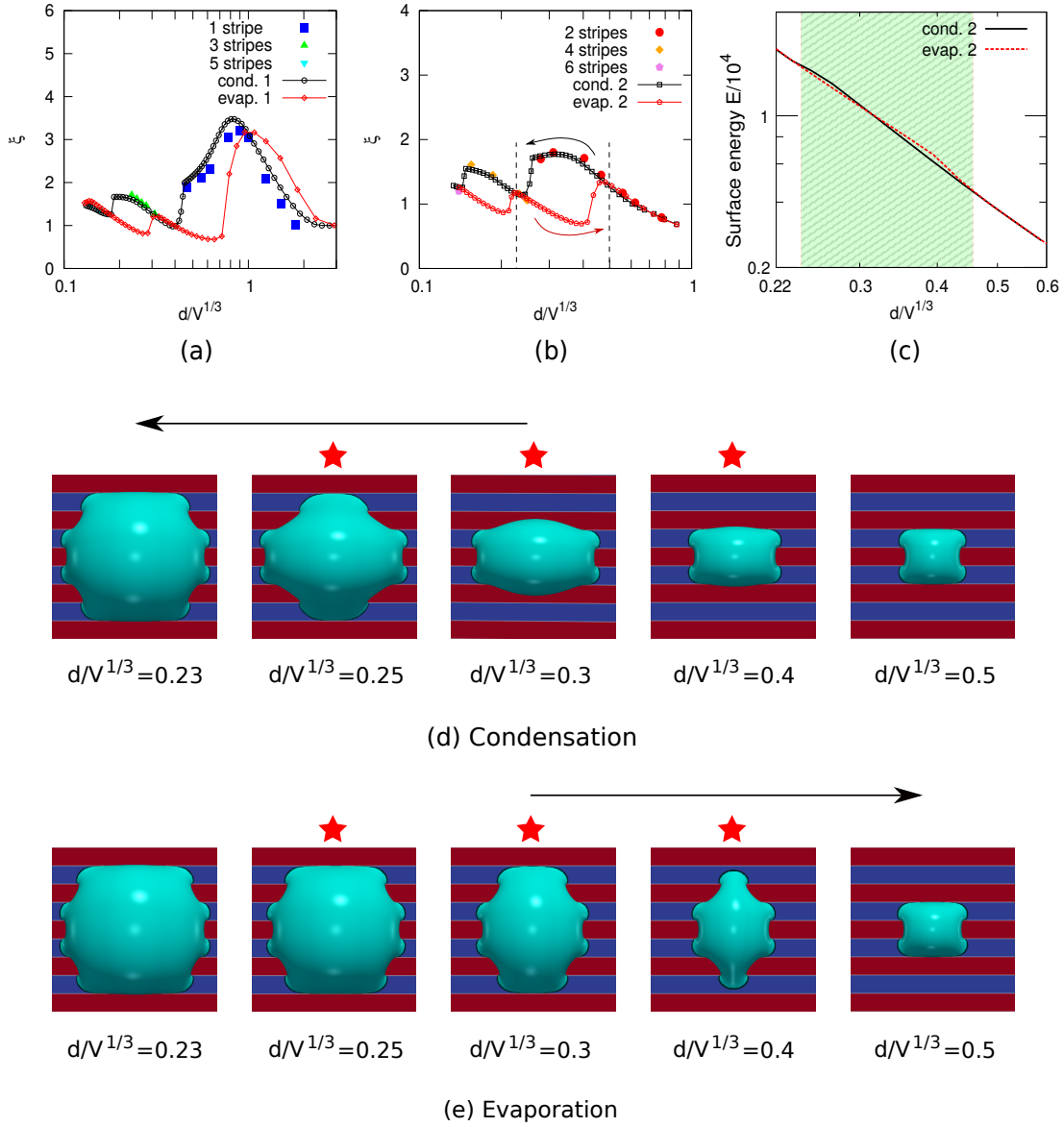


Figure 4.11.: (a) and (b) Droplet aspect ratio ξ as a function of $d/V^{1/3}$ for the condensation and evaporation of a droplet on positions 1 and 2. The colored symbols and the two condensation lines are directly taken from Figure 4.9(a). The red lines with rhombuses and with pentagons are the first and second evaporation lines, respectively. (c) The surface energy evolution of a condensing (black solid line) and an evaporating droplet (red dashed line) in the area $d/V^{1/3} \in [0.22, 0.6]$. The hysteresis area is highlighted with the green color. (d) and (e) Droplet morphological transitions in the condensation and evaporation processes. The arrows indicate the corresponding evolution directions and the stars annotate typical droplet-shapes in the hysteresis area.

consistent with the evolution of the ratio ξ shown in Figure 4.11(b). The surface energy analysis reveals that through different moving paths, the droplet may reach different equilibrium states. It is concluded that the equilibrium shape is dependent not only on the initial state, but also on the moving path, by which the equilibrium state is achieved.

4.3.3. Influence of perturbations on the morphological transition

I now consider the effect of perturbations on the morphological transition of droplets slowly condensing on chemically striped surface. Initially, three droplets are deposited on the chemically striped surface and stay at equilibrium. At $t = 0$, perturbations are introduced to the droplets and thereafter the perturbations are switched off right away. The perturbations obey a Gauss distribution with mean value 0 and variance 1. The intensity of the perturbations is indicated by the amplitude and here three values 0.1, 0.3, 0.9 are used.

As can be seen in Figure 4.12, at $t = 0$ the droplets adopt different shapes influenced by perturbations with different intensities. As the perturbations become stronger, asymmetric effect is more pronounced. In Figure 4.12(a) and (b), the perturbations are so weak that the morphological transitions of droplets are still symmetric, which allows the droplets to cover 1-3-5 stripes during condensations. Contrary to the cases in (a) and (b), I find that the large perturbation (amplitude=0.9) promotes a break

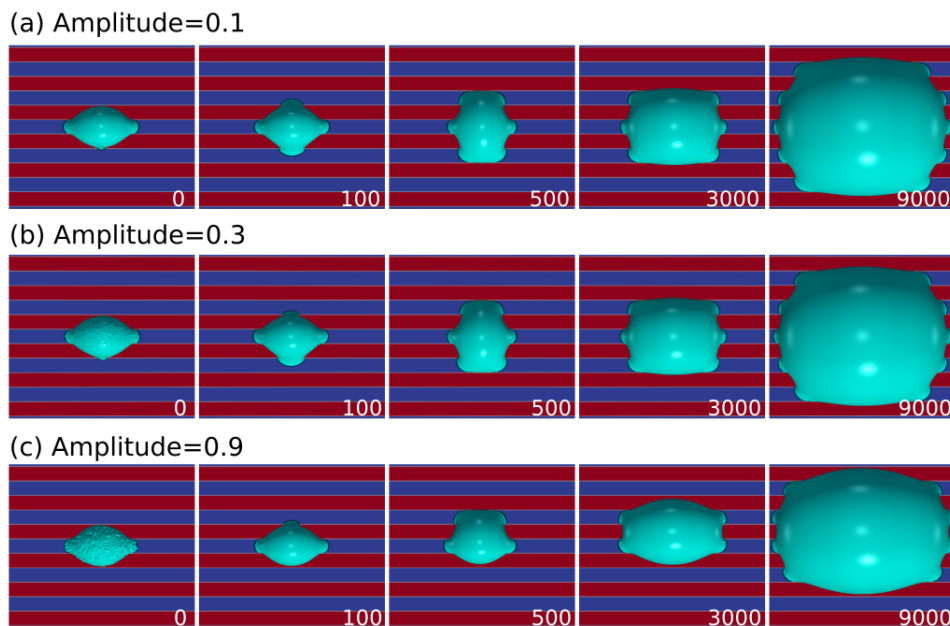


Figure 4.12.: Influence of perturbations on the droplet morphological transitions in the condensation processes. The numbers at the bottom right corner in the snapshots indicate the dimensionless time. Droplets at time $t = 0$ are disturbed by perturbations obeying a Gauss distribution with different amplitudes (a) amplitude=0.1, (b) amplitude=0.3, (c) amplitude=0.9.

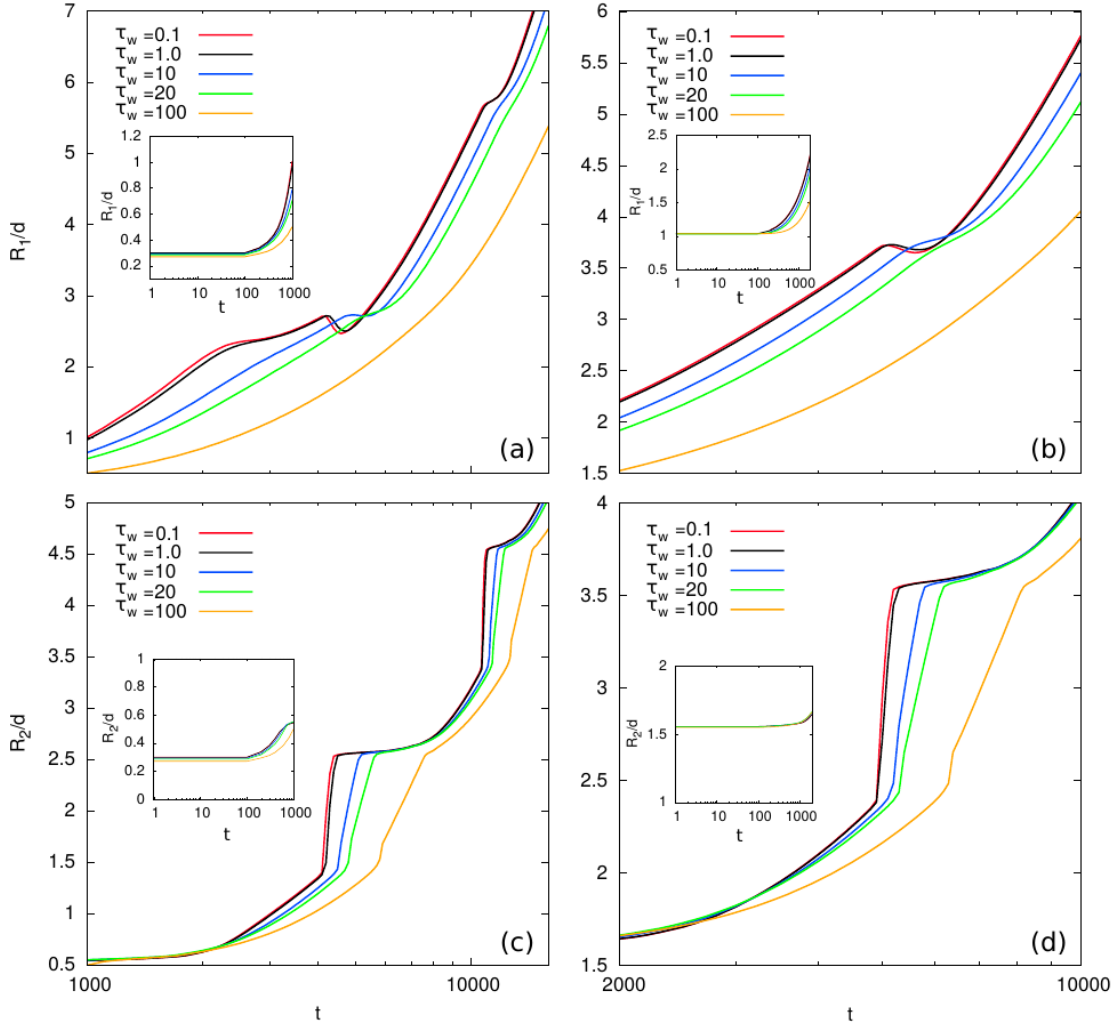


Figure 4.13.: The dimensionless directional contact radii R_1/d and R_2/d as a function of time for the condensations at position 1 and 2. R_1 and R_2 are measured along the lines parallel and perpendicular to the stripes, respectively. d represents the stripe width. Curves with different colors indicate the results for different τ_w values. The insets describe the results for the starting time. (a) and (c) are for the condensations at position 1. (b) and (d) are for the condensations at position 2.

of symmetry, as shown in (c). The droplet covers 1-2-4 stripes, as the volume increases. This suggests that large perturbations can lead to different moving paths of droplets. The intensity of the perturbation, which can trigger the broken symmetry, is dependent on droplet sizes, physical properties of fluids, and stripe widths. Since it is out of the scope of this study, I leave this interesting topic to a future work.

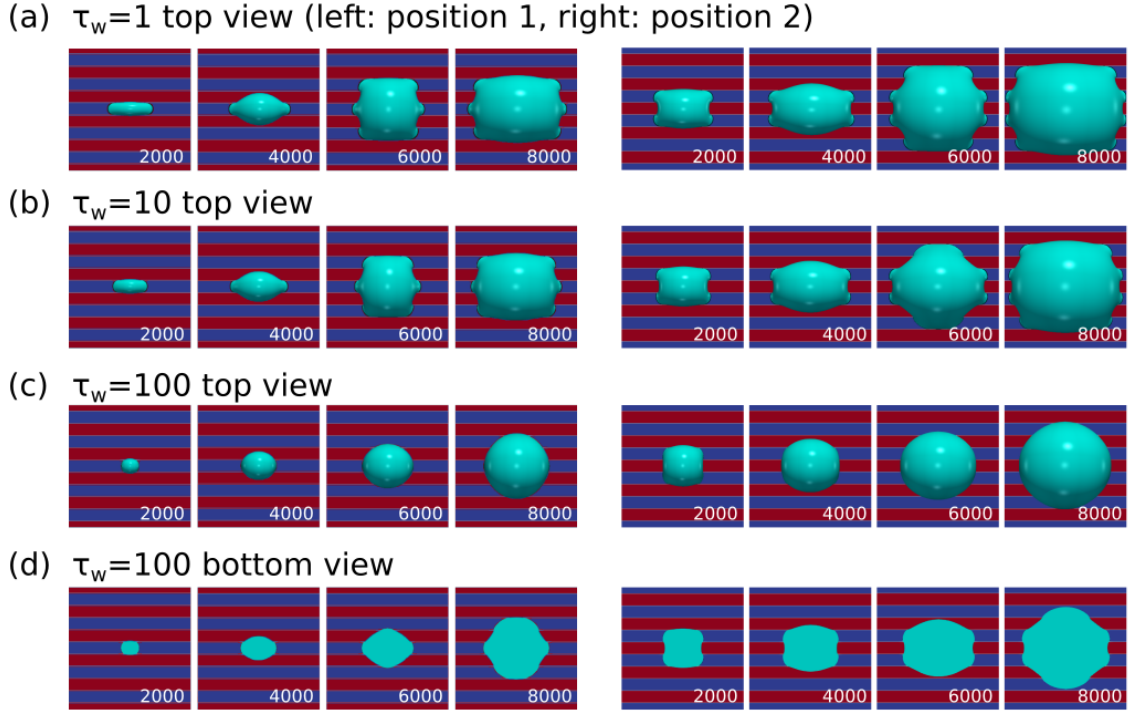


Figure 4.14.: Snapshots of droplet morphological transitions in condensation processes for different τ_w values. The left parts present the condensations at position 1 while the right parts correspond to the condensations at position 2. The numbers at the bottom right corner in the snapshots indicate the dimensionless time. (a)-(c) Top views for $\tau_w=1, 10, 100$. (d) Bottom views for $\tau_w=100$.

4.3.4. Droplet phase change in non-equilibrium states

Given that the physical properties of fluids have an impact on the morphological transition of droplet during condensation and evaporation, I carry out simulations of droplets condensing on chemically striped surface by using various τ_w . As discussed above, $\tau_w \sim \rho\nu L$ and it is related to the physical properties such as density and viscosity of the fluid. The stripe width is the same as above, i.e., $d = 30$. At $t = 0$, tiny droplets at equilibrium states on positions 1 and 2 of the chemically striped surface begin to condensate. As condensations take place, I track the base radius of the droplets in the directions parallel and perpendicular to the stripes. The dimensionless directional contact radii R_1/d and R_2/d as a function of time are plotted in Figure 4.13, where (a) and (c) are for the condensations at position 1, and (b) and (d) depict the condensations at position 2. The curves with different colors represent the results for different τ_w values. The insets describe the results for the starting time from $t = 1$ to $t = 1000$. The condensations result in an extension movements of the contact lines, and the continuous increase in the base radii in the parallel direction is observed in Figure 4.13(a) and (b). The fluctuations at $t = 4000$ and $t = 10000$ in (a) and at $t = 5000$ in (b) are caused by the jump movements of the contact lines in the perpendicular direction. In the direction perpendicular

to the stripes, the contact lines exhibit a stick-slip-jump” behavior. When the droplet center is at position 1, the contact line is pinned at the boundary where $R_2/d = 0.5, 2.5, 4.5$ and begins to jump at $R_2/d = 1.5$ and $R_2/d = 3.5$ (see Figure 4.13(c)). When the droplet center is placed at position 2, the contact line is pinned at the boundary where $R_2/d = 1.5, 3.5$ and begins to jump at $R_2/d = 2.5$ (see Figure 4.13(d)). It is noteworthy that as τ_w increases, the movements of contact lines slow down and the droplets are pushed far from the equilibrium shapes. This is proved by the temporal evolutions of the droplet-shapes with different τ_w , as shown in Figure 4.14. Especially when $\tau_w = 100$, the contact line moves so slow that the droplet is driven by the condensation far from the equilibrium state, and the droplet presents a form of sphere. In this condition, the condensation rate is high compared with the movement of the contact line. This is reasonable, since large viscosity and density slow down the contact line movements while the driving force for the condensation is kept constant. It is also found that the curves for $\tau_w = 0.1$ and $\tau_w = 1$ almost coincide with each other, which suggests that the contact line movements are not sensitive to low values of τ_w , since small τ_w describes slow interfacial phenomena and the processes can be considered as quasi-equilibrium.

Similarly, simulations of droplets evaporating on chemically striped surface using different τ_w are performed. The base radius in the direction parallel to the stripes continuously decreases, while in the perpendicular direction, stick-slip-jump” behavior appears, as presented in Figure 4.15, where (a) and (c) describe the evaporations at position 1, and (b) and (d) show the evaporations at position 2. The initial states of the droplets in (c) and (d) are different, which results in distinct morphological transitions. In (c) the droplet contact line undergoes a slip movement from $t = 0$ to $t = 1000$, while in (d) the droplet contact line sticks at the stripe boundary from $t = 0$ to $t = 1000$. Again, a large τ_w leads to slow movements of the contact lines. In Figure 4.15(e) (i)-(iii), the left and right parts show the droplet shape evolutions for the evaporations at position 1 and 2, respectively, with different τ_w . It is observed that the contact lines recede slower for larger τ_w . For instance, for the situation where the droplet center is on position 1, as displayed in Figure 4.15(a), (c), and the left parts of (e), at $t = 2600$, due to the contact pinning, droplets with different τ_w have the same contact radius in the perpendicular direction (R_2). While the contact radius in the parallel direction (R_1) increases as τ_w rises. The evaporations on position 2 exhibit the same phenomenon, as displayed in Figure 4.15(b), (d), and the right parts of (e).

4.4. Summary

In this study, the capability of the phase-field method based on the AC model for simulating the equilibrium shapes, the spreading dynamics and phase change of droplets are validated and the numerical model is shown to be highly robust. Then the equilibrium shapes of droplets deposited on chemically striped patterned surfaces are investigated by using the phase-field model. By changing the droplet volumes V , the widths of the stripes d and the initial positions from which the droplets are released, I obtain a functional relationship between the droplet aspect ratio ξ and the scaled stripe width $d/V^{1/3}$, which I find is the same as the situation of a slowly condensing droplet on a chemically striped pat-

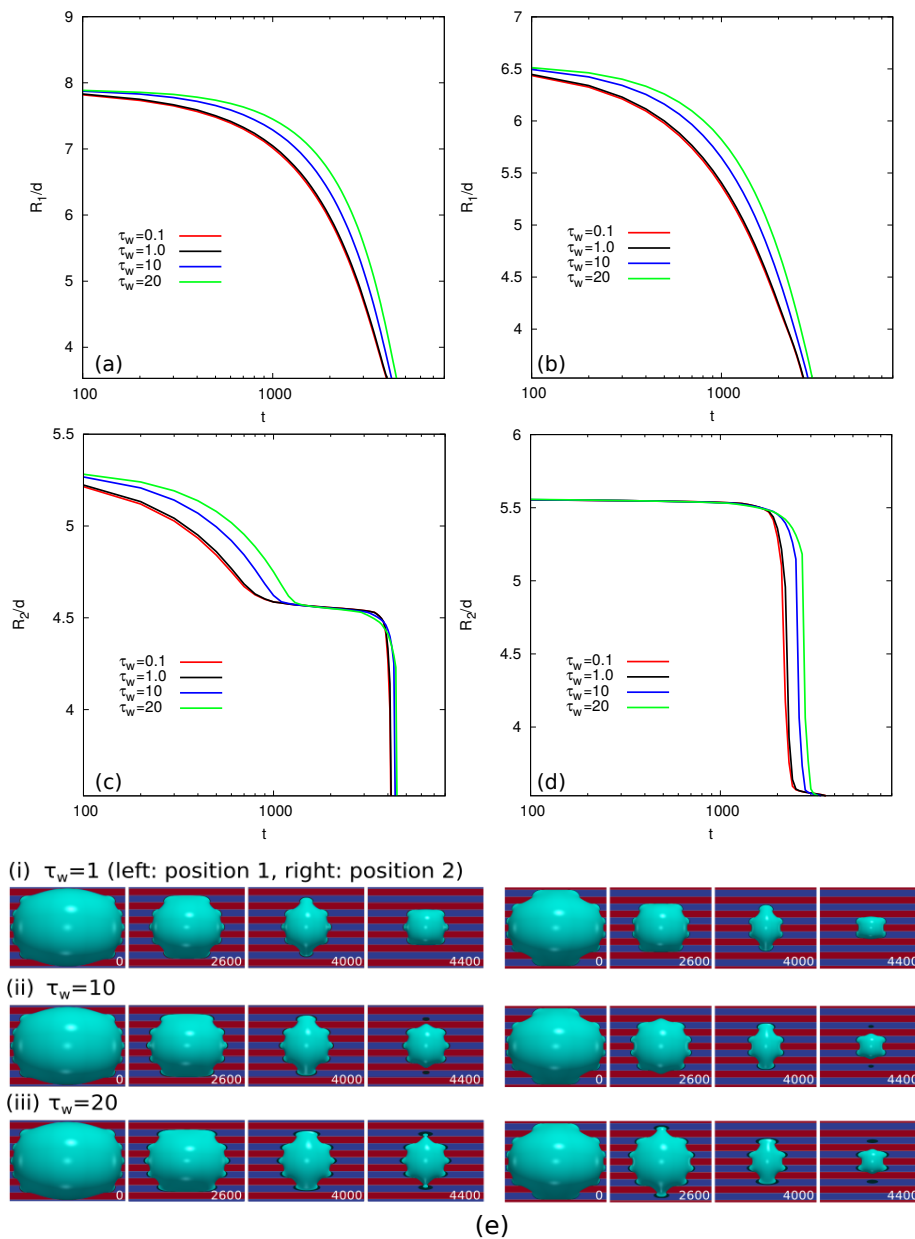


Figure 4.15: (a)-(d) The dimensionless directional contact radii R_1/d and R_2/d as a function of time for the evaporations at position 1 and 2. R_1 and R_2 are measured along the lines parallel and perpendicular to the stripes, respectively. d represents the stripe width. Lines with different colors present the results for different τ_w values. (a) and (c) are for the evaporations at position 1. (b) and (d) are for the evaporations at position 2. (e) Snapshots of droplet morphological transitions in evaporation processes for different τ_w values. The left parts illustrate the evaporations at position 1 while the right parts correspond to the evaporations at position 2. The numbers at the bottom right corner in the snapshots indicate the dimensionless time. (i)-(iii) in (e) are top views for $\tau_w = 1, 10, 20$.

terned surface. I believe that this is the first work that shows the similarity between the two spreading processes. According to the number of the wetted hydrophilic stripes, the diagram of ξ versus $d/V^{1/3}$ is divided into six areas. Within each area excluding I, for a fixed value of $d/V^{1/3}$, the droplets have two different equilibrium shapes, whereas on the boundaries (the intersections of the two condensation lines), the droplets have a unique equilibrium shape. It can be concluded that there are either one or two energy minimum states for the droplet-deposition on a chemically striped patterned surface. This result confirms the study of Gea Jódar et al. [176]. The morphological diagram Figure 4.9(a) reveals a relation between the droplet aspect ratio and the scaled stripe width and can be used to predict the equilibrium shapes of droplets deposited on chemically striped surface.

By studying the stick-slip-jump movement of a condensing droplet, I have explained how the equilibrium shapes of droplets are affected by the three important factors: V , d and initially deposited positions. The change fashion of the droplet aspect ratio ξ is caused by the different energy barriers parallel and perpendicular to the stripes when the droplet spreads over the surface. The stick-slip-jump movement is described by the different change modes of the contact angles parallel and perpendicular to the stripes (θ_1 and θ_2). It is demonstrated that the model described by Equation (4.3) remains valid for the prediction of the equilibrium droplet-shapes on chemically striped surface when the droplet size is comparable to the stripe width. To further explore the influence of the moving paths to the equilibrium shapes of droplets, simulations of the droplet evaporation are performed and compared with condensation processes. A typical hysteresis phenomenon is observed, which is attributed to the difference of the receding and advancing contact line movements. The surface energy analyses show that in the hysteresis area, the surface energies of the condensing and evaporating droplets for a fixed ratio $d/V^{1/3}$ are different. It is proved that through distinct moving paths, the droplets can reach different states of energy minimum and thus achieve different equilibrium shapes. Moreover, the influence of perturbations on droplet morphological transition is explored. As expected, large perturbations can lead to different moving paths of droplets. This suggests that the droplet-shapes can be manipulated through some perturbations, such as vibration, external electric-field etc. In addition, the phase change in non-equilibrium states is explored. By modifying the value of τ_w in the dynamic contact angle boundary condition, it is found that a large τ_w slows down the contact line kinetics. This inspires us that the droplet-shapes and kinetics time scale can be controlled by changing the physical properties of droplets, e.g. the density or viscosity. The comprehensive prediction of the droplets in this work is of significant importance for applications of surface design, fluid control, and smart microelectronics.

In this work, I concentrate on the situation where the droplet size is comparable to the stripe width and 1-6 hydrophilic stripes are wetted by the droplets in our simulations (in total maximal 11 hydrophilic and hydrophobic stripes). Our study can be regarded as a supplement to the study of Jansen et al. [178] and the present results converge to their results as $d/V^{1/3}$ decreases.

It should be emphasized that during the condensation and evaporation processes, I assume that the rate of phase change is sufficient slow such that the influence of fluid dynamics can be neglected. However, if the phase change rate is relatively high, to get further insights into the dynamics of the

contact line or the droplet shape evolution on chemically patterned surfaces, Navier-Stokes equations must be coupled in our model, which will be discussed in a forthcoming work. In addition, more complex patterned surfaces with various features such as chessboard-, circle- and star-shaped patterns will be focused on in a future work.

In summary, I have addressed the following points which have not been discussed in literature:

- I obtain a morphological diagram (Figure 4.9(a)), which reveals the similarity between the slowly condensing droplets and the droplet deposition. It can be used to predict the equilibrium droplet shapes.
- I have also found special points where unique equilibrium shape appears. This finding may have potential application in the fields of inkjet printing, biologics and microfluidics, where a fine control of droplet shape is necessary.
- The characterization of the drop anisotropies and the stick-slip-jump” behavior can be well described by the change fashion of directional contact angles. The validity of the model described by Equation (4.3) to predict the equilibrium droplet-shapes on chemically striped surface is extended.
- Through the shape comparisons between slowly condensing and evaporating droplets, a hysteresis phenomenon is found. This reveals that I can find more equilibrium droplet-shapes by manipulating droplets through different moving paths.
- The influence of perturbations on the droplet morphological transition is addressed.
- Phase change in non-equilibrium states is explored.

5. Single droplet on chemically patterned surfaces: A combined study through theoretical and numerical methods

After the investigation of droplet wetting behaviors on chemically striped patterned surfaces, more complicated patterned surfaces are taken into consideration in this chapter. The different equilibrium shapes of a single droplet deposited on three typical chemically patterned surfaces are theoretically and numerically investigated. A simplified analytical model and generalized analytical model are proposed to predict the equilibrium shapes of droplets. Phase-field simulations are accordingly conducted to confirm the predictions. Sections 5.1-5.2 were published in Ref. [183] and its supplemental document. Sections 5.3-5.4 were published in Ref. [184] and its supplemental document. The structures are slightly adjusted without changing the original contents.

5.1. Simplified analytical model and simulation setups

5.1.1. The calculation of the total interfacial energy

I consider a sessile droplet on a chemically patterned solid surface surrounded by a gas phase, as illustrated in Fig. 5.1. The droplet arrives at the equilibrium state by minimizing the total interfacial energy. The total interfacial energy of a droplet deposited on a chemically patterned surface is given by

$$E = A_{lg}\gamma_{lg} + \int_{A_{ls}} (\gamma_{ls} - \gamma_{gs})dA, \quad (5.1)$$

where A_{lg} and A_{ls} are the areas of the liquid-gas interface and liquid-solid interface, respectively. γ_{lg} , γ_{ls} , and γ_{gs} denote the liquid-gas, liquid-solid, and gas-solid interfacial energies, respectively. It is assumed that the droplet base line (red dashed line) forms an ellipse with semi-axes a and b . The liquid-gas interface is described with circular arcs (yellow dashed line) passing through the droplet apex and the contact line. These circular arcs have a varying curvature radius which is formulated as

$$r_c(\varphi) = \frac{r_b^2(\varphi) + h^2}{2h}, \quad (5.2)$$

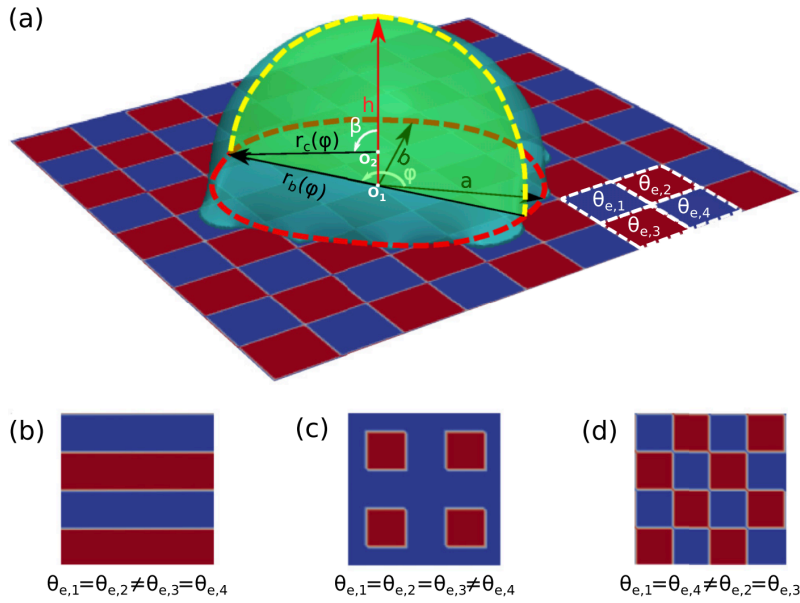


Figure 5.1.: Schematic illustration of the geometric assumptions of the droplet. (A) The red dashed ellipse (with center O_1 semi-axes a and b) is the droplet base line. r_b denotes the base radius. (B) The top part of the yellow dashed circle (above the black line passing through O_1) refers to the circular arc on the liquid-gas interface with the circle center O_2 and radius r_c . h is the droplet height. φ and β represent polar angles on the surfaces of the red dashed ellipse and yellow dashed arc, respectively.

where r_b and h are the base radius and droplet height, respectively. φ represent polar angle of the base ellipse. The base radius r_b is given by:

$$r_b(\varphi) = \frac{ab}{\sqrt{a^2 \sin^2(\varphi) + b^2 \cos^2(\varphi)}}. \quad (5.3)$$

The volume of the droplet V_d is described as:

$$V_d = \frac{\pi}{6} h(3ab + h^2). \quad (5.4)$$

The area of the liquid-gas interface A_{lg} can be formulated as

$$A_{lg} = \int_0^{2\pi} r_c^2(\varphi)(1 - \cos \beta) d\varphi, \quad (5.5)$$

where β is the polar angle between the rays from O_2 to the apex of the cap (the red line in Fig. 1) and the base line of the droplet (the red dashed line). β is given by

$$\beta = \arccos \frac{r_c(\varphi) - h}{r_c(\varphi)}. \quad (5.6)$$

From Eq. (5.2) to Eq. (5.6), for a droplet with certain volume, the area of the liquid-gas interface A_{lg} can be determined by the two parameters a and b , thus, the first term of interfacial energy in Eq. (5.1), $A_{lg}\gamma_{lg} = A_{lg}(a, b)\gamma_{lg} = E_1(a, b)$. Here I set γ_{lg} a dimensionless value $\gamma_{lg} = 1$. The second term of the interfacial energy in Eq. (5.1) can be calculated through the integration:

$$E_2 = \int_{A_{ls}} (\gamma_{ls} - \gamma_{gs}) dA = \int_0^{2\pi} \int_0^{r_b} r f_k(r, \varphi) dr d\varphi. \quad (5.7)$$

The chemical heterogeneities of the solid surface $\gamma_{ls} - \gamma_{gs} = f_k(r, \varphi)$ ($k = 1, 2, 3$ denote the striped, chocolate, and chessboard patterns, respectively) are described as follows

$$\gamma_{ls} - \gamma_{gs} = \begin{cases} f_1(r, \varphi) = \gamma_m + \gamma_0 \tanh(\xi \cos \delta_1) & \text{striped pattern} \\ f_2(r, \varphi) = \gamma_m + \gamma_0 \tanh[\xi(\cos \delta_1 \cos \delta_2 - \cos \delta_1 - \cos \delta_2)] & \text{chocolate pattern} \\ f_3(r, \varphi) = \gamma_m + \gamma_0 \tanh(\xi \cos \delta_1 \cos \delta_2) & \text{chessboard pattern} \end{cases} \quad (5.8)$$

with $\delta_1 = (\pi r \sin \varphi + i\pi L)/L$ and $\delta_2 = (\pi r \cos \varphi + j\pi L)/L$. γ_m and γ_0 are the mean surface energy difference and the amplitude of the heterogeneity, respectively. Presently, I set $\gamma_m = 0$, $\gamma_0 = 0.5$, i.e. the static equilibrium contact angles on the hydrophilic and hydrophobic areas are 60° and 120° , respectively. The characteristic length L denotes the width of the stripe for the striped pattern and the lattice length for the chocolate and chessboard patterns. ξ is a constant parameter controlling the sharpness of the chemical pattern and $i, j = 0, \pm 1, \pm 1/2, \dots$ are parameters depicting the center point position of the droplet base line, which will be specified in the following. Considering the importance of the droplet wetted area near the contact line, I use an average function $f_k(r_b, \varphi)$ to approximate $f_k(r, \varphi)$ and Eq. 5.7 is simplified as:

$$E_2 = \int_{A_{ls}} (\gamma_{ls} - \gamma_{gs}) dA = \int_0^{2\pi} \frac{1}{2} r_b^2 f_k(r_b, \varphi) d\varphi. \quad (5.9)$$

After the integration, the interfacial energy of the liquid-solid interface has four degrees of freedom, namely, $E_2 = \int_{A_{ls}} (\gamma_{ls} - \gamma_{gs}) dA = E_2(a, b, i, j)$. For a certain patterned surface and droplet position (i.e. for certain values of i, j), E_2 can be described as a function of a and b . The equilibrium droplet shapes are predicted by minimizing the total interfacial energy E in terms of a and b when i, j are fixed. A detailed discussion about the influence of i, j for given parameters a and b is elucidated in the subsection 5.1.3.

5.1.2. Simulation setups

The two-phase AC model is applied to simulate equilibrium shapes. The system evolution equations for the order parameter are discretized by the central finite difference method and the explicit Euler scheme with Message Passing Interface (MPI) techniques. The simulations are performed in 3D geometries by using an equidistant mesh with a spacing of $\Delta x = \Delta y = \Delta z = 1$. The simulation parameters are $\tau = 1$, $\tau_w = 1$, $\varepsilon = 1$, and the numerical stability of the simulations is guaranteed by choosing a fine time step $\Delta t < \tau(\Delta x)^2 / (12\gamma_{lg})$ according to the von Neumann stability analysis. In the simulations, the length x , time t , and energy E are nondimensionalized by the characteristic length $x^* = 1 \times 10^{-5}$ m, the characteristic time $t^* = 1 \times 10^{-9}$ s, and the characteristic energy $E^* = 1 \times 10^{-11}$ J, respectively. In the present work, transformed dimensionless parameters are used.

In the simulations, the droplets initially have a form of cuboid, as shown in the first snapshot ($t = t_0$) in the top and bottom rows of Fig. 5.2(B). Parameters a and b in the simulations are chosen near the points 1 and 2 in Fig. 5.2(A), so that the surface energy minima can be reached.

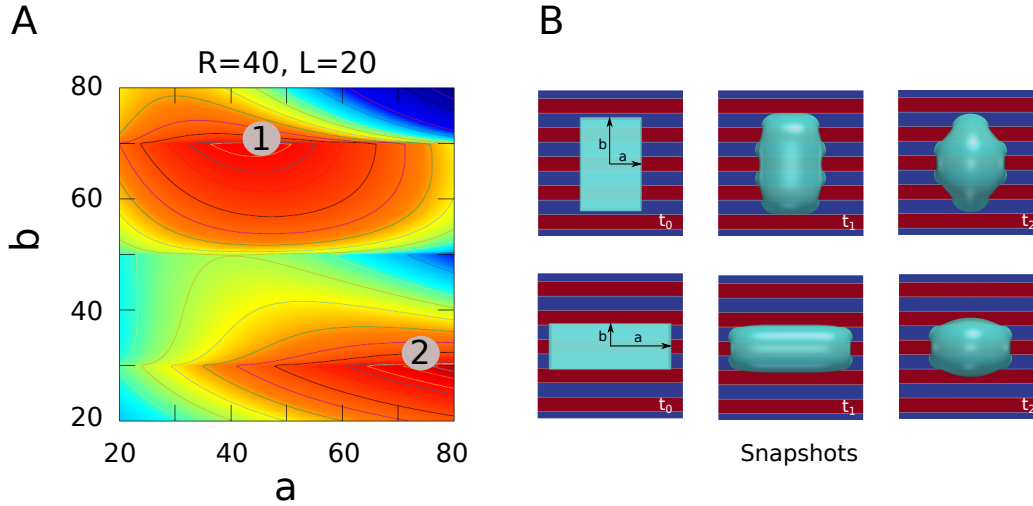


Figure 5.2.: (A) Surface energy landscape of a droplet on chemically striped patterned surface (The effective radius of the droplet is $R = 40$, stripe width is $L = 20$ and the droplet base center is on the hydrophobic stripe). Point 1 and 2 are the two energy minima. (B) Snapshots of droplet-shape evolution from initial states to equilibrium states. The top and bottom rows correspond to the points 1 and 2 in (A), respectively.

5.1.3. Validation of the high symmetry property of equilibrated droplets

Fig. 5.3 – Fig. 5.5 illustrate the total interfacial energy of droplets on the three chemically patterned surfaces as a function of i (and j). As shown in Fig. 5.3(A), the total interfacial energy changes periodically with i and the energy minima are achieved when the droplet base center lies on the center of hydrophilic ($a = 60$, $b = 50$) or hydrophobic stripes ($a = 45$, $b = 70$). The coordinate of the droplet base center position is described in Fig. 5.3(B). The red points ($i = \pm 1, \pm 3, \dots$) are on the center of hydrophilic stripes, while the blue points ($i = 0, \pm 2, \pm 4, \dots$) are on the center of hydrophobic ones.

Fig. 5.4(A)-(C) display the surface energy landscape of droplets on chocolate-patterned surfaces as a function of droplet base center position i and j . (A), (B), and (C) correspond to droplets with ($a = 50$, $b = 50$), ($a = 70$, $b = 50$), and ($a = 65$, $b = 65$), respectively. The total interfacial energy evolves periodically with i and j . In (A), energy minima (red color) appear at ($j = 2p$, $i = 2q$) with $p, q \in \mathbb{Z}$, e.g. P_1 . The energy minima in (B) and (C) are at ($j = 2p + 1$, $i = 2q$), e.g. P_2 and ($j = 2p + 1$, $i = 2q - 1$), e.g. P_3 , respectively. P_1 , P_2 , and P_3 are high symmetry points on the chocolate-patterned surface, as displayed in Fig. 5.4(D).

Fig. 5.5(A)-(C) display the surface energy landscape of droplets on chessboard-patterned surfaces as a function of droplet base center position i and j . (A), (B), and (C) correspond to droplets with ($a = 52$, $b = 52$), ($a = 60$, $b = 60$), and ($a = 45$, $b = 57$), respectively. The total interfacial energy also evolves periodically with i and j . In (A), energy minima appear at ($j = 2p$, $i = 2q$), e.g. P_1 . The energy minima in (B) and (C) are at ($j = 2p$, $i = 2q + 1$), e.g. P_2 and ($j = 2p - 1/2$, $i = 2q + 1/2$) or ($j' = \sqrt{2}p$, $i' = \sqrt{2}q + 1/\sqrt{2}$) in the rotated coordinate system, e.g. P_3 , respectively. P_1 , P_2 , and P_3

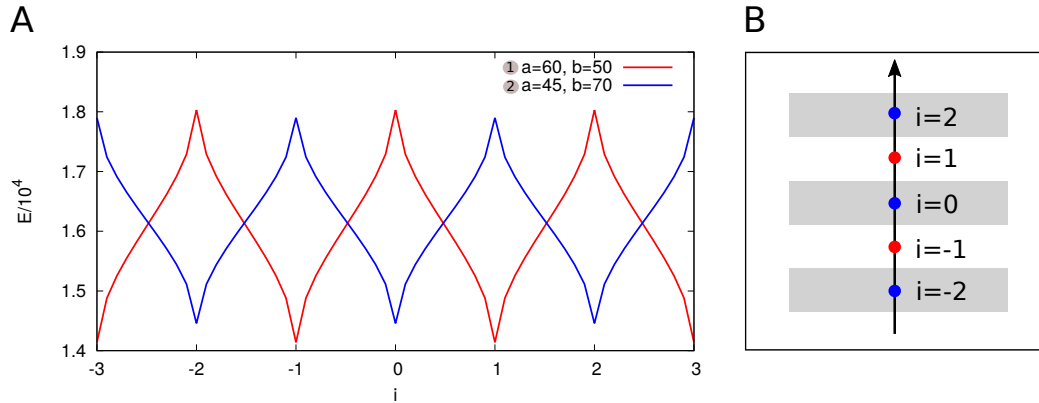


Figure 5.3.: (A) Surface energy of two droplets ($a = 60$, $b = 50$ and $a = 45$, $b = 70$, illustrated with red and blue lines, respectively) on chemically striped patterned surfaces as a function of droplet base center positions i (The effective radius ($R = (3V_d/4\pi)^{1/3}$, V_d is droplet volume) of the droplets is $R = 40$, stripe width is $L = 20$). The energy minima of the red and blue lines correspond to the points 1 and 2 in the energy landscapes shown in Fig. 5.6, respectively. (B) Sketch of the surface topology and the coordinates of droplet base center positions when energy minima are achieved (grey: hydrophobic, $i = 0, \pm 2, \pm 4, \dots$; white: hydrophilic, $i = \pm 1, \pm 3, \dots$).

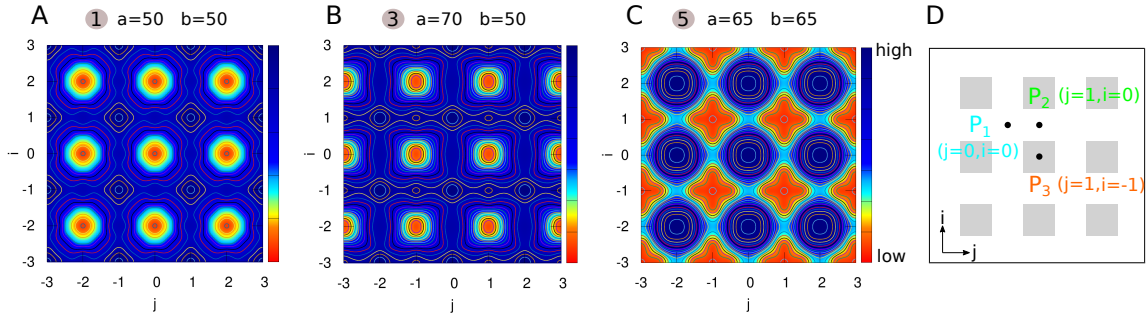


Figure 5.4.: (A)-(C) Surface energy landscape of droplets on chocolate-patterned surfaces as a function of droplet base center positions when a, b varies (The effective radius of the droplet is $R = 40$, lattice width is $L = 20$ and i and j indicate the coordinate of the droplet base center). (A): $a = 50$, $b = 50$, (B): $a = 70$, $b = 50$, and (C): $a = 65$, $b = 65$. The energy minima (red color) in (A), (B), and (C) correspond to the points 1, 3, and 5 in the energy landscapes shown in Fig. 5.7, respectively. (D) Sketch of the surface topology and the three typical coordinates of droplet base center positions when energy minima are achieved (grey: hydrophobic, white: hydrophilic). $P_1 : (j = 0, i = 0)$, $P_2 : (j = 1, i = 0)$, and $P_3 : (j = 1, i = -1)$.

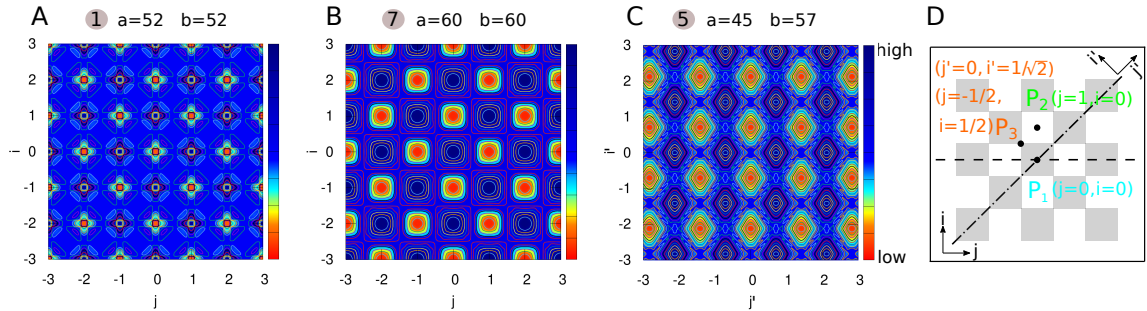


Figure 5.5.: (A)-(C) Surface energy landscape of droplets on chessboard-patterned surfaces as a function of droplet base center positions when a, b varies (The effective radius of the droplet is $R = 40$, lattice width is $L = 20$ and i and j indicate the coordinate of the droplet base center). (A): $a = 52$, $b = 52$, (B): $a = 60$, $b = 60$, and (C): $a = 45$, $b = 57$. The energy minima (red color) in (A), (B), and (C) correspond to the points 1, 7, and 5 in the energy landscapes shown in Fig. 5.8, respectively. (D) Sketch of the surface topology and the three typical coordinates of droplet base center positions when energy minima are achieved (grey: hydrophobic, white: hydrophilic). $P_1 : (j = 0, i = 0)$, $P_2 : (j = 0, i = 1)$, and $P_3 : (j = -1/2, i = 1/2)$ or $(j' = 0, i' = 1/\sqrt{2})$ in the rotated coordinate system.

are high symmetry points on the chessboard-patterned surface, as displayed in Fig. 5.5(D). In summary, the center point (j, i) of the elliptical base is considered in the numerical energy minimizations, and multi-stability is found. Moreover, the distribution of the energy minima implies the chemical

property of the patterned surface. The center point of any local minimum for the three patterned surfaces is proven to be one out of a set of high symmetry points.

5.2. Droplet shape analysis by using the simplified model

5.2.1. Striped patterned surfaces

I now present the analytical predictions and simulation results of droplets on chemically striped patterned surface. In Fig. 5.6(a)-(c), I illustrate the surface energy landscapes of droplets in terms of the parameters a and b as well as the corresponding snapshots of the equilibrated droplets via PF model. In the simulations, the droplets with a given volume initially have a form of cuboid with various aspect ratios in the contact area.

Suitable aspect ratios and initial positions of the droplets are chosen, such that the surface energy minima predicted by the analytical model can be reached. As shown in the first picture of Fig. 5.6(a)(III), a and b are the semi-axes of the elliptic base line of droplets, which are parallel and perpendicular to the stripes, respectively. The surface energy minima indicated by different numbers in the energy diagrams correspond to the snapshots labeled with the same number. The effective droplet radii $R = (3V_d/4\pi)^{1/3}$ in Fig. 5.6(a), (b), and (c) are 40, 50, and 90, respectively. The blue and red stripes in the snapshots denote the hydrophilic and hydrophobic ones with the same stripe width $L = 20$. In Fig. 5.6(a)(III), the red dashed ellipses denote the analytical results, corresponding to the coordinate of the energy minimum points in the energy diagrams. A good agreement is observed between the analytical solution and the numerical simulations and three equilibrated droplets are found. Similarly, as illustrated in Fig. 5.6(b) and (c), 4 and 5 equilibrium shapes are found for the droplets with $R = 50$ and $R = 90$, respectively. By using the same methods, I obtain droplet configurations for different droplet sizes, as depicted in Fig. 5.6(d), where the ratio R/L ranges from 2 to 9. Both the number of the equilibrium shapes and the tendency of the analytical results show a satisfactory agreement with the simulation results. Because of the contact line pinning in the direction perpendicular to the stripes, the value of b is well predicted by the analytical model. However, for large a , the analytical predictions of a deviate from the simulations, which is caused by the assumption of the analytical model that the liquid-gas interface is described with circular arcs. While this is obviously not the case when the droplet aspect ratio a/b is relatively large and the deformation of the contact lines takes an important role. From Fig. 5.6(d), I conclude that the number of the equilibrium droplet-shapes (or the local energy minima) remains constant as the droplet volume increases within a certain range (e.g. $R/L = 2, 3, 4$), while a further rise of the droplet volume results in an increase in the number of equilibrium droplets (e.g. from $R/L = 4$ to $R/L = 5$).

5.2.2. Chocolate patterned surfaces

Afterwards, a two-dimensional periodic solid surface pattern, the chocolate pattern, is considered. In this pattern, the size of the lattices and the distance between them both are set to be 20. The

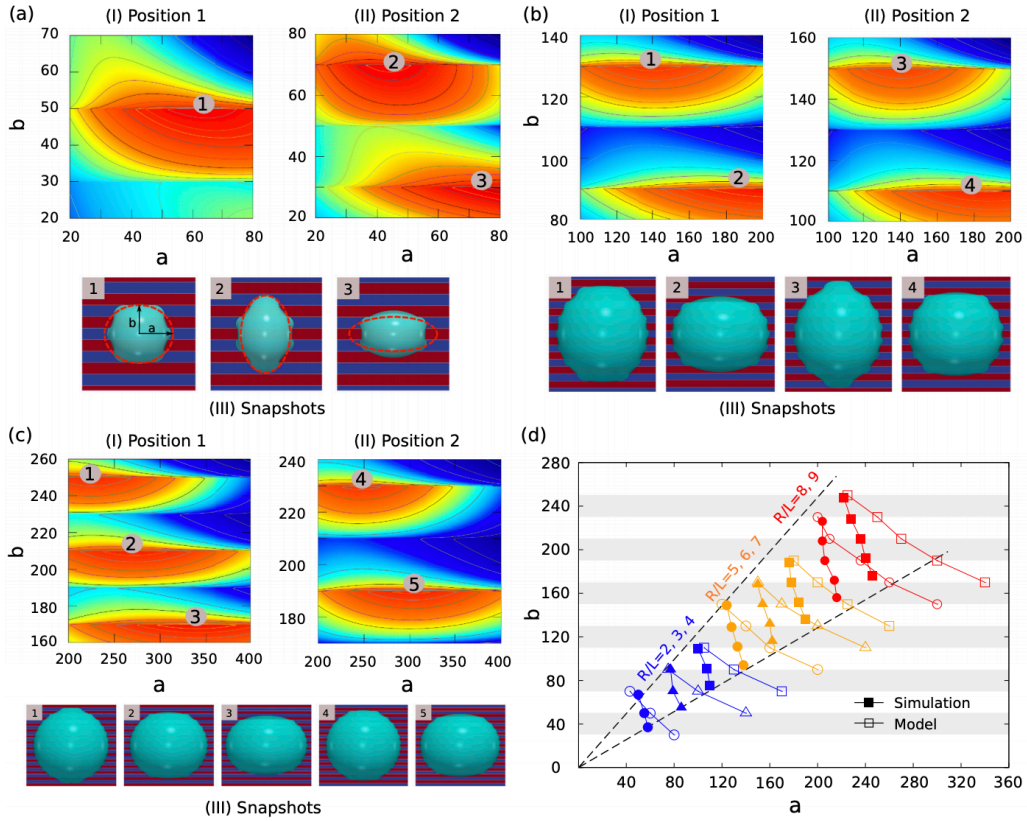


Figure 5.6.: (a)-(c) Surface energy landscapes in the a - b space and snapshots of sessile droplets on chemically striped patterned surfaces with different droplet sizes ((a): $R/L = 2$, (b): $R/L = 5$, (c): $R/L = 9$). The chemical heterogeneities are described by $f_1(r, \varphi)$ in Eq. (5.8). At equilibrium, the droplet base center stays either on the center of the blue (hydrophilic) stripe (namely position 1 and $i = 1$) or on the center of the red (hydrophobic) one (i.e. position 2 and $i = 0$). The energy landscapes are accordingly calculated when the droplet base centers are on these two different positions. The contour lines indicate the energy levels (red for low energy and blue for high energy states) and the color changes from blue to red illustrate the decrease of the energy. The energy minima are indicated by different numbers, corresponding to the snapshots labeled with the same number. The red dashed ellipses in (a)(III) denote the analytical results, which can be read from the corresponding energy landscapes. (d) Predicted droplet configurations for different droplet sizes. The filled and empty symbols describe the simulation and analytical results, respectively. The two dashed lines are guide lines to highlight a trend in the data.

effective droplet radius is $R = 40$. In the simulations, the droplets initially have a cuboid form with different aspect ratios and then evolve to equilibrium shapes. Fig. 5.7(a)-(c) show the surface energy landscapes for droplets with the base center points on P_1 ($j = 0, i = 0$), P_2 ($j = 1, i = 0$), and P_3 ($j = 1, i = -1$), respectively (see Fig. 5.7(d)). Fig. 5.7(e) illustrates the simulation results of the

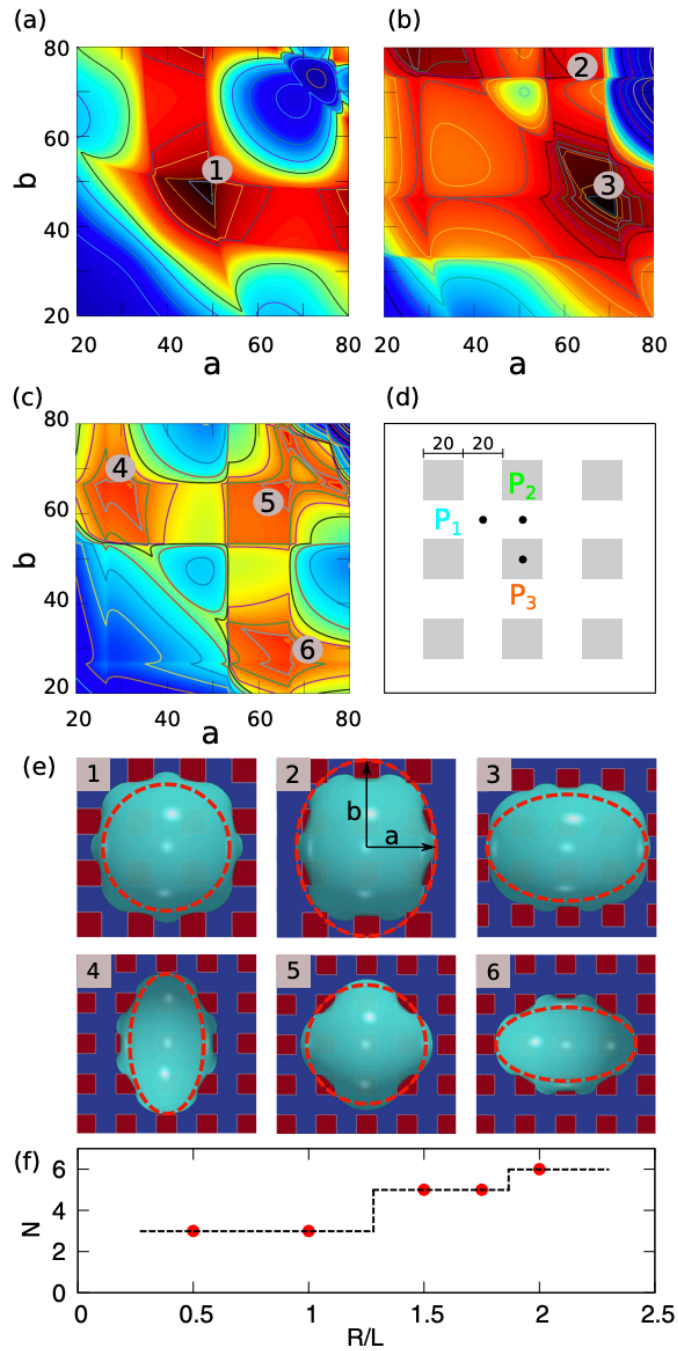


Figure 5.7.: (a)-(c) Surface energy landscapes for chocolate-patterned surfaces. The chemical heterogeneities are described by $f_2(r, \varphi)$ in Eq. (5.8). The energy minima are indicated by different numbers, corresponding to the snapshots in E labeled with the same number. (d) Sketch of the surface topology and three base centers of droplets (grey: hydrophobic, white: hydrophilic). The droplet shapes in (a), (b), and (c) correspond to the positions P_1 , P_2 , and P_3 . (e) Snapshots of equilibrated droplets through PFM (blue: hydrophilic, red: hydrophobic). The red dashed ellipses denote the analytical results. (f) The number N of equilibrium shapes of droplets as a function of R/L . The black dashed line is the guide line.

equilibrium shapes of droplets. The energy minima indicated by different numbers correspond to the snapshots in Fig. 5.7(e) labeled with the same number. The red dashed ellipses in Fig. 5.7(e) are the analytical predictions, which show good agreement with the simulation results. It is found that the energy diagrams (a) and (c) are symmetric with respect to the line $a = b$, while in (b) this symmetric characteristic disappears. This is because the topologies in a and b directions are the same for the points P_1 and P_3 , while for the point P_2 the topologies vary in the two directions. In comparison to the droplets with the same size ($R = 40$) on the striped patterned, more local energy minima are found for droplets on the chocolate-patterned surface. Furthermore, by changing the droplet volume, I have found a functional relation between the number of equilibrium shapes of droplets N and the droplet size R/L , as illustrated in Fig. 5.7(f). The red points indicate the predicted values of N for

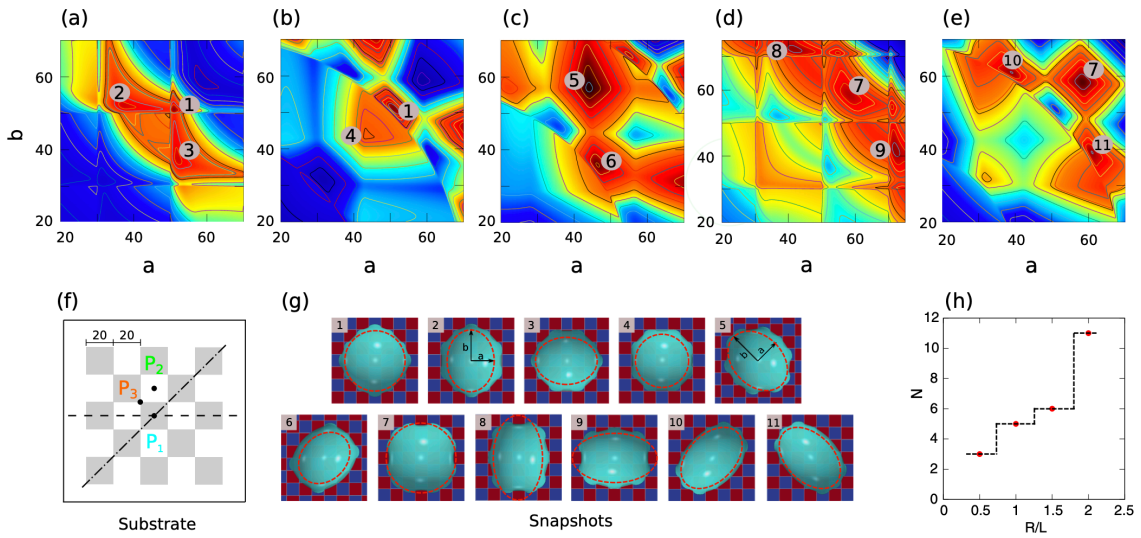


Figure 5.8.: (a)-(e) Surface energy landscapes for chessboard-patterned surfaces. (a) and (d) correspond to the situations when the directions of a and b are horizontal and vertical, respectively, as shown in (g)2. The chemical heterogeneities are described by $f_3(r, \varphi)$ in Eq. (5.8). (b), (c), and (e) describe the energy landscapes in a rotated coordinate system and the directions of a and b are shown in (g)5. In the rotated system, δ_1 and δ_2 in $f_3(r_b, \varphi)$ are substituted by δ'_1 and δ'_2 , respectively, with $\delta'_1 = (\delta_1 + \delta_2)/\sqrt{2}$ and $\delta'_2 = (\delta_1 - \delta_2)/\sqrt{2}$. The energy minima are indicated by different numbers, corresponding to the snapshots in (g) labeled with the same number. (f) Schematic description of the surface topology and three base center points of equilibrated droplets (grey: hydrophobic, white: hydrophilic). The two lines indicate two possible directions of the semi-axis a . (a) & (b), (d) & (e), and (c) correspond to P_1 , P_2 , and P_3 , respectively. (g) Snapshots of equilibrated droplets via PFM (blue: hydrophilic, red: hydrophobic). The red dashed ellipses denote the analytical results. (h) The number N of equilibrium shapes of droplets as a function of R/L . The black dashed line is the guide line.

different R/L . The black dashed line highlights the functional tendency, showing that larger droplets tend to have more equilibrium patterns.

5.2.3. Chessboard patterned surfaces

I further utilize the analytical model and PF model to scrutinize the equilibrated droplets on a more complex pattern, the chessboard pattern. The effective droplet radius is $R = 40$ and the lattice length of the chessboard is $L = 20$. Fig. 5.8(a) and (d) show the energy landscapes for droplets deposited on the positions P_1 ($j = 0, i = 0$) and P_2 ($j = 0, i = 1$), respectively. Fig. 5.8(b), (c), and (e), which is achieved by rotating the coordinate system by 45° (the directions of a and b are shown in Fig. 5.8(g)(5)), illustrate the energy landscapes corresponding to the positions P_1, P_3 ($j = -1/2, i = 1/2$) and P_2 , respectively. It is found that the analytical predictions (red dashed ellipses in Fig. 5.8(g)) match very well with the PF simulations. With the aid of the present model, 11 equilibrated droplet-patterns are found for the chessboard-patterned surface with the initial setup $R = 40$ and $L = 20$. The number N of equilibrium shapes of droplets as a function of the droplet size R/L is displayed in Fig. 5.8(h). The results reveal that the increase in the droplet size leads to more equilibrium shapes of droplets. Currently, I focus on the equilibrium features of droplets on chemically patterned surface and the capabilities of the analytical model. Systematic studies of parameters such as contact angles will be presented in a future work.

5.2.4. Summary and conclusion

Fig. 5.9 illustrates how the complexity of the pattern influences the number of equilibrated droplets. Here, I introduce a parameter – energy discontinuous line density ρ (see the caption in Fig. 5.9) to characterize the complexity of the pattern. From striped patterned surface to chocolate-patterned and chessboard-patterned surface, the density of the energy discontinuous line rises, which increases the complexity of the energy landscape (e.g. see energy landscapes in Fig. 5.6(a), Fig. 5.7, and Fig. 5.8) and thus leads to more and more equilibrated droplets. This increase tendency is more pronounced for larger droplets ($R/L=2$) than for smaller ones ($R/L=1.5$ and 0.5). The underlying reason is that more energy discontinuous lines are covered by the large droplets and therefore more stable states tend to occur. While for small droplets, the number of covered discontinuous lines is relatively reduced and the equilibrated states are not as many as that for large droplets.

To conclude, I have presented a strategy for delineating the equilibrated droplet-patterns on programmable chemically patterned surfaces via calculating the surface energy landscapes. I have applied and validated the strategy by studying equilibrium shapes of droplets on three selected substrate patterns. Together with numerical simulations, I have found almost all of the the potential existing energy minima and the corresponding equilibrium droplet-shapes, while this is not possible by the Cassie-Baxter model. It has been revealed that the increase in the droplet volume or the complexity of the surface (e.g. by introducing more hydrophilic-hydrophobic boundary lines) most likely gives rise to more surface energy minima. Hence, numerous droplet patterns can be quantitatively obtained

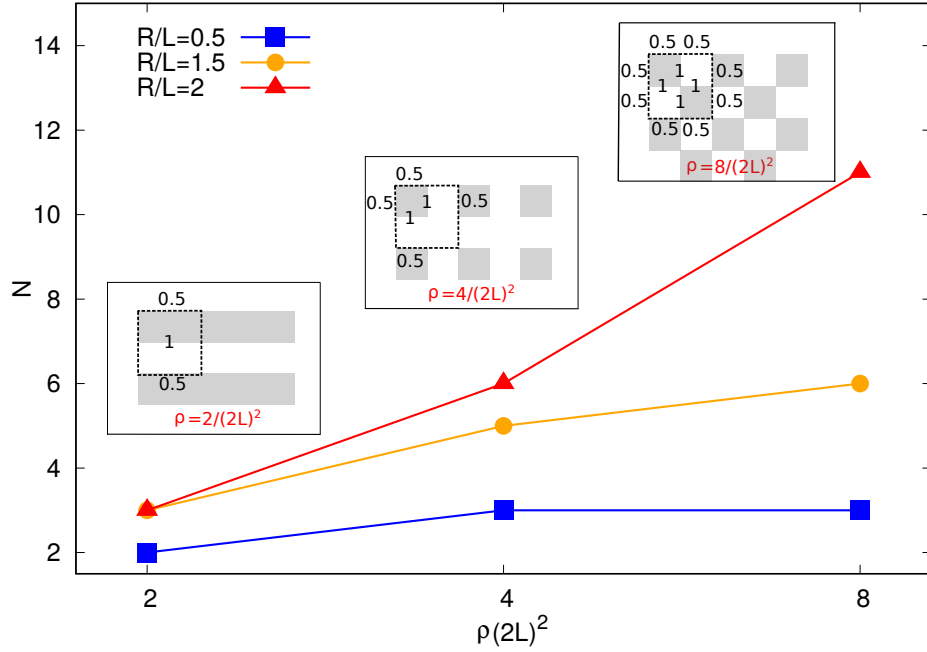


Figure 5.9.: The number N of equilibrium droplet-shapes as a function of the energy discontinuous line density $\rho := n/(2L)^2$ for different patterned surfaces, Here, n is the total effective number of pinning lines within a square cell with an area of $(2L)^2$. The three insets indicate how ρ is calculated for different patterned surfaces. The numbers “1” and “0.5” shown in the cells stand for the effective number of pinning lines. The lines with different colors denote the results for droplets with different sizes (blue: $R/L = 0.5$, orange: $R/L = 1.5$, red: $R/L = 2$).

by tuning the droplet volume or the morphologies of the surfaces. This new insight paves an alternative way to better understand wetting behaviors on chemically patterned surfaces. Our approach can be straightforwardly extended to study droplets deposited on a variety of chemically patterned surfaces and offers essential guidelines for a vast range of applications in microfluidics, inkjet printing, and biomedical science [10, 185]. However, on real heterogeneous surfaces, the contact line is highly non-linear and far more complex than the present approximation of ellipse. In this case, an infinitely dimensional Fourier series should be adopted to depict the triple line, which gives rise to an infinitely dimensional energy landscape. To find the complete set of the local energy minima in such an infinitely dimensional energy landscape is challenging and cannot be achieved by the present model.

5.3. Generalized analytical model and modified CB model

In this section, I extend the analytical method, which was depicted in section 5.1. I here apply this analytical approach to scrutinize wetting of chemically patterned surfaces with various characteristic lengths, contact angles, and ratios of the hydrophilic area to the hydrophobic one, which were not contemplated in the previous work. In comparison with the model in section 5.1, three major improvements are recounted here: (i) A new parameter λ is introduced in the nonlinear functions depicting the chemical heterogeneities of the substrate. With this new parameter, it is convenient to manipulate the ratio of the hydrophilic area to the hydrophobic area. (ii) A new parameter χ is employed to control the lattice roundness of the chocolate patterned surface. (iii) Most importantly, a modified Cassie-Baxter model is proposed here for a comparison with the analytical approach.

To address the improvements above, the functions $f_k(r, \varphi)$ are extended as

$$\begin{cases} f_1 = \gamma_m + \gamma_0 \tanh[\xi(\cos \delta_1 - \lambda)] \\ f_2 = \gamma_m + \gamma_0 \tanh\{\xi[(\cos \delta_1 - \lambda)(\cos \delta_2 - \lambda) - \chi(\cos \delta_1 + \cos \delta_2)]\} \\ f_3 = \gamma_m + \gamma_0 \tanh[\xi(\cos \delta_1 - \lambda)(\cos \delta_2 - \lambda)] \end{cases} \quad (5.10)$$

with $\delta_1 = (2\pi r \sin \varphi + i\pi L)/L$ and $\delta_2 = (2\pi r \cos \varphi + j\pi L)/L$. Here, γ_m and γ_0 are the mean surface energy density difference and the amplitude of the heterogeneity, respectively. For example, the parameter set ($\gamma_m = 0, \gamma_0 = 0.5$) corresponds to the situation where the static equilibrium contact angles on the hydrophilic (θ_1) and hydrophobic (θ_2) areas are 60° and 120° , respectively. The sharpness of the chemical pattern is controlled by the parameter ξ . The index $i, j = 0, \pm 1, \pm 1/2, \dots$ depicts the center point position of the droplet base line. Figure 5.10 highlights all the possible coordinates of the index, with respect to which the equilibrated droplets are symmetric on the three chemically patterned surfaces. For the striped patterned surface (Figure 5.10(a)), the red points P_1 ($i = \pm 1, \pm 3, \dots$) are on

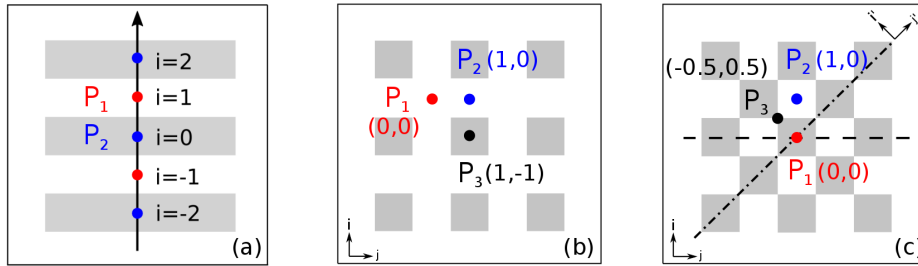


Figure 5.10.: (a)-(c) Sketches of the surface topology for three chemically patterned surfaces: "stripe," "chocolate," and "chessboard." Here, the grey and white areas denote hydrophobic and hydrophilic surfaces, respectively. The coordinates of the droplet base center positions at equilibrium are highlighted by P_1 , P_2 and P_3 . (a) $P_1 : i = 1, P_2 : i = 0$. (b) $P_1 : (j = 0, i = 0)$, $P_2 : (j = 1, i = 0)$, and $P_3 : (j = 1, i = -1)$. (c) $P_1 : (j = 0, i = 0)$, $P_2 : (j = 0, i = 1)$, and $P_3 : (j = -1/2, i = 1/2)$ or $P_1 : (j' = 0, i' = 0)$, $P_2 : (j' = 1/\sqrt{2}, i' = 1/\sqrt{2})$, and $P_3 : (j' = 0, i' = 1/\sqrt{2})$. The indexes with primes for the last three points are in the rotated coordinate system.

the center of the hydrophilic stripes (white), while the blue points P_2 ($i = 0, \pm 2, \pm 4, \dots$) locate on the center of the hydrophobic ones (grey). For the chocolate and chessboard patterned surfaces, the droplet base center points P_1 , P_2 , and P_3 with the coordinates (j, i) are indicated in Figure 5.10(b) and (c), respectively. It should be noticed that P_1 , P_2 , and P_3 are periodically distributed on the surfaces and the validation for the high symmetry property of these positions has been fully discussed in section 5.1. The characteristic length is defined as $L := L_{dry} + L_{wet}$, where L_{dry} and L_{wet} are the respective characteristic length for the hydrophobic and hydrophilic areas. For instance, L_{dry} (L_{wet}) stands for the width of a hydrophobic (hydrophilic) stripe for the striped surfaces. For the chocolate and chessboard patterns, L_{dry} and L_{wet} denote the length of the hydrophobic lattice and the distance in the direction of j or i between two neighbouring hydrophobic lattices (Figure 5.10(b) and (c)), respectively.

I define a parameter $\nu := L_{wet}/L_{dry}$ to characterize the area ratio of the hydrophilic to the hydrophobic regions on the three chemically patterned surfaces. This parameter ν is manipulated by varying λ in the functions f_1 , f_2 , f_3 . Here, I select three typical values of $\nu = 1 : 1$, $1 : 2$, $1 : 3$, corresponding to $\lambda = \cos 90^\circ$, $\cos 60^\circ$, $\cos 45^\circ$, respectively. For these three values of ν , the contours $f_k(x, y)$ of the three chemically patterned surfaces are shown in Figure 5.11(a)-(c), where I have made the following coordinate transformation: $x = r \cos \varphi$ and $y = r \sin \varphi$. It is found that the three functions with selected parameters perfectly describe the desired heterogeneity of the three typical chemically patterned surfaces. In particular, the parameter χ in f_2 is introduced to control the roundness of the isolated hydrophobic areas (red areas in Figure 5.11(b)).

In the following, I will propose a modified CB model to address the equilibrated droplets on chemically patterned surfaces. Firstly, let us revisit the classical CB model, which delineates the average contact angle $\bar{\theta}$ of droplets on chemically heterogeneous surfaces:

$$\bar{\theta} = \arccos(x_1 \cos \theta_1 + x_2 \cos \theta_2). \quad (5.11)$$

Here, x_m represents the area fraction of the surface component with the corresponding equilibrium contact angle θ_m , $m = 1, 2$. In the current work, the area fractions x_m range from 0.25 to 0.75. The average angle $\bar{\theta}$ actually reflects the energy minimum state of droplets and reveals the wettability of the chemically heterogeneous surface.

I assume that an equilibrated droplet on the chemically patterned surface is delineated by a spherical cap (see Figure 5.12), whose contact angle reads $\bar{\theta}$. This spherical cap is described by the following equations

$$\begin{cases} V_d = \pi(3r_b^2 + h^2)/6 & \text{volume} \\ h = r_c(1 - \sin \bar{\theta}) & \text{height} \\ r_b = r_c \sin \bar{\theta} & \text{base radius.} \end{cases} \quad (5.12)$$

Here, r_c and r_b both are constants. When the droplet volume V_d and $\bar{\theta}$ are given, r_b is obtained via Eq. (5.12), namely, $r_b = r_b(V_d, \bar{\theta})$. The base line of an equilibrated droplet may deviate from the circular shape (red circle in Figure 5.12) and exhibits an elliptical morphology as assumed in the previous section. In this case, I use the contact area $A_{sl} = \pi r_b^2$ of the circular base area as a reference

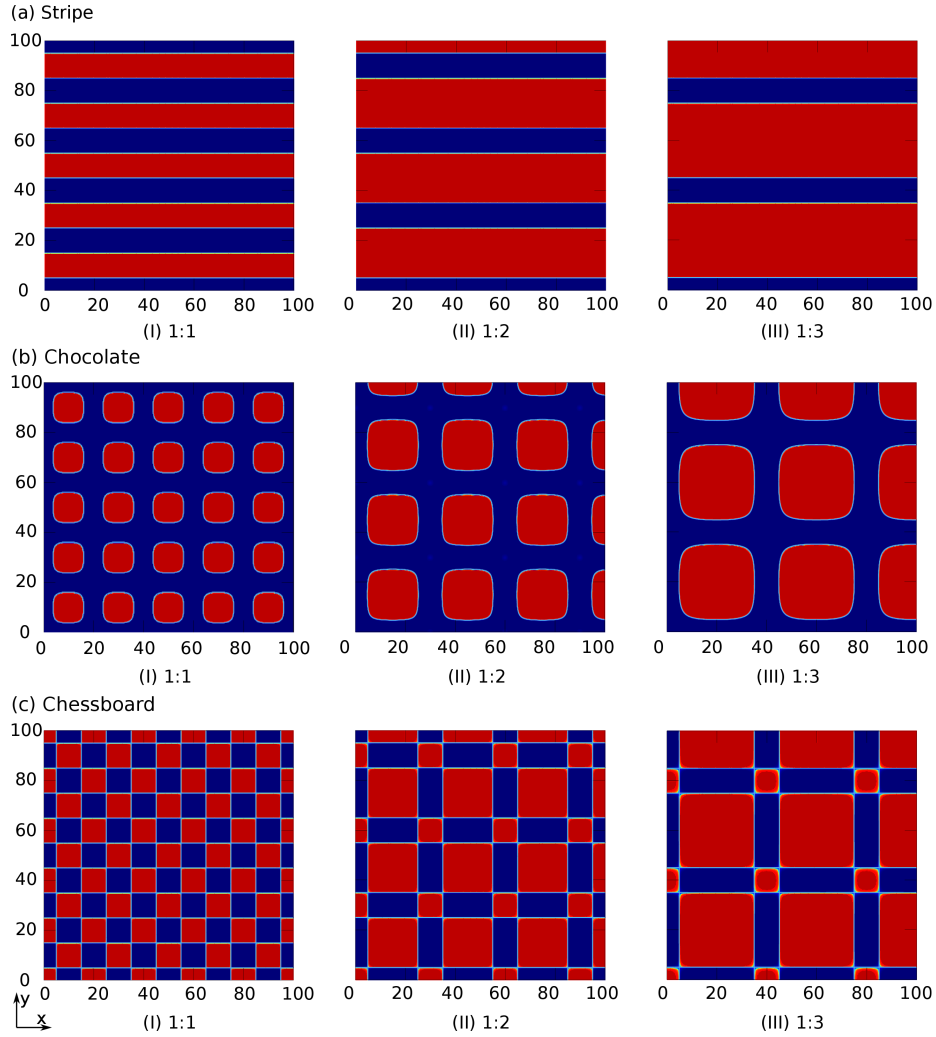


Figure 5.11.: (a)-(c) Contour plot of the functions $f_1(x, y)$, $f_2(x, y)$, $f_3(x, y)$ describing the heterogeneities of the three chemically patterned surfaces: stripe, chocolate, and chessboard, respectively. Here, $x = r \cos \varphi$ and $y = r \sin \varphi$. r is the r coordinate in polar coordinate system. The patterns are obtained by setting $\gamma_m = 0$, $\gamma_0 = 0.5$, $\xi = 100$. The characteristic lengths L in (I), (II), (III) are 20, 30, and 40, respectively. The ratios ν for 1:1, 1:2, and 1:3 correspond to $\lambda = \cos 90^\circ$, $\cos 60^\circ$, $\cos 45^\circ$, respectively. In (b)(I), (II), (III), I set $\chi = 0.55, 0.13, 0.10$, respectively. The red and blue color show $f_k = -0.5$ or 0.5 , corresponding to hydrophilic and hydrophobic area, respectively.

value to appraise the one of the elliptical base area, i.e. $\pi ab = \Psi(V_d, \bar{\theta})$, where $\Psi = \pi r_b^2$. The proposed modified CB model will be compared with the PF simulations in the following.

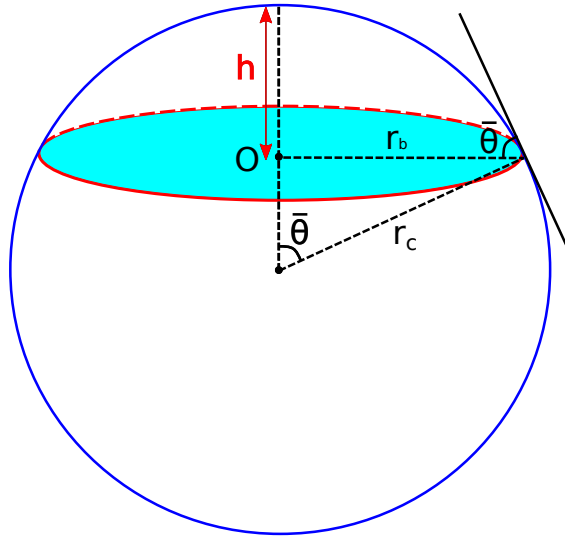


Figure 5.12.: Droplet morphology in a form of spherical cap. The liquid-solid contact area is highlighted in the cyan color.

5.4. Droplet shape analysis by using the generalized model

In this section, by using the generalized analytical methods and the two-phase AC model, I study the influence of droplet sizes, contact angles, and the ratios of the hydrophilic area to the hydrophobic area upon the equilibrium morphologies. Here, three typical chemically patterned surfaces, namely, striped, chocolate,” and chessboard” patterned surfaces are considered.

5.4.1. Droplet size

In this part, the contact angles on hydrophilic and hydrophobic areas are set as 60° and 120° , respectively, i.e. $\theta_1 = 60^\circ$, $\theta_2 = 120^\circ$. The characteristic length in Eq. (5.10) is a constant value $L = 40$. With varying the droplet volume V_d , I use the ratio R/L to characterize the effect of the droplet size on the equilibrium patterns. Here, R is the effective radius of the droplet, which is calculated according to $R = (3V_d/4\pi)^{1/3}$.

In Figure 5.13, I present the surface energy landscapes for droplets with different volumes as well as the corresponding equilibrated states on the chocolate-patterned surface. For the sake of conciseness, the simulation setups, the energy maps, and the snapshots of the equilibrated droplets on the other two patterns (striped and chessboard patterned surfaces) are fully described in the Appendix B. From (I) to (III) in Figure 5.13, the size of the droplets varies from $R/L = 0.75$ to $R/L = 0.25$. The hydrophobic square lattices (red) have a width of $L_{dry} = L/2 = 20$ and the distance between two neighbouring lattices is $L_{wet} = L/2 = 20$. In each panel, the surface energy landscapes in (A), (B), and (C) are for droplets with base center positions on P_1 , P_2 , and P_3 , respectively. The energy minima in the deep blue region are sequentially numbered, corresponding to the snapshots of the PF simulation results labeled with the same number in (D). As an example, I compare the base line (red

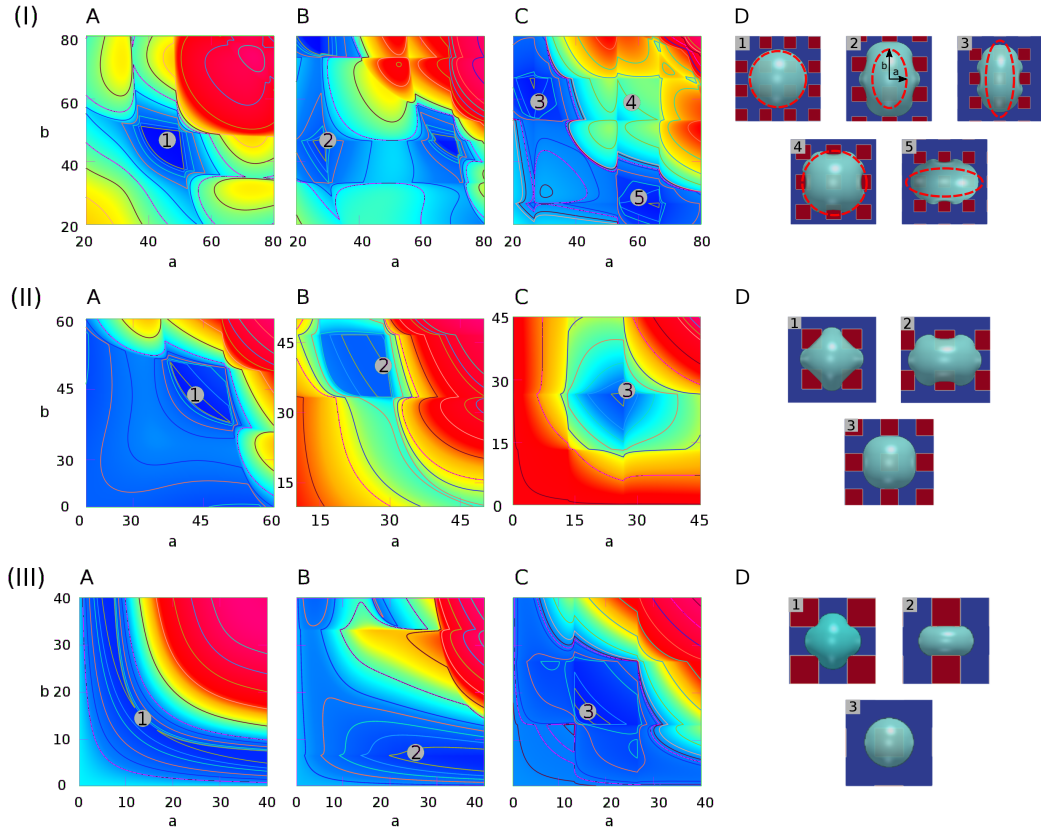


Figure 5.13.: Surface energy landscapes for droplets with different sizes on chocolate patterned surfaces and snapshots of equilibrated droplets through PF simulations. (I) $R/L = 0.75$, (II) $R/L = 0.5$, (III) $R/L = 0.25$. The chemical heterogeneities are described by $f_2(r, \varphi)$ in Eq. (5.10) with the following parameters: $\gamma_m = 0$, $\gamma_0 = 0.5$, $\xi = 100$, $L = 40$, $\lambda = 0$, $\chi = 0.55$. The energy minima are specified by different numbers, corresponding to the snapshots in (D) labeled with the same number. The surface energy landscapes for (A), (B), and (C) depict the systems with the droplet base center positions on P_1 , P_2 , and P_3 , respectively. (D) Snapshots of equilibrated droplets via PF simulations (blue: hydrophilic, red: hydrophobic).

dashed ellipse) of the droplets from the analytical model with the one from the PF simulations in (I)(D). The elliptic base line with semi-axes a, b from the analytical model is obtained from the coordinates of the energy minima in the energy landscapes. It is observed that the analytical predictions of the energy landscapes have a satisfactory agreement with the simulation results. Actually, the elliptical base line can be considered as an average approximation for the curved triple line of the droplets. This model is more accurate when the aspect ratio a/b is closer 1. This can be confirmed by the fact that the first and fourth snapshots from PF simulations in (I)(D) agree excellently with the analytical model (red dashed lines), while the other snapshots with a/b far away from 1 show relatively large deviations from the analytical predictions.

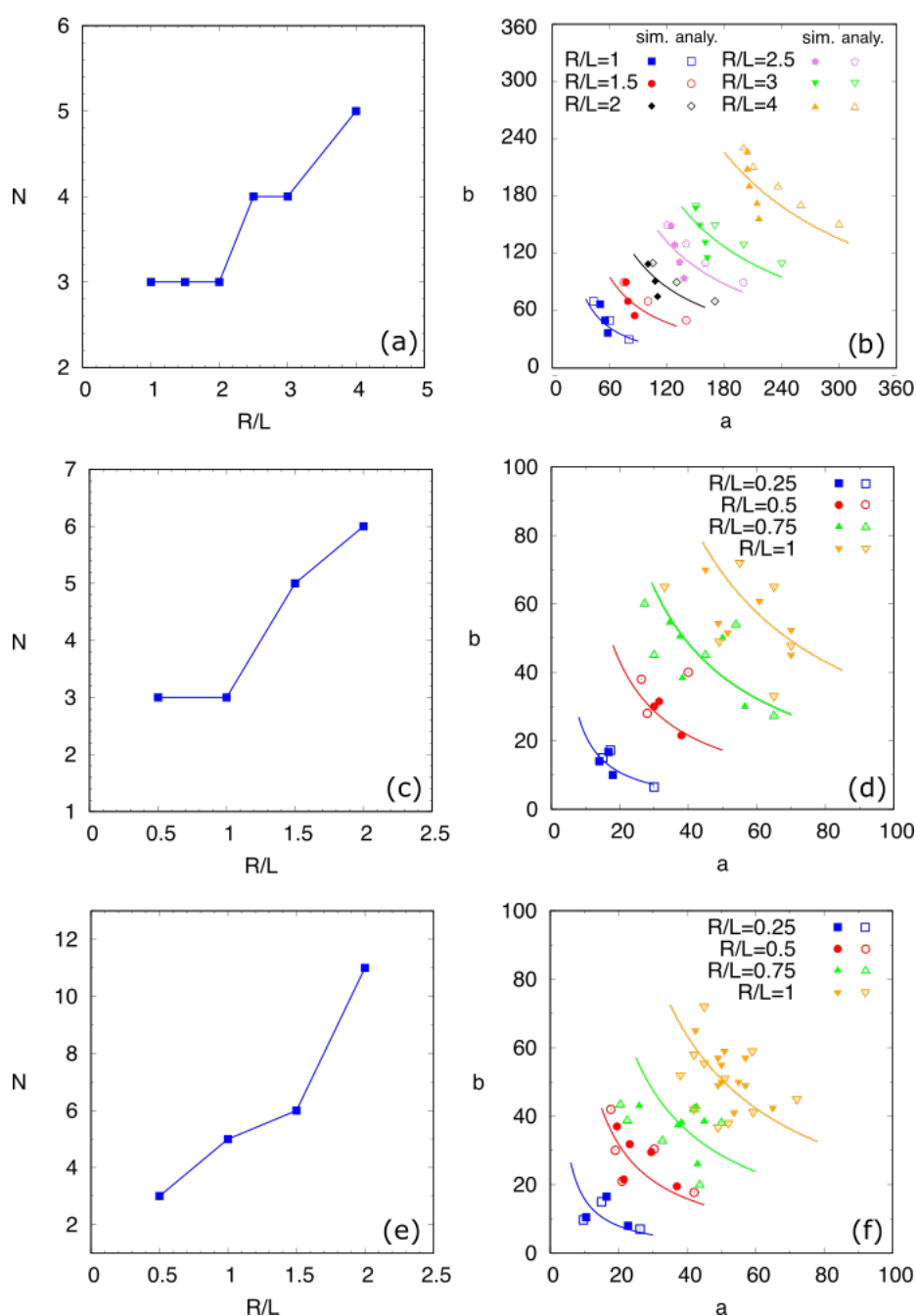


Figure 5.14.: The number N and the morphologies of the equilibrated droplets on three typical chemically patterned surfaces in dependence of the droplet sizes. (a)&(b), (c)&(d), and (e)&(f) are for striped, chocolate-patterned, and chessboard-patterned surfaces, respectively. (a), (c), and (e) depict the relation N versus R/L . (b), (d), and (f) describe the equilibrated droplet morphologies with different sizes predicted by PF simulations (filled symbols), in comparison with the energy-map model (hollow symbols) and the modified CB model (solid curves).

Through the energy-map method and the PF simulations, I obtain the influence of the droplet size on the quantity N and the morphologies of the equilibrated droplets on the three typical chemically patterned surfaces, as illustrated in Figure 5.14. Here, the top ((a), (b)), medium ((c), (d)), and bottom ((e), (f)) rows correspond to the striped, chocolate-patterned, and chessboard patterned surfaces, respectively. As shown in Figure 5.14 (a), (c), and (e), the equilibrated quantity N increases with the ratio R/L . This reveals that large droplets tend to have more equilibrium shapes for all the three patterned surfaces. Moreover, a comparison between Figure 5.14 (a), (c), and (e) shows that for a fixed ratio R/L , the number of the equilibrium state increases with an increase in the complexity of the surface pattern, i.e. striped-patterned surface \rightarrow chocolate-patterned surfaces \rightarrow chessboard-patterned surfaces. The underlying reason for the effect of the droplet volume and the complexity of the patterned surfaces is as follows. An increase in the droplet volume and the complexity of the patterned surfaces both gives rise to more covered energy discontinuous lines, which have a pinning effect for the spreading of the droplets. Due to this pinning effect from the increased amount of the discontinuous lines, more possible equilibrated droplet shapes are prone to appear.

Figure 5.14(b), (d), and (f) depict the droplet base radii a and b at equilibrium from PF simulations (filled symbols) and energy-map model (hollow symbols) in comparison with the modified CB model (solid curves). The scenarios for droplets with different sizes are distinguished by different colors. As I can see, for each volume, the simulation results coincide with the one from the energy-map model. Besides, the coloured solid curves are consistent very well with the same coloured symbols. Certain deviations of the energy-map model from the PF simulations are due to the strongly curved contact line of the droplets, which is caused by the pinning effect on the hydrophilic-hydrophobic discontinuous lines on the surfaces. While in our energy-map model, I have applied an elliptical base line to averagely describe the triple line. Nevertheless, the good agreement between the simulations, energy landscape method, and the modified CB model implies the capability as well as the justifiability of the proposed approaches. It should be noticed that in the present work, there exists a limit for the aspect ratio a/b . When the value a/b is beyond the limit, the droplet becomes slender with super high/low aspect ratio. In this case, interfacial instabilities may take place, leading to the breakup of the droplets. This topic is out of the scope of the present study and will be addressed in a forthcoming work.

Until now I have benchmarked the analytical model by studying the number and the shapes of the equilibrated droplets with various volumes on the three typical chemically patterned surfaces. As the droplet volume increases, for a certain patterned surface, more equilibrated droplet shapes appear. In the modified CB model, I assume that the different equilibrated droplets with the same volume on a certain surface tend to have the same liquid-solid contact area. This hypothesis has been confirmed by PF simulations. For instance, as shown in Figure 5.14(b), (d), and (f), for each droplet size, the results from the PF simulations and the energy landscape method (filled and hollow symbols) locate near the corresponding curve $\pi ab = \text{constant}$. This reveals that the equilibrated droplets have approximately the same contact area $A_{ls} = \pi ab$. The slight deviation of the symbols from the solid curves is by dint of the disparity between the curved contact line in simulations and the postulated elliptical based line

in the analytical model. Furthermore, the distinct droplet shapes on the chemically patterned surfaces are attributed to the pinning effect on the hydrophilic/hydrophobic boundaries. Big droplets have large contact areas and long contact line which crosses more hydrophilic/hydrophobic boundaries, leading to an increase in the number of the equilibrium shapes.

5.4.2. Contact angle

In this section, I systematically investigate the equilibrated droplet shapes affected by the contact angles on hydrophilic and hydrophobic areas. The difference between the contact angles $\Delta\theta := \theta_2 - \theta_1$ is divided into three groups: $\Delta\theta = 30^\circ, 45^\circ, 60^\circ$. As listed in Table 5.1, in each group, four pairs of contact angles (θ_1, θ_2) are chosen. In the following simulations, the blue and the red areas of the substrates correspond to the low contact angle (θ_1) and the high contact angle (θ_2), respectively. The characteristic length is constant $L = 40$. Droplets with the same size ($R/L = 1$) on three typical chemically patterned surfaces are focused on.

Table 5.1.: The setup of contact angles

$\Delta\theta$	30°	45°	60°
	$(30^\circ, 60^\circ)$	$(45^\circ, 90^\circ)$	$(30^\circ, 90^\circ)$
Contact angle pairs	$(60^\circ, 90^\circ)$	$(75^\circ, 120^\circ)$	$(60^\circ, 120^\circ)$
(θ_1, θ_2)	$(90^\circ, 120^\circ)$	$(90^\circ, 135^\circ)$	$(90^\circ, 150^\circ)$
	$(120^\circ, 150^\circ)$	$(135^\circ, 180^\circ)$	$(120^\circ, 180^\circ)$

As three typical examples, Figure 5.15(I), (II), and (III) display the surface energy landscapes and the snapshots of the simulated equilibrium droplets on the chocolate-patterned surface for contact angle pairs $(30^\circ, 90^\circ)$, $(90^\circ, 150^\circ)$, $(120^\circ, 180^\circ)$, respectively. The surface energy landscapes (A), (B), and (C) in each panel correspond to droplets with base centers locating on P_1 , P_2 , and P_3 , respectively. The energy minima in the energy maps are labeled with different numbers, corresponding to the simulation snapshots indicated by the same number in (D). The geometrical parameters for the patterned surface are the same as the ones in Figure 5.13. For brevity, the energy landscapes and the snapshots of the equilibrated droplet shapes for striped and chessboard patterned surfaces are included in Appendix B.

By using the above mentioned energy landscape model together with PF simulations, I find all the possible equilibrium droplet shapes on the three chemically patterned surfaces for the contact angle pairs tabulated in Table 5.1. The number N of the equilibrium droplet shapes versus $\bar{\theta}$ and $\Delta\theta$ is illustrated in Figure 5.16(a), (d), (g) and Figure 5.16(b), (e), (h), respectively. Here, the first, second, and last row correspond to the striped, chocolate, and chessboard patterned surfaces, respectively. For the three patterned surfaces, the following similarities (i)-(ii) and differences (iii) are observed: (i) For all the three surfaces, N decreases with $\bar{\theta}$ and remains almost a constant when $\bar{\theta} \gtrsim 100^\circ$. For instance, for the chocolate-patterned surface (Figure 5.16(d)) and $\bar{\theta} \geq 100^\circ$, I observe $N = 3$ and these three states are shown in Figure 5.15 (II) and (III), where the droplet base centers locate at the positions P_1 ,

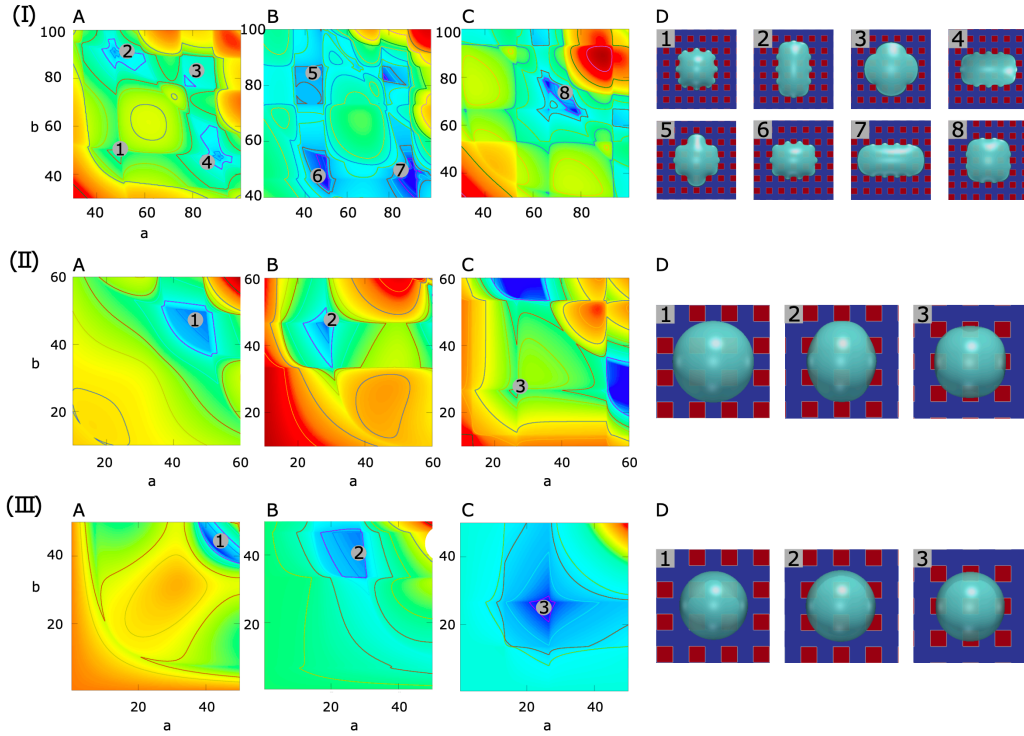


Figure 5.15.: Surface energy landscapes for droplets on chocolate-patterned surfaces with different contact angles and corresponding snapshots of equilibrated droplets by PF simulations. (I) $\theta_1 = 30^\circ, \theta_2 = 90^\circ$, (II) $\theta_1 = 90^\circ, \theta_2 = 150^\circ$, (III) $\theta_1 = 120^\circ, \theta_2 = 180^\circ$. The chemical heterogeneities are depicted by $f_1(r, \varphi)$ in Eq. (5.10) with $\xi = 100, L = 40, \lambda = 0, \chi = 0.55$. The mean value γ_m and the amplitude γ_0 of the surface energy density are set according to the contact angle pairs. The energy minima are shown by different numbers, corresponding to the snapshots in (C) labeled with the same number. The surface energy landscapes for (A), (B) and (C) represent the setups where the droplet base center positions are on P_1, P_2 and P_3 , respectively. (D) Snapshots of equilibrated droplets through PF simulations (blue: hydrophilic, red: hydrophobic).

P_2 , and P_3 , respectively. With a decrease in $\bar{\theta}$, the energy landscape becomes more intricate (see e.g. Figure 5.15 (I)), where the quantity of the equilibrium states rises. The underlying reason is that with a decrease in $\bar{\theta}$, the liquid-solid contact area is enlarged, which leads to more discontinuous lines covered by the droplets. Hence, N increases with a decrease in $\bar{\theta}$. (ii) For all the three patterned surfaces, N increases with a decrease in $\Delta\theta$ when $\Delta\theta < 0$. This is because that when $\Delta\theta < 0$ deviates farther from 0, on the one hand, the pinning effect is more pronounced, and on the other hand, $\bar{\theta}$ decreases. (iii) Different results are observed for distinct patterned surfaces when $\Delta\theta > 0$. For the striped and chocolate patterned surfaces, N remains a constant, whereas N increases with $\Delta\theta$ for the chessboard patterned surface. The former observation is owing to the relatively small contact area resulting from a high value of $\bar{\theta} \geq 100^\circ$. The latter one is as a result of the high density for the discontinuous lines, which gives rise to more chance for pinning. For the striped and chocolate patterned surfaces,

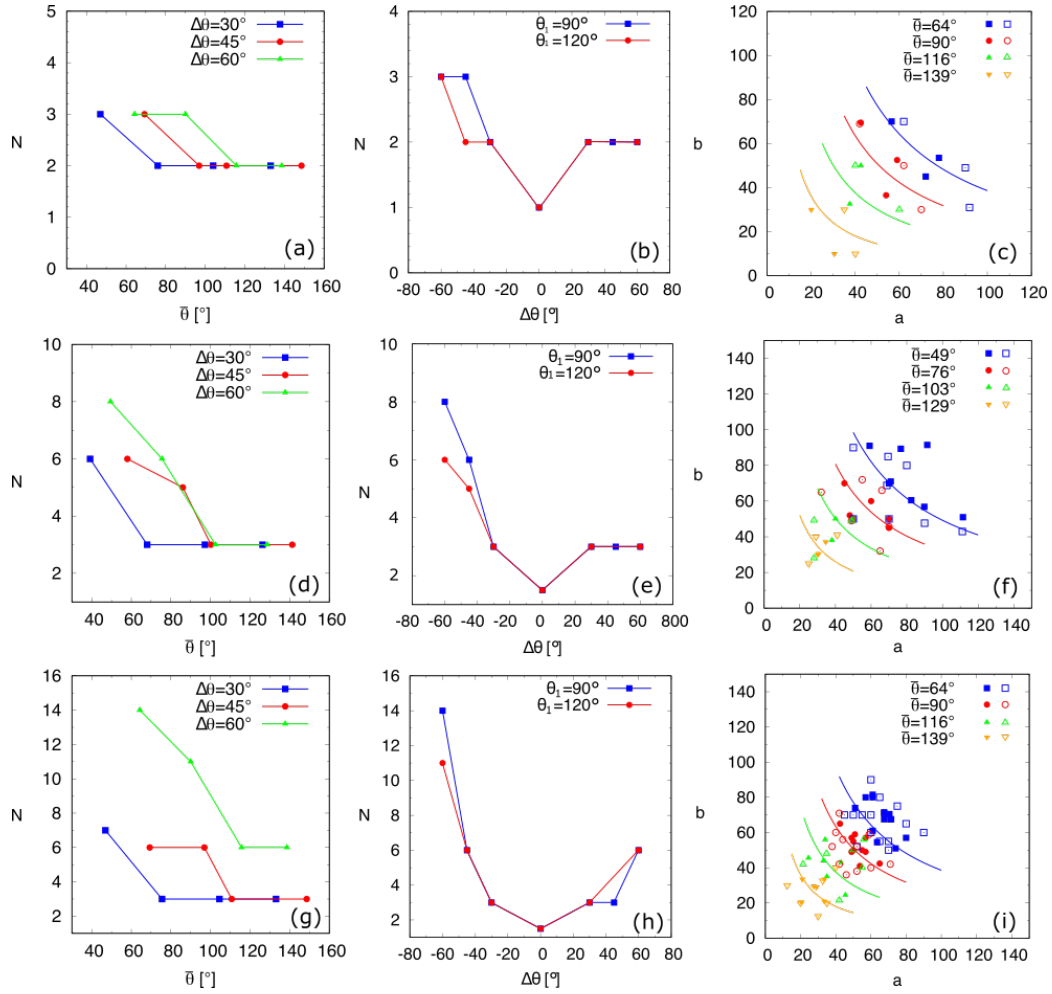


Figure 5.16.: The number and the morphologies of the equilibrated droplets on three typical chemically patterned surfaces in dependence of the contact angles. (a)&(b)&(c), (d)&(e)&(f), and (g)&(h)&(i) are for striped, chocolate-patterned, and chessboard-patterned surfaces, respectively. (a)&(d)&(g) and (b)&(e)&(g) illustrate N versus $\bar{\theta}$ and $\Delta\theta$, respectively. Here, $\Delta\theta$ varies from -60° to 60° , which is achieved by fixing θ_1 , (e.g. $\theta_1 = 90^\circ, 120^\circ$) and changing θ_2 . (c), (f), and (i) depict the equilibrated droplet morphologies with different average contact angles predicted by PF simulations (filled symbols), in comparison with the energy-map model (hollow symbols) and the modified CB model (solid curves).

although the pinning effect becomes stronger with an increase in $\Delta\theta$ when $\Delta\theta > 0$, the number of pinning lines is not as many as the one for the chessboard pattern, when the size of the droplets is comparable with the characteristic length. In contrast, for the chessboard pattern, the high density of the discontinuous lines facilitates the occurrence of more equilibrated shapes when the pinning effect is reinforced with a rise in $\Delta\theta$. From the relations N vs. $\bar{\theta}$ and N vs. $\Delta\theta$, I should set low values of $\bar{\theta}$ as well as high values of $|\Delta\theta|$ to obtain more equilibrated droplets, and vice versa.

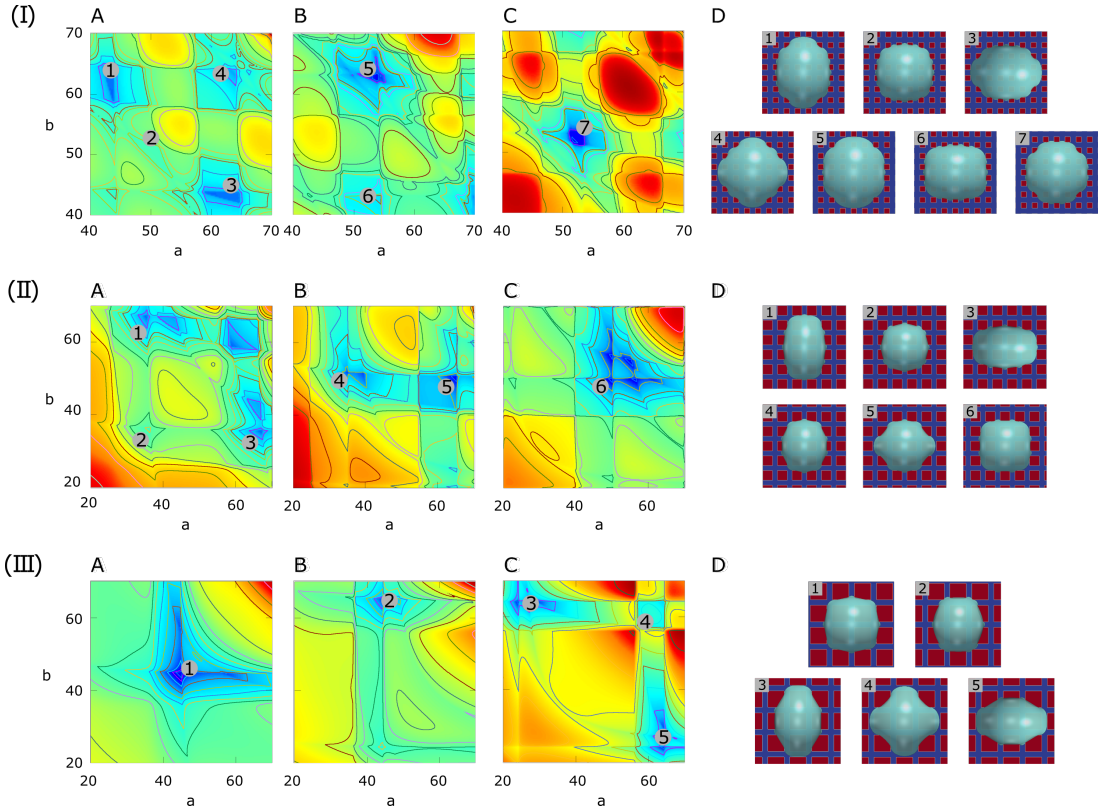


Figure 5.17.: Surface energy landscapes for droplets on chocolate patterned surfaces with different area fractions of hydrophilic and hydrophobic areas and corresponding snapshots of equilibrated droplets through PF simulations. The droplet size is set as $R = 40$. The chemical heterogeneities are described by $f_2(r, \varphi)$ in Eq. (5.10) with $\gamma_m = 0$, $\gamma_0 = 0.5$, $\xi = 100$. The ratios for (I) $\nu = 1 : 1$, (II) $\nu = 1 : 2$, (III) $\nu = 1 : 3$ correspond to $(L = 20, \lambda = 0, \chi = 0.55)$, $(L = 30, \lambda = \cos 60^\circ, \chi = 0.13)$, $(L = 40, \lambda = \cos 45^\circ, \chi = 0.10)$, respectively. The energy minima are designated by different numbers, corresponding to the snapshots in (D) indicated with the same number. The surface energy landscapes for (A), (B) and (C) correspond to the droplet base center positions P_1 , P_2 and P_3 , respectively. (D) Snapshots of equilibrated droplets through PF simulations (blue: hydrophilic, red: hydrophobic).

Figure 5.16(c), (f), and (i) describe the values (a, b) of equilibrated droplets from the PF simulations (filled symbols) and the energy landscape model (hollow symbols) for different $\bar{\theta}$. These results are compared with the modified CB model (solid curves). As $\bar{\theta}$ decreases, for droplets with the same size, the contact area tends to increase and therefore the curve $ab = \Psi(V_d; \bar{\theta})$ from the modified CB model translates upper right (see Eq. (5.12)).

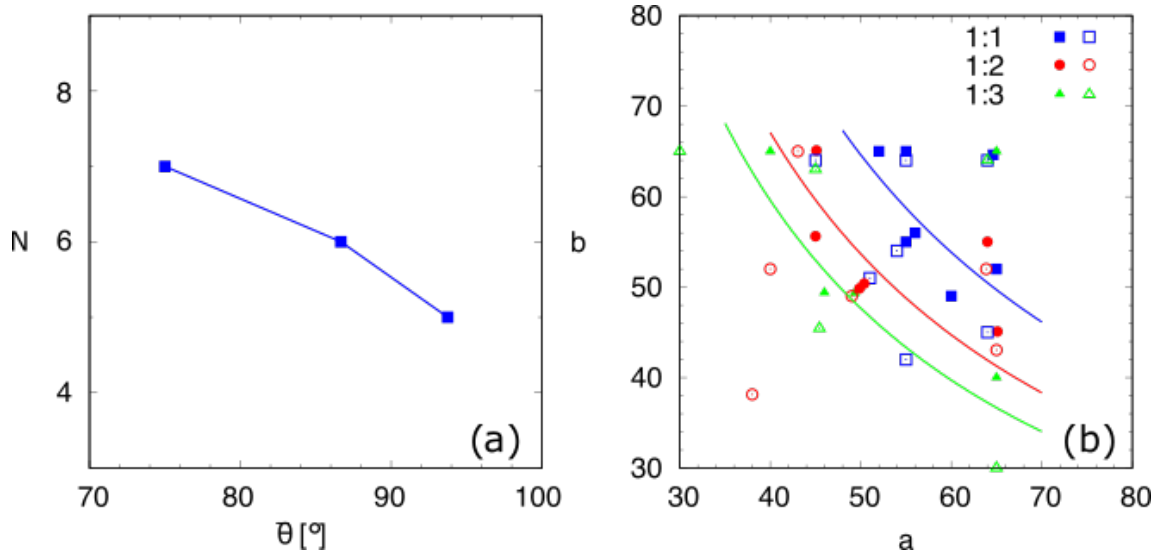


Figure 5.18.: (a) The number N of the equilibrium droplet shapes on chocolate patterned surfaces as a function of $\bar{\theta}$. (b) Equilibrium morphologies of droplets on chocolate patterned surfaces with different fractions of hydrophilic and hydrophobic areas predicted by PF simulations (filled symbols) compared with the energy landscape model (hollow symbols) and the modified CB model (solid curves).

5.4.3. The ratio of the hydrophilic area to the hydrophobic area

Apart from changing θ_1 and θ_2 , the average contact angle $\bar{\theta}$ can also be adjusted by tuning the area ratio of the hydrophilic area to the hydrophobic area while fixing the intrinsic contact angles on these two areas. In this part, I set the contact angles on the hydrophilic and hydrophobic areas as $\theta_1 = 60^\circ$ and $\theta_2 = 120^\circ$, respectively. As aforementioned, the area ratio of the hydrophilic area to the hydrophobic area is characterized by the parameter ν . For the chocolate patterned surfaces, I set $\nu = 1 : 1, 1 : 2, 1 : 3$ for the present investigation. To avoid repeated discussion of the similar wetting behaviors, the striped and chessboard-patterned surfaces will not be further discussed in this section.

For the chocolate-patterned surfaces with $\nu = 1 : 1, 1 : 2, 1 : 3$, the surface energy landscapes and the snapshots of the equilibrated droplets from the PF simulations are shown in Figure 5.17 (I), (II), and (III), respectively. The number N and the coordinate (a, b) of the local minima in the surface energy landscapes both are well corroborated by the simulations, as illustrated in Figure 5.18(a) and (b), respectively. Noteworthy, I have converted the ratio ν into the average contact angle by using Eq. (5.11). As ν decreases, i.e. $\bar{\theta}$ increases, the equilibrated droplet becomes spherical successively and N decreases. This finding coincides very well with the results in Figure 5.16. The comparison between the simulation results, the energy landscape model, and the modified CB model is illustrated in Figure 5.18(b), where sound agreement is obtained.

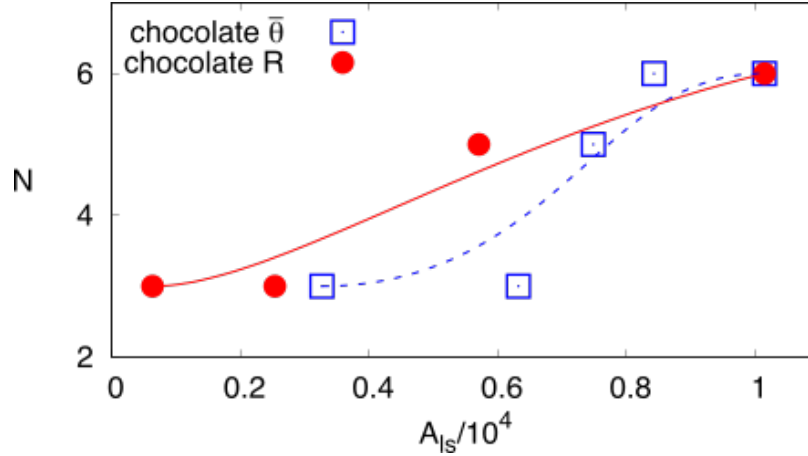


Figure 5.19: Functional relation between N and A_{ls} for droplets on the chocolate-patterned surface.

The hollow squares and filled circles depict two distinct cases, where A_{ls} is changed by setting different average contact angle $\bar{\theta}$ and droplet radii R , respectively. The solid and dashed lines are the corresponding fitting curves.

5.4.4. Summary and Conclusions

In this study, I have shed light on the equilibrium morphologies of droplets on three typical chemically patterned surfaces. Because of the contact line pinning effect, the droplets reach different energy minimum states and thus achieve distinct equilibrium shapes. The number of equilibrated droplets as well as the equilibrium morphologies both are dependent on the droplet sizes, contact angles, and the ratios of the hydrophilic area to the hydrophobic area. These influence factors have been systematically discussed in this work. Our discussion is based on a combination of the surface energy landscape method with the phase-field simulations. It has been shown that the analytical predictions from the surface energy landscape approach are well consistent with the PF simulations. Noteworthy, in pure experiments or simulations, it probably requires a number of tries to find all the equilibrium states with varying parameters and even likely to miss some equilibrium morphologies if the number of the experimental samples is not sufficient large. This demonstrates that the energy landscape model may be used as a guidance table for experiments and simulations without blind attempts.

Furthermore, I have noticed that the number of the equilibrium droplet shapes for all the three chemically patterned surfaces increases with the droplet volume. This tendency is due to the fact that an increase in the droplet volume leads to an enlarged contact area between droplets and the substrates, so that the triple lines cross more energy discontinuous lines. On these discontinuous lines, the pinning effect occurs, resulting in more equilibrium shapes of droplets. Similarly, I have varied the contact angles on the hydrophilic and hydrophobic areas while fixing the droplet volume. I have figured out that as the average contact angle decreases i.e. the substrate is globally relatively hydrophilic, the contact area between the droplet and substrate increases, which leads to a rise in the number of the equilibrated states. To sum up, the increase in the volume or the decrease in the average contact angle engenders more equilibrium shapes of droplets. The average contact angles

can be controlled either by changing the intrinsic contact angles on the hydrophilic and hydrophobic areas or the area ratio of these two components. It should be noticed that although both decreasing average contact angle and increasing volume lead to a large droplet-substrate contact area and thus facilitate more equilibrium states, a universal behavior for the number of the equilibrium states N versus the contact area A_{ls} does not exist. In Figure 5.19, I plot the functional relation between N and A_{ls} for droplets on the chocolate-patterned surface. Here, different A_{ls} are obtained by changing the average contact angle $\bar{\theta}$ (hollow squares) or droplet radius R (filled circles). As A_{ls} increases, N rises. Although the tendencies are similar between these two curves, the quantities of the equilibrium states for the same A_{ls} are not always the same. This reveals that N is not uniquely dependent on A_{ls} . Other aspects such as the pinning force, droplet height may also take an important role for the stability analysis of the droplets. Given the limit of the content, these factors will not be further discussed.

I have further investigated the morphology properties of the equilibrated droplets on different patterned surfaces. For a certain chemically patterned surface, the surface energy landscape method in combination with the PF simulations has been adopted to find the possible equilibrium shapes of droplets. These results have been compared with the modified CB model proposed in this work. It has been shown that the simulation results coincide with the modified CB model. This demonstrates that the proposed modified CB model is more robust and accurate to delineate the droplet shapes, especially the base area. Therefore, the classical CB model has been successfully extended to be able to predict the equilibrium droplet shapes which are not necessary in a shape of spherical cap. The comprehensive predictions of the droplet shapes in this work are of significant importance for applications of droplet manipulation and the findings open a promising avenue for a delicate control of droplet formation as well as for the design of functional surfaces.

It should be emphasized that our model can be easily further extended to other chemically patterned surfaces whose heterogeneities are symmetric. In the present work, I have assumed that the droplet has a form of quasi-spherical cap with an elliptical contact base line on the substrate. However, it is beyond the validity of our model if the chemical pattern is extremely complex, where the droplet shapes become asymmetric.

6. Single droplet on chemically patterned surfaces: theoretical calculation, phase-field simulation, and experiments

By utilizing the generalized analytical method, the PF model described in the last chapter, and the experimental method, wetting behaviors of droplets on a chemically patterned surface are further investigated. Typical anisotropic wetting shapes identified by these three distinct methods are compared. The surface energies of the anisotropic wetting morphologies are quantitatively examined to address the most energetically stable wetting state. Moreover, a series of non-rotational symmetric droplet shapes is newly reported. Furthermore, the evolution of anisotropic wetting shapes in a quasi-equilibrium evaporation process is revealed. This chapter was published in Ref. [186]

6.1. Methods

The equilibrium droplet shapes on chemically patterned substrates are analyzed by using an analytical model, phase-field simulations, and experiments. The former two methods are described in the last chapter, which both are based on minimizing the free energy of the system. Here, key information for the analytical model is provided.

In the analytical model, the chemical heterogeneities in the (x, y) -plane (x -axis is in the lateral direction and y -axis is perpendicular to x -axis) of the substrate surface are described by the following expression

$$\gamma_{ls} - \gamma_{gs} = \gamma_m + \gamma_0 \tanh \xi [\cos(\delta_1 - \lambda) \cos(\delta_2 - \lambda) - \chi(\cos \delta_1 + \cos \delta_2)]. \quad (6.1)$$

The parameters γ_m and γ_0 indicate the mean surface energy density difference and the amplitude of the heterogeneity, respectively. The variables δ_1 and δ_2 are function arguments which are dependent on the coordinate (x, y) of droplet base center. The other parameters ξ , λ , and χ control the sharpness, area ratio, and roundness of the wettability pattern, respectively. A proof for the validity of Eq. (6.1) and the interpretation for the controlling parameters are provided in Appendix C. In this chapter, the length x , density ρ , surface tension γ and other variables are non-dimensionalized by the characteristic parameters, $x^* = 1 \times 10^{-4}$ m, $\rho^* = 998$ kg/m³, and $\gamma^* = 72.8 \times 10^{-3}$ N/m, respectively.

All experiments were conducted with chemically patterned micro-arrays provided by Aquarray (Eggenstein-Leopoldshafen, Germany) on microscopic slides from Schott Nexterion (Jena, Germany).

The substrate is a glass slide patterned with hydrophilic (apparent contact angle $\theta_{a,wet} = 0^\circ$) spots surrounded by (super)hydrophobic ($\theta_{a,dry} = 160 \pm 10^\circ$) area. The square (Fig. C.2A) and circle (Fig. C.2B) patterns are used for comparison, as can be found in Appendix C.

Equilibrium shapes of distilled water droplets were recorded by using a Keyence BZ-9000 optical microscope (Keyence Corporation, Osaka, Japan). All the stable droplet configurations were captured by depositing the droplet center on different positions. Side-view and diagonal-view pictures of drops were performed with a DSA 25 contact angle goniometer (Krüss, Hamburg, Germany). The scale is determined by the device syringe, on which the camera was focused. The heights were determined by using the image analysis software, ImageJ.

The evaporation experiment was conducted with an initial volume $20 \mu L$ distilled water droplet sitting on the patterned substrates. The relative humidity and temperature were 20% and $20^\circ C$, respectively. The evaporation images were recorded by a Keyence VHX-7000 optical microscope (Keyence Corporation, Osaka, Japan).

6.2. Droplet shape analysis

6.2.1. Analysis of top views

Fig. 6.1 illustrates the results for the equilibrium shapes of the droplets from the three different methods. Two exemplary droplet volumes are considered, $V = V_0$ (Fig. 6.1A) and $V = 4V_0$ (Fig. 6.1B). The images (a), (b), and (c) in the first row show the surface free energy landscapes $E_v(a, b)$ from the analytical approach for droplets with base center on three different positions: (a) center of four neighboring hydrophilic lattices, (b) between two adjacent hydrophilic lattices, (c) on a hydrophilic lattice. The equilibrium shapes of the droplets on these three different positions (a), (b) and (c) from the simulations are illustrated in (d), (e), and (f), respectively. The numbered surface energy minima, 1, 2 and 3 in (a), (b), and (c) correspond to an equilibrium shape of the droplet. The baseline of the equilibrated droplet is depicted by the values (a, b) at the highlighted positions 1-3 in the surface energy landscape. For comparison, the red dashed lines in (d), (e), and (f) show the baseline of the droplet from the analytical method, where good agreement is observed. The third rows (g), (h), and (i) display the experimental results for the equilibrated droplets with the base centers on the positions (a), (b), and (c), respectively. The experimental results show excellent agreements with the simulations as well as with the analytical model. Instead of spreading equally in all directions on a flat homogeneous surface, the spreading of the drop on the wettability pattern is determined by its initial state (e.g. initial position and initial shape), which leads to several different equilibrium droplet shapes. Although the analytical model loses its accuracy in describing the sharp corners of the droplet base, it can be considered as an average and approximate description of the droplet shapes, which serves as a guidance to identify different equilibrium droplet shapes and the dependence of droplet positions. To better address the droplet shapes with sharp corners, I will further develop a modified analytical model that considers the droplet base as a shape of polygon in a forthcoming work.

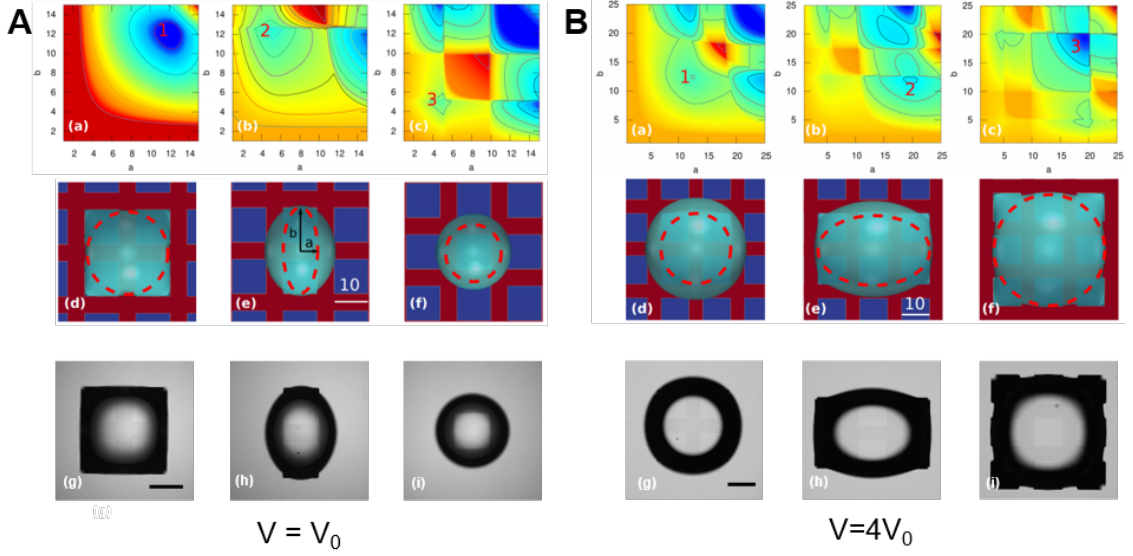


Figure 6.1.: Surface free energy landscapes and equilibrium shapes for droplets on a chemically patterned surface. The energy maps (a), (b), and (c) in the first row are surface free energy landscapes in the $a - b$ space when the droplet base center is placed on three symmetric points of the patterned substrate: (a) in between four neighboring hydrophilic lattices, (b) between two adjacent hydrophilic lattices, (c) on the hydrophilic lattice. The contour lines indicate the levels of surface energy, which decreases from red to blue regions. The energy minima are labeled with numbers 1-3, whose coordinates (a, b) describe the semi-axes of the droplet base line. The second and third rows illustrate the equilibrium shapes of droplets obtained from simulations ((d)-(f)) and experiments ((g)-(i)). In (d)-(f), the hydrophilic and hydrophobic areas are highlighted in blue and red color, respectively. The red dashed ellipses on the simulation snapshots (d)-(f) are theoretical results corresponding to the coordinates (a, b) of the energy minima indicated in (a)-(c). (A) $V = V_0 = 5 \mu L$, (B) $V = 4V_0 = 20 \mu L$. Scale bar: 1 mm (or 10 in dimensionless value).

For the convenience of discussion, I name the three typical equilibrium droplet configurations for each volume as $N_x \times N_y$ patterns, where N_x and N_y denote the number of the covering hydrophilic lattices in the x and y dimensions, respectively. For instance, for droplet with $V = V_0$, I have obtained three patterns, namely, 2×2 (Fig. 6.1A(d)), 1×2 (Fig. 6.1A(e)), and 1×1 (Fig. 6.1A(f)) patterns.

I further compare the equilibrium morphologies of droplets from simulation and experiments for different volumes (Fig. C.3). In Fig. C.3 A-D, the droplet volume varies from $2V_0$ to $8V_0$. Overall, the simulations match very well with the experiments except the droplet states in Fig. C.2A(c) and Fig. C.2D(a) (Appendix C). Fig. 6.2 addresses the disagreement between the experimental and simulation results towards these two states. As shown in Fig. 6.2A(a), two local minima are observed in the surface energy landscape for $V = 8V_0$, as indicated by the numbers 1 and 2. The semi-axes of both energy minima states are equal but the latter one is less than the former one. Two distinct simulations,

(i) one with gravity and (ii) the other one without gravity, are performed. The equilibrated states for (i) and (ii) are shown in Fig. 3A(b) and Fig. 6.2A(c), respectively. The red dashed lines depict the results from the analytical method. The former one was previously shown in Fig. C.3D(a) (Appendix C) and this state corresponds to the energy minimum 1. The latter one corroborates the experimental result illustrated in Fig. 6.2A(d) or Fig. C.3D(d) (Appendix C). This equilibrium state is correlated with the energy minimum state 2, where the base radius $a = b$ is smaller than the one in Fig. 6.2A(b). On the other hand, it is very likely that due to the mechanical heterogeneity (or roughness), the pinning effect in the experiment seems to be stronger than the one in the simulation, since the substrate is ideally smooth in simulation setups. This relatively stronger pinning force prevents the outward spreading of the droplet in the experiment. By this way, the gravity induced pressure force cannot surmount the pinning effect of the surface tension and the energy minimum state 2 with a smaller semi-axes $a = b$ is captured by experiments. Feng et al. reported that even nano-sized roughness of the glass substrate can affect the static and sliding wetting behaviors [187]. However, quantifying the influence of mechanical heterogeneity (or roughness) of the substrate is very challenging and remains an open question. In addition, modelling of the roughness is a challenging task because it requires to resolve rather even smaller scales which is not the objective of the current paper. The inconsistency of Fig. 6.2A(b) (with gravity) and Fig. 6.2A(d) is probably caused by the difference in the strength of the pinning force in the experiment and simulation. To further examine the vying relationship between the pinning force and gravity, I conducted a special simulation with zero gravity (Fig. 6.2A(c) or simulation (ii)), as mentioned above. The simulated droplet with zero gravity equivalently describes the situation where gravity is fully compensated by the pinning force, which shows good agreement with the experimental result Fig. 6.2A(d). The discussion of Fig. 6.2A demonstrates that the two vying forces, i.e., the pinning force and gravity jointly determine the equilibrium pattern of droplets with relatively large volumes. Nevertheless, the good agreements for smaller droplets shows the strong competency of the analytical approach for the capillarity dominant situation.

For volumes $2V_0-6V_0$ shown in Fig. C.2 (Appendix C), the good consistency between the simulation and experimental results indicates the dominant effect of the surface tension over the gravity for comparatively small volume droplets. On the other hand, due to the uncertainty of the surface roughness, the pinning effect in the experiment seems to be stronger than the one in the simulation, which prevents the outward spreading of the droplet. By this way, the gravity induced pressure force cannot surmount the pinning effect of the surface tension and the energy minimum state 2 with a smaller semi-axes $a = b$ is captured by experiments. The satisfactory agreement between the results in Fig. 6.2A(c) and Fig. 6.2A(d) again demonstrates the strong competency of the analytical approach, which can be used to effectively guide the experimental design and simulation analysis.

Fig. 6.2B presents typical non-rotational symmetric equilibrium morphologies from experiments and PF simulations. In the PF simulations for Fig. 6.2B(b) and (d), I initially set up a droplet in the shape of gongen. In contrast to the initial cuboid covering 3×3 hydrophilic lattices for the simulations in Fig. S2A(c) and in Fig. 6.1B(f), the base area of the initial gongen does not cover the hydrophilic lattices 1, 2, 3 in Fig. 6.2B(b) and the hydrophilic lattice 4 in Fig. 6.2B(d). Driven by the surface energy mini-

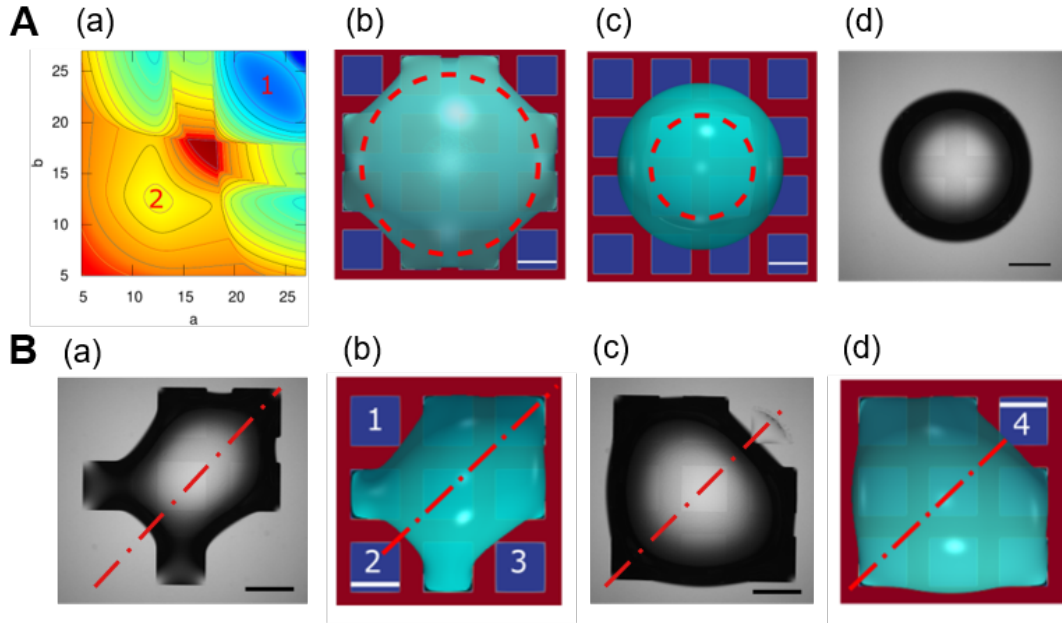


Figure 6.2.: A. (a) The surface energy landscape $E_v(a, b)$ for $V = 8V_0$ ($40 \mu L$) with droplet base center on the center of four neighboring hydrophilic lattices. (b) and (c) top views for an equilibrated droplet with and without gravity from the PF simulation. The red dashed lines in (b) and (c) show the analytical results which correspond to the energy minima 1 and 2 in (a), respectively. (d) Optical image of the droplet for $V = 8V_0$ ($40 \mu L$) via experiment. The droplet centers are shifted away from the patch centers. B. Equilibrium morphologies with unique symmetric axis. (a) and (b) Experimental and simulation results for $V = 2V_0$ ($10 \mu L$), respectively. (c) and (d) Experimental and simulation results for $V = 4V_0$ ($20 \mu L$), respectively. The red dot dashed lines illustrate corresponding symmetric axes. Scale bar: 1 mm (or 10 in dimensionless value).

mization, the initially filled gengen evolves to the non-rotation-symmetric equilibrium morphologies, as demonstrated in Fig. 6.2B(b) and (d), which confirm the experiments in Fig. 6.2B(a) and (c), respectively. Noteworthy, these equilibrium morphologies are also axisymmetric and the corresponding symmetric axes are highlighted with dot dashed lines. In this case, the pinning forces in the direction of the dot dashed line and in the direction perpendicular to the dot dashed line both can be compensated. However, the analytical prediction towards this kind of geometry is out of the scope of the present work, and this problem will be tackled in a forthcoming work.

Apart from the square-pattern substrate, a circle-pattern substrate is also considered to examine the capability of the analytical and numerical models. Fig. 6.3 illustrates the prediction of the energy map method and compares the experimental and simulation results for the equilibrated droplet shapes on the circle-pattern substrate. All the simulations coincide with the experiments and all rotationally symmetric geometries (i.e. (1)-(4) in Fig. 6.3B and C) can be fully predicted by the energy maps. Noteworthy, in both simulations and experiments, a non-rotationally symmetric pattern is observed, as

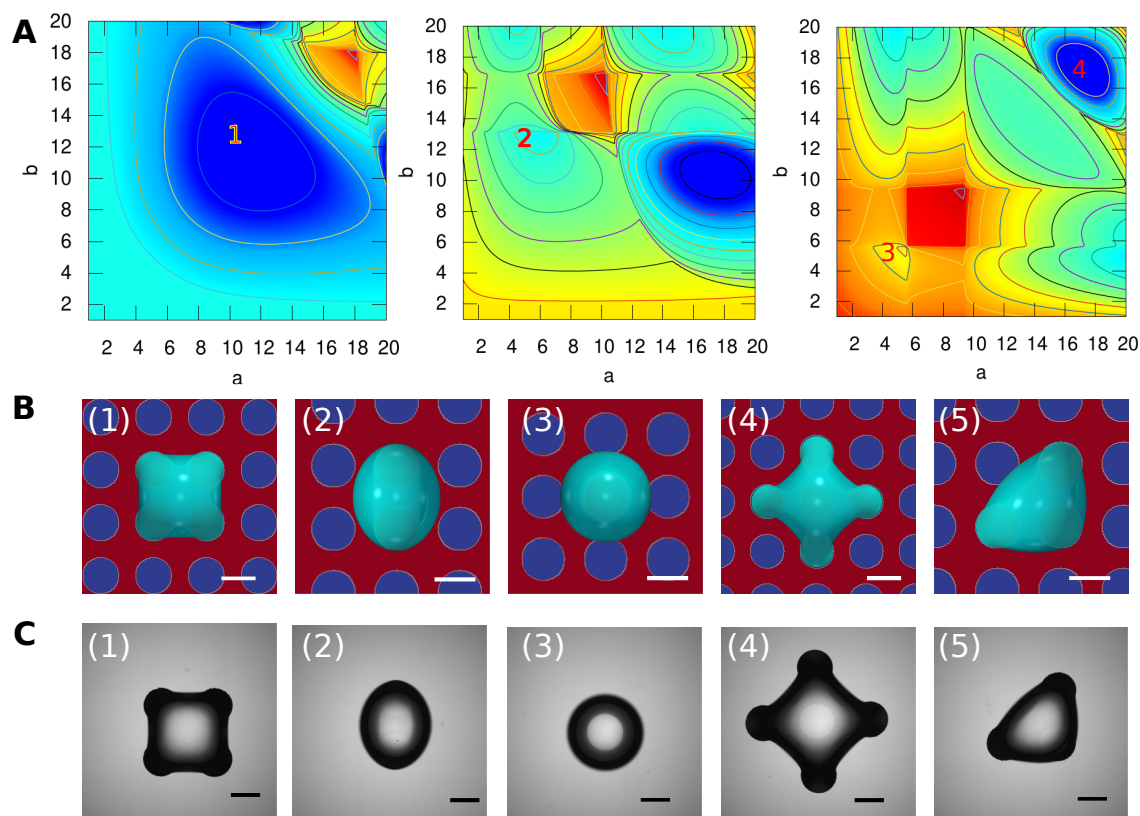


Figure 6.3.: (A) Surface energy landscapes for droplets with $V = V_0$ ($5 \mu L$) on a circle-patterned surface (see more details in Fig. C.2B for the patterned substrate). The three energy maps correspond to the case when the droplet center is placed on the positions (a), (b), and (c) described in Fig 6.1. The energy minima are labeled with numbers 1-4, corresponding to the snapshots in (B) and (C) marked with the same numbers. (B) and (C) Top view comparison for droplets with a volume of $V = V_0$ ($5 \mu L$) on a circle-patterned surface. Scale bar: 1 mm (or 10 in dimensionless value).

shown by the 5th panel in Fig. 6.3B and C. This droplet pattern and the droplet patterns in Fig. 6.2B(a)(c) describe the case where droplet centers are shifted away from the three typical symmetric points (a), (b) and (c). In these cases, the pinning force around the contact line leads to axially symmetric patterns. The phase-field model can be straightforwardly used to simulate the axially symmetric patterns with appropriate initial filling of the droplet. To analytically address the situation where droplet centers are shifted away from the symmetric points, one possible way to extend the present analytical method is to assume that the droplet base line is in a shape of polygon which will be explored in a forthcoming work. In this work, I mainly focus on the rotationally symmetric droplets and the aim is to show that the analytical and numerical models are robust to confirm the equilibrium configurations of droplets.

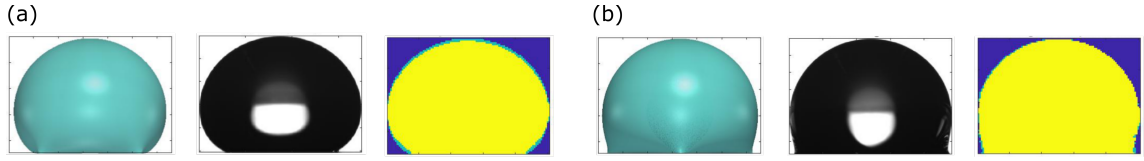


Figure 6.4.: Comparison of (a) side lateral and (b) side diagonal views for droplets with $V = 4V_0$ ($20 \mu L$). The snapshots of droplets via simulations and experiments are normalized to the same width and then overlapped. The differences of the normalized snapshots are highlighted in cyan.

6.2.2. Analysis of side views

To investigate more details about the droplet shapes on the square-pattern substrate, I turn to contrast the side views of the equilibrium shapes. In Fig. 6.4, I compare the droplet side views in two directions, (a): the lateral direction, and (b): the diagonal direction, which are labeled as side lateral view and side diagonal view, respectively. As a typical example, I choose the volume $V=4V_0$ and analyze the equilibrium shape with the droplet covering a 2×2 hydrophilic lattice pattern (see also Fig. 6.1B(d)). Simulation and experimental images are converted to grayscale and binarized using the 0.7-quantile (value underneath which 70% of all brightness values are) of pixels followed by a morphological opening and hole-filling. The maximum horizontal extent of the segment is determined, and the image is accordingly cut and resized, such that the extents in the x -direction for the experimental and simulation images are the same. The normalized simulation and experiment segments are then overlaid, and the differences between them are highlighted in cyan color, as shown by the normalized yellow droplets next to the experimental snapshots. The deviation is characterized by the ratio of the number of differing pixels to the whole number of pixels corresponding to the bigger segment. The comparison of the deviation between the simulation and experiments for different volumes is depicted in Table 6.1, where satisfactory agreement is observed.

6.2.3. Analysis of droplet height and surface energy

In Fig. 6.5, I study the droplet shapes more quantitatively by scrutinizing the droplet height h and the total surface energy E for different droplet volumes. Fig. 6.5(a), (b), and (c) show the droplet height versus the volume via theoretical, numerical, and experimental methods, respectively. Fig. 6.5(d) and (e) present the surface energy versus the volume through theoretical calculation and numerical sim-

Table 6.1.: Deviation rate for the pixels of the experimental and simulation images.

volume	side lateral view	side diagonal view
V_0	5.38%	11.19%
$2V_0$	12.44%	5.23%
$4V_0$	4.04%	1.27%

6. Single droplet on chemically patterned surfaces: theoretical calculation, phase-field simulation, and experiments

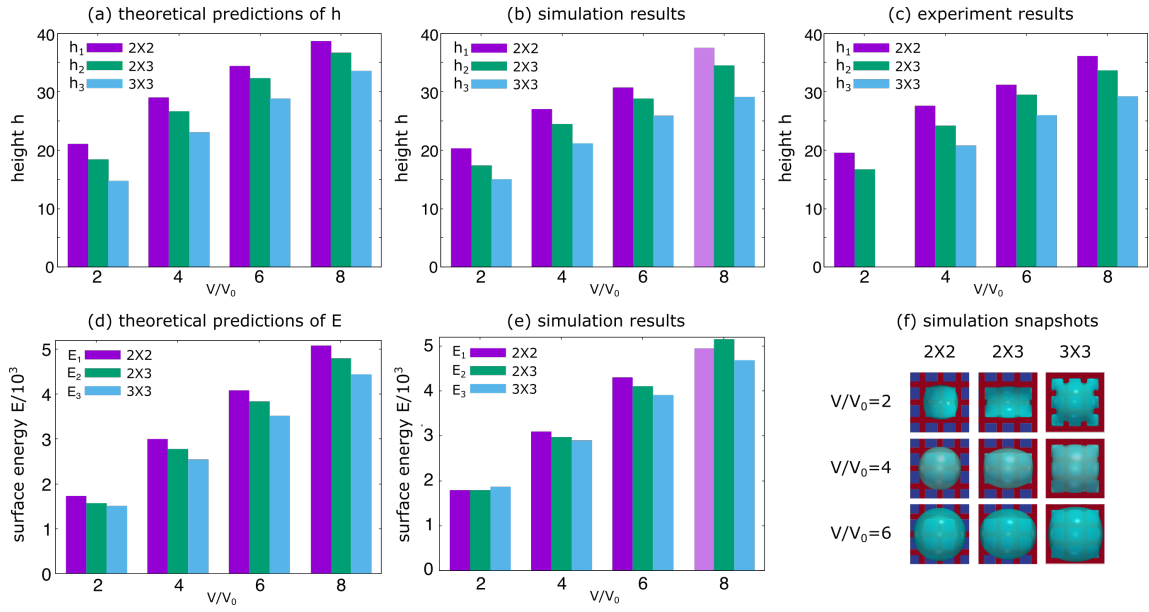


Figure 6.5.: Comparison of droplet height and surface energy. (a), (b), and (c) theoretical, simulation, and experimental results for droplet height, respectively. (d) and (e) theoretical and numerical analysis of surface energies. (f) Snapshots of top views for typical equilibrium shapes of droplets with volume varying from $2V_0$ to $6V_0$. In (a)-(e) the bars colored in violet, green, and blue correspond to the equilibrated droplets covering the hydrophilic (blue) lattices patterns of 2×2 , 2×3 , and 3×3 , as exhibited in (f). The pink bars in (b) and (e) present the 2×2 patterned droplet via PF simulation without gravity, as illustrated in Fig. 6.2(c). Droplet height h and surface energy E are nondimensionalized by x^* and $\gamma^* x^{*2}$, respectively.

ulations, respectively. For each volume, I focus on three typical equilibrium droplet configurations, i.e. the 2×2 , 2×3 , and 3×3 patterns, as illustrated in Fig. 6.5(f) and the corresponding data for h and E are depicted by the violet, green, and blue bars in the histograms. The simulation data of the 2×2 pattern for $V = 8V_0$ in Fig. 6.5(b) and (e) (pink bars) is based on the simulation results without gravity (Fig. 6.2(c)), the equilibrium shape of which coincides with the experiments. The simulation results with zero-gravity equivalently describe the situation where gravity is fully compensated by the pinning force, similar to the case in the experiment. The experimental data of the 3×3 pattern for $V = 2V_0$ is precluded in Fig. 6.5(c), due to the inconsistency observed in Fig. 6.1(a). Despite of this inconsistency, the results for the droplet height and the surface energy obtained from theoretical, numerical, and experiment show a very good agreement with each other. For each pattern, the droplet height and surface energy increase almost linearly with the volume. For a constant volume, both the droplet height and the surface energy decrease as the droplet pattern changes from 2×2 to 2×3 , and to 3×3 , except the surface energy for $V=2V_0$. This observation indicates that for a constant volume, among all possible equilibrium states, an applanate droplet covering more hydrophilic lattices is generally more energetically stable than a towering droplet covering less hydrophilic lattices.

It should be noticed that the surface energies of the 2×3 and 3×3 patterns for $V=2V_0$ are underestimated in the analytical method. This underestimation is mainly for calculating the surface energy of the droplet cap. In fact, the baseline is curved which leads to convex and concave surfaces for the liquid-gas interface. This fact is overlooked in the theoretical model because of the circular arc assumption. However, the PF simulation is capable of modeling the realistic curved baseline as well as the convex and concave liquid-gas surface. From the simulation results, the 3×3 pattern has a higher surface energy than the 2×2 and 2×3 patterns for $V=2V_0$. The relatively high energy state of the 3×3 pattern for $V=2V_0$ as well as the aforementioned uncertain surface roughness in the experiment explains why this pattern is hard to be obtained in experiments (Fig. C.3A(c) in Appendix C).

6.2.4. Analysis of droplet evaporation

To further clarify the functional relationships of surface energy E and droplet height h versus volume V/V_0 , droplet evaporation via simulations and experiments is carried with an initial volume $V = 4V_0$. In this evaporation study I use the 2×2 pattern for both the experimental and modeling. Fig. 6.6(a) demonstrates the comparison of simulation and experimental results at different times with different droplet volumes varying from $V = 4V_0$ to $V = 0.8V_0$. The simulation results perfectly capture the morphology of the evaporating droplet observed in experiments.

Fig. 6.6(b) illustrates the height h and the base area A_{ls} of the droplet evolving with the volume from the simulation (dot-dashed lines) and the analytical model (circles). For small volumes ($\leq 2V_0$), droplet heights from the simulations and the analytical model agree very well with each other. For large volumes ($\geq 2V_0$), the droplet height h from the simulations is slightly less than the one of the analytical model. This deviation is because of the consideration of the gravity in the numerical simulation, which plays a vital role for large volume droplets, while the gravitational force is overlooked in the analytical method. The inset describes the base contact lines of evaporating droplets with volumes decreasing from $4V_0$ to V_0 . The increment of the droplet volume for any two neighbouring base lines is uniform, i.e. $\Delta V = 0.5V_0$. These contact lines are concentric circles and each of them corresponds to an energy minimum with $a = b$ in the surface energy landscape. By using the average radius $\bar{r} = (r_1 + r_4)/2$ (r_1 -base radius for $V = V_0$, r_4 -base radius for $V = 4V_0$) of the concentric circles and assuming a spherical cap for the evaporating droplet, the base area and the height of the evaporating droplet are shown by the blue and red solid lines, respectively. This assumption corresponds to a reference state with a constant base area (horizontal solid blue line), which is related to the so-called constant contact radius (CCR) evaporation mode. The base contact area of the evaporating droplet from the simulation (blue dashed line) decreases with decreasing the volume and the relative change quantity is about 10% when the volume decreases from $4V_0$ to V_0 . Moreover, the CCR contact area is almost an average value for that of the simulation results. Furthermore, the droplet height of the CCR mode (red solid line) matches very well with the analytical results (red circles).

The surface energy versus volume is presented in Fig. 6.6(c). The simulation results (dot-dashed line) agree very well with the analytical method (blue circles). The inset shows the energy maps for the highlighted states A, B, and C. For comparison, the surface energy of the CCR model is calculated

6. Single droplet on chemically patterned surfaces: theoretical calculation, phase-field simulation, and experiments

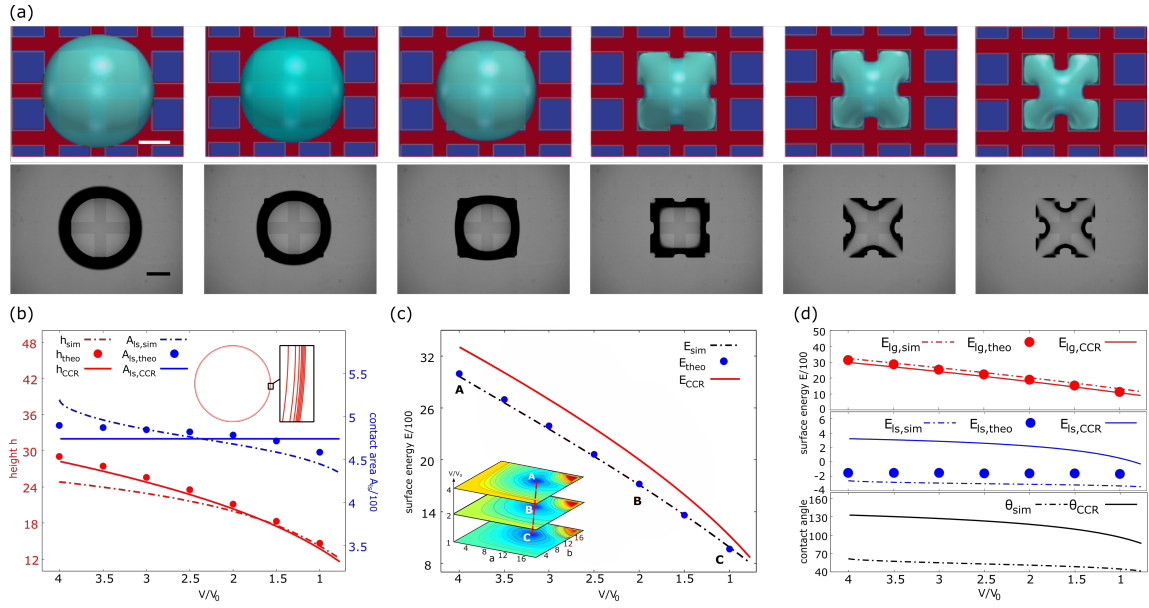


Figure 6.6.: (a) Comparison of droplet morphologies when a droplet evaporates from $4V_0$ to $0.8V_0$ ($20\text{--}4\ \mu\text{L}$). Top and bottom rows illustrate the simulation and experimental results, respectively. From left to right, the droplet snapshots in experiment were taken at the time 0, 15, 30, 45, 50, 51.5 min, respectively. (b) Droplet height and liquid-solid contact area as functions of the droplet volume. The dot-dashed lines, circles, and solid lines represent results from the PF simulations, the energy map method, and the CCR evaporation model, respectively. The inset shows the evolution of the droplet base line via the energy map method as the volume decreases from $4V_0$ to V_0 . In the CCR evaporation model, I assume that the droplet is in the shape of a spherical cap with a constant liquid-substrate contact area $A_{ls} = \pi[(r_1 + r_4)/2]^2$ with r_1 and r_4 denoting the base radii calculated from the energy map method for $V = V_0$ and $V = 4V_0$, respectively. (c) Comparison of surface energy evolution as the droplet evaporates from $4V_0$ to $0.8V_0$. Inset in left down side: Energy maps for equilibrium droplet with $V/V_0 = 1, 2, 4$. The points A, B, C denote the corresponding energy minima in the $a - b$ space. (d) Top and middle: Comparison of the surface energy evolution for the droplet cap and the droplet base. Bottom: Comparison of contact angle evolution obtained through PF simulation and CCR evaporation model. θ_{sim} is calculated through $\cos \theta_{sim} = (\cos \theta_{e,wet} x_{wet} + \cos \theta_{e,dry} x_{dry})$ with x_{wet} (x_{dry}) indicating the hydrophilic (hydrophobic) area fraction covered by the droplet. θ_{CCR} is the apparent contact angle for the droplet in the CCR model. Droplet height h and surface energy E are nondimensionalized by x^* and $\gamma^* x^{*2}$, respectively. Scale bar: 1 mm (or 10 in dimensionless value).

(red solid line), which is greater than the simulation and analytical results. This is due to an overestimation for the surface energy of the liquid-solid base area in the CCR evaporation model, as confirmed in Fig. 6.6(d). The surface energies of the liquid-gas cap E_{lg} and the liquid-solid base area E_{ls} versus volume are presented in the top and middle panels of Fig. 6.6(d), respectively. For the surface en-

ergy E_{lg} (Fig. 6.6(d), top), the simulation results (dot-dashed line), the analytical predictions (circles), and CCR model (dashed line) coincide with each other. However, as shown in the middle panel of Fig. 6.6(d), the CCR model overestimates the surface energy E_{ls} . The surface energy E_{ls} in the CCR model is calculated by using the equation $E_{ls,CCR} = -A_{ls,CCR}\gamma_{lg} \cos \theta_{CCR}$. Given the invariant of $A_{ls,CCR}\gamma_{lg}$, the decrease of the surface energy $E_{ls,CCR}$ with the volume is due to the change of the apparent contact angle θ_{CCR} , as presented in the bottom figure of Fig. 6.6(d). Here, θ_{CCR} is calculated based on a spherical cap for the liquid-gas interface, i.e. $\theta_{CCR} = 1 - 2h^2/(h^2 + \bar{r}^2)$. Analogously, in the simulations, I utilize an effective contact angle θ_{sim} to describe the surface energy $E_{ls,sim}$, i.e. $E_{ls,sim} = -A_{ls,sim}\gamma_{lg} \cos \theta_{sim}$. The contact angle θ_{sim} is calculated through the well-known Cassie-Baxter concept: $\cos \theta_{sim} = \cos \theta_{e,wet}x_{wet} + \cos \theta_{e,dry}x_{dry}$ with x_{wet} (x_{dry}) indicating the hydrophilic (hydrophobic) area fraction covered by the droplet. In summary, the overestimation of the total surface energy in the CCR model is attributed to the exaggerated surface energy $E_{ls,CCR}$. The good agreement between the simulations and the analytical method proves again the strong advantage of the energy map method in describing the droplet states on chemically patterned surfaces.

6.3. Conclusion

In this work, I have studied the equilibrium shapes of droplets on chemically patterned substrates, when the droplet size is comparable to the surface heterogeneity. In this case, the classic Cassie's equation [37] loses its validity. Instead of investigating the contact angles [45], I quantitatively addressed this problem by utilizing a combination of an analytical model, numerical simulation, and experiments. Besides, from the perspective of thermodynamics, I analyzed the surface energies of the equilibrium droplets to predict different shapes. To the best of our knowledge, this is among the most pioneering works [188, 189] fully describing equilibrated droplets on patterned substrate in a quantitative manner. The shapes, heights, and surface energies of the droplets varying with positions and volumes have been comprehensively studied. All the three methods display an excellent agreement with each other. For a certain-sized droplet, different typical equilibrium states can be identified, similar to the observation of Brandon et al. [190]. In addition, the most energetically stable state can be revealed through our method. The identification of different energy minimum states facilitates an accurate control of droplet shapes at will.

Moreover, on regular patterns, I have observed non-rotationally symmetric droplet shapes, which was previously merely observed on irregularly patterned surfaces [191]. This is the first report for these special wetting morphologies on regularly patterned surfaces confirmed both by simulations and experiments.

Furthermore, I have analyzed the evolution of the droplet geometry and energy states for quasi-equilibrium evaporating droplets. In comparison with Ref. [192], the present numerical simulation is capable of capturing the evolution of the droplet shape for continuously decreasing volumes. The simulation results of the evaporation and energy map predictions match convincingly with the experimental results. Our analysis demonstrates that although there is a strong pinning effect on the

boundaries between the superhydrophilic and superhydrophobic areas, the droplet evaporation differs from the ideal CCR mode since the contact line moves slowly inwards, similar to the observations of Ramos et al. and Zhang et al. [193, 194]. The proposed energy map method has shown its great potential to scrutinize not only the equilibrium shape of droplets but also the quasi-equilibrium evaporating droplets on chemically patterned surfaces.

The present analytical model is, however, constrained to merely describe small droplets with highly symmetric geometry and the influence of gravity is neglected. It needs to be further extended to depict more general shapes such as non-rotationally symmetric shapes induced by the strong pinning effect and applanate droplet shapes pressed by gravity. In these cases, I need to introduce additional parameters and geometry assumptions to characterize the largely deformed contact lines as well as the droplet cap. Other important issues remaining to be tackled in the future are the modeling of fast movement and instability of droplets on a designed surface. Possible endeavors in this direction might be solving the Cahn-Hilliard-Navier-Stokes equations [195] with well-defined wetting boundary conditions. Nonetheless, the present strategy may shed light on a wide range of applications of ink-jet printing, coatings, droplet arrays, and droplet-based microfluidics or bio-microfluidics [196].

7. Multiphase droplets on chemically heterogeneous surfaces

In chapters 4-6, a single droplet on chemically patterned substrates was considered, and the whole system is described with a liquid-gas system with wetting boundaries. This chapter investigates multiphase-droplets on chemically patterned substrates, which is a three-phase system with wetting boundary conditions. In this chapter, a multi-phase AC model will be adopted to model the whole system. In section 7.1 a static problem, namely, liquid-liquid confinement is studied. In section 7.2 quasi-static movements of multiphase-droplets driven by surface energy are presented. At last, in section 7.3, a summary and remarks are given. Section 7.1 was published in Ref. [197].

7.1. Liquid-liquid confinement

Water was used as a barrier to confine low-surface-tension liquids (LSTLs) as a liquid analogue of a solid well (Fig. 7.1(A)). The water barrier itself was confined in a hydrophilic surface area surrounded by hydrophobic surface areas, in which the hydrophilic area enclosed a hydrophobic area. Then, an LSTL was deposited to the hydrophobic surface area within the water wall, which spread out and was confined in the shape predetermined by the shape of the water barrier.

To understand the different shapes obtained at the water-solvent interface and to support the experimental observations, liquid wells were simulated with a multiphase AC type phase-field model

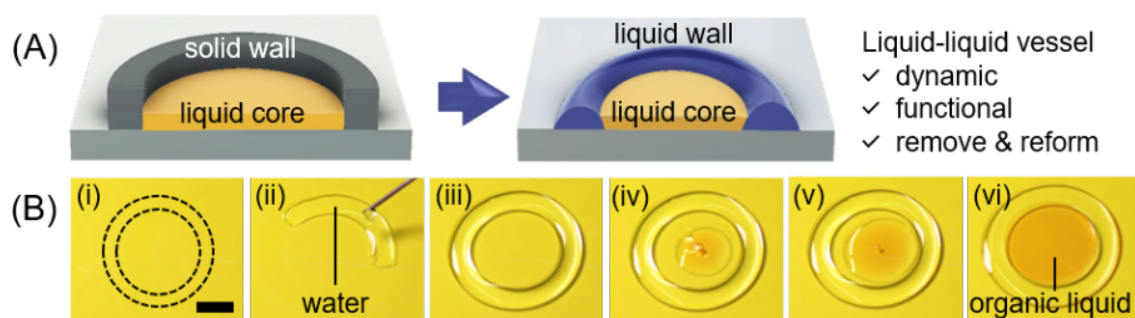


Figure 7.1.: (A) Scheme of a liquid contained in a solid vessel (left) and inside liquid water walls, that is, a liquid well (right). (B) Formation of a circular liquid well. Water forms a ring on the hydrophilic surface area (dashed line). The organic solvent (1-nonanol, dyed with Oil Red O) is then added into the liquid well. Scale bars: 5 mm.

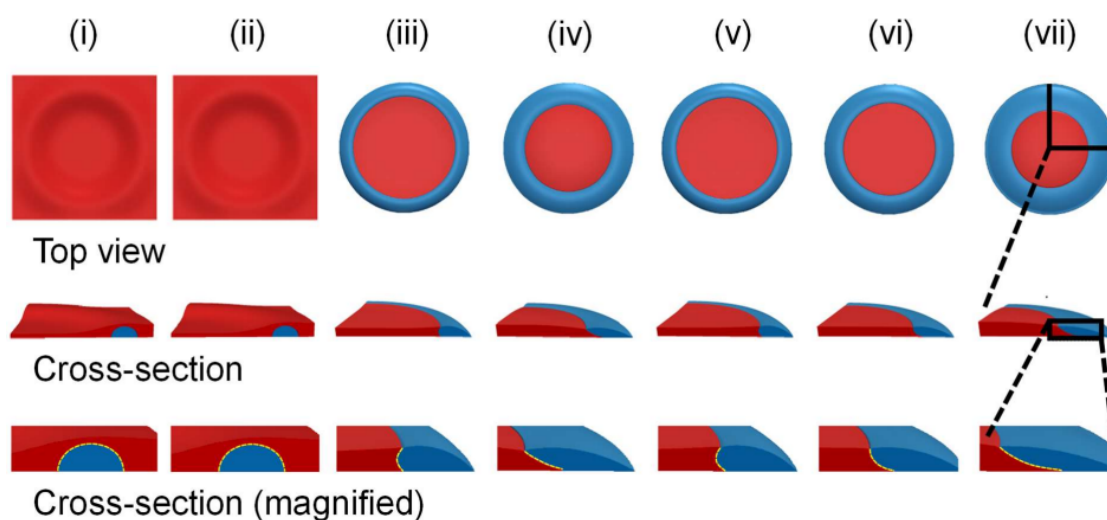


Figure 7.2.: Phase-field simulation for the confinement of 1-nonanol (red) in a ring of water (blue).

Each simulation (i-vii) is based on a different set of the surface and interfacial tensions γ_{oa} (organic-air), γ_{ow} (organic-water), and γ_{wa} (water-air). The surface and interfacial tensions ($\gamma_{oa}, \gamma_{ow}, \gamma_{wa}$) were (i) (28.0, 8.8, 72.86) mN/m [198, 199], (ii) (28.0, 8.8, 44) mN/m, (iii) (28.0, 8.8, 36.43) mN/m, (iv) (28.0, 8.8, 21.86) mN/m, (v) (36.43, 8.8, 44) mN/m, (vi) (44, 8.8, 44) mN/m, and (vii) (51, 8.8, 44) mN/m. The assumed volumes were $100 \mu L$ (1-nonanol) and $60 \mu L$ (water), respectively. The inner and outer diameters of the hydrophilic surface area are 14 mm and 18 mm, respectively. The first row shows a top view, the second row shows a cross section and the third row highlights the cross section at the interface of 1-nonanol and water.

(Fig. 7.2). Coupling the phase-field model with an appropriate boundary condition at the wall can capture the Young's contact angle as well as the so-called Neumann's triangle at a multiple phase junction via minimizing the total free energy of the system. A detailed description of the multiphase AC type phase-field model can be found in chapter 3, or the work from Ben Said et al. [52].

According to Neumann's triangle rule, the formation of a stable three-phase contact line between an organic liquid, water, and air, is possible if the sum of the surface tensions γ_{oa} (organic liquid-air) and γ_{ow} (organic liquid-water) is greater than γ_{wa} (water-air) [198]. It was hypothesized, that the same requirement ($\gamma_{ow} + \gamma_{oa} > \gamma_{wa}$) must be fulfilled to confine an organic liquid by a wall of water. Since the surface tension of the water-air interface is high ($\gamma_{wa} = 72.86$ mN/m), this is the case for n-hexadecane ($\gamma_{oa} = 26.95$ mN/m, $\gamma_{ow} = 55.3$ mN/m) but not for 1-nonanol ($\gamma_{oa} = 28.0$ mN/m, $\gamma_{ow} = 8.8$ mN/m) [199, 200, 201]. It was concluded that for solvents with low surface and interfacial tensions such as 1-nonanol no stable contact line with water can be established and therefore the confinement is not possible (Fig. 7.2(i)). However, if the Gibbs adsorption isotherm, i.e. the change in surface tensions due to the partial solubility of water in 1-nonanol and vice versa (1.76 mol/L and 1.94 mmol/L, respectively) [202, 203] is considered, the phase-field model is able to predict a stable

confinement as observed experimentally. According to Lee et al., the equilibrium surface tension for the water-air interface is reduced from 72.86 to 44 mN/m under the reported experimental conditions due to the dissolution of 1-nonanol in water [203]. Since the exact amount of 1-nonanol dissolving into the liquid wall is unknown and there is a paucity of literature for the Gibbs adsorption of water at the 1-nonanol-air interface, I considered a range of plausible values for γ_{oa} and γ_{wa} in the simulation. The interfacial tension γ_{ow} (1-nonanol-water) was determined experimentally to be 8.8 mN/m and was kept constant for all simulations, since it mutually considers the Gibbs adsorption. For $\gamma_{ow} + \gamma_{oa} < \gamma_{wa}$ no stable three-phase contact line can be established and 1-nonanol moves over the water wall (Fig. 7.2 (i) and (ii)). When the value of γ_{wa} was reduced to 36.43 mN/m (Fig. 7.2 (iii)) and 21.86 mN/m (Fig. 7.2 (iv)), stable contact lines were observed. As the value γ_{wa} reduces, the 1-nonanol-water interface tilts inward, which is consistent with the experimental observation (Fig. 7.1B). When the value of γ_{oa} is increased from 36.43 to 44 and 51 mN/m (Fig. 7.2 (v)-(vii)) while fixing the values of γ_{wa} and γ_{ow} (44 and 8.8 mN/m, respectively), stable contact lines also come into being and the 1-nonanol-water interface is gradually tilted inward as well. The simulations based on the phase-field model confirmed the hypothesis, that formation of a stable three-phase contact line and thus liquid wells are possible if the condition $\gamma_{ow} + \gamma_{oa} > \gamma_{wa}$ met. When literature values for the surface and interfacial tension (γ_{ow}, γ_{oa}) are contemplated, this is the case for n-hexadecane but not for 1-nonanol. However, a variation in the surface tensions at the liquid-air interfaces because of the partial solubility of 1-nonanol with water can enable a transition from an instable to a stable liquid well. This explanation could be applied to other low surface tension liquids, such as toluene or n-octane, which fail to fulfill the criterion $\gamma_{ow} + \gamma_{oa} > \gamma_{wa}$ but nevertheless can be contained by a water well [201]. Moreover, the specific set of interfacial tensions ($\gamma_{ow}, \gamma_{oa}, \gamma_{wa}$) strongly influences the shape of the organic-water interface, which is most likely the reason for the experimentally observed difference between the shapes of the 1-nonanol-water and the n-hexadecane-water interfaces. The sets of surface tensions (Fig. 7.2, iv) ($\gamma_{ow}, \gamma_{oa}, \gamma_{wa}$)=(28, 8.8, 21.86) mN/m and (Fig. 7.2, vii) ($\gamma_{ow}, \gamma_{oa}, \gamma_{wa}$)=(51, 8.8, 44) mN/m are the most likely possible parameters to reproduce the stable triple junctions of water-1-nonanol-air and water-1-nonanol-substrate, which were observed experimentally (Fig. 7.1B).

The influence of Gibbs adsorption on the interfacial tensions between different phases also explains the experimental observation that a droplet of 1-nonanol deposited on the water surface formed a droplet instead of forming a wetting layer. A similar phenomenon was also reported for the formation of a liquid lens for the benzene-on-water system, where the water-air surface tension is reduced from 72.8 mN/m to 62.4 mN/m due to the dissolution of benzene in water [204].

7.2. Multiphase droplets manipulation on solid substrate

Using the multiphase AC model, the movements of multiphase droplets (namely, droplets 1 and 2) on a substrate is investigated. The substrate is designed to show different hydrophobicity for the multiphase droplets, as illustrated in Figure 7.3(A). Driven by the gradient of surface energy, the droplets move from the hydrophobic area to the hydrophilic area. Figure 7.3(B) shows the time evolution of

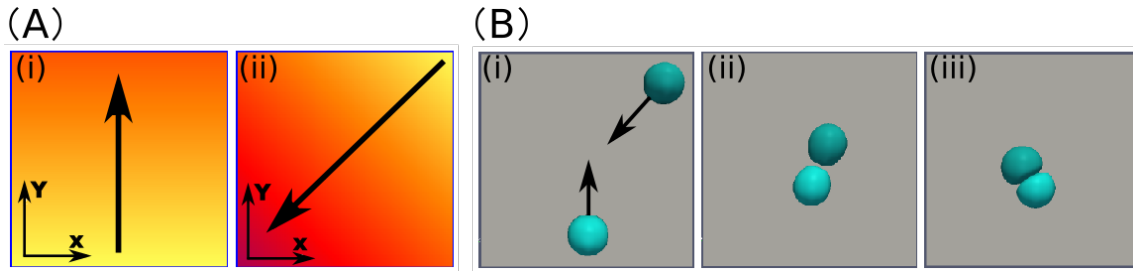


Figure 7.3.: (A) (i) and (ii) Schematic of surface hydrophobicity for droplets 1 and 2, respectively. From yellow to red color, the surface become more and more hydrophilic. The arrays indicate the direction of the surface energy gradient. (B) (i)-(iii) Time evolution of droplets 1 (bright green) and 2 (dark green) on the substrate. (i) Initial states. (ii) The two droplets meet with each other. (iii) Droplet collision and deformation. The interfacial tensions between each two phases are the same, i.e. $\gamma_{12}=\gamma_{1a}=\gamma_{2a}$ (a stands for air) [205].

the two droplets. Droplet 1 moves along the y -direction, while droplet 2 moves along the diagonal direction. The two droplets meet with each other and then collide and deform. This test case is to show the capability of the multiphase AC model for modeling the multiphase droplets movements on a designed substrates, which may have potential applications in the lab on a chip system. Further validations and developments of this model need to be done to handle the fast movements under complex conditions.

7.3. Summary and remarks

In this chapter, the Allen-Cahn-type multiphase phase-field model is applied to study the liquid-liquid confinement and the slow movement of multiphase droplets on a solid substrate. Similar to the former chapter, the problems can be considered as an equilibrium or a quasi-equilibrium problem. The driving force of the multiphase system is the minimizing of the free energy. For the liquid-liquid confinement problem, I used several combinations for the values of the interfacial tensions to explore the influence of Gibbs absorption on the change of interfacial tensions. However, to model the real Gibbs absorption effect, I must introduce diffusion equations to the current model or tend to use a multiphase CH model. This is one potential direction that I could further explore. Since I currently focus on the static states of the liquid-liquid confinement and the slow movement of droplets on a substrate, it is reasonable to regardless of the influence of the fluid flow. To further extend the capability of the phase-field model to address the phenomenon with a strong convection effect, a couple with Navier-Stokes equations is essential. The couple of two-phase CH equations with NS equations is presented in chapter 3, and the validation of Cahn-Hilliard-Navier-Stokes (CHNS) equations will be discussed in chapter 9.

8. Droplet on mechanically heterogeneous surfaces

In chapters 4-7, chemically patterned substrates were considered, while this chapter investigates droplets on mechanically heterogeneous surfaces. The aim is to contemplate how the topology of the substrate influence the droplet wetting behaviors. In section 8.1 the AC model is validated for modeling droplets in a wedge structure. In section 8.2, the criterion for droplet permeation in a pore structure is studied in detail. At last, summaries and conclusions are provided in section 8.3. This chapter has been submitted to *Physical Review Letters*.

8.1. Validation of the numerical model for droplet in a pore structure

Here, the capability of the model to simulate equilibrium states of droplets in a wedge is validated. According to [206], regardless of the influence of gravity, the overall equilibrium shape of the droplet in a wedge under the studied conditions is a truncated sphere, as confirmed by the experimental snapshots in Fig 8.1b-d, where circular fits to the droplet profile are illustrated. Based on this concept, the 2D droplet in the wedges with varying open angles and static contact angles is simulated. The open angle 2φ ranges from 26° to 37° and contact angle θ changes from 140° to 162° , similar to the setups of [206]. The droplet radius is also the same as the one in the paper of [206]. Initially, the circled droplet is released to the 2D wedge and the droplet evolves to an equilibrium state. In Fig 8.1a, the distance x_0 of the droplet center from the wedge apex as a function of the contact angle θ is plotted. The colored symbols indicate the simulation results for different setups of $(\theta, 2\varphi)$. The dashed lines present the theoretical prediction based on the assumption that the equilibrated droplet is a part of a circle. The inset illustrates the geometric parameters of the equilibrium state of the droplet in a wedge. The points labeled by b , c , and d correspond to the simulation snapshots, where the droplet shapes also show a great agreement with the dashed circular fits. The good consistency of the simulation results with the experiments and theoretical predictions reveals the capability of the numerical model to simulate the wetting behavior in confined geometry. Thereafter the numerical model is utilized to simulate the droplet movement in a funnel-like pore structure. As shown in Fig 8.2, the circled droplets are initially released in the left part of the pore and the inner wall is tangential to the droplet profile. The open angle of the left part is 60° and the ratio of the initial droplet diameter to the narrowest pore diameter is $D/L = 3$. Driven by the capillary force, the droplet spreads along the channel wall and reaches an equilibrium state eventually. In (a) and (b) the contact angle is set as

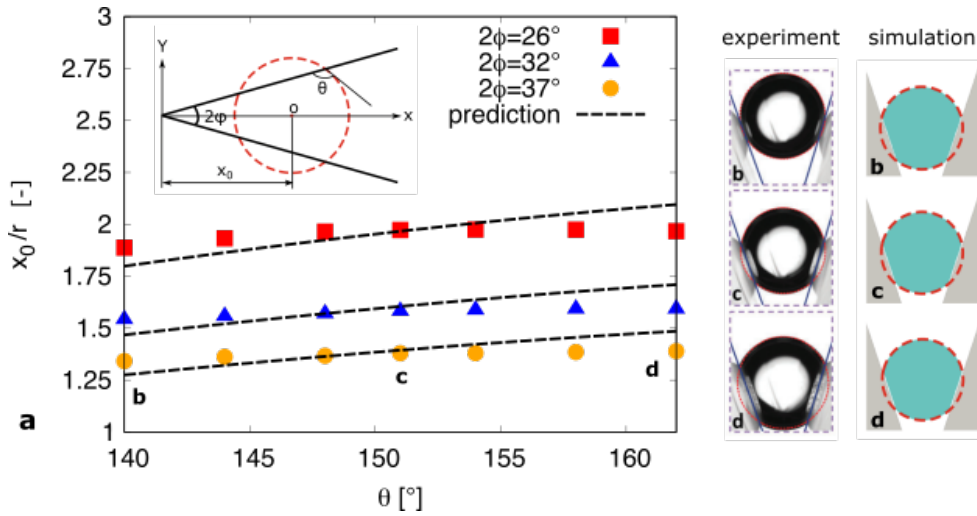


Figure 8.1.: Validation of phase-field method for modeling equilibrium state of droplets in a wedge. (a) The distance x_0 of the droplet center O from the wedge apex as a function of contact angle θ . The simulated data points (colored symbols) show 2D-droplets with radius $r = 0.98$ mm (the same size as the $4 \mu L$ -droplet in [206]) in three wedges with opening angles 2ϕ ranging from 26° to 37° . The black dashed lines are theoretical predictions in 2D, modified from the 3D version in [206] (The 2D model: $x_0/r = \sqrt{\frac{\pi}{-\pi+2\theta-\sin^2\theta} \frac{\cos(\pi-\theta)}{\sin\phi}}$). The inset denotes the schematic equilibrated droplet profile in a wedge with labeling geometric parameters. (b)-(c) Equilibrium droplet morphologies for open angles $2\phi = 37^\circ$ and contact angles $\theta = 140^\circ, 151^\circ, 162^\circ$, respectively. Left: Experimental results from [206]; Right: Present 2D-simulation results. The red dashed lines are circular fits of droplet profiles.

60° , and 120° , respectively. It is observed that the droplets in (a) with relative hydrophilic substrate penetrate the right (narrow pore) part, while the droplet in (b) with hydrophobic substrate shows no penetration. This reveals that wettability takes an important role in penetration. In the following, how the wettability together with the other two parameters - the open angle and droplet size affect the droplet penetration behavior in this confined geometry is comprehensively investigated.

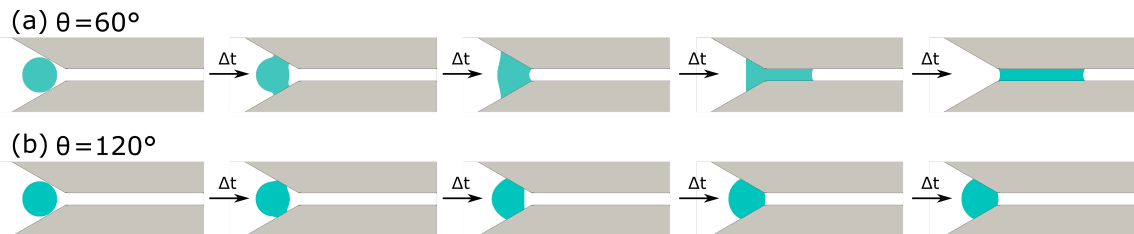


Figure 8.2.: Droplet evolution with time in a funnel-like pore structure for different contact angles θ . (a) $\theta = 60^\circ$, (b) $\theta = 120^\circ$. The open angle for the structure are $2\phi = 60^\circ$. The ratio of the droplet diameter to the tunnel diameter D/L is set as 3.

8.2. Analysis of the criterion for droplet permeation in a pore structure

8.2.1. Analytical model

To theoretically determine whether the penetration happen, I need to specify the parameterisation for the geometry of the droplet, as illustrated in Fig. 8.3. I propose two models to predict the droplet penetration behavior. Model 1 is a simplified model and it is described with the schematics (a) and (b). I assume that the critical state of the equilibrium droplet is either a part of circle (situation (a)), or just a whole circle (situation (b)) with curvature radius R . In (a), the circle with solid line depicts the initial state of the droplet. Because of the volume preservation, I have:

$$S_I - 2S_{II} = \pi D^2/4. \quad (8.1)$$

Here, S_I is the area of the dashed circle and S_{II} denotes the area of the arch MN confined by the angle $\angle MON$. Then I have

$$R^2(2\theta - \sin(2\theta) - \pi) = \pi D^2/4. \quad (8.2)$$

To meet with the wetting boundary condition in the narrow pore, i.e. $R = 0.5L/\cos(\pi - \theta)$, I obtain

$$\frac{D}{L} = \sqrt{\frac{2\theta - \sin(2\theta) - \pi}{\pi \cos^2 \theta}}, \quad (8.3)$$

which is independent of φ . This model is only valid when $D/L \gg 1$ with a very small open angle, otherwise the droplet deviates largely from a part of spherical shape. Actually, this equation precisely describe the droplet in a straight tube and the equilibrium shape is part of a circle (i.e. $\varphi = 0$ in Fig. 8.3(a)). However, for large open angle (e.g. $\varphi > 90^\circ$), if I only consider the spreading inside the pore, I could directly obtain the classic equation for the droplet adsorption criterion, as displayed in Fig. 8.3(b):

$$\frac{D}{L} = -\frac{1}{\cos \theta}. \quad (8.4)$$

The difference between Eq. 8.3 and Eq. 8.4 is due to the influence of the side walls out of the narrow part of the pore. I ambiguously divide the model 1 into two parts namely, model 1a for $\varphi \in [0, \pi/2)$ and model 1b for $\varphi \in [\pi/2, \pi]$.

In model 2, I propose a more accurate model to address the influence of the open angle, as presented in Fig. 8.3(c) for $\varphi \in [0, \pi/2]$ and (d) for $\varphi \in [\pi/2, \pi]$, respectively. The green color highlights the critical droplet shape and the red and blue dashed circles fit the droplet profiles in the two sides, showing that the droplet has the same curvature in the both sides. The derivation of model 2 is as follows:

When $\varphi \in (0, \pi/2]$ (see Fig. 8.3(c)),

$$S_{III} + S_{IV} + S_V = \pi D^2/4. \quad (8.5)$$

Here, S_{III} , S_{IV} , and S_V are the surface areas for the arch M_1M_2 confined by $\angle M_1O_2M_2$, the arch N_1N_2 confined by $\angle N_1O_1N_2$, and the trapezoid $M_1M_2N_1N_2$, respectively. thus I have $S_{III} =$

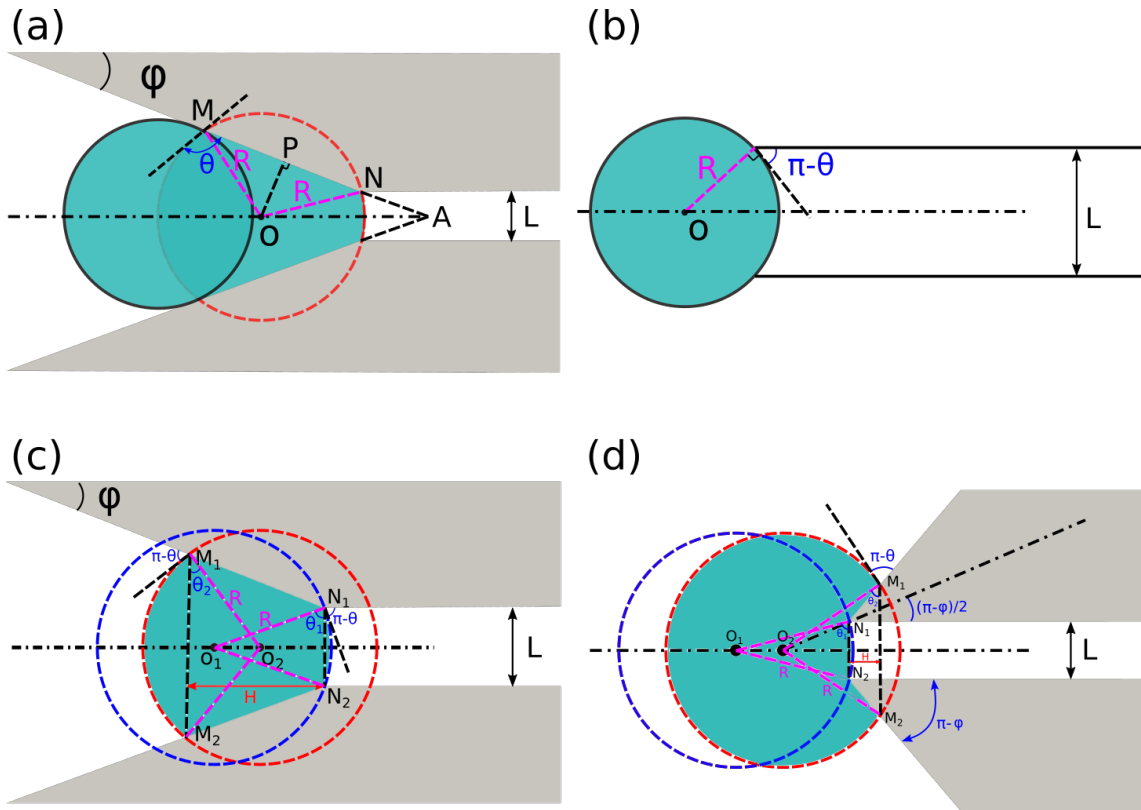


Figure 8.3.: Schematic of droplet penetration into pore structures. In (a), (c) and (d) the pore has an open angle 2φ with narrowest pore diameter L . (a) The circle with black solid line depicts the initial state and the droplet with fitted red dashed circle approximately corresponds to a critical state that the droplet cannot totally penetrate into the narrow part. The initial droplet diameter is D . Here, I assume $D \gg L$ and φ is very small. The red fitted circle centering at O has a radius R and intersects with the substrate at the points M and N . N is exactly on the funnel throat. The dot dashed line goes through the point O and the open angle apex A . The black dashed line through M is the tangent line of the red circle and thus θ represents the contact angle. The line OP is normal to the substrate surface. (b) Regardless of open angle and droplet spreading takes place only inside the pore with diameter L . In (c) and (d), the green color indicates exactly the critical droplet shape that are not able to totally penetrate into the narrow part. The red and blue dashed circles with radii R fit the droplet profiles in the left and right sides, respectively. M_1, M_2, N_1, N_2 are contact points of the three phases. (c): $\varphi \in (0, \pi/2]$. (d): $\varphi \in [\pi/2, \pi]$. $\theta_1 = \angle O_1 N_1 N_2$, $\theta_2 = \angle O_2 M_1 M_2$.

$R^2(\pi/2 - \theta_1 - \sin \theta_1 \cos \theta_1)$, $S_{IV} = R^2(\pi/2 - \theta_2 - \sin \theta_2 \cos \theta_2)$, and $S_V = 0.5(L + 2R \cos \theta_2)H$. Here, $H = (R \cos \theta_2 - 0.5L)/\tan(\varphi)$ is the height of the trapezoid $M_1M_2N_1N_2$. Then I obtain:

$$(R/L)^2(\pi - \theta_1 - \theta_2 - 0.5 \sin 2\theta_1 - 0.5 \sin 2\theta_2 + \cos^2 \theta_2 \cot \varphi) - 0.25 \cot \varphi = \pi(D/L)^2/4. \quad (8.6)$$

with $R = 0.5L/\cos(\pi - \theta)$, $\theta_1 = \pi - \theta$, and $\theta_2 = \pi - \theta - \varphi$, I have at last

$$\frac{D}{L} = \sqrt{\frac{-\pi + 2\theta + \varphi + 0.5[\sin(2\theta + 2\varphi) + \sin 2\theta] + 0.5 \cot \varphi [\cos(2\theta + 2\varphi) - \cos 2\theta]}{\pi \cos^2 \theta}}. \quad (8.7)$$

When $\varphi \in [\pi/2, \pi]$ (see Fig. 8.3(d)),

$$S_{III} + S_{IV} - S_V = \pi D^2/4. \quad (8.8)$$

In this case, S_{III} and S_V have the same formulations as above, while S_{IV} is expressed as $S_{IV} = R^2(\pi/2 + \theta_2 + \sin \theta_2 \cos \theta_2)$ with $\theta_2 = -\pi + \theta + \varphi$. The height of the trapezoid $M_1M_2N_1N_2$ becomes $H = (R \cos \theta_2 - 0.5L)/\tan(\pi - \varphi)$. From Eq. 8.8, I could finally obtain:

$$\frac{D}{L} = \sqrt{\frac{-\pi + 2\theta + \varphi + 0.5[\sin(2\theta + 2\varphi) + \sin 2\theta] + 0.5 \cot(\varphi) [\cos(2\theta + 2\varphi) - \cos 2\theta]}{\pi \cos^2 \theta}}. \quad (8.9)$$

which is exactly the same as the situation for $\varphi \in (0, \pi/2]$. In particular, when $D/L = \sin^{-1}(\pi/2 - \varphi/2) = \cos^{-1}(\pi - \theta)$, the red and blue dashed circles in Fig. 8.3(c)(d) coincide with each other, i.e. M_i and N_i ($i = 1, 2$) coincide with each other. This droplet state is also the same as in Fig. 8.3(b). In the following I call this state as a transition state with $(\varphi = \varphi_t, \theta = \theta_t)$. (φ_t, θ_t) obeys the linear relation:

$$\varphi_t/2 + \theta_t = \pi. \quad (8.10)$$

Note that Eq. 8.9 is valid for $H \geq 0$, i.e. $\theta \leq \theta_t$ or $\varphi \leq \varphi_t$.

Specially, when $\varphi = 0$, the droplet will form a symmetric liquid bridge for each D/L :

$$\frac{D}{L} = \sqrt{\frac{-\pi + 2\theta + \sin(2\theta) + 4(H/L) \cos^2 \theta}{\pi \cos^2 \theta}}. \quad (8.11)$$

when $H = L \tan(\pi - \theta)$, the droplet is part of a circle, then

$$\frac{D}{L} = \sqrt{\frac{-\pi + 2\theta - \sin(2\theta)}{\pi \cos^2 \theta}}, \quad (8.12)$$

which is exactly the same as model 1b. When $0 < H < L \tan(\pi - \theta)$ and $H > L \tan(\pi - \theta)$, the droplet shapes are symmetric but not a part of circle. This is out of the scope of the current work and will not be further discussed.

8.2.2. Analysis of the droplet penetration behavior

In this part, I use the numerical model and analytical model described above to investigate the droplet penetration behavior in pore structures. I analyze the influence of the open angle, contact angle and droplet size to the droplet final state. Droplets are initially put on the left part and contact the the substrate. I systematically change the open angle and contact angle and observe the final states of

the droplets. Fig. 8.4(a) shows the simulation snapshots for the final states of droplets in the size of $D/L = 3$ for different contact angles and open angles. In Fig. 8.4(b), I plot the penetration states for the simulations in the range for $\varphi \in [10^\circ, 150^\circ]$ and $\theta \in [80^\circ, 140^\circ]$. The squares and triangles indicate the states of penetration and no penetration, respectively. Additionally, I plot the theoretical predictions of the critical states of droplets using model 1 and model 2 with dot dashed line and solid

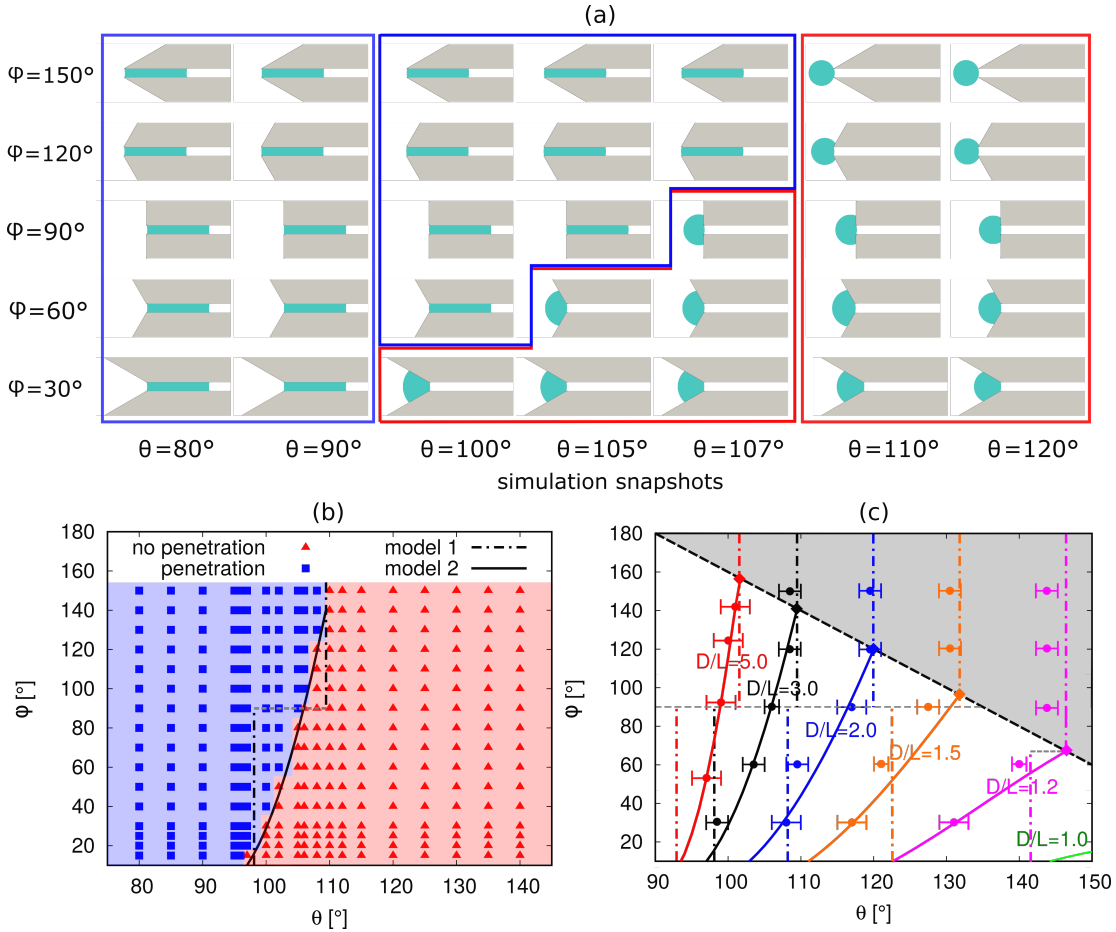


Figure 8.4.: Regime diagrams for the droplet final states in pore structures with varying φ and θ . (a) Simulation snapshots for final states of droplets ($D/L = 3$) with varying φ and θ . (b) Regime diagram for the penetration states of the droplet with $D/L = 3$. Blue squares: totally penetration into the narrow part; Red triangles: no penetration. I plot the critical lines predicted by model 1 (dot dashed line divided by the gray dashed line. Top: model 1b; Bottom: model 1a) and model 2 (solid line). In (c), I vary D/L from 1 to 5 and plot the corresponding critical lines (highlighted with different colors) predicted by model 1 and model 2. The colored rhombus points are intersections of model 1 and 2 and the black dashed line described by Eq. 8.10 going through these points denotes the upper limit of model 2. The circle points with error bars indicate the simulation confirmed critical penetration states.

line, respectively. The model 2 is excellently consistent with the simulation confirmed boundary in the range for $\varphi \in [10^\circ, 140^\circ]$. As expected, model 1 shows very good agreement for the range of $\varphi > 140^\circ$ and $\varphi < 20^\circ$. It is further observed that, for a certain open angle, large contact angle tend to prevent the penetration. Whereas for a certain intermediate contact angle, large open angle facilitate the penetration. Moreover, for the hydrophilic regime with $\varphi \leq 96^\circ$ (or the hydrophobic regime with $\varphi \geq 110^\circ$) the droplet will always (never) penetrate the narrow part of the pore, independent of the open angles.

Similar to the Fig. 8.4(b), in Fig. 8.4(c), I vary the droplet size from $D/L = 1$ to $D/L = 5$ and draw the corresponding critical lines predicted by model 1 and 2 with dot dashed and solid lines, respectively. The colored circle points with error bars indicate the simulation confirmed critical states. The intersections between model 1 and model 2 are illustrated with the rhombus points and the black dashed line described by Eq. 8.10 going these points divides the whole region into two regimes, namely the gray zone and the white zone. It is found that the simulation results coincide excellently with model 1b in the gray zone and the model 2 in the white zone. This implies that the droplets in the gray zone don't spread onto the slop surface in the outside of the pore. As can be found in Fig. 8.4(a), the droplet is of a circular shape for the condition ($\theta = 120^\circ, \varphi = 150^\circ$), which is rather consistent with the situation for Fig 8.3(b) but not Fig 8.3(d).

For a certain sized droplet, the critical contact angle increases with the open angle until a certain value φ_t is achieved. Above this value, the critical contact angle will no longer change. These transition points (θ_t, φ_t) are just the intersections between model 1b and model 2. It is also noted that both θ_t and φ_t increase with the droplet size, showing that large droplets tend to be affected in a wider range of open angles and narrower range of contact angles than the small droplet. Moreover, the critical lines become more and more steep as the droplet size enlarged, which reveals that the changes in open angle have more profound impact on the smaller droplets. Furthermore, it is noted that model 1a shows good agreement for large droplets (e.g. $D/L = 3$ or 5) with lower open angles (e.g. $\theta < 20^\circ$). Interestingly, as the droplet size increases, model 1 and model 2 tend to show smaller deviation. It is to be expected, when $D/L \gg 1$, the curvature is not largely affected by the open angle anymore. In this case, the critical contact angle asymptotically approaches 90° . This explains the classic conclusion in the textbook why large droplets cannot spontaneously penetrate non-wetting capillaries.

In Fig. 8.5(a)-(c), I keep the open angle constant ($\varphi = 30^\circ$) and show the combined influence of the droplet size and contact angle. In (a) and (b) I illustrate the simulation snapshots of the droplet final states for varying contact angles and droplet sizes, respectively. In Fig. 8.5(c) I display the penetration states of the simulation results in the range for $D/L \in [1, 4.2]$ and $\theta \in [40^\circ, 150^\circ]$. Moreover, I plot the theoretical predictions of model 1a and model 2, showing a very good agreement with the simulated regime boundary. Note that model 2 is more precise and model 1a overestimates the critical contact angle for small droplet ($D/L < 2$). I observe that for a certain sized droplet, smaller contact angles facilitate the penetration and for a certain hydrophobic contact angle, small droplets are prone to penetrate the narrow part of the pore. Especially, for the hydrophilic region ($\varphi \leq 90^\circ$), no matter how large the droplet is, penetration is inevitable. In Fig. 8.5(d) I draw the model 2 predicted critical

lines for a series of open angles. All the critical lines show the same tendency, and the critical contact angle increases with the decreasing droplet size. I find that smaller droplets are more sensitive to the change in the open angle, while large droplets are more robust to the influence of the open angle. All the critical lines are asymptotically approaching 90° as the droplet become extremely large. It is found that large open angle drives the critical line upwards, showing that large open angle favors the penetration of the droplet. In particular, for a very small open angle (e.g. $\varphi = 10^\circ$), the critical line intersects with the line $D/L = 1$ (dashed line) around $\theta = 145^\circ$, revealing that the pore with very low open angle and superhydrophobic substrate could be able to even prevent the penetration of droplets with $D/L < 1$ (see the inset in Fig. 8.5(d)). This finding may have potential applications in filter systems, e.g. surgical mask for preventing tiny droplets.

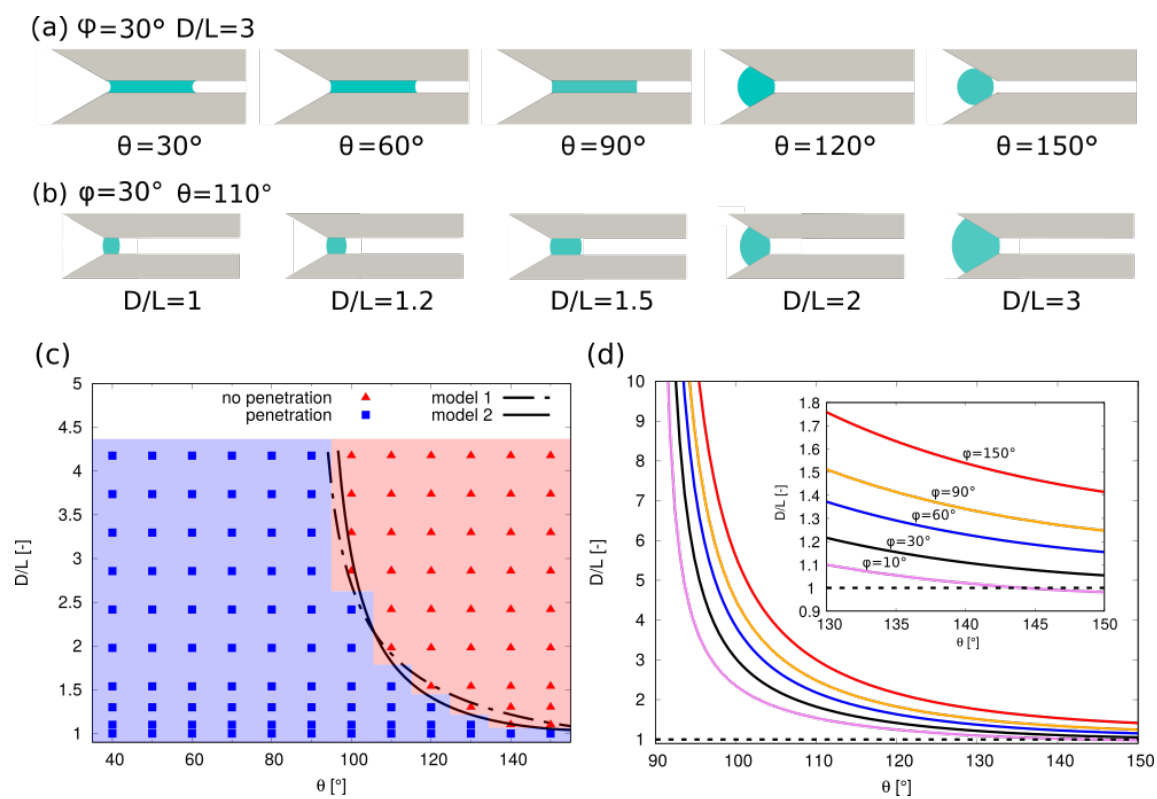


Figure 8.5.: Regime diagram for droplet final states in pore structures with different D/L and θ . The half open angle is kept constant with $\varphi = 30^\circ$ in (a)-(c). (a) Droplet final states influenced by the contact angle θ . (b) Droplet final states influenced by the droplet size D/L . In (c) the blue squares and red triangles indicate whether droplet penetration happens or not. The solid and dot dashed lines describe the theoretical predictions with model 1a and 2, respectively. In (d) I vary φ from 10° to 150° (highlighted with different colors) and plot the predictions with model 2. The inset displays a zoom of the diagram in the range of $\theta \in [130^\circ, 150^\circ]$.

8.3. Summaries and conclusions

The droplet penetration behavior into a pore structure is investigated for a wide range of droplet sizes, contact angles and open angles by using phase-field simulations and theoretical analysis. Based on the geometric analysis of droplet shapes and the pore structures, I proposed a simplified model (model 1a for small φ and model 1b for large φ) and a precise model (model 2, valid for $\varphi \leq \varphi_t$). Through comprehensive simulations, regime maps on penetration versus no penetration are provided. The simulated regime boundaries show excellent agreements with the proposed theoretical models. Overall, for a certain sized droplet, the critical contact angle increases with the open angle. However, there exists a certain value of the open angle ($2\varphi_t$), above which the critical contact angle keeps constant. Thus the model 1b is valid for the situation of $\varphi \geq \varphi_t$. Furthermore, for a certain open angle, the critical contact angle increases with the decreasing droplet size and smaller droplet tend to be sensitive to the influence of the open angle. To sum up, our findings demonstrate that the curvatures outwards and inwards and the wettability of the substrate accurately control the droplet penetration behavior, in consistency with the Young-Laplace law and the Young's law. The thorough study of the combined influence of the open angle, droplet size and contact angle to the droplet penetration paves a novel way to better understand wetting behaviors in a pore structure. And our observations may provide essential guidelines for the applications including the design of microfluidics, filter system for preventing droplets, drainage system, oil recovery system, and so on.

Part IV.

Results and discussion: Dynamic problems

9. Droplet dynamics on solid heterogeneous surfaces

In chapters 4-8, static or quasi-static problems were discussed and as a gradient descent method, the AC model is very efficient to deal with these problems. However, this chapter focuses on dynamic problems such as the dewetting and breakup processes. In this case, the naturally conserved model CH model coupled with NS equations (i.e. CHNS model) should be used. In sections 9.1-9.3 the CHNS model is validated for modeling the fast spreading of droplets, droplet impacting on mechanically and chemically heterogeneous substrates. In section 9.4, the CHNS model is applied to address thin liquid film dewetting on chemically patterned substrates. This chapter has not been submitted to any peer-reviewed journals.

9.1. Validation of the CHNS model for fast spreading on homogeneous surfaces

In this section, the capability of the CHNS model is validated for simulating the fast spreading of the droplet on homogeneous surfaces. The simulation setups are according to the experiment work from Bird et al. [80]. They released water droplets with radius $R = 0.82\text{mm}$ on four different substrates ($\theta_{eq}=3^\circ, 43^\circ, 117^\circ, 180^\circ$) to see how the surface chemistry affects the shape of the droplet as it spreads. The early stages of the droplet spreading were concerned, as illustrated in Fig. 9.1(a) (left part), the evolution of droplet shapes on the four different substrates are distinguished. Accordingly, I run the corresponding simulations under the same conditions to reproduce the experimental results (9.1(a) (right part)). The dynamic contact angle $\theta_D < 90^\circ$ is immediately formed for the superhydrophilic surface with $\theta_{eq} = 3^\circ$, while it maintains greater than 90° ($\theta_D > 90^\circ$) for the case $\theta_{eq} = 117^\circ$. For the case of $\theta_{eq} = 43^\circ$, θ_D undergoes a transition to 90° . As a reference case with $\theta_{eq} = 180^\circ$, the droplet keeps the nonwetting spherical shape all the time. The generation of capillary waves is perfectly reproduced for the cases of the partial wetting in the simulations. In addition, in 9.1(b), I compare the time evolution of the droplet base radii for the three partial wetting cases, where the simulation results (solid lines) agree very well with the experiments (symbols). Note that, in the simulations I introduce the time relaxation parameter τ_w in the boundary condition to have a better fitting. I choose the non-dimensional values of $\tau_w = 1500, 2600, 1$, and 1 for the cases (i)-(iv). For the details of the nondimensionalization, please tend to chapter 3, and here I only list the reference values in Table 9.1.

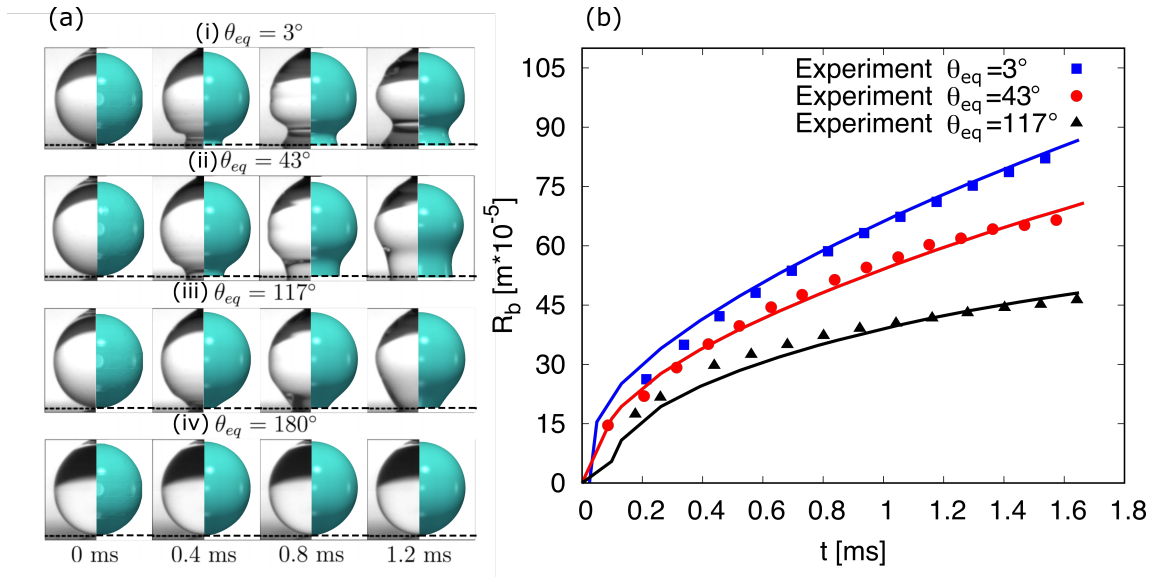


Figure 9.1.: Comparison of droplet shape evolution on different substrates. (a) Snapshots of droplet shapes. Left: Experiments from [80]. Right: Present simulations. From (i) to (iv) the equilibrium contact angle $\theta_{eq} = 3^\circ, 43^\circ, 117^\circ, 180^\circ$. (b) Comparison of base radius evolution with time. The symbols and solid lines denote experimental results from [80] and simulation results, respectively.

The simulation setups for the following two validation cases in sections 9.2 and 9.3 are also according to the reference values listed in table 9.1.

Table 9.1.: Reference values for nondimensionalization.

Reference values	Value	Unit
Length x^*	$2 \cdot 10^{-5}$	[m]
Viscosity ν^*	$1.0 \cdot 10^{-3}$	$[\frac{kg}{ms}]$
Surface tension σ^*	$7.28 \cdot 10^{-2}$	$[\frac{kg}{s^2}]$

9.2. Validation of the CHNS model for droplet dynamics on mechanically heterogeneous surfaces

In this section, the CHNS model is further validated to simulate the droplet impacting process on a flat superhydrophobic substrate with point-like superhydrophobic macrotextures. The point-like macrotexture makes the impacting droplets rebound as rings, reducing the contact time with the substrate. Fig. 9.2 shows the comparison of the experimental result (top row) from [207] and the present simulation result (bottom row). The droplet spreads quickly to form a pancake shape and

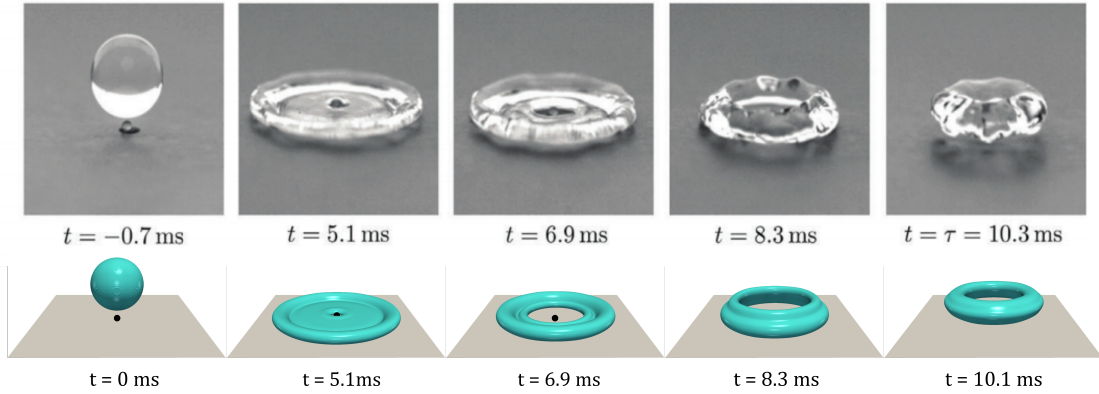


Figure 9.2.: Snapshots of a water droplet with radius $R = 1.6$ mm impacting the point-like defect on a superhydrophobic substrate at the velocity $u = 1.2$ m/s (centered impact). Top: Experiment from [207]. Bottom: Present simulation. The contact angle in the simulation is set as $\theta = 160^\circ$.

then the droplet center is punctured by the point-like defect. The thin film in the center spreads outwards and comes across the retreating rim, leading to the rebound of the droplet in a ring shape. The simulation perfectly reproduces the impacting process and shows great consistency both in the shape evolution and timescale.

In Fig. 9.3 the high-angle views and cross-sections of the droplet impacting process is displayed to show the ring formation (at $t = 3.7$ ms), the collision between opposite rims (at $t = 6.1$ ms) and the rebound (at $t = 6.7$ ms). In this simulation, droplet with radius $R=1.3$ mm and impact velocity $u = 1.28$ m/s was considered. The top and bottom panels are the LB simulation from [207] and the present PF simulation, where excellent agreement is observed.

The excellent consistency between the present PF simulation and the experiment and simulation of Chantelot et al. [207] demonstrates the robustness and justifiability of the CHNS model.

9.3. Validation of the CHNS model for droplet dynamics on chemically patterned surface

The CHNS model is further validated by comparing the experimental work of Song et al. [208], in which the water droplet impacting on a superhydrophobic stripe coated hydrophilic surface was considered. In Fig. 9.4, the droplet impact process and the shape evolution with time are illustrated. The top panel (a) and (b) are sides and top views for the present simulation. As a reference, the bottom panel (c) and (d) denote the experimental results from [208]. It is observed that the spreading is inhibited along the direction of the superhydrophobic stripe in the early stage (from $t = 0$ ms to $t = 4.4$ ms), whereas in the last stage, the droplet retracts rapidly on the superhydrophobic stripe. This leads to the splitting of the droplet into two parts. The PF simulation precisely captures the character of the droplet evolution and the timescale also shows an excellent agreement.

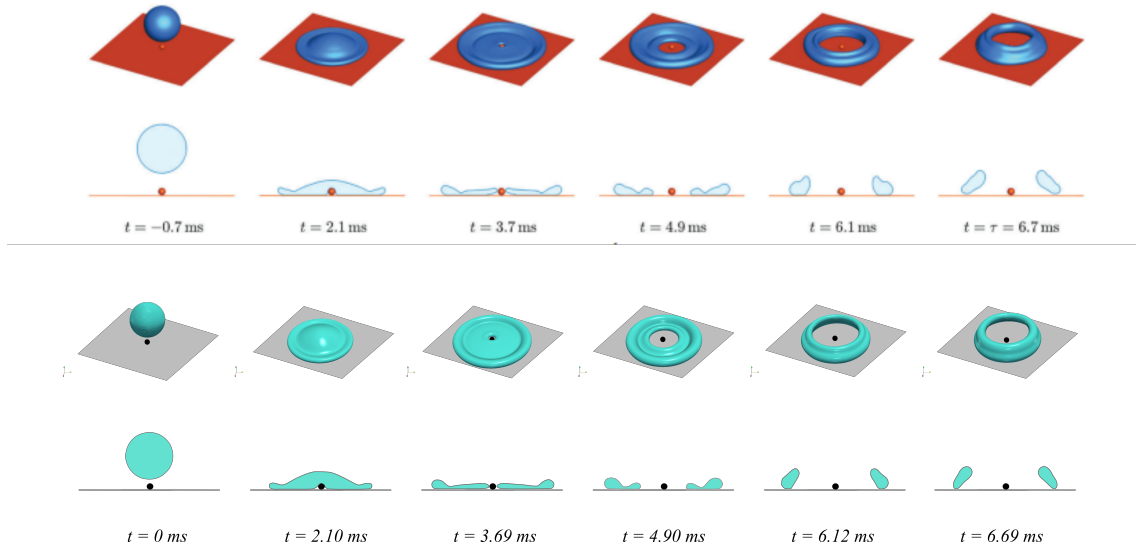


Figure 9.3.: Simulation of a droplet ($R = 1.3$ mm) impacting at ($u = 1.28$ m/s) a substrate textured by a sphere with radius $r = 0.2$ mm. Top panel: Lattice-Boltzmann simulation from [207]. Bottom panel: Present phase-field simulation. For each panel high-angle views and cross-sections are shown in the first and second rows respectively.

9.4. Analysis of thin liquid film dewetting on chemically patterned surfaces

After the validation of the CHNS model, the model is applied to simulate the thin-film dewetting process on chemically patterned surfaces.

As illustrated in the Fig. 9.5 (a) and (b), the thin-films are initially placed on a two-lattice-patterned and a four-lattice-patterned surfaces, respectively. θ_{phi} represents the contact angle of the hydrophilic areas (blue), and it keeps constant as 20° . θ_{pho} denotes the contact angle of the hydrophobic area (red) and it is changed among the following values: 60° , 90° , 120° , 160° . B represents the whole width of the two neighbouring hydrophilic lattices and the hydrophobic area between them, i.e., $B = 2B_{phi} + B_{pho}$. For the two-lattice-patterned surface, $B_{phi} = 100$ and $B_{pho} = 50$. $L = 400$ denotes the length of the hydrophilic pattern. For the four-lattice-patterned surface, $B_{phi} = 100$ and $B_{pho} = 25$. H_0 is the initial height of the thin liquid film.

In the presented study, the influence of two factors on the breakup behavior of the liquid film is investigated, namely, (i) the difference of the contact angles in the hydrophilic and hydrophobic areas $\Delta\theta$; (ii) the thickness of the liquid film H_0 . Therefore, in the following, these two parameters are systematically changed.

In Fig. 9.6, I display the evolution of liquid films with varying θ_{pho} . From (a) to (d), as θ_{pho} increases, the thin-film retracts more and more quickly. In (a) θ_{pho} or $\Delta\theta$ is not high enough to make the thin-film breakup, while in (b)-(c), the thin-film breaks up and generates a satellite droplet on the

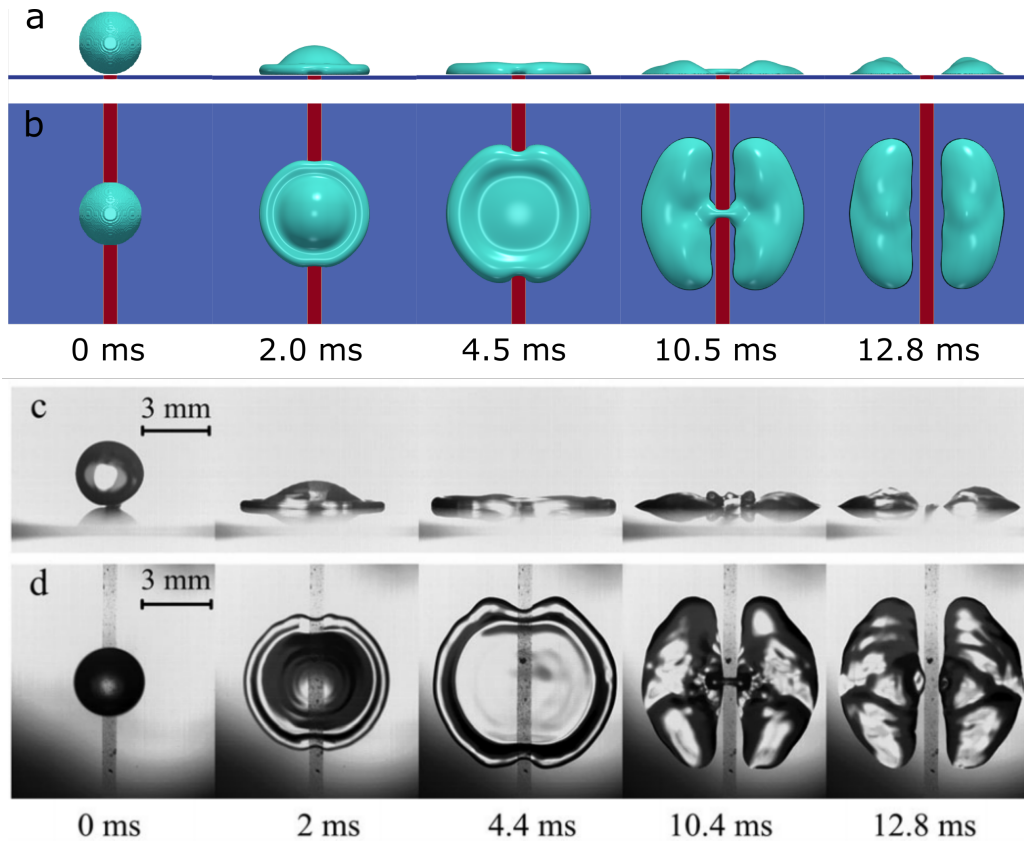


Figure 9.4.: Impinging processes of droplets with diameter 3.1 mm on the superhydrophobic stripe coated hydrophilic surface. The impact velocity is $u=0.97$ m/s. The contact angles on hydrophilic and hydrophobic areas are $\theta_{phi} = 50^\circ$, $\theta_{pho} = 165^\circ$, respectively. (a) and (b) Side and top views for present simulation. (c) and (d) Side and top views for the experiment from [208].

hydrophobic area. Interestingly, larger $\theta_{pho} \Delta\theta$ leads to a larger satellite droplet and it is observed in (d) that the satellite droplet even rebounds from the substrate eventually.

To have better control of the generation of the satellite droplet, I turn to the four-lattice-patterned surface. In Fig. 9.7(a)-(d), I also change θ_{pho} from 60° to 160° , similar to the setups of the two-lattice-patterned surface discussed above. In (a), low value of θ_{pho} cannot generate the satellite droplet, whereas in (b)-(d), the high value of θ_{pho} facilitates the formation of the satellite droplet and in (d) it even causes the rebound of the satellite droplet. What is different from the situation of the two-lattice-patterned surface is that the size of the satellite droplet is independent of θ_{pho} . This finding reveals that the size of the satellite droplet is controllable through an elaborate design of the lattice pattern.

I now take a close look at the detailed dynamic process of the dewetting processes. Fig. 9.8(a) and (b) present the relative width W/W_0 of the liquid bridges caused by the dewetting on the hydrophobic area of the two-lattice-patterned and the two-lattice-patterned surfaces, respectively. The insets show how the width W of the liquid bridge is measured, and W_0 is the initial width of the liquid bridge

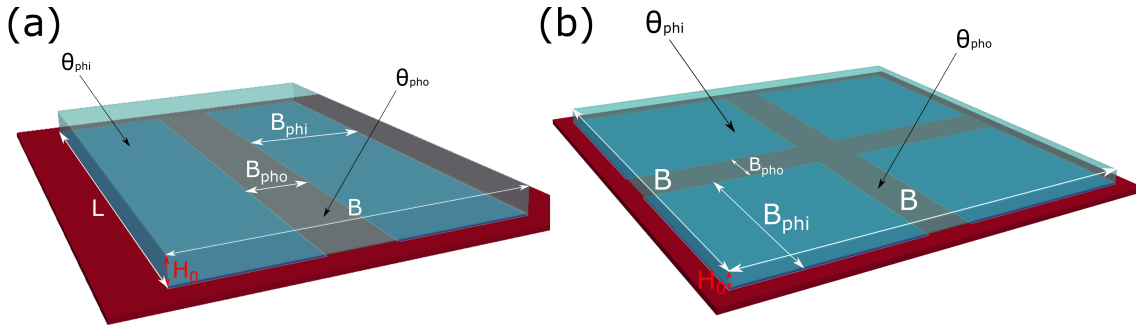


Figure 9.5.: Simulation parameters of the liquid film on chemically patterned surfaces. (a) Two-lattice-patterned substrate. (b) Four-lattice-patterned substrate. θ_{phi} represents the contact angle of the hydrophilic area (blue), and it keeps constant $\theta_{phi} = 20^\circ$. θ_{pho} denotes the contact angle of the hydrophobic area (red) and it varies from 60° to 160° . H_0 represents the initial height of the liquid film. L denotes the length of the hydrophilic pattern on the two-lattice-patterned surface. B represents the whole width of the two neighboring hydrophilic lattices and the hydrophobic area between them, i.e., $B = 2B_{phi} + B_{pho}$.

in the direction of the measurement (dashed lines in the insets). The colored solid lines represent the time evolution of W/W_0 for different setups of θ_{pho} . It is observed that these lines firstly decline quickly and then they are convergent to certain values except for the green lines ($\theta_{pho} = 160^\circ$), which rapidly go to zero, corresponding to the situation of the rebound of the satellite droplet. The red lines ($\theta_{pho} = 60^\circ$) are convergent to a high value of W/W_0 , since the thin-films don't break up and form a stable single large droplet (see Fig. 9.6(a)(iv) and Fig. 9.7(a)(iv)). The black and blue lines in Fig. 9.8(a) ($\theta_{pho} = 90^\circ, \theta_{pho} = 120^\circ$) slowly approach zero is because the generated satellite droplets are so small that the base radii of them are hard to be captured on the hydrophobic area.

Finally, the influence of the initial height of the thin-film on the breakup behavior is investigated. In Fig. 9.9(a)-(d), I vary the initial height H_0 from 10 to 20, 30, and 40. It is found that the low value of the initial height H_0 ($H_0=10, 20$) result in the breakup while high values ($H_0=30, 40$) lead to stable single droplets. Moreover, the thin-films with lower heights tend to generate a satellite droplet during the breakups. These findings can be confirmed by the diagrams (e) and (f), where I plot the time evolutions for the relative width W/W_0 and the relative height H/H_0 under different initial heights H_0 . The red and blue lines in (e) ($H_0=10, 20$) rapidly go down to zero, showing that the dewetting causes the breakups. The breakups lead to the generation and rebound of the satellite droplets and the tiny satellite droplets will disappear because of the curvature effect in the PF model. This explains why the red and blue lines in (f) increase sharply and then go down promptly. The black and green lines ($H_0=30, 40$) in (e) and (f) both are convergent to stable values, showing that stable single droplets come into being.

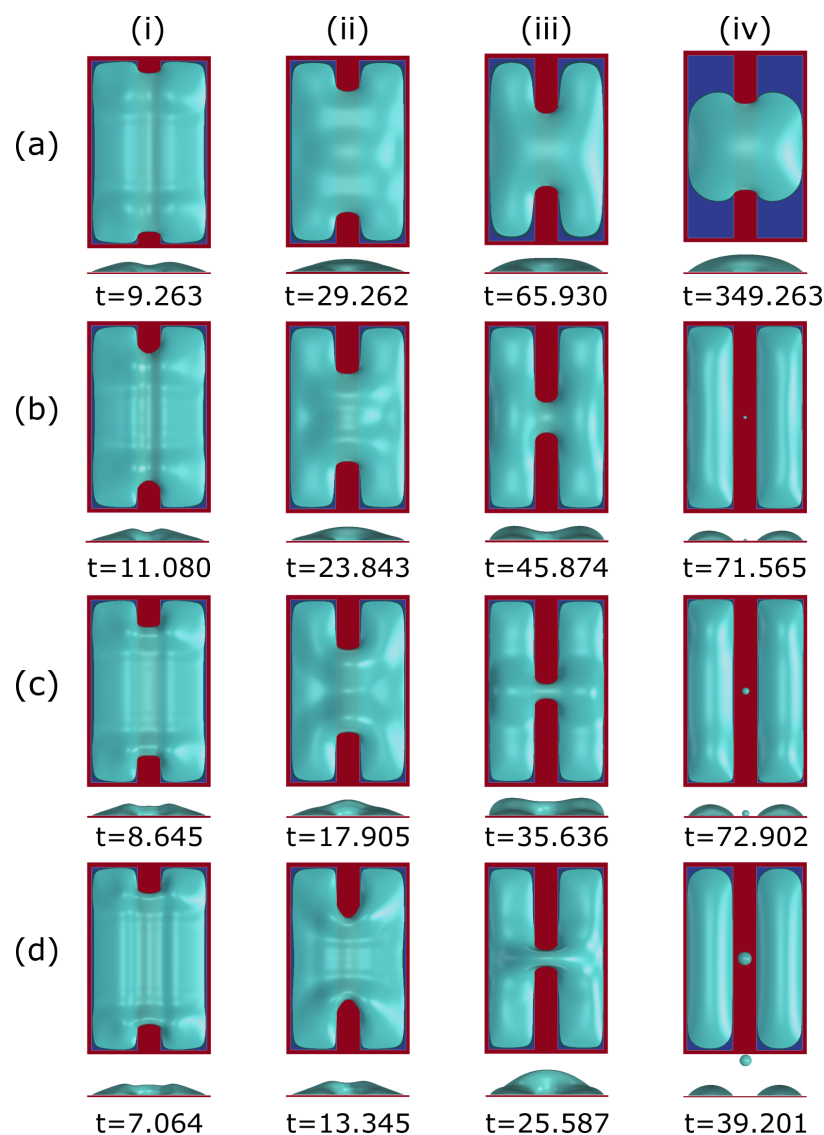


Figure 9.6.: Simulation results for the evolution of the liquid film with $H_0=10$ placed on the stripe patterned substrate. From (a) to (d) the hydrophobic contact angles θ_{pho} are 60° , 90° , 120° , and 160° respectively, while $\theta_{phi} = 20^\circ$ keeps constant [209].

9.5. Summary

In this chapter, the CHNS model is firstly validated to simulate the fast spreading dynamics of droplets on homogeneous substrates influenced by the wettability, the droplet impact process on a flat superhydrophobic substrate with point-like superhydrophobic macrot textures, and the droplet splitting process on a superhydrophobic stripe coated hydrophilic surface. PF simulations show excellent agreements with the results from the literature. After the validations, the model was applied to analyze the thin-film dewetting process on chemically patterned surfaces. Here, the two-lattice-patterned surface and four-lattice-patterned surface were considered. I systematically investigated the influence of the

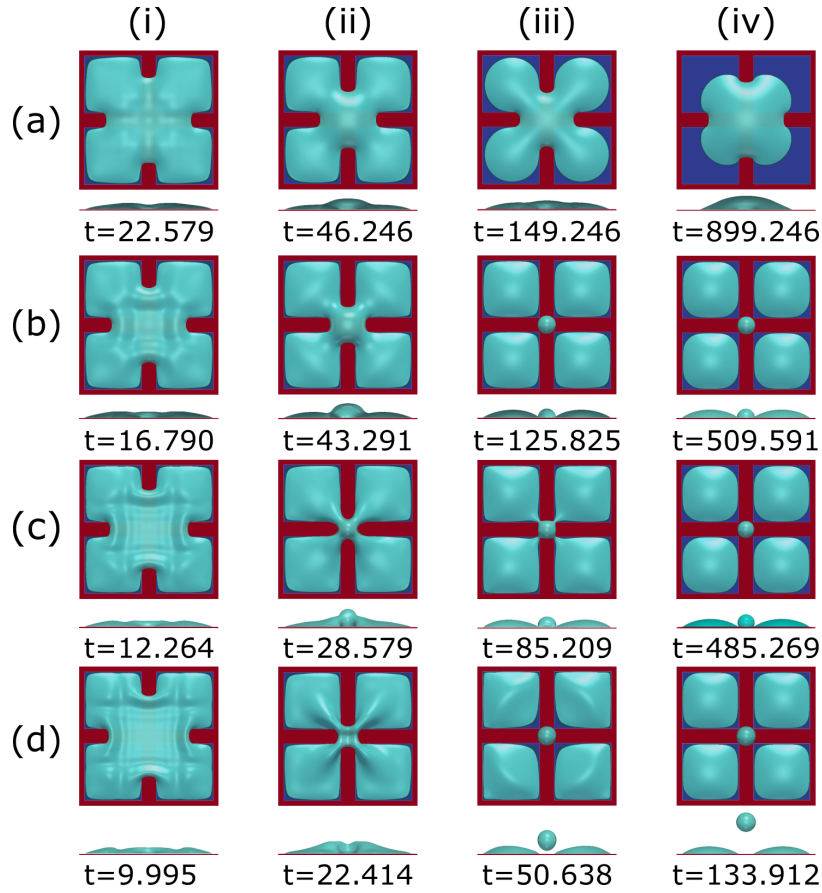


Figure 9.7.: Simulation results of liquid film with $H_0=10$ placed on the lattice patterned substrate. From (a) to (d) the hydrophobic contact angles θ_{rho} are 60° , 90° , 120° , and 160° respectively, while $\theta_{phi} = 20^\circ$ keeps constant [209].

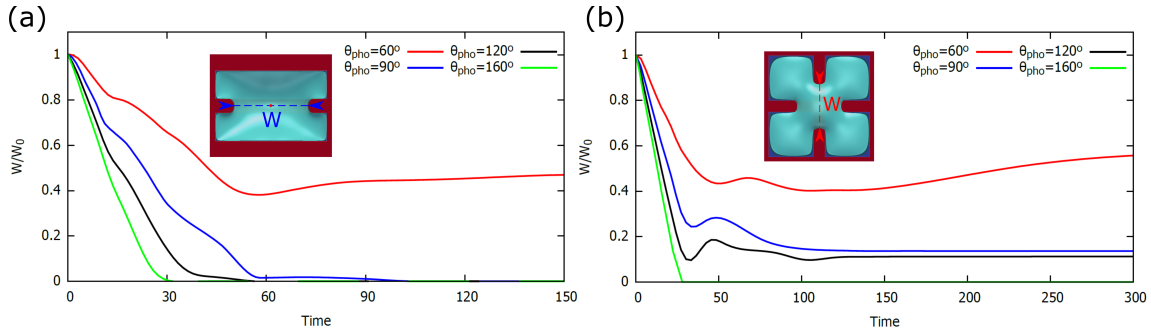


Figure 9.8.: The relative width W/W_0 of the liquid bridge as a function of time. W_0 is the initial width of the liquid film along the measure lines in the insets. (a) On the two-lattice-patterned substrate, $W_0 = L = 400$. (b) On the four-lattice-patterned substrate, $W_0 = B = 250$. The colored solid lines denote the simulations with different values of θ_{rho} . $\theta_{phi} = 20^\circ$ keeps constant for all simulations [209].

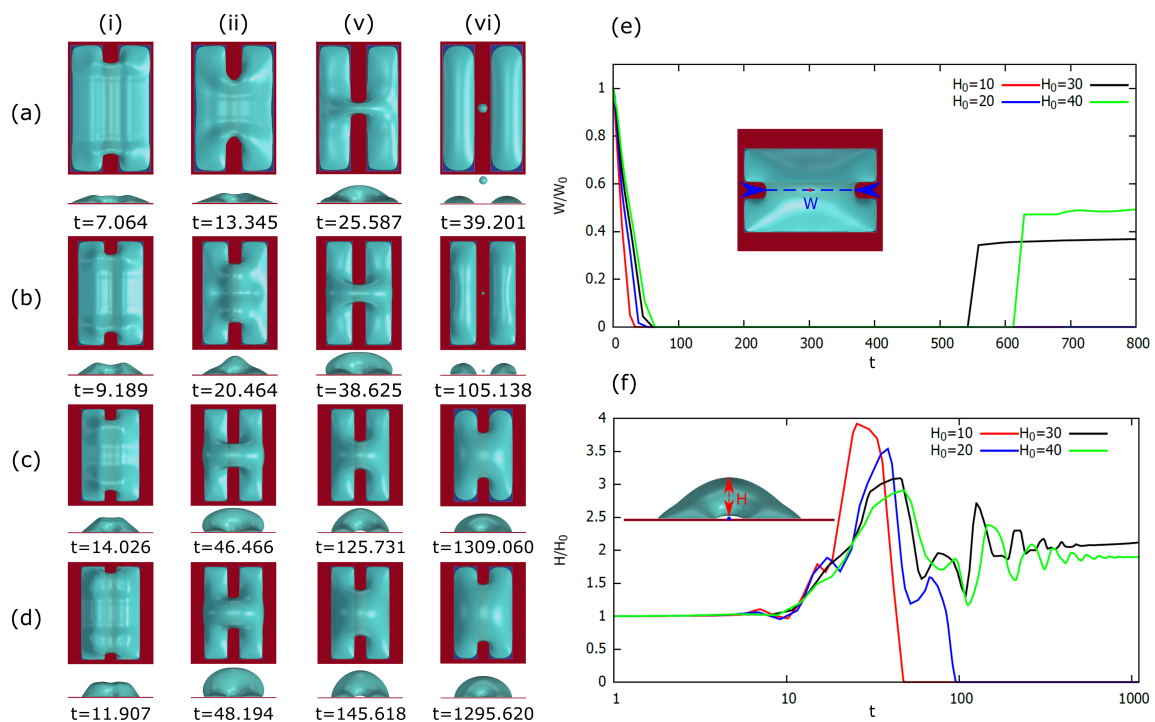


Figure 9.9.: (a)- (d) Simulation results for the evolution of the liquid film with $H_0=10, 20, 30, 40$, respectively. The liquid films are placed on the stripe patterned substrate with $\theta_{phi} = 60^\circ$ and $\theta_{pho} = 160^\circ$. The relative width W/W_0 and relative height H/H_0 of the liquid bridge as functions of time are shown in (e) and (f), respectively. The colored solid lines denote the simulations with different initial heights H_0 . The insets illustrate how the width and height are measured [209].

contact angles on the hydrophobic area θ_{pho} , the initial height H_0 of the thin-film to the breakup behaviors. Interestingly, I have also found the formation of the satellite droplet caused by the thin-film breakups, which is closely related to θ_{pho} and H_0 , and the pattern distribution. However, due to the limit of contents in the present thesis, some important parameters such as the pattern size and distance, the physical properties including viscosity, surface tension, etc, have not been examined. A thorough study of these parameters is essential. Another direction that is worth exploring is the introduction of complex chemical patterns to have better control of the satellite droplets formation, which has potential applications in the fields of microfluidics, electronic devices, and smart printing.

Part V.

Conclusion and outlook

10. Conclusion and outlook

10.1. Conclusion and remarks

In this dissertation, droplet wetting behaviors on chemically and mechanically structured surfaces have been addressed by using two types of phase-field models, namely the AC model and the CH model. For the investigation of equilibrium or quasi-equilibrium problems, the AC model was utilized. While for the study of droplet dynamic problems the CH model was adopted. Both of the phase-field models have been immensely validated against the results from the literature, showing the strong robustness of the phase-field models.

For the equilibrium or quasi-equilibrium problems, the morphological transition of a single droplet on chemically striped substrates was first contemplated. It is found that the droplet shapes and the number of equilibrium shapes both are enormously influenced by the scaled stripe width and droplet positions. The validity of a reported analytical model [170] describing the functional relationship between the droplet aspect ratio and the directional contact angles has been extended to the situation where the droplet size is comparable to the stripe width. Moreover, it was proved that different droplet shapes can be obtained via different moving paths, showing a typical hysteresis phenomenon. The findings may have potential application in the fields of inkjet printing, biologics, and microfluidics, where a fine control of droplet shape is necessary.

Given the existence of multiple equilibrium shapes for a certain-sized droplet on chemically patterned surfaces, then here comes an open question: Can we theoretically predict different equilibrium shapes of droplets on chemically patterned substrates? To answer this question, a concise mathematical-physical model was established to describe the droplet configurations on three chemically patterned surfaces. In this analytical model, it is assumed that at equilibrium, the droplet baseline forms an ellipse with semi-axes a and b and the liquid-gas interface is described with circular arcs. Based on this geometric assumption, it can be proved that the surface energy E of the droplet on a certain position has only two degrees of freedom, i.e. $E = E(a, b)$. By minimizing the surface energy in terms of a and b , the different equilibrium shapes of droplets can be predicted via the local energy minima in the energy map $E(a, b)$. The proposed energy map method was corroborated by the phase-field simulations.

Thereafter, the energy map method was further generalized to scrutinize droplets on chemically patterned surfaces with various characteristic lengths, contact angles, and ratios of the hydrophilic area to the hydrophobic one. Additionally, a modified Cassie-Baxter model was proposed to predict the equilibrium droplet shapes which are not necessarily in the shape of a spherical cap. The generalized

energy map method has been confirmed by the phase-field simulations. The proposed energy map method and modified Cassie-Baxter model are able to address the anisotropic wetting problems where the droplet size is comparable to the surface heterogeneity, which is beyond the limit of the classic Cassie-Baxter model [37, 38]. Moreover, the energy landscape model and the modified Cassie-Baxter model can serve as a guidance table for experiments and simulations without blind attempts.

The energy map method together with the phase-field model was further applied to quantitatively analyze the droplet anisotropic wetting morphologies either in a static state or in a quasi-static evaporation process, which shows excellent consistency with real experiments. Interestingly, non-rotationally symmetric droplet shapes on the regularly chemical-patterned surfaces have been found both in phase-field simulations and experiments. The non-rotationally symmetric geometry is, however, beyond the limit of the current energy map method. Nevertheless, the proposed energy map method and the finding of the equilibrated non-rotationally symmetric droplet shapes on regular patterns provide essential guidelines for a better understanding of the anisotropic wetting morphologies of droplets.

The static state and quasi-static movement of multiphase droplets on chemically heterogeneous surfaces have been simulated by the multi-phase AC model. For the liquid-liquid confinement on a ring-patterned substrate, several combinations for the values of the interfacial tensions were set to explore the influence of Gibbs absorption on the interfacial tensions. By comparing the simulation results with the experimental observations, the interfacial tensions can be estimated, which explains the liquid lens phenomenon that a droplet of 1-nonanol deposited on the surface of water formed a droplet instead of spreading over the water surface.

After the study of droplet wetting on chemically patterned substrates, the topology of the substrate was also concerned. Droplet wetting behaviors in a pore structure were theoretically and numerically investigated. Considering the influence of droplet sizes, contact angles, and open angles of the substrates, a criterion for droplet permeation in the single pore structure was theoretically predicted which agrees excellently with the simulations via the AC model. It was found that for a certain-sized droplet, the critical contact angle increases with the open angle. Furthermore, for a certain open angle, the critical contact angle increases with decreasing the droplet size, and smaller droplets tend to be more sensitive to the change of the open angle. The findings demonstrated that the curvature difference and the wettability of the substrate determine the droplet penetration behavior, controlled by the Young-Laplace law and the Young's law, respectively. The observations have great significance for the applications including the design of microfluidics, filter system for preventing droplets, drainage system, oil recovery system, and so on.

To address the droplet dynamics on solid substrates, CHNS model was validated against the data from the literature. Three typical cases including the fast spreading of a droplet, droplet impacting on mechanically heterogeneous substrate, droplet splitting on the chemically patterned substrate were presented, where excellent agreements with results from literature were achieved. After the validation, the CHNS model was utilized to analyze the thin liquid film dewetting process on chemically patterned surfaces. It was observed that the controllable satellite droplet formation on chemically

patterned surfaces can be achieved by tuning the contact angles, liquid volume, pattern distribution, and so on. The strategy and findings may have potential applications in the fields of microfluidics, electronic devices, and smart printing.

10.2. Future directions

The present dissertation mainly investigated the droplets on regularly chemically patterned substrates and in the future, some more complicated patterns which are specifically designed [210] or irregularly distributed can be contemplated in the numerical model and the analytical models. Moreover, for the investigation of mechanically heterogeneous surfaces, only a single 2D pore structure was considered. In the next steps, 3D pore structures and other topologically structured substrates should be studied. The interaction of droplets with rough surfaces [211] and the design of functional surfaces with the desired hydrophilicity [212] should be further explored. The mechanism for Cassie-Wenzel transition on these functional surfaces should be revealed [213], which is of great significance for the droplet manipulation technique applied in a wide range of areas.

Since the CHNS model has been successfully validated to simulate droplet dynamics on heterogeneous substrates, it can be applied to address the droplet impacting and spreading process on different substrates. The contact time of impacting droplets on the surface [214], the spreading velocity [94], the breakup [215], and coalescence [216, 217, 218] of droplets on different heterogeneous substrates can be further investigated.

Note that the evaporation and condensation studied in the present thesis were in quasi-equilibrium states and the AC model with a constant driving force was applied to model the phase change. However, to accurately describe the phase change where both diffusion and convection are involved, the CHNS model with well defined free energy function should be established, which can be used to explore interesting phenomena such as the Leidenfrost effect [219, 220, 221], evaporation induced attraction-repulsion of droplets [222], and evaporation induced chasing of droplets [222, 223], etc.

The multi-phase droplets wetting problems were modeled by the multi-phase AC method, and the studied droplets were in static or quasi-static states with constant interfacial tensions. However, to model the fast movement of the multi-phase droplets on substrates, NS equations should be coupled in the original model. If a more complicated situation e.g. the non-equilibrium physicochemical hydrodynamics involved multi-phase system is considered, the multi-phase CHNS model with wetting boundary conditions should be developed. Typical phenomena of this kind of system are the well-known “coffee ring” effect [224], Marangoni bursting [121, 122], and fingering instability [48] on substrates and others mentioned in chapters 1 and 2.

Part VI.

Appendices

A. Calculation of double-well function

The code for calculating the double-well function is presented as follows.

Listing A.1: $f_c.m$

```
1 clear all;
2 %for c=0.01:0.01:0.99
3 %f_c      = T*(c*log(c)+(1-c)*log(1-c))+chi*c*(1-c);
4 %f_c_prime = T*(log(c)-log(1-c))+chi*(1-2*c);
5 kappa = 2;
6 %kappa=eps*sigma
7 %chi=3.78
8 %T=1;
9 for T=0.5:0.05:1.5
10 c_e1=fsolve(@(x) T*(log(x)-log(1-x))+3.78*(1-2*x), 0.02);
11 c_e2=fsolve(@(x) T*(log(x)-log(1-x))+3.78*(1-2*x), 0.97);
12 f_c_e1=T*(c_e1*log(c_e1)+(1-c_e1)*log(1-c_e1))+ 3.78*c_e1*(1-c_e1);
13 sigma=quad(@(x) 2*sqrt(kappa*(T*(x*log(x)+(1-x)*log(1-x))+1*3.78*x
    *(1-x)-f_c_e1)), c_e1, c_e2);
14 fprintf("%f %f %f %f %f\n", T, sigma, c_e1, c_e2, f_c_e1);
15 endfor
```


B. Prediction of droplet shapes

In this section, some more details for the equilibrium droplet shapes on striped and chessboard-patterned surfaces under the influence of three factors: (a) droplet sizes, (b) contact angles, and (c) the ratios of the hydrophilic area to the hydrophobic one are discussed. In sections B. 1-B. 3, the results of the energy landscape methods and the PF simulations for droplets on these two patterned surfaces are illustrated. In section B. 4, the code for the energy landscape model is provided. The whole section was published in the supplemental information of Ref. [184].

B.1. Droplet size

In this part, the contact angles on the hydrophilic and hydrophobic areas of the striped and chessboard-patterned surfaces are set as 60° and 120° , respectively, i.e. $\theta_1 = 60^\circ$, $\theta_2 = 120^\circ$. The characteristic length is a constant value $L = 40$. With varying the droplet size R/L , I obtain the corresponding energy maps and simulation results.

Figure B.1 presents the results from the analytical model and the PF simulation for droplets with different sizes on the striped patterned surface. From (I) to (III), the ratio R/L varies from 1 to 4.5. In each panel, (A) and (B) depict the surface energy landscapes in terms of a and b for droplets with base centers on position 1 and 2, respectively. The energy minima in the deep blue regions are indicated by different numbers and correspond to the snapshots of the PF simulation results labeled with the same number in (C). The blue and red stripes in the snapshots depict the hydrophilic and hydrophobic areas with width $L_{wet} = L_{dry} = L/2 = 20$. The red dashed ellipses with semi-axes a, b in (I)(C) represent the analytical results, which are obtained from the coordinates of the energy minima in the energy landscapes. It is observed that the analytical predictions of the energy landscapes have a good agreement with the simulation results. Moreover, as the ratio R/L increases from 1 to 4.5, the number of equilibrated droplets rises from 3 to 5.

Next, I turn to scrutinize the equilibrium shapes of droplets on a more complex pattern, the chessboard pattern. The surface energy landscapes and the corresponding snapshots of the equilibrated droplets from the PF simulations are illustrated in Figure B.2 and Figure B.3, respectively. In this scenario, I vary the droplet size from $R/L = 0.75$ to $R/L = 0.25$. The hydrophobic/hydrophilic square lattices (red/blue) have a width of $L_{dry} = L_{wet} = L/2 = 20$. Because of the high symmetry of the chessboard pattern, the elliptical base line of droplets may have a symmetric-axis which is rotated counterclockwise by 45° with respect to the horizontal direction, as sketched by the dot dashed line in Figure 5.10(c). The corresponding surface energy landscapes are calculated in a rotated system with $\delta'_1 = (\delta_1 + \delta_2)/\sqrt{2}$ and $\delta'_2 = (\delta_1 - \delta_2)/\sqrt{2}$ and the results are shown in Figure B.2(B), (D), and (E)

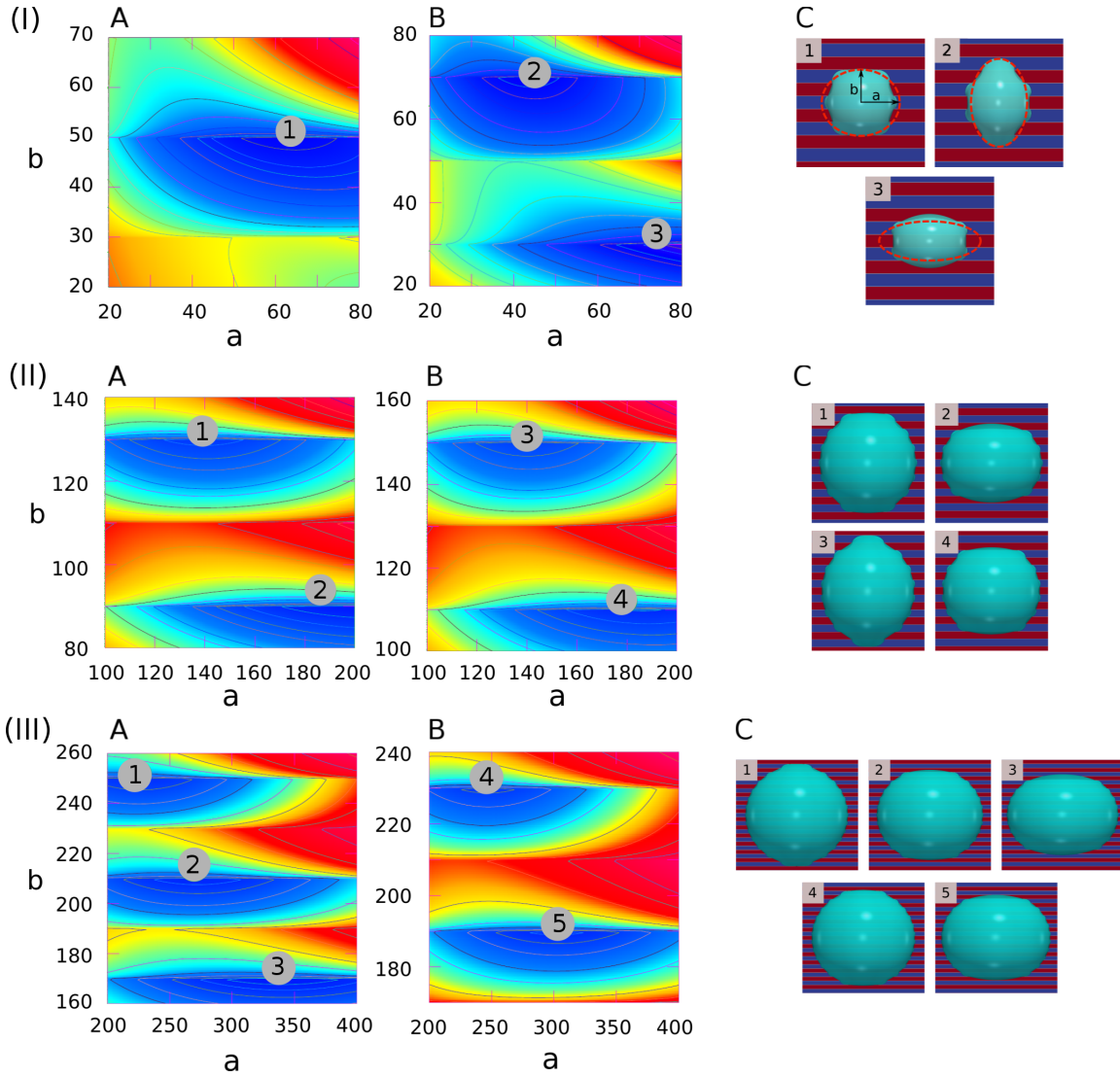


Figure B.1.: Surface energy landscapes for droplets with different sizes on the chemically striped patterned surfaces and the snapshots of the equilibrated droplets via PF simulations. (I) $R/L = 1$, (II) $R/L = 2.5$, (III) $R/L = 4.5$, The chemical heterogeneities are described by $f_1(r_b, \varphi)$ in Eq. 5.10 with the following parameters: $\gamma_m = 0$, $\gamma_0 = 0.5$, $\xi = 100$, $L = 40$, $\lambda = 0$. At equilibrium, the droplet base center stays either on $P_1 (i = 1)$ (the center of the hydrophilic stripes, in blue color) or $P_2 (i = 0)$ (the center of the hydrophobic stripes, in red color). The energy landscapes are accordingly calculated by using different values of i . The contour lines indicate the energy levels (red for high values and blue for low values). The energy minima are highlighted by different numbers in (A) and (B) in each panel, corresponding to the snapshots labeled with the same number in (C). The red dashed ellipses with semi-axes a, b in (I)(C) show the analytical results from the energy landscape method. Reproduced with permission from Ref. [183]. Copyright 2019 American Physical Society.

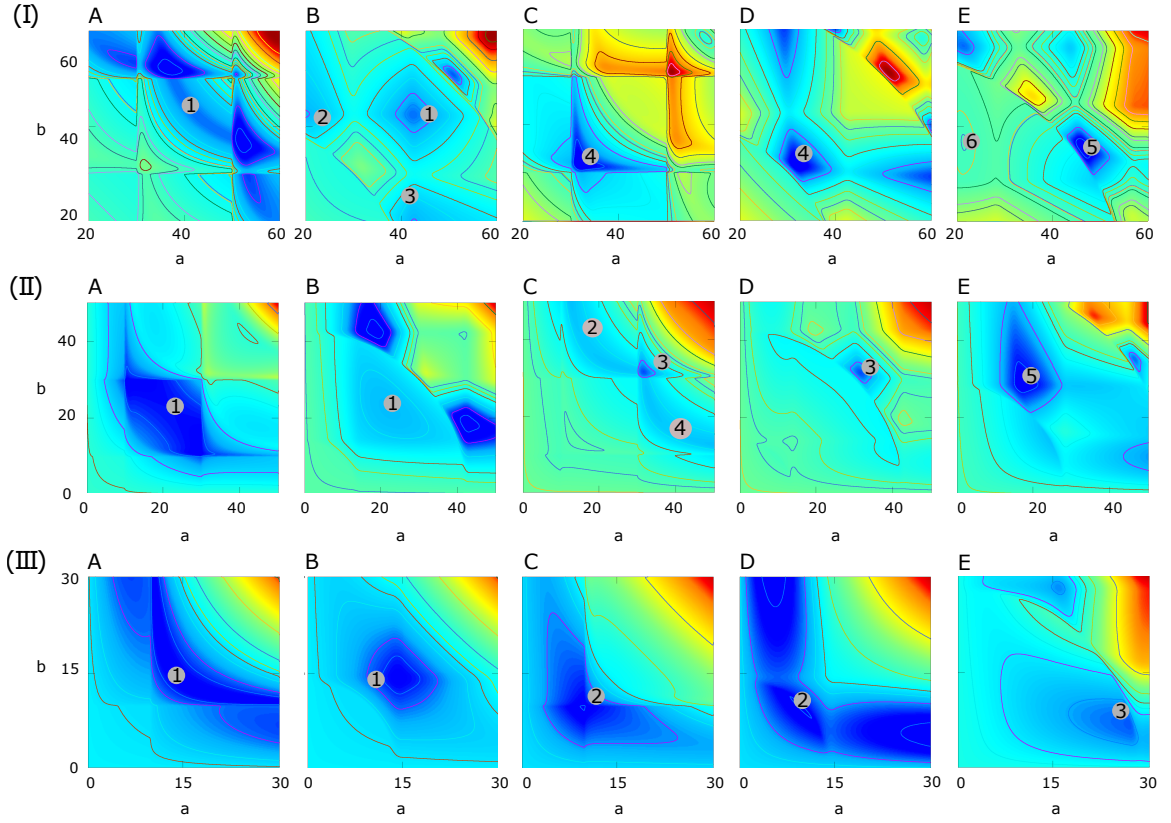


Figure B.2.: Surface energy landscapes for droplets with different sizes on the chessboard-patterned surfaces and the snapshots of the equilibrated droplets through PF simulations (I) $R/L = 0.75$, (II) $R/L = 0.5$, (III) $R/L = 0.25$. The chemical heterogeneities are described by $f_3(r, \varphi)$ in Eq. 5.10 with $\gamma_m = 0$, $\gamma_0 = 0.5$, $\xi = 100$, $L = 40$, $\lambda = 0$. The energy minima are illustrated by different numbers inside the gray circles. The equilibrated states at these energy minima are sequentially shown in Figure B.3(I)-(III). The surface energy landscapes for (A)&(B), (C)&(D), and (E) correspond to droplets with base center positions on P_1 , P_2 , and P_3 , respectively. In each panel, (A) and (C) describe the situation where a and b are in the horizontal and vertical directions, respectively. While (B), (D), and (E) depict a system which is rotated counterclockwise by 45° . In the rotated system, δ_1 and δ_2 in $f_3(r, \varphi)$ are substituted by δ'_1 and δ'_2 , respectively, with $\delta'_1 = (\delta_1 + \delta_2)/\sqrt{2}$ and $\delta'_2 = (\delta_1 - \delta_2)/\sqrt{2}$.

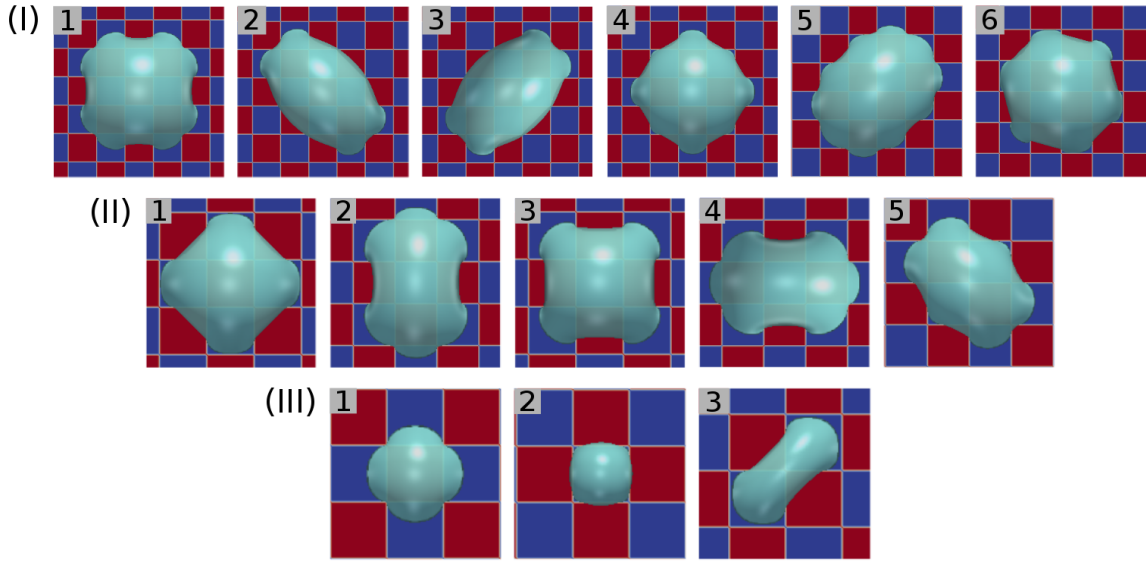


Figure B.3.: Snapshots for the equilibrated droplets with different sizes on the chessboard patterned surface via PF simulations (blue: hydrophilic, red: hydrophobic) (I) $R/L = 0.75$, (II) $R/L = 0.5$, (III) $R/L = 0.25$.

in each panel. Typical equilibrated droplet morphologies for the energy minima in Figure B.2(I) (B) are displayed in Figure B.3(I) (2) and (3). It is noteworthy that in Figure B.2 (I) (C) and (D), which correspond to the non-rotated and rotated systems, respectively, the values of a and b are the same at the minimal energy states. These two energy minima actually predict an identical equilibrated shape, as shown in Figure B.3(I) (4). The similar findings are observed in Figure B.3(II) (1) and (3) as well as in Figure B.3(III) (1) and (2). Similar to the striped and chocolate patterned surfaces, the increase in the droplet size leads to more equilibrium shapes.

B.2. Contact angle

In this section, I investigate the equilibrated droplet shapes affected by the contact angles on the hydrophilic (θ_1) and hydrophobic (θ_2) areas. The chosen parameters for θ_1 and θ_2 are shown in Table 5.1. The characteristic length is constant $L = 40$. Droplets with the same size ($R/L = 1$) on the two chemically patterned surfaces are considered.

As three typical examples, Figure B.4(I), (II), and (III) display the surface energy landscapes and the snapshots of the simulated equilibrium droplets on the striped-patterned surface for contact angle pairs $(30^\circ, 90^\circ)$, $(90^\circ, 150^\circ)$, $(120^\circ, 180^\circ)$, respectively. From (I) to (III) as $\bar{\theta}$ increases, the equilibrated morphologies tend to approach a spherical shape. Moreover, the number of the equilibrium states in (II) and (III) is less than that in (I).

I further turn to the chessboard pattern. Figure B.5(I), (II), and (III) picture the surface energy landscapes for droplets on the chessboard patterned surfaces for contact angles $(30^\circ, 90^\circ)$, $(90^\circ, 150^\circ)$, and $(120^\circ, 180^\circ)$, respectively. In each panel, (A)&(B), (C)&(D), and (E) are for droplets with base

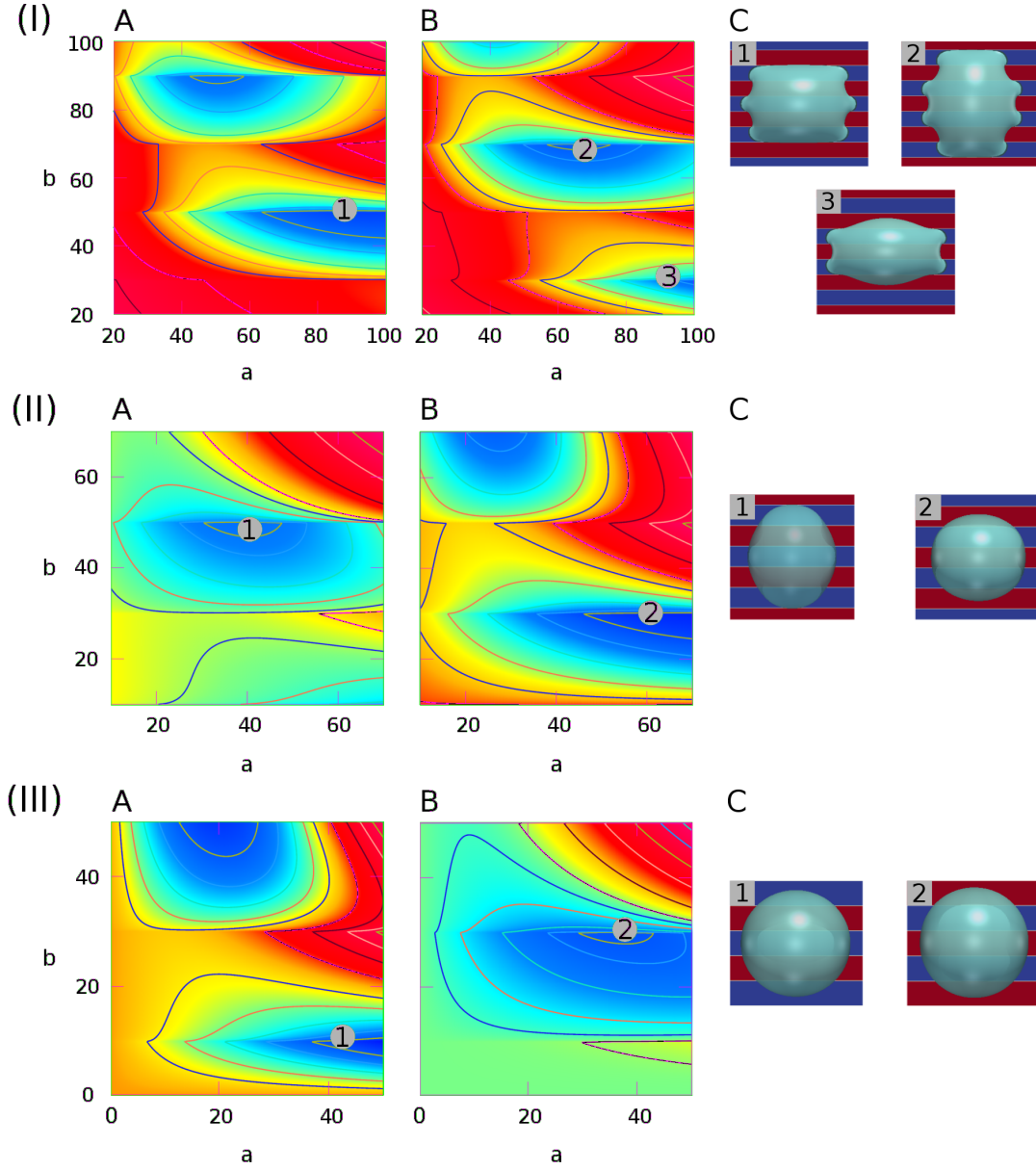


Figure B.4.: Surface energy landscapes for droplets on the striped patterned surfaces with different contact angles and the corresponding snapshots of the equilibrated droplets from the PF simulations. (I) $\theta_1 = 30^\circ, \theta_2 = 90^\circ$, (II) $\theta_1 = 90^\circ, \theta_2 = 150^\circ$, (III) $\theta_1 = 120^\circ, \theta_2 = 180^\circ$. The chemical heterogeneities are described by $f_1(r, \varphi)$ in Eq. 5.10 with $\xi = 100, L = 40, \lambda = 0$. The parameters γ_m, γ_0 are adjusted according to the contact angle pairs. The energy minima are indicated by different numbers, corresponding to the snapshots in (C) labeled with the same number. The surface energy landscapes for (A) and (B) delineate the situation where the droplet base center positions are on P_1 and P_2 , respectively. (C) Snapshots of the equilibrated droplets through PF simulations (blue: hydrophilic, red: hydrophobic).

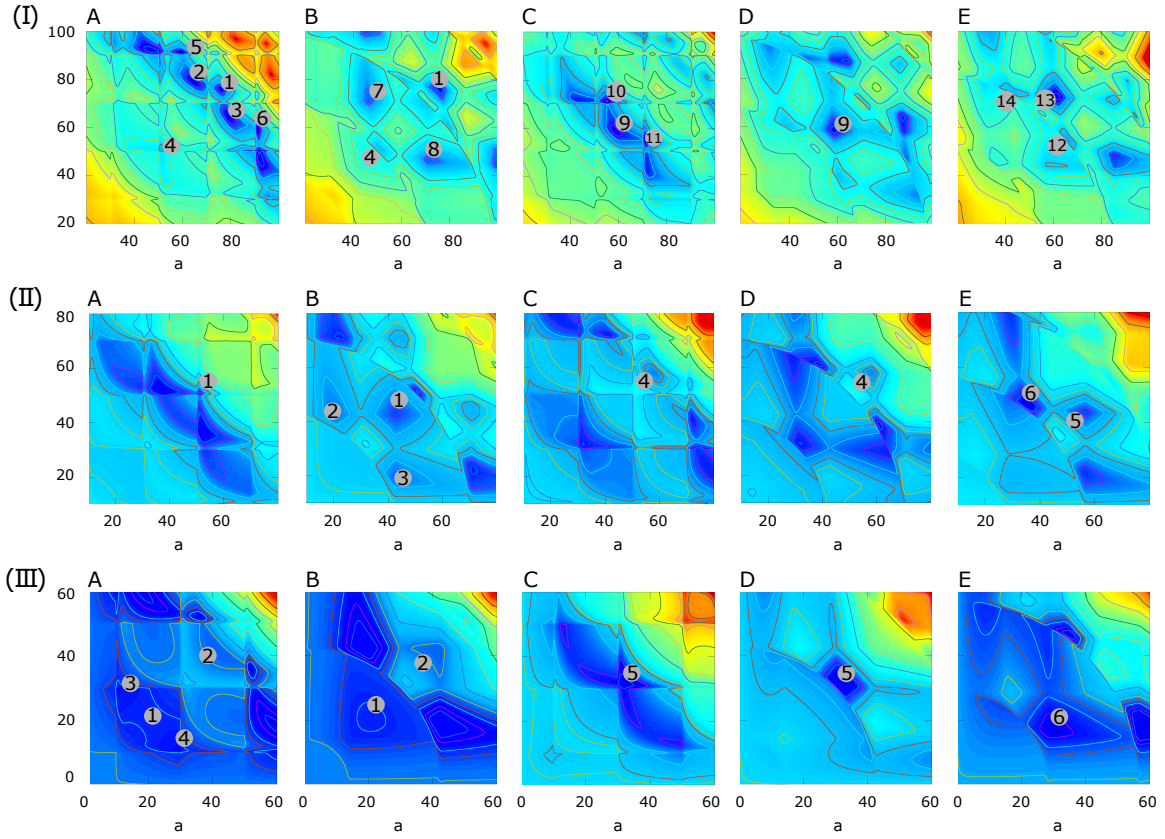


Figure B.5.: Surface energy landscapes for droplet on the chessboard-patterned surfaces with different contact angles and the corresponding snapshots of the equilibrated droplets through PF simulations (I) $\theta_1 = 30^\circ, \theta_2 = 90^\circ$, (II) $\theta_1 = 90^\circ, \theta_2 = 150^\circ$, (III) $\theta_1 = 120^\circ, \theta_2 = 180^\circ$. The chemical heterogeneities are described by $f_3(r_b, \varphi)$ in Eq. 5.10 with $\xi = 100, L = 40, \lambda = 0$. The parameters γ_m, γ_0 are modified according to the contact angle pairs. The energy minima are indicated by different numbers, corresponding to the snapshots in Figure B.6(I)-(III) labeled with the same number. The surface energy landscapes for (A)&(B), (C)&(D), and (E) correspond to the droplet base center positions on P_1, P_2 , and P_3 , respectively. (A) and (C) describe the situation where a and b are in the horizontal and vertical directions, respectively, while (B), (D), and (E) depict a system which is rotated counterclockwise by 45° . In the rotated system, δ_1 and δ_2 in $f_3(r, \varphi)$ are substituted by δ'_1 and δ'_2 , respectively, with $\delta'_1 = (\delta_1 + \delta_2)/\sqrt{2}$ and $\delta'_2 = (\delta_1 - \delta_2)/\sqrt{2}$.

centers on P_1, P_2 , and P_3 , respectively, among which (B), (D), and (E) are calculated in the rotated system. Figure B.6 (I), (II), and (III) shows the snapshots of the simulated equilibrium droplet shapes, corresponding to the sequentially indicated energy minima in Figure B.5 (I), (II), and (III), respectively. Since the density of the hydrophilic/hydrophobic lines for the chessboard patterned surfaces is higher than that of the striped and chocolate patterned surfaces, the energy landscapes become much more complex, which causes a substantial increase in the number of the equilibrated droplet shapes. The

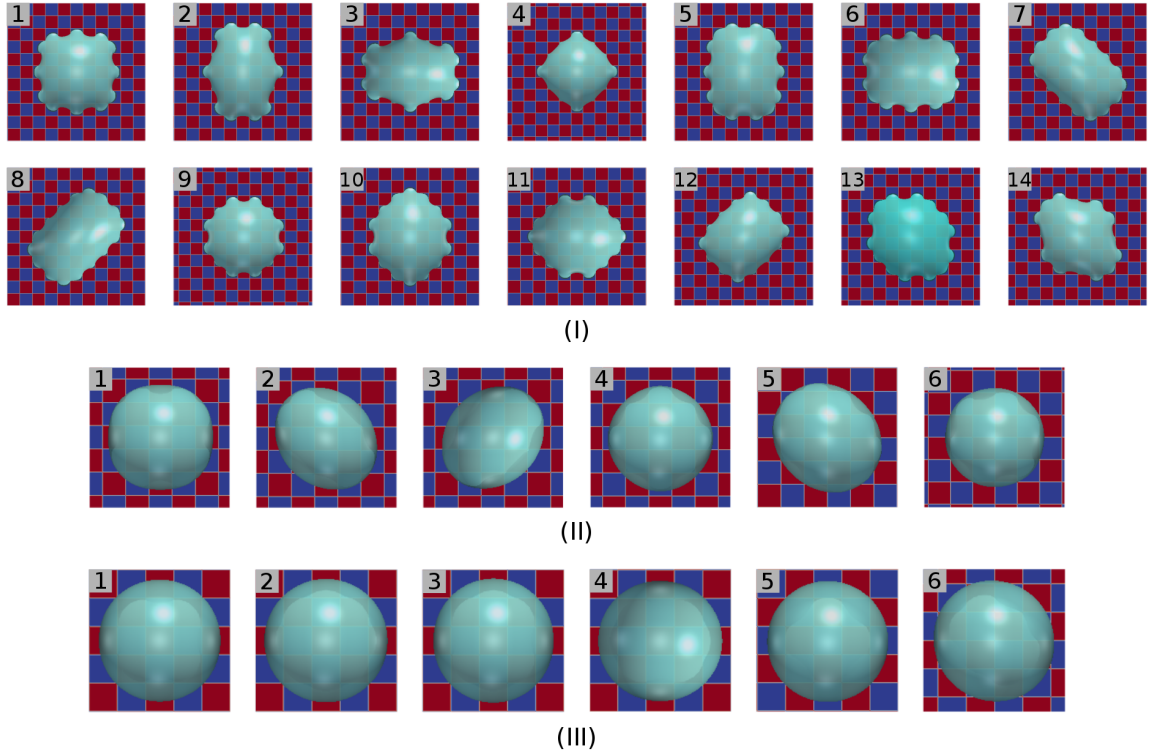


Figure B.6.: Snapshots of the equilibrated droplets on the chessboard patterned surfaces through PF simulations (blue: hydrophilic, red: hydrophobic) (I) $\theta_1 = 30^\circ, \theta_2 = 90^\circ$, (II) $\theta_1 = 90^\circ, \theta_2 = 150^\circ$, (III) $\theta_1 = 120^\circ, \theta_2 = 180^\circ$.

tendency that the evolution of the droplet morphologies towards a spherical shape with an increase in the average contact angle is also observed in this case.

B.3. The ratio of the hydrophilic area to the hydrophobic area

The average contact angle $\bar{\theta}$ can also be adjusted by tuning the area ratio of the hydrophilic area to the hydrophobic area while fixing the intrinsic contact angles on these two areas. Here, I set the contact angles on the hydrophilic and hydrophobic areas as $\theta_1 = 60^\circ$ and $\theta_2 = 120^\circ$, respectively.

The area ratio of the hydrophilic area to the hydrophobic area is characterized by the parameter ν . For the striped surfaces with $\nu = 1 : 1, 1 : 2, 1 : 3$, the surface energy landscapes and the snapshots of the equilibrated droplets from the PF simulations are shown in Figure B.7 (I), (II), and (III), respectively. A good agreement between the energy landscape model and the PF model is observed. As ν decreases, the equilibrated droplet becomes spherical successively and N decreases.

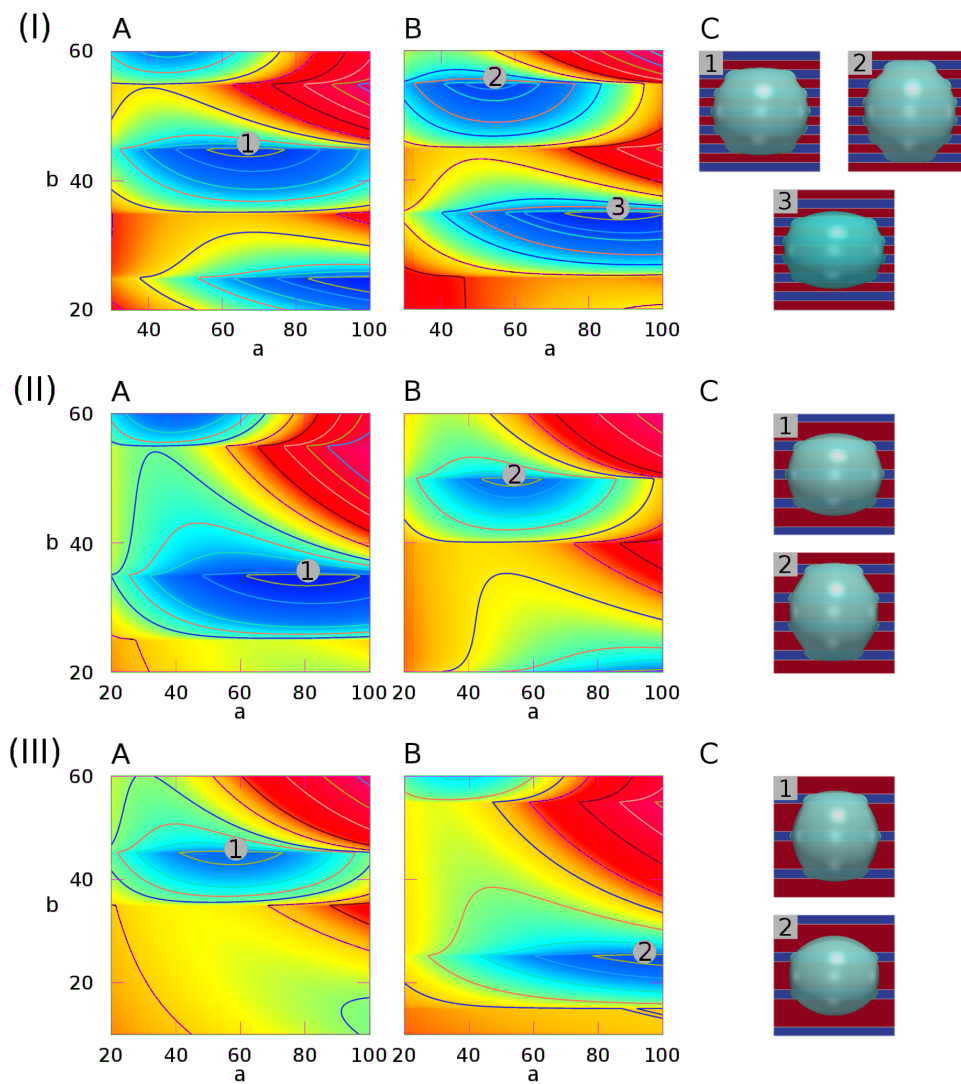


Figure B.7.: Surface energy landscapes for droplets on the striped surfaces with different area fractions of the hydrophilic and hydrophobic areas and the corresponding snapshots of equilibrated droplets through PF simulations. The ratios for (I) $\nu = 1 : 1$, (II) $\nu = 1 : 2$, (III) $\nu = 1 : 3$ correspond to three different setups with $(L = 20, \lambda = 0)$, $(L = 30, \lambda = \cos 60^\circ)$, $(L = 40, \lambda = \cos 45^\circ)$, respectively. The droplet size is set as $R = 40$. The chemical heterogeneities are described by $f_1(r, \varphi)$ in Eq (7) with $\gamma_m = 0$, $\gamma_0 = 05$, $\xi = 100$. The energy minima are marked by different numbers, corresponding to the snapshots in (C) labeled with the same number. The energy landscapes in (A) and (B) are for the situations where the droplet base center positions are on P_1 and P_2 , respectively. (C) Snapshots of the equilibrated droplets via simulations (blue: hydrophilic, red: hydrophobic).

B.4. Code for the energy landscape model

In this section, the code for calculating the surface energy landscapes is provided. For different patterned surfaces, the corresponding descriptions of f_k are used.

Listing B.1: surfaceEnergy.m [184]

```

1 function y=f(phi)
2 global prop;
3 %(gamma_m,gamma_0) -> (theta_1,theta_2), here (pi/3,2*pi/3)
4 gamma_m = 0;
5 gamma_0 = 0.5;
6 L       = 40; %L is the characteristic length
7
8
9 r = (prop.a_f*prop.b_f)/sqrt(prop.a_f**2*sin(phi)**2
10 +prop.b_f**2*cos(phi)**2); %r is here base radius.
11
12 %gab_difference is f_k=gamma_ls - gamma_gs (k=1,2,3)
13
14 %striped-pattern, here xi=100
15 gab_difference = gamma_m+gamma_0*tanh(100*
16 cos(2*pi*r*cos(phi)/L));
17
18 %chocolate-pattern
19 %gab_difference = gamma_m + gamma_0*tanh(100*(cos(2*pi*r*cos(phi)/L)
20 %*cos(2*pi*r*sin(phi)/L)
21 %-cos(2*pi*r*cos(phi)/L)
22 %-cos(2*pi*r*sin(phi)/L)));
23
24 %chessboard-pattern no rotation
25 %gab_difference = gamma_m+gamma_0*tanh(100*
26 %cos(2*pi*r*cos(phi)/L)*
27 %cos(2*pi*r*sin(phi)/L));
28
29 %chessboard-pattern rotation 45 deg
30 %r*cos(phi)->sqrt(0.5)*r*(sin(phi)+cos(phi))
31 %r*sin(phi)->sqrt(0.5)*r*(sin(phi)-cos(phi))
32 %gab_difference = gamma_m + gamma_0*tanh(100*
33 %cos(2*pi*sqrt(0.5)*r*(sin(phi)+cos(phi))/L)
34 %*cos(2*pi*sqrt(0.5)*r*(sin(phi)-cos(phi))/L));

```

```

35
36 %y is to calculate surface energy in liquid–solid contact area
37 %part (bottom).
38 y = 0.5*r**2* gab_difference;
39
40 endfunction
41
42 function z=cap(fai)
43 global prop;
44
45 r_numerator = (prop.a_f*prop.b_f);
46 r_denominator = sqrt(prop.a_f**2*sin(fai)**2+prop.b_f**2*cos(fai)
47 **2)
47 r = r_numerator / r_denominator; %r is base radius
48 r_c = (r**2+prop.h_f**2)/(2*prop.h_f); %r_c is curvature
49 radius.
49 beta = acos((r_c-prop.h_f)/r_c); %beta
50 z = r_c**2*(1-cos(beta)); %z is to calculate surface
51 energy in liquid–gas interface
51 %part (cap).
52
53 endfunction
54
55 R = 40;
56 V = (4/3)*pi*R**3;
57 L = 40;
58
59 global prop;
60 fp=fopen("sigma_r40.dat", 'w');
61
62 for a=0.5:1:120
63     for b=0.5:1:120
64         prop.a_f = a;
65         prop.b_f = b;
66         h = fsolve(@(x) (pi/6)*x*(3*a*b+x**2)-V,1);
67         prop.h_f = h;
68         surface_bottom = 4*quad("f", 0, pi/2); %surface energy in
69         A_ls

```

```
69     surface_ellipse_cap = 4*quad("cap", 0, pi/2); %surface energy
       in A_lg
70     sigma                = surface_bottom + surface_ellipse_cap; %
       total surface energy
71     fprintf(fp, '%f %f %f\n', a, b, sigma);
72     endfor
73     fprintf(fp, '\n');
74     endfor
75
76     fclose(fp);
```


C. Supplemental information to chapter 6

C.1. Discussion of the controlling parameters for chemical patterns

The chemical heterogeneities in the (x, y) -plane of the substrate surface are described by the following expression

$$\gamma_{ls} - \gamma_{gs} = \gamma_m + \gamma_0 \tanh \xi [\cos(\delta_1 - \lambda) \cos(\delta_2 - \lambda) - \chi(\cos \delta_1 + \cos \delta_2)]. \quad (\text{C.1})$$

I keep the liquid-gas surface tension γ_{lg} constant ($\gamma_{lg} = 1$ in dimensionless value). The parameters γ_m and γ_0 jointly determine the difference in the surface tension $\gamma_{ls} - \gamma_{gs}$ and thereby the static contact angles on the hydrophilic and hydrophobic areas. As shown in Fig. C.1C(a), I set three pairs of (γ_m, γ_0) to change the surface energy on hydrophilic and hydrophobic areas. For example, $(\gamma_m = 0.5, \gamma_0 = 0.5)$, $(\gamma_m = 0, \gamma_0 = 0.5)$, $(\gamma_m = 0, \gamma_0 = 1)$ correspond to $(\theta_{e,wet} = 0^\circ, \theta_{e,dry} = 90^\circ)$, $(\theta_{e,wet} = 60^\circ, \theta_{e,dry} = 120^\circ)$, $(\theta_{e,wet} = 0^\circ, \theta_{e,dry} = 180^\circ)$, respectively. The variables δ_1 and δ_2 are function arguments which are dependent on the coordinate (x, y) of droplet base center: $\delta_1 = (2\pi y + i\pi L)/L$, $\delta_2 = (2\pi x + j\pi L)/L$. The indexes i and j are used to control the offset of the pattern position. The length L is defined as $L := L_{dry} + L_{wet}$, where L_{dry} and L_{wet} are the respective characteristic lengths for the hydrophobic and hydrophilic areas. In the present work the characteristic length for a hydrophilic spot is 1 mm and the distance between two neighboring hydrophilic spots is 0.5 mm. So I have $L_{dry} = 5$, $L_{wet} = 10$, and $L = 15$ in dimensionless form.

As illustrated in Fig. C.1A and B, the parameters χ and λ control the roundness and area ratio of the wettability pattern, respectively. Fig. C.1C(b) displays how the sharpness of the pattern is adjusted by ξ .

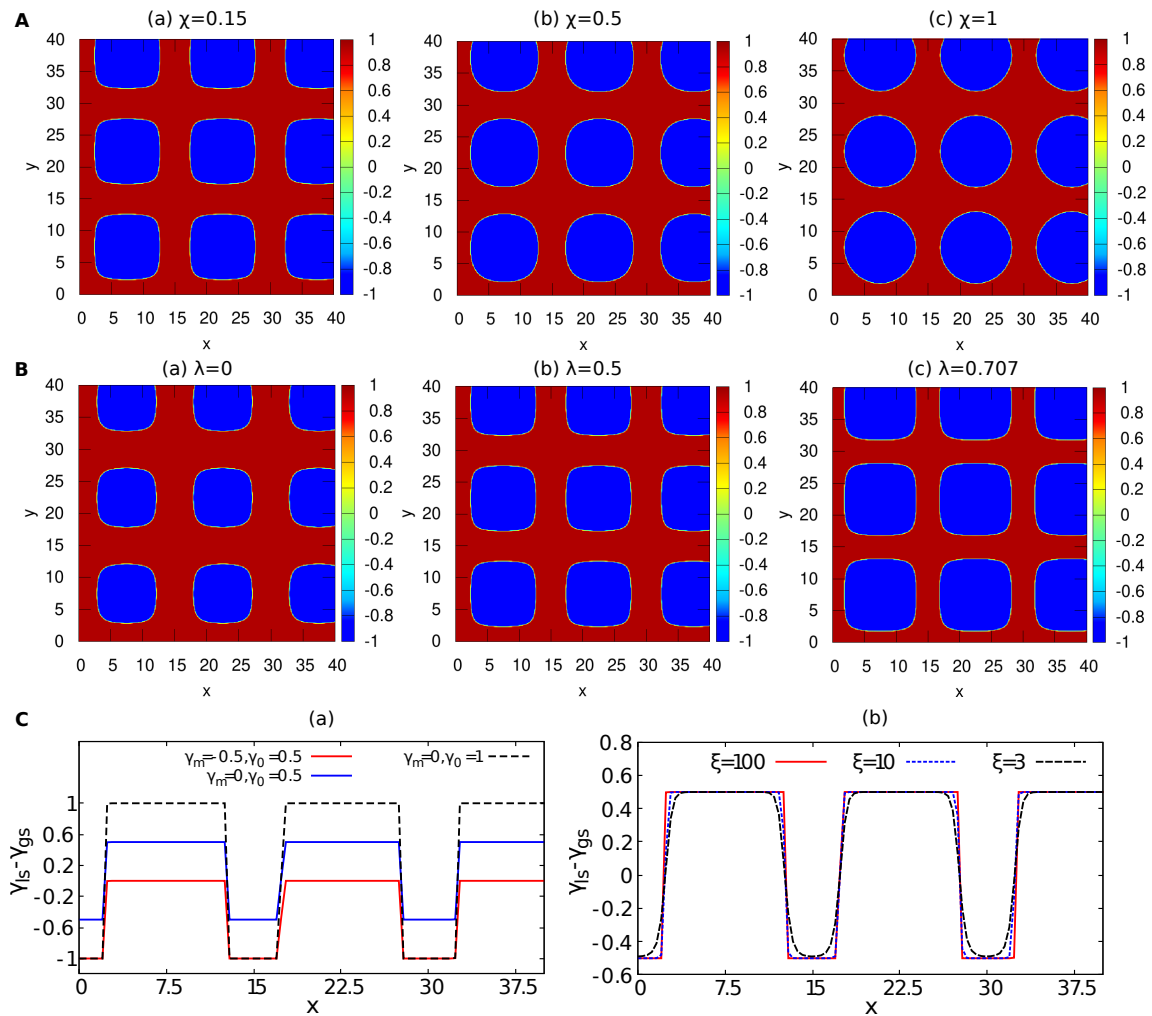


Figure C.1.: (A) and (B) Contour plot of the function $\gamma_{ls} - \gamma_{gs}$ in x - y space for different χ and λ , respectively. $\gamma_m = 0$, $\gamma_0 = 1$, $L = 15$, and $\xi = 100$. (C) (a) and (b) The heterogeneities $\gamma_{ls} - \gamma_{gs}$ as a function of x for different pairs of (γ_m, γ_0) and ξ when $y = 7.5$, respectively. In (C) I set $L = 15$, $\lambda = 0.5$, and $\chi = 0.15$.

C.2. Pattern information

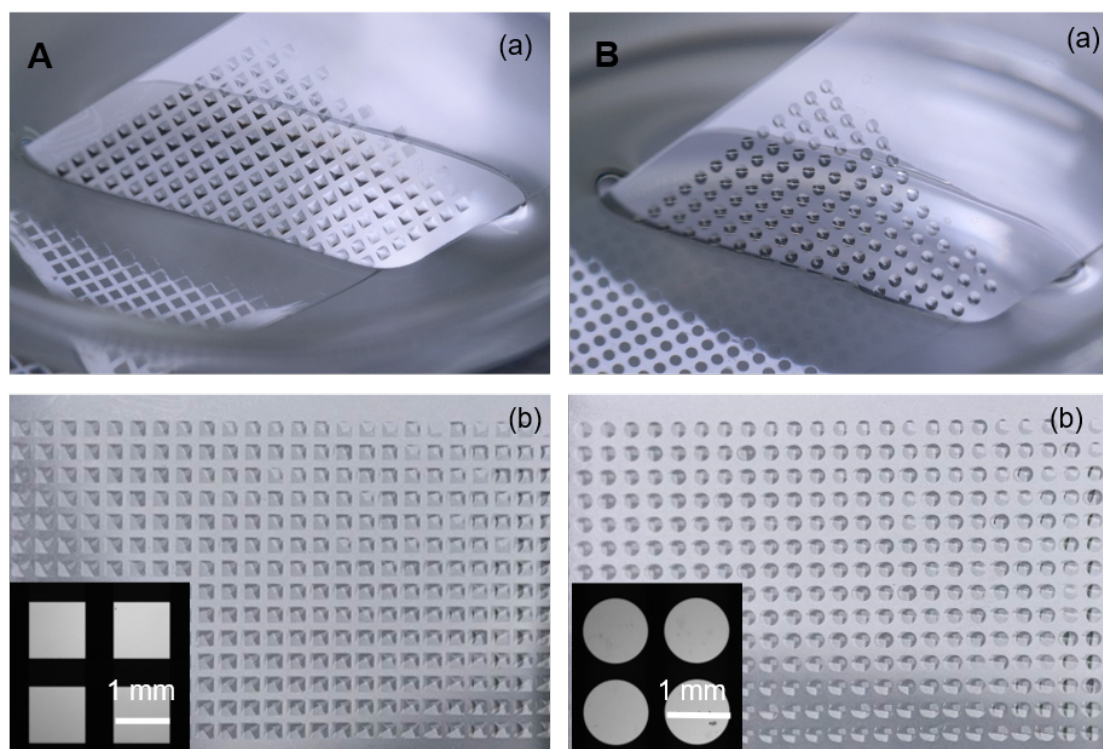


Figure C.2.: Photos of the glass slides with wettability pattern of (A) square array and (B) circle array after dipping in the glass with distilled water. The hydrophobic mesh restricts the liquid in the hydrophilic square and circle spots. The modification is done by two steps UV-light driven thiol-ene modification through the photomask (A, B: left corner below). The black parts of the photomask form hydrophobic areas, light grey –hydrophilic pattern.

C.3. Shape comparison

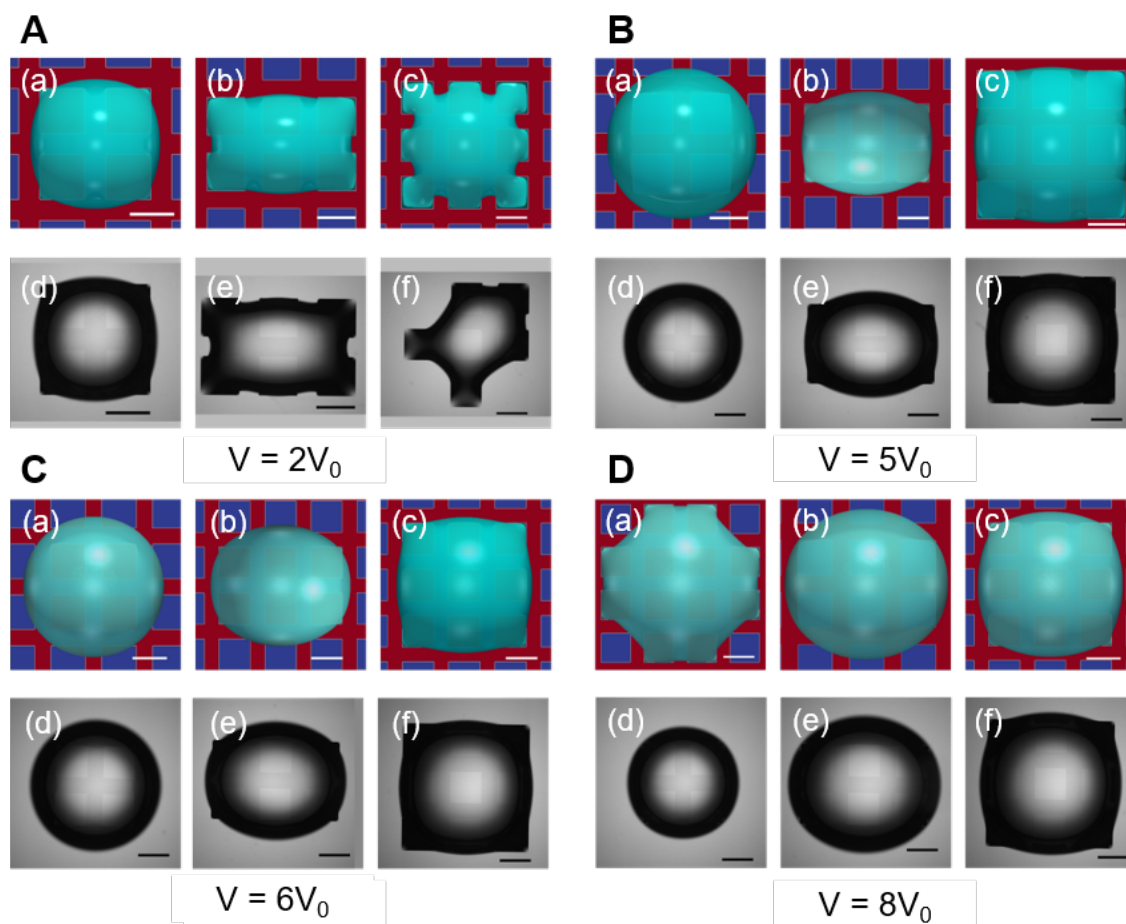


Figure C.3.: A-D: Top view comparison for droplet with volumes $V = 2V_0$, $5V_0$, $6V_0$, and $8V_0$. $V_0 = 5\mu L$. Scale bar: 1 mm (or 10 in dimensionless value).

C.4. Calculation of Bond number

The Bond number is defined as $Bo := (\rho_l - \rho_g)gL_c^2/\gamma_{lg} = (L_c/\lambda_c)^2$, indicating the importance of the gravitational force compared to the surface tension force. The parameter L_c is the characteristic length of a droplet. The parameter $\lambda_c = \sqrt{\gamma_{lg}/[(\rho_l - \rho_g)g]}$ is the capillary length, which is 2.7 mm for water with normal gravity. Here, I choose the initial radius R_i of the droplet as the characteristic length, i.e. $L_c = R_i = \sqrt[3]{3V/4\pi}$. The calculated Bond numbers for droplets with different volumes in the present work are listed in Table C.1. According to Ref. [225], when $Bo > 0.6$, the influence of gravity becomes noticeable. In chapter 6, the 40 μL -droplet ($Bo = 0.62$) also showed the importance of gravity, as discussed in Fig. 6.2A.

Table C.1.: Calculation of Bond numbers.

volume	Bo
$V_0(5\mu L)$	0.15
$2V_0(10\mu L)$	0.25
$4V_0(20\mu L)$	0.39
$6V_0(30\mu L)$	0.51
$8V_0(40\mu L)$	0.62

D. List of Symbols

Symbols	Description	Unit
a	semiaxe of an ellipse in the x direction	[m]
A	temporal wetted areas of a droplet	[m ²]
A_f	final wetted areas of a droplet	[m ²]
A_{lg}	surface area for liquid-gas interface	[m ²]
A_{ls}	surface area for liquid-solid interface	[m ²]
b	semiaxe of an ellipse in the y direction	[m]
B_{phi}	initial thin-film width on hydrophilic area	[m]
B_{pho}	initial thin-film width on hydrophobic area	[m]
c	order parameter in the Cahn-Hilliard model	[-]
d	stripe width	[m]
D	droplet diameter	[m]
D_0	initial droplet diameter	[m]
\vec{e}_z	unit vector in the z direction	[m]
E	total surface energy	[J]
F	free energy functional	[J]
\vec{g}	gravity acceleration	[m/s ⁻²]
h	droplet height	[m]
H	temporal thin-film height	[m]
H_0	initial thin-film height	[m]
$\bar{\bar{I}}$	unit tensor	[-]
K_{ij}	gradient energy matrix	[-]
M	mobility	[m ³ s/kg]
\vec{n}	normal vector	[-]
p	pressure	[N/m ²]
\vec{q}	generalized gradient vector	[-]
r	radial coordinate	[m]
r_b	droplet base radius	[m]
r_c	curvature radius	[m]
R	droplet radius	[m]
S	liquid-solid boundary	[m ²]
t	time	[s]
\vec{u}	velocity	[m/s]
V, V_d	droplet volume	[m ³]
x	x-coordinate	[m]
y	y-coordinate	[m]
z	z-coordinate	[m]

Symbols	Description	Unit
Bo	Bond number	[-]
Cn	Cahn number	[-]
Pe	Peclet number	[-]
Re	Reynolds number	[-]
We	Weber number	[-]
β	polar angle	[°]
γ	surface tension	[N/m]
ϵ	interface width parameter	[m]
θ	contact angle	[°]
$\bar{\Theta}$	Korteweg stress tensor	[J/m ³]
λ_1, λ_2	Lagrange multiplier	[J/m ³]
ν	viscosity	[kg/ms]
ρ	density	[kg/m ³]
σ	surface tension coefficient	[N/m]
τ	relaxation coefficient	[J/m ⁴]
ξ	droplet aspect ratio	[-]
χ_{ij}	interaction parameter between components i and j	[-]
ϕ	order parameter in the Allen-Cahn model	[-]
φ	polar angle of the ellipse	[°]
Ω	domain volume	[m ³]

E. List of Abbreviations

AC	Allen-Cahn
CB	Cassie-Baxter
CCA	constant contact angle
CCR	constant contact radius
CH	Cahn-Hilliard
CHNS	Cahn-Hilliard-Navier-Stokes equations
NS	Navier-Stokes equations
PF	phase-field
PDE	partial differential equation
LB	lattice Boltzmann

List of Figures

1.1.	Morning dews on a leaf [1].	3
1.2.	Droplet splitting and simultaneous arrayed reactions on a hydrophobic surface with hydrophilic areas. Different chemicals predeposited on the hydrophilic areas independently reacts with the splitted droplets simultaneously after splitting [9].	4
1.3.	Schematic of the hotspot cooling technique in a sealed vapor chamber. The top (bottom) plate is the superhydrophilic evaporator (superhydrophobic condenser) [13]. . .	4
1.4.	(a) Scanning electron micrographs of 7.8-nm-thick copper rings with various widths following pulsed laser exposure. (b) Simulation results via thin-film model (Similar to Cahn-Hilliard model [19]). Here, the light blue background indicates the original ring. As the width of the ring increases, the ring transitions from a purely Rayleigh-Plateau-type instability to a situation where both thin-film instability and Rayleigh-Plateau-type instability coexist [20].	5
2.1.	Schematic of Young's equation, which describes a mechanical force balance on the three-phase contact line.	8
2.2.	Droplet on rough surfaces. (a) Wenzel state. (b) Cassie-Baxter state.	8
2.3.	Partial image of an isopropanol drop with (a) ethylene glycol (volume fraction $\phi_v = 0.1$) and (b) dodecane ($\phi_v = 0.1$) spreading on a silicon wafer. The surface tension gradient between isopropanol and ethylene glycol is around 10 times greater than for dodecane. (c) The thickness profiles of the drop in (a) and (b) are highlighted in red and blue colors, corresponding to the red and blue dashed lines in (a) and (b) [48]. . .	10
2.4.	(a) Condensation on a strip patterned surface. The hydrophilic glass and hydrophobic OTS can be recognized by the condensed droplet size: small(large) droplets correspond to hydrophobic OTS (hydrophilic glass). (b) Static water drop on the strip patterned surface. (c) Sliding drop on an inclined substrate. Top right: Lateral view. Bottom left: Contact line view. (d) Stick-slip moving behaviors of the droplet front and rear contact points [81].	12
2.5.	Left: Simulation of a dewetting polymer rim and pinch-off of a single droplet highlighted with dashed lines. Right: Magnification of the highlighted droplet [105]. . . .	13
2.6.	Evaporating sessile droplet on a substrate with locally non-uniform evaporation flux.	13
2.7.	A binary drop of alcohol and water on a bath of sunflower oil. The binary drop spreads and fragments into a myriad of tiny droplets [121].	14

3.1.	The free energy \tilde{f} as a function of concentration c : $\tilde{f}(c) = c \ln c + (1 - c) \ln(1 - c) + 3.78c(1 - c)$. The two points (0.0273, -0.0249) and (0.9727, -0.0249) are the free energy minimum states, corresponding to the gas and liquid bulk phases, respectively.	24
4.1.	Snapshots of droplets and sensitivity study depending on the Cahn number: (a) droplet at initial time, (b) and (c) droplets at equilibrium on two different surfaces, (d) simulation results on two different surfaces for different values of Cn . The red circles and blue squares show the simulation results on surfaces with equilibrium contact angles $\theta_{e,wet} = 41^\circ$ and $\theta_{e,dry} = 106^\circ$ respectively. The red and blue dashed lines correspond to the two equilibrium contact angles $\theta_{e,wet} = 41^\circ$ and $\theta_{e,dry} = 106^\circ$	30
4.2.	The cosine of the equilibrium contact angle versus $(\gamma_{gs} - \gamma_{ls})/\gamma_{lg}$. Blue squares show the simulation results and the contact angles of droplets at final states are measured by using a modified marching square algorithm [166, 167]. The red line corresponds to the theoretical prediction of Young's law.	31
4.3.	Validation of the numerical model through comparison with analytical power laws. (a) Temporal evolution of the dimensionless wetted area of droplets spreading on a surface ($\theta_e = 41^\circ$). A_f and A are final and temporal wetted areas of the droplet, respectively. Different colored squares indicate the simulation results for different τ_w values. The solid curves correspond to the fitting curves of the exponential power law proposed by Lavi and Marmur [168]. (b) Temporal evolution of the dimensionless volume of an evaporating droplet suspended in vapor without wetting. V_0 and V are initial and temporal volumes of the droplet, respectively. The blue squares show the simulation results and the solid line indicates the fitting line in accordance with the well-known D^2 -law [169]. The insets in (a) and (b) are the snapshots showing the simulation scenes.	32
4.4.	Snapshots of droplets deposited on striped patterned surface for different liquid volumes. (a) Experimental results. Reprinted with permission from Ref. [170]. Copyright 2012 American Chemical Society. (b) Present simulation results. The top rows in (a) and (b) illustrate the droplet shapes in the direction parallel to the stripes and the bottom rows depict the droplet shapes in the perpendicular direction. The hydrophilic and hydrophobic stripes in (a) are 12 and 6 in dimensionless width, respectively. The dimensionless width of the 80 pL (initial dimensionless diameter 53) droplet in the perpendicular direction is 65. The solid lines are baselines of the surface and dashed lines show the droplet width in the parallel direction.	33

-
- 4.5. Temporal evolution of droplet shape for spreading and evaporation processes: (I) bottom view of a droplet with constant volume spreading on striped patterned surface, (II) bottom view of a droplet evaporating on striped patterned surface. (a)-(h): Experimental and LB simulation results. Reprinted with permission from Ref. [171]. Copyright 2013 American Physical Society. (i)-(l): Present simulation results. The hydrophilic and hydrophobic stripes ($\theta_{e,wet} = 40^\circ$ and $\theta_{e,dry} = 110^\circ$) are indicated by blue and red stripes in the present simulations, respectively. 34
- 4.6. Snapshots of droplet evaporation on striped patterned surface: (I) LB simulation from Yu et al. Reprinted with permission from Ref. [172]. Copyright 2017 Elsevier. (a) $t = 10^5 \delta_t$, (b) $t = 1.35 \times 10^5 \delta_t$, (c) $t = 1.4 \times 10^5 \delta_t$ and (d) $t = 3.05 \times 10^5 \delta_t$. δ_t is the time step. (II) Present simulation. (a) $t = 0.4 \times 10^3$, (b) $t = 1 \times 10^3$, (c) $t = 1.2 \times 10^3$ and (d) $t = 2.6 \times 10^3$. The equilibrium contact angles for hydrophilic and hydrophobic stripes are $\theta_{e,wet} = 60^\circ$ and $\theta_{e,dry} = 120^\circ$, respectively. 35
- 4.7. Contact angle and non-dimensional base radius of an evaporating droplet as a function of time in the perpendicular direction (left) and the parallel direction (right) on striped patterned surface. δ_t is the time step. (a)-(d) LB simulation from Yu et al. Reproduced with permission from Ref. [172]. Copyright 2017 Elsevier. The legends are added by the present authors. (e)-(h) Present simulation. 36
- 4.8. Surface energy evolution and snapshots of droplet spreading. Position 1 is above the center line of a blue stripe and position 2 is above the center line of a red stripe. The numbers at the bottom right corner in the snapshots indicate the dimensionless time. (a) $d/V^{1/3} = 0.19$. (b) $d/V^{1/3} = 0.62$ 37
- 4.9. Morphological diagram: (a) Droplet aspect ratio ξ as a function of $d/V^{1/3}$. Symbols show the results of droplet deposition from a series of independent simulations with different ratios of $d/V^{1/3}$. Different colored symbols indicate the equilibrium shapes covering different number of hydrophilic stripes. The black solid lines with circles and with squares are the first and second condensation lines, respectively, corresponding to the droplets initially deposited on the positions 1 and 2. The diagram is divided into 6 areas according to the number n of the wetted hydrophilic stripe(s). I: $n = 1$, II: $n = 1$ and 2, III: $n = 2$ and 3, IV: $n = 3$ and 4, V: $n = 4$ and 5, VI: $n = 5$ and 6. (b) Surface energy evolution as a function of $d/V^{1/3}$ in the area $d/V^{1/3} \in [0.15, 0.4]$. The red solid line and the blue dashed line correspond to the first and second condensations, respectively. The orange rhombus and green triangle denote the intersections. (c), (d) and (e) Equilibrium droplet-shapes in the areas I, II and III, respectively. In the left and right three images of (c), droplets are released on the positions 1 and 2, respectively. At the top and the bottom pictures in (d) and (e), droplets are deposited on the positions 1 and 2, respectively. 39

- 4.10. (a) and (b) Directional contact angles θ_1 and θ_2 as a function of $d/V^{1/3}$ for the first and second condensation. θ_1 is described by Cassie-Baxter equation and θ_2 is measured along the line perpendicular to the stripes and passing through the droplet center. (c) and (d) Droplet aspect ratio ξ as a function of $d/V^{1/3}$ for the first and second condensation, obtained from simulations (blue lines with squares) and the model of Jansen et al. [178] (red line with circle points). (e) and (f) Droplet morphological transitions in phases 1-3 for the first and second condensation. 42
- 4.11. (a) and (b) Droplet aspect ratio ξ as a function of $d/V^{1/3}$ for the condensation and evaporation of a droplet on positions 1 and 2. The colored symbols and the two condensation lines are directly taken from Figure 4.9(a). The red lines with rhombuses and with pentagons are the first and second evaporation lines, respectively. (c) The surface energy evolution of a condensing (black solid line) and an evaporating droplet (red dashed line) in the area $d/V^{1/3} \in [0.22, 0.6]$. The hysteresis area is highlighted with the green color. (d) and (e) Droplet morphological transitions in the condensation and evaporation processes. The arrows indicate the corresponding evolution directions and the stars annotate typical droplet-shapes in the hysteresis area. 44
- 4.12. Influence of perturbations on the droplet morphological transitions in the condensation processes. The numbers at the bottom right corner in the snapshots indicate the dimensionless time. Droplets at time $t = 0$ are disturbed by perturbations obeying a Gauss distribution with different amplitudes (a) amplitude=0.1, (b) amplitude=0.3, (c) amplitude=0.9. 45
- 4.13. The dimensionless directional contact radii R_1/d and R_2/d as a function of time for the condensations at position 1 and 2. R_1 and R_2 are measured along the lines parallel and perpendicular to the stripes, respectively. d represents the stripe width. Curves with different colors indicate the results for different τ_w values. The insets describe the results for the starting time. (a) and (c) are for the condensations at position 1. (b) and (d) are for the condensations at position 2. 46
- 4.14. Snapshots of droplet morphological transitions in condensation processes for different τ_w values. The left parts present the condensations at position 1 while the right parts correspond to the condensations at position 2. The numbers at the bottom right corner in the snapshots indicate the dimensionless time. (a)-(c) Top views for $\tau_w=1, 10, 100$. (d) Bottom views for $\tau_w=100$ 47

- 4.15. (a)-(d) The dimensionless directional contact radii R_1/d and R_2/d as a function of time for the evaporations at position 1 and 2. R_1 and R_2 are measured along the lines parallel and perpendicular to the stripes, respectively. d represents the stripe width. Lines with different colors present the results for different τ_w values. (a) and (c) are for the evaporations at position 1. (b) and (d) are for the evaporations at position 2. (e) Snapshots of droplet morphological transitions in evaporation processes for different τ_w values. The left parts illustrate the evaporations at position 1 while the right parts correspond to the evaporations at position 2. The numbers at the bottom right corner in the snapshots indicate the dimensionless time. (i)-(iii) in (e) are top views for $\tau_w=1, 10, 20$ 49
- 5.1. Schematic illustration of the geometric assumptions of the droplet. (A) The red dashed ellipse (with center O_1 semi-axes a and b) is the droplet base line. r_b denotes the base radius. (B) The top part of the yellow dashed circle (above the black line passing through O_1) refers to the circular arc on the liquid-gas interface with the circle center O_2 and radius r_c . h is the droplet height. φ and β represent polar angles on the surfaces of the red dashed ellipse and yellow dashed arc, respectively. 54
- 5.2. (A) Surface energy landscape of a droplet on chemically striped patterned surface (The effective radius of the droplet is $R = 40$, stripe width is $L = 20$ and the droplet base center is on the hydrophobic stripe). Point 1 and 2 are the two energy minima. (B) Snapshots of droplet-shape evolution from initial states to equilibrium states. The top and bottom rows correspond to the points 1 and 2 in (A), respectively. 56
- 5.3. (A) Surface energy of two droplets ($a = 60, b = 50$ and $a = 45, b = 70$, illustrated with red and blue lines, respectively) on chemically striped patterned surfaces as a function of droplet base center positions i (The effective radius ($R = (3V_d/4\pi)^{1/3}$, V_d is droplet volume) of the droplets is $R = 40$, stripe width is $L = 20$). The energy minima of the red and blue lines correspond to the points 1 and 2 in the energy landscapes shown in Fig. 5.6, respectively. (B) Sketch of the surface topology and the coordinates of droplet base center positions when energy minima are achieved (grey: hydrophobic, $i = 0, \pm 2, \pm 4, \dots$; white: hydrophilic, $i = \pm 1, \pm 3, \dots$). 57
- 5.4. (A)-(C) Surface energy landscape of droplets on chocolate-patterned surfaces as a function of droplet base center positions when a, b varies (The effective radius of the droplet is $R = 40$, lattice width is $L = 20$ and i and j indicate the coordinate of the droplet base center). (A): $a = 50, b = 50$, (B): $a = 70, b = 50$, and (C): $a = 65, b = 65$. The energy minima (red color) in (A), (B), and (C) correspond to the points 1, 3, and 5 in the energy landscapes shown in Fig. 5.7, respectively. (D) Sketch of the surface topology and the three typical coordinates of droplet base center positions when energy minima are achieved (grey: hydrophobic, white: hydrophilic). $P_1 : (j = 0, i = 0), P_2 : (j = 1, i = 0),$ and $P_3 : (j = 1, i = -1)$ 58

- 5.5. (A)-(C) Surface energy landscape of droplets on chessboard-patterned surfaces as a function of droplet base center positions when a, b varies (The effective radius of the droplet is $R = 40$, lattice width is $L = 20$ and i and j indicate the coordinate of the droplet base center). (A): $a = 52, b = 52$, (B): $a = 60, b = 60$, and (C): $a = 45, b = 57$. The energy minima (red color) in (A), (B), and (C) correspond to the points 1, 7, and 5 in the energy landscapes shown in Fig. 5.8, respectively. (D) Sketch of the surface topology and the three typical coordinates of droplet base center positions when energy minima are achieved (grey: hydrophobic, white: hydrophilic). $P_1 : (j = 0, i = 0)$, $P_2 : (j = 0, i = 1)$, and $P_3 : (j = -1/2, i = 1/2)$ or $(j' = 0, i' = 1/\sqrt{2})$ in the rotated coordinate system. 58
- 5.6. (a)-(c) Surface energy landscapes in the a - b space and snapshots of sessile droplets on chemically striped patterned surfaces with different droplet sizes ((a): $R/L = 2$, (b): $R/L = 5$, (c): $R/L = 9$). The chemical heterogeneities are described by $f_1(r, \varphi)$ in Eq. (5.8). At equilibrium, the droplet base center stays either on the center of the blue (hydrophilic) stripe (namely position 1 and $i = 1$) or on the center of the red (hydrophobic) one (i.e. position 2 and $i = 0$). The energy landscapes are accordingly calculated when the droplet base centers are on these two different positions. The contour lines indicate the energy levels (red for low energy and blue for high energy states) and the color changes from blue to red illustrate the decrease of the energy. The energy minima are indicated by different numbers, corresponding to the snapshots labeled with the same number. The red dashed ellipses in (a)(III) denote the analytical results, which can be read from the corresponding energy landscapes. (d) Predicted droplet configurations for different droplet sizes. The filled and empty symbols describe the simulation and analytical results, respectively. The two dashed lines are guide lines to highlight a trend in the data. 60
- 5.7. (a)-(c) Surface energy landscapes for chocolate-patterned surfaces. The chemical heterogeneities are described by $f_2(r, \varphi)$ in Eq. (5.8). The energy minima are indicated by different numbers, corresponding to the snapshots in E labeled with the same number. (d) Sketch of the surface topology and three base centers of droplets (grey: hydrophobic, white: hydrophilic). The droplet shapes in (a), (b), and (c) correspond to the positions P_1, P_2 , and P_3 . (e) Snapshots of equilibrated droplets through PFM (blue: hydrophilic, red: hydrophobic). The red dashed ellipses denote the analytical results. (f) The number N of equilibrium shapes of droplets as a function of R/L . The black dashed line is the guide line. 61

- 5.8. (a)-(e) Surface energy landscapes for chessboard-patterned surfaces. (a) and (d) correspond to the situations when the directions of a and b are horizontal and vertical, respectively, as shown in (g)2. The chemical heterogeneities are described by $f_3(r, \varphi)$ in Eq. (5.8). (b), (c), and (e) describe the energy landscapes in a rotated coordinate system and the directions of a and b are shown in (g)5. In the rotated system, δ_1 and δ_2 in $f_3(r_b, \varphi)$ are substituted by δ'_1 and δ'_2 , respectively, with $\delta'_1 = (\delta_1 + \delta_2)/\sqrt{2}$ and $\delta'_2 = (\delta_1 - \delta_2)/\sqrt{2}$. The energy minima are indicated by different numbers, corresponding to the snapshots in (g) labeled with the same number. (f) Schematic description of the surface topology and three base center points of equilibrated droplets (grey: hydrophobic, white: hydrophilic). The two lines indicate two possible directions of the semi-axis a . (a) & (b), (d) & (e), and (c) correspond to P_1 , P_2 , and P_3 , respectively. (g) Snapshots of equilibrated droplets via PFM (blue: hydrophilic, red: hydrophobic). The red dashed ellipses denote the analytical results. (h) The number N of equilibrium shapes of droplets as a function of R/L . The black dashed line is the guide line. . . . 62
- 5.9. The number N of equilibrium droplet-shapes as a function of the energy discontinuous line density $\rho := n/(2L)^2$ for different patterned surfaces, Here, n is the total effective number of pinning lines within a square cell with an area of $(2L)^2$. The three insets indicate how ρ is calculated for different patterned surfaces. The numbers "1" and "0.5" shown in the cells stand for the effective number of pinning lines. The lines with different colors denote the results for droplets with different sizes (blue: $R/L = 0.5$, orange: $R/L = 1.5$, red: $R/L = 2$). 64
- 5.10. (a)-(c) Sketches of the surface topology for three chemically patterned surfaces: "stripe", "chocolate", and "chessboard." Here, the grey and white areas denote hydrophobic and hydrophilic surfaces, respectively. The coordinates of the droplet base center positions at equilibrium are highlighted by P_1 , P_2 and P_3 . (a) $P_1 : i = 1, P_2 : i = 0$. (b) $P_1 : (j = 0, i = 0), P_2 : (j = 1, i = 0),$ and $P_3 : (j = 1, i = -1)$. (c) $P_1 : (j = 0, i = 0), P_2 : (j = 0, i = 1),$ and $P_3 : (j = -1/2, i = 1/2)$ or $P_1 : (j' = 0, i' = 0), P_2 : (j' = 1/\sqrt{2}, i' = 1/\sqrt{2}),$ and $P_3 : (j' = 0, i' = 1/\sqrt{2})$. The indexes with primes for the last three points are in the rotated coordinate system. 65
- 5.11. (a)-(c) Contour plot of the functions $f_1(x, y), f_2(x, y), f_3(x, y)$ describing the heterogeneities of the three chemically patterned surfaces: "stripe", "chocolate", and "chessboard", respectively. Here, $x = r \cos \varphi$ and $y = r \sin \varphi$. r is the r coordinate in polar coordinate system. The patterns are obtained by setting $\gamma_m = 0, \gamma_0 = 0.5, \xi = 100$. The characteristic lengths L in (I), (II), (III) are 20, 30, and 40, respectively. The ratios ν for 1:1, 1:2, and 1:3 correspond to $\lambda = \cos 90^\circ, \cos 60^\circ, \cos 45^\circ$, respectively. In (b)(I), (II), (III), I set $\chi = 0.55, 0.13, 0.10$, respectively. The red and blue color show $f_k = -0.5$ or 0.5 , corresponding to hydrophilic and hydrophobic area, respectively. . 67
- 5.12. Droplet morphology in a form of spherical cap. The liquid-solid contact area is highlighted in the cyan color. 68

- 5.13. Surface energy landscapes for droplets with different sizes on chocolate patterned surfaces and snapshots of equilibrated droplets through PF simulations. (I) $R/L = 0.75$, (II) $R/L = 0.5$, (III) $R/L = 0.25$. The chemical heterogeneities are described by $f_2(r, \varphi)$ in Eq. (5.10) with the following parameters: $\gamma_m = 0$, $\gamma_0 = 0.5$, $\xi = 100$, $L = 40$, $\lambda = 0$, $\chi = 0.55$. The energy minima are specified by different numbers, corresponding to the snapshots in (D) labeled with the same number. The surface energy landscapes for (A), (B), and (C) depict the systems with the droplet base center positions on P_1 , P_2 , and P_3 , respectively. (D) Snapshots of equilibrated droplets via PF simulations (blue: hydrophilic, red: hydrophobic). 69
- 5.14. The number N and the morphologies of the equilibrated droplets on three typical chemically patterned surfaces in dependence of the droplet sizes. (a)&(b), (c)&(d), and (e)&(f) are for striped, chocolate-patterned, and chessboard-patterned surfaces, respectively. (a), (c), and (e) depict the relation N versus R/L . (b), (d), and (f) describe the equilibrated droplet morphologies with different sizes predicted by PF simulations (filled symbols), in comparison with the energy-map model (hollow symbols) and the modified CB model (solid curves). 70
- 5.15. Surface energy landscapes for droplets on chocolate-patterned surfaces with different contact angles and corresponding snapshots of equilibrated droplets by PF simulations. (I) $\theta_1 = 30^\circ, \theta_2 = 90^\circ$, (II) $\theta_1 = 90^\circ, \theta_2 = 150^\circ$, (III) $\theta_1 = 120^\circ, \theta_2 = 180^\circ$. The chemical heterogeneities are depicted by $f_1(r, \varphi)$ in Eq. (5.10) with $\xi = 100$, $L = 40$, $\lambda = 0$, $\chi = 0.55$. The mean value γ_m and the amplitude γ_0 of the surface energy density are set according to the contact angle pairs. The energy minima are shown by different numbers, corresponding to the snapshots in (C) labeled with the same number. The surface energy landscapes for (A), (B) and (C) represent the setups where the droplet base center positions are on P_1 , P_2 and P_3 , respectively. (D) Snapshots of equilibrated droplets through PF simulations (blue: hydrophilic, red: hydrophobic). 73
- 5.16. The number and the morphologies of the equilibrated droplets on three typical chemically patterned surfaces in dependence of the contact angles. (a)&(b)&(c), (d)&(e)&(f), and (g)&(h)&(i) are for striped, chocolate-patterned, and chessboard-patterned surfaces, respectively. (a)&(d)&(g) and (b)&(e)&(h) illustrate N versus $\bar{\theta}$ and $\Delta\theta$, respectively. Here, $\Delta\theta$ varies from -60° to 60° , which is achieved by fixing θ_1 , (e.g. $\theta_1 = 90^\circ, 120^\circ$) and changing θ_2 . (c), (f), and (i) depict the equilibrated droplet morphologies with different average contact angles predicted by PF simulations (filled symbols), in comparison with the energy-map model (hollow symbols) and the modified CB model (solid curves). 74

- 5.17. Surface energy landscapes for droplets on chocolate patterned surfaces with different area fractions of hydrophilic and hydrophobic areas and corresponding snapshots of equilibrated droplets through PF simulations. The droplet size is set as $R = 40$. The chemical heterogeneities are described by $f_2(r, \varphi)$ in Eq. (5.10) with $\gamma_m = 0$, $\gamma_0 = 0.5$, $\xi = 100$. The ratios for (I) $\nu = 1 : 1$, (II) $\nu = 1 : 2$, (III) $\nu = 1 : 3$ correspond to $(L = 20, \lambda = 0, \chi = 0.55)$, $(L = 30, \lambda = \cos 60^\circ, \chi = 0.13)$, $(L = 40, \lambda = \cos 45^\circ, \chi = 0.10)$, respectively. The energy minima are designated by different numbers, corresponding to the snapshots in (D) indicated with the same number. The surface energy landscapes for (A), (B) and (C) correspond to the droplet base center positions P_1 , P_2 and P_3 , respectively. (D) Snapshots of equilibrated droplets through PF simulations (blue: hydrophilic, red: hydrophobic). 75
- 5.18. (a) The number N of the equilibrium droplet shapes on chocolate patterned surfaces as a function of $\bar{\theta}$. (b) Equilibrium morphologies of droplets on chocolate patterned surfaces with different fractions of hydrophilic and hydrophobic areas predicted by PF simulations (filled symbols) compared with the energy landscape model (hollow symbols) and the modified CB model (solid curves). 76
- 5.19. Functional relation between N and A_{ts} for droplets on the chocolate-patterned surface. The hollow squares and filled circles depict two distinct cases, where A_{ts} is changed by setting different average contact angle $\bar{\theta}$ and droplet radii R , respectively. The solid and dashed lines are the corresponding fitting curves. 77
- 6.1. Surface free energy landscapes and equilibrium shapes for droplets on a chemically patterned surface. The energy maps (a), (b), and (c) in the first row are surface free energy landscapes in the $a-b$ space when the droplet base center is placed on three symmetric points of the patterned substrate: (a) in between four neighboring hydrophilic lattices, (b) between two adjacent hydrophilic lattices, (c) on the hydrophilic lattice. The contour lines indicate the levels of surface energy, which decreases from red to blue regions. The energy minima are labeled with numbers 1-3, whose coordinates (a, b) describe the semi-axes of the droplet base line. The second and third rows illustrate the equilibrium shapes of droplets obtained from simulations ((d)-(f)) and experiments ((g)-(i)). In (d)-(f), the hydrophilic and hydrophobic areas are highlighted in blue and red color, respectively. The red dashed ellipses on the simulation snapshots (d)-(f) are theoretical results corresponding to the coordinates (a, b) of the energy minima indicated in (a)-(c). (A) $V = V_0 = 5 \mu L$, (B) $V = 4V_0 = 20 \mu L$. Scale bar: 1 mm (or 10 in dimensionless value). 81

- 6.2. A. (a) The surface energy landscape $E_v(a, b)$ for $V = 8V_0$ ($40 \mu L$) with droplet base center on the center of four neighboring hydrophilic lattices. (b) and (c) top views for an equilibrated droplet with and without gravity from the PF simulation. The red dashed lines in (b) and (c) show the analytical results which correspond to the energy minima 1 and 2 in (a), respectively. (d) Optical image of the droplet for $V = 8V_0$ ($40 \mu L$) via experiment. The droplet centers are shifted away from the patch centers. B. Equilibrium morphologies with unique symmetric axis. (a) and (b) Experimental and simulation results for $V = 2V_0$ ($10 \mu L$), respectively. (c) and (d) Experimental and simulation results for $V = 4V_0$ ($20 \mu L$), respectively. The red dot dashed lines illustrate corresponding symmetric axes. Scale bar: 1 mm (or 10 in dimensionless value). 83
- 6.3. (A) Surface energy landscapes for droplets with $V = V_0$ ($5 \mu L$) on a circle-patterned surface (see more details in Fig. C.2B for the patterned substrate). The three energy maps correspond to the case when the droplet center is placed on the positions (a), (b), and (c) described in Fig 6.1. The energy minima are labeled with numbers 1-4, corresponding to the snapshots in (B) and (C) marked with the same numbers. (B) and (C) Top view comparison for droplets with a volume of $V = V_0$ ($5 \mu L$) on a circle-patterned surface. Scale bar: 1 mm (or 10 in dimensionless value). 84
- 6.4. Comparison of (a) side lateral and (b) side diagonal views for droplets with $V = 4V_0$ ($20 \mu L$). The snapshots of droplets via simulations and experiments are normalized to the same width and then overlapped. The differences of the normalized snapshots are highlighted in cyan. 85
- 6.5. Comparison of droplet height and surface energy. (a), (b), and (c) theoretical, simulation, and experimental results for droplet height, respectively. (d) and (e) theoretical and numerical analysis of surface energies. (f) Snapshots of top views for typical equilibrium shapes of droplets with volume varying from $2V_0$ to $6V_0$. In (a)-(e) the bars colored in violet, green, and blue correspond to the equilibrated droplets covering the hydrophilic (blue) lattices patterns of 2×2 , 2×3 , and 3×3 , as exhibited in (f). The pink bars in (b) and (e) present the 2×2 patterned droplet via PF simulation without gravity, as illustrated in Fig. 6.2(c). Droplet height h and surface energy E are nondimensionalized by x^* and $\gamma^* x^{*2}$, respectively. 86

- 6.6. (a) Comparison of droplet morphologies when a droplet evaporates from $4V_0$ to $0.8V_0$ ($20\text{-}4\ \mu\text{L}$). Top and bottom rows illustrate the simulation and experimental results, respectively. From left to right, the droplet snapshots in experiment were taken at the time 0, 15, 30, 45, 50, 51.5 min, respectively. (b) Droplet height and liquid-solid contact area as functions of the droplet volume. The dot-dashed lines, circles, and solid lines represent results from the PF simulations, the energy map method, and the CCR evaporation model, respectively. The inset shows the evolution of the droplet base line via the energy map method as the volume decreases from $4V_0$ to V_0 . In the CCR evaporation model, I assume that the droplet is in the shape of a spherical cap with a constant liquid-substrate contact area $A_{ls} = \pi[(r_1 + r_4)/2]^2$ with r_1 and r_4 denoting the base radii calculated from the energy map method for $V = V_0$ and $V = 4V_0$, respectively. (c) Comparison of surface energy evolution as the droplet evaporates from $4V_0$ to $0.8V_0$. Inset in left down side: Energy maps for equilibrium droplet with $V/V_0=1, 2, 4$. The points A, B, C denote the corresponding energy minima in the $a - b$ space. (d) Top and middle: Comparison of the surface energy evolution for the droplet cap and the droplet base. Bottom: Comparison of contact angle evolution obtained through PF simulation and CCR evaporation model. θ_{sim} is calculated through $\cos \theta_{sim} = (\cos \theta_{e,wet} x_{wet} + \cos \theta_{e,dry} x_{dry})$ with x_{wet} (x_{dry}) indicating the hydrophilic (hydrophobic) area fraction covered by the droplet. θ_{CCR} is the apparent contact angle for the droplet in the CCR model. Droplet height h and surface energy E are nondimensionalized by x^* and $\gamma^* x^{*2}$, respectively. Scale bar: 1 mm (or 10 in dimensionless value). 88
- 7.1. (A) Scheme of a liquid contained in a solid vessel (left) and inside liquid water walls, that is, a liquid well (right). (B) Formation of a circular liquid well. Water forms a ring on the hydrophilic surface area (dashed line). The organic solvent (1-nonanol, dyed with Oil Red O) is then added into the liquid well. Scale bars: 5 mm. 91
- 7.2. Phase-field simulation for the confinement of 1-nonanol (red) in a ring of water (blue). Each simulation (i-vii) is based on a different set of the surface and interfacial tensions γ_{oa} (organic-air), γ_{ow} (organic-water), and γ_{wa} (water-air). The surface and interfacial tensions ($\gamma_{oa}, \gamma_{ow}, \gamma_{wa}$) were (i) (28.0, 8.8, 72.86) mN/m [198, 199], (ii) (28.0, 8.8, 44) mN/m, (iii) (28.0, 8.8, 36.43) mN/m, (iv) (28.0, 8.8, 21.86) mN/m, (v) (36.43, 8.8, 44) mN/m, (vi) (44, 8.8, 44) mN/m, and (vii) (51, 8.8, 44) mN/m. The assumed volumes were $100\ \mu\text{L}$ (1-nonanol) and $60\ \mu\text{L}$ (water), respectively. The inner and outer diameters of the hydrophilic surface area are 14 mm and 18 mm, respectively. The first row shows a top view, the second row shows a cross section and the third row highlights the cross section at the interface of 1-nonanol and water. 92

- 7.3. (A) (i) and (ii) Schematic of surface hydrophobicity for droplets 1 and 2, respectively. From yellow to red color, the surface become more and more hydrophilic. The arrays indicate the direction of the surface energy gradient. (B) (i)-(iii) Time evolution of droplets 1 (bright green) and 2 (dark green) on the substrate. (i) Initial states. (ii) The two droplets meet with each other. (iii) Droplet collision and deformation. The interfacial tensions between each two phases are the same, i.e. $\gamma_{12}=\gamma_{1a}=\gamma_{2a}$ (a stands for air) [205]. 94
- 8.1. Validation of phase-field method for modeling equilibrium state of droplets in a wedge. (a) The distance x_0 of the droplet center O from the wedge apex as a function of contact angle θ . The simulated data points (colored symbols) show 2D-droplets with radius $r = 0.98$ mm (the same size as the $4 \mu L$ -droplet in [206]) in three wedges with opening angles 2φ ranging from 26° to 37° . The black dashed lines are theoretical predictions in 2D, modified from the 3D version in [206] (The 2D model: $x_0/r = \sqrt{\frac{\pi}{-\pi+2\theta-\sin^2\theta} \frac{\cos(\pi-\theta)}{\sin\varphi}}$). The inset denotes the schematic equilibrated droplet profile in a wedge with labeling geometric parameters. (b)-(c) Equilibrium droplet morphologies for open angles $2\varphi = 37^\circ$ and contact angles $\theta = 140^\circ, 151^\circ, 162^\circ$, respectively. Left: Experimental results from [206]; Right: Present 2D-simulation results. The red dashed lines are circular fits of droplet profiles. 96
- 8.2. Droplet evolution with time in a funnel-like pore structure for different contact angles θ . (a) $\theta = 60^\circ$, (b) $\theta = 120^\circ$. The open angle for the structure are $2\varphi = 60^\circ$. The ratio of the droplet diameter to the tunnel diameter D/L is set as 3. 96
- 8.3. Schematic of droplet penetration into pore structures. In (a), (c) and (d) the pore has an open angle 2φ with narrowest pore diameter L . (a) The circle with black solid line depicts the initial state and the droplet with fitted red dashed circle approximately corresponds to a critical state that the droplet cannot totally penetrate into the narrow part. The initial droplet diameter is D . Here, I assume $D \gg L$ and φ is very small. The red fitted circle centering at O has a radius R and intersects with the substrate at the points M and N . N is exactly on the funnel throat. The dot dashed line goes through the point O and the open angle apex A . The black dashed line through M is the tangent line of the red circle and thus θ represents the contact angle. The line OP is normal to the substrate surface. (b) Regardless of open angle and droplet spreading takes place only inside the pore with diameter L . In (c) and (d), the green color indicates exactly the critical droplet shape that are not able to totally penetrate into the narrow part. The red and blue dashed circles with radii R fit the droplet profiles in the left and right sides, respectively. M_1, M_2, N_1, N_2 are contact points of the three phases. (c): $\varphi \in (0, \pi/2]$. (d): $\varphi \in [\pi/2, \pi]$. $\theta_1 = \angle O_1 N_1 N_2$, $\theta_2 = \angle O_2 M_1 M_2$ 98

8.4.	Regime diagrams for the droplet final states in pore structures with varying φ and θ . (a) Simulation snapshots for final states of droplets ($D/L = 3$) with varying φ and θ . (b) Regime diagram for the penetration states of the droplet with $D/L = 3$. Blue squares: totally penetration into the narrow part; Red triangles: no penetration. I plot the critical lines predicted by model 1 (dot dashed line divided by the gray dashed line. Top: model 1b; Bottom: model 1a) and model 2 (solid line). In (c), I vary D/L from 1 to 5 and plot the corresponding critical lines (highlighted with different colors) predicted by model 1 and model 2. The colored rhombus points are intersections of model 1 and 2 and the black dashed line described by Eq. 8.10 going through these points denotes the upper limit of model 2. The circle points with error bars indicate the simulation confirmed critical penetration states.	100
8.5.	Regime diagram for droplet final states in pore structures with different D/L and θ . The half open angle is kept constant with $\varphi = 30^\circ$ in (a)-(c). (a) Droplet final states influenced by the contact angle θ . (b) Droplet final states influenced by the droplet size D/L . In (c) the blue squares and red triangles indicate whether droplet penetration happens or not. The solid and dot dashed lines describe the theoretical predictions with model 1a and 2, respectively. In (d) I vary φ from 10° to 150° (highlighted with different colors) and plot the predictions with model 2. The inset displays a zoom of the diagram in the range of $\theta \in [130^\circ, 150^\circ]$	102
9.1.	Comparison of droplet shape evolution on different substrates. (a) Snapshots of droplet shapes. Left: Experiments from [80]. Right: Present simulations. From (i) to (iv) the equilibrium contact angle $\theta_{eq} = 3^\circ, 43^\circ, 117^\circ, 180^\circ$. (b) Comparison of base radius evolution with time. The symbols and solid lines denote experimental results from [80] and simulation results, respectively.	108
9.2.	Snapshots of a water droplet with radius $R = 1.6$ mm impacting the point-like defect on a superhydrophobic substrate at the velocity $u = 1.2$ m/s (centered impact). Top: Experiment from [207]. Bottom: Present simulation. The contact angle in the simulation is set as $\theta = 160^\circ$	109
9.3.	Simulation of a droplet ($R = 1.3$ mm) impacting at ($u = 1.28$ m/s) a substrate textured by a sphere with radius $r = 0.2$ mm. Top panel: Lattice-Boltzmann simulation from [207]. Bottom panel: Present phase-field simulation. For each panel high-angle views and cross-sections are shown in the first and second rows respectively.	110
9.4.	Impinging processes of droplets with diameter 3.1 mm on the superhydrophobic stripe coated hydrophilic surface. The impact velocity is $u=0.97$ m/s. The contact angles on hydrophilic and hydrophobic areas are $\theta_{phi} = 50^\circ, \theta_{pho} = 165^\circ$, respectively. (a) and (b) Side and top views for present simulation. (c) and (d) Side and top views for the experiment from [208].	111

9.5.	Simulation parameters of the liquid film on chemically patterned surfaces. (a) Two-lattice-patterned substrate. (b) Four-lattice-patterned substrate. θ_{phi} represents the contact angle of the hydrophilic area (blue), and it keeps constant $\theta_{phi} = 20^\circ$. θ_{pho} denotes the contact angle of the hydrophobic area (red) and it varies from 60° to 160° . H_0 represents the initial height of the liquid film. L denotes the length of the hydrophilic pattern on the two-lattice-patterned surface. B represents the whole width of the two neighboring hydrophilic lattices and the hydrophobic area between them, i.e., $B = 2B_{phi} + B_{pho}$	112
9.6.	Simulation results for the evolution of the liquid film with $H_0=10$ placed on the stripe patterned substrate. From (a) to (d) the hydrophobic contact angles θ_{pho} are 60° , 90° , 120° , and 160° respectively, while $\theta_{phi}=20^\circ$ keeps constant [209].	113
9.7.	Simulation results of liquid film with $H_0=10$ placed on the lattice patterned substrate. From (a) to (d) the hydrophobic contact angles θ_{pho} are 60° , 90° , 120° , and 160° respectively, while $\theta_{phi}=20^\circ$ keeps constant [209].	114
9.8.	The relative width W/W_0 of the liquid bridge as a function of time. W_0 is the initial width of the liquid film along the measure lines in the insets. (a) On the two-lattice-patterned substrate, $W_0 = L = 400$. (b) On the four-lattice-patterned substrate, $W_0 = B = 250$. The colored solid lines denote the simulations with different values of θ_{pho} . $\theta_{phi}=20^\circ$ keeps constant for all simulations [209].	114
9.9.	(a)- (d) Simulation results for the evolution of the liquid film with $H_0=10, 20, 30, 40$, respectively. The liquid films are placed on the stripe patterned substrate with $\theta_{phi}=60^\circ$ and $\theta_{pho}=160^\circ$. The relative width W/W_0 and relative height H/H_0 of the liquid bridge as functions of time are shown in (e) and (f), respectively. The colored solid lines denote the simulations with different initial heights H_0 . The insets illustrate how the width and height are measured [209].	115
B.1.	Surface energy landscapes for droplets with different sizes on the chemically striped patterned surfaces and the snapshots of the equilibrated droplets via PF simulations. (I) $R/L = 1$, (II) $R/L = 2.5$, (III) $R/L = 4.5$, The chemical heterogeneities are described by $f_1(r_b, \varphi)$ in Eq. 5.10 with the following parameters: $\gamma_m = 0$, $\gamma_0 = 0.5$, $\xi = 100$, $L = 40$, $\lambda = 0$. At equilibrium, the droplet base center stays either on $P_1(i = 1)$ (the center of the hydrophilic stripes, in blue color) or $P_2(i = 0)$ (the center of the hydrophobic stripes, in red color). The energy landscapes are accordingly calculated by using different values of i . The contour lines indicate the energy levels (red for high values and blue for low values). The energy minima are highlighted by different numbers in (A) and (B) in each panel, corresponding to the snapshots labeled with the same number in (C). The red dashed ellipses with semi-axes a, b in (I)(C) show the analytical results from the energy landscape method. Reproduced with permission from Ref. [183]. Copyright 2019 American Physical Society.	128

- B.2. Surface energy landscapes for droplets with different sizes on the chessboard-patterned surfaces and the snapshots of the equilibrated droplets through PF simulations (I) $R/L = 0.75$, (II) $R/L = 0.5$, (III) $R/L = 0.25$. The chemical heterogeneities are described by $f_3(r, \varphi)$ in Eq. 5.10 with $\gamma_m = 0$, $\gamma_0 = 0.5$, $\xi = 100$, $L = 40$, $\lambda = 0$. The energy minima are illustrated by different numbers inside the gray circles. The equilibrated states at these energy minima are sequentially shown in Figure B.3(I)-(III). The surface energy landscapes for (A)&(B), (C)&(D), and (E) correspond to droplets with base center positions on P_1 , P_2 , and P_3 , respectively. In each panel, (A) and (C) describe the situation where a and b are in the horizontal and vertical directions, respectively. While (B), (D), and (E) depict a system which is rotated counterclockwise by 45° . In the rotated system, δ_1 and δ_2 in $f_3(r, \varphi)$ are substituted by δ'_1 and δ'_2 , respectively, with $\delta'_1 = (\delta_1 + \delta_2)/\sqrt{2}$ and $\delta'_2 = (\delta_1 - \delta_2)/\sqrt{2}$ 129
- B.3. Snapshots for the equilibrated droplets with different sizes on the chessboard patterned surface via PF simulations (blue: hydrophilic, red: hydrophobic) (I) $R/L = 0.75$, (II) $R/L = 0.5$, (III) $R/L = 0.25$ 130
- B.4. Surface energy landscapes for droplets on the striped patterned surfaces with different contact angles and the corresponding snapshots of the equilibrated droplets from the PF simulations. (I) $\theta_1 = 30^\circ, \theta_2 = 90^\circ$, (II) $\theta_1 = 90^\circ, \theta_2 = 150^\circ$, (III) $\theta_1 = 120^\circ, \theta_2 = 180^\circ$. The chemical heterogeneities are described by $f_1(r, \varphi)$ in Eq. 5.10 with $\xi = 100$, $L = 40$, $\lambda = 0$. The parameters γ_m, γ_0 are adjusted according to the contact angle pairs. The energy minima are indicated by different numbers, corresponding to the snapshots in (C) labeled with the same number. The surface energy landscapes for (A) and (B) delineate the situation where the droplet base center positions are on P_1 and P_2 , respectively. (C) Snapshots of the equilibrated droplets through PF simulations (blue: hydrophilic, red: hydrophobic). 131
- B.5. Surface energy landscapes for droplet on the chessboard-patterned surfaces with different contact angles and the corresponding snapshots of the equilibrated droplets through PF simulations (I) $\theta_1 = 30^\circ, \theta_2 = 90^\circ$, (II) $\theta_1 = 90^\circ, \theta_2 = 150^\circ$, (III) $\theta_1 = 120^\circ, \theta_2 = 180^\circ$. The chemical heterogeneities are described by $f_3(r, \varphi)$ in Eq. 5.10 with $\xi = 100$, $L = 40$, $\lambda = 0$. The parameters γ_m, γ_0 are modified according to the contact angle pairs. The energy minima are indicated by different numbers, corresponding to the snapshots in Figure B.6(I)-(III) labeled with the same number. The surface energy landscapes for (A)&(B), (C)&(D), and (E) correspond to the droplet base center positions on P_1, P_2 , and P_3 , respectively. (A) and (C) describe the situation where a and b are in the horizontal and vertical directions, respectively, while (B), (D), and (E) depict a system which is rotated counterclockwise by 45° . In the rotated system, δ_1 and δ_2 in $f_3(r, \varphi)$ are substituted by δ'_1 and δ'_2 , respectively, with $\delta'_1 = (\delta_1 + \delta_2)/\sqrt{2}$ and $\delta'_2 = (\delta_1 - \delta_2)/\sqrt{2}$ 132

B.6.	Snapshots of the equilibrated droplets on the chessboard patterned surfaces through PF simulations (blue: hydrophilic, red: hydrophobic) (I) $\theta_1 = 30^\circ, \theta_2 = 90^\circ$, (II) $\theta_1 = 90^\circ, \theta_2 = 150^\circ$, (III) $\theta_1 = 120^\circ, \theta_2 = 180^\circ$	133
B.7.	Surface energy landscapes for droplets on the striped surfaces with different area fractions of the hydrophilic and hydrophobic areas and the corresponding snapshots of equilibrated droplets through PF simulations. The ratios for (I) $\nu = 1 : 1$, (II) $\nu = 1 : 2$, (III) $\nu = 1 : 3$ correspond to three different setups with $(L = 20, \lambda = 0)$, $(L = 30, \lambda = \cos 60^\circ)$, $(L = 40, \lambda = \cos 45^\circ)$, respectively. The droplet size is set as $R = 40$. The chemical heterogeneities are described by $f_1(r, \varphi)$ in Eq (7) with $\gamma_m = 0$, $\gamma_0 = 0.5$, $\xi = 100$. The energy minima are marked by different numbers, corresponding to the snapshots in (C) labeled with the same number. The energy landscapes in (A) and (B) are for the situations where the droplet base center positions are on P_1 and P_2 , respectively. (C) Snapshots of the equilibrated droplets via simulations (blue: hydrophilic, red: hydrophobic).	134
C.1.	(A) and (B) Contour plot of the function $\gamma_{ls} - \gamma_{gs}$ in x-y space for different χ and λ , respectively. $\gamma_m = 0$, $\gamma_0 = 1$, $L = 15$, and $\xi = 100$. (C) (a) and (b) The heterogeneities $\gamma_{ls} - \gamma_{gs}$ as a function of x for different pairs of (γ_m, γ_0) and ξ when $y = 7.5$, respectively. In (C) I set $L = 15$, $\lambda = 0.5$, and $\chi = 0.15$	140
C.2.	Photos of the glass slides with wettability pattern of (A) square array and (B) circle array after dipping in the glass with distilled water. The hydrophobic mesh restricts the liquid in the hydrophilic square and circle spots. The modification is done by two steps UV-light driven thiol-ene modification through the photomask (A, B: left corner below). The black parts of the photomask form hydrophobic areas, light grey –hydrophilic pattern.	141
C.3.	A-D: Top view comparison for droplet with volumes $V = 2V_0, 5V_0, 6V_0$, and $8V_0$. $V_0 = 5\mu L$. Scale bar: 1 mm (or 10 in dimensionless value).	142

List of Tables

5.1. The setup of contact angles	72
6.1. Deviation rate for the pixels of the experimental and simulation images.	85
9.1. Reference values for nondimensionalization.	108
C.1. Calculation of Bond numbers.	143

Bibliography

- [1] S. Hung. *Stephen Hung photography–Morning dews*. 2016. URL: <https://shungphotography.com/2016/09/21/morning-dews/> (visited on 04/13/2021).
- [2] S. Kim, Z. Wu, E. Esmaili, J. J. Dombroskie, and S. Jung. “How a raindrop gets shattered on biological surfaces”. In: *Proceedings of the National Academy of Sciences* 117.25 (2020), pp. 13901–13907.
- [3] D. Lohse and E. Villermaux. “Double threshold behavior for breakup of liquid sheets”. In: *Proceedings of the National Academy of Sciences* 117.32 (2020), pp. 18912–18914.
- [4] C. Duez, C. Ybert, C. Clanet, and L. Bocquet. “Wetting controls separation of inertial flows from solid surfaces”. In: *Physical Review Letters* 104.8 (2010), p. 084503.
- [5] E. Jambon-Puillet, W. Bouwhuis, J. Snoeijer, and D. Bonn. “Liquid helix: How capillary jets adhere to vertical cylinders”. In: *Physical Review Letters* 122.18 (2019), p. 184501.
- [6] R. D. Deegan, O. Bakajin, T. F. Dupont, G. Huber, S. R. Nagel, and T. A. Witten. “Contact line deposits in an evaporating drop”. In: *Physical Review E* 62.1 (2000), p. 756.
- [7] R. Das. *Printing technologies find their place in printed electronics*. 2017. URL: <https://www.idtechex.com/en/research-article/printing-technologies-find-their-place-in-printed-electronics/10920> (visited on 04/13/2021).
- [8] H. Minemawari, T. Yamada, H. Matsui, J. Tsutsumi, S. Haas, R. Chiba, R. Kumai, and T. Hasegawa. “Inkjet printing of single-crystal films”. In: *Nature* 475.7356 (2011), pp. 364–367.
- [9] H. Li, W. Fang, Z. Zhao, A. Li, Z. Li, M. Li, Q. Li, X. Feng, and Y. Song. “Droplet precise self-splitting on patterned adhesive surfaces for simultaneous multidetection”. In: *Angewandte Chemie International Edition* 59.26 (2020), pp. 10535–10539.
- [10] E. Ueda, F. L. Geyer, V. Nedashkivska, and P. A. Levkin. “Droplet Microarray: facile formation of arrays of microdroplets and hydrogel micropads for cell screening applications”. In: *Lab on a Chip* 12.24 (2012), pp. 5218–5224.
- [11] R. Seemann, M. Brinkmann, T. Pfohl, and S. Herminghaus. “Droplet based microfluidics”. In: *Reports on Progress in Physics* 75.1 (2011), p. 016601.
- [12] A. C. Arias, J. D. MacKenzie, I. McCulloch, J. Rivnay, and A. Salleo. “Materials and applications for large area electronics: solution-based approaches”. In: *Chemical Reviews* 110.1 (2010), pp. 3–24.

- [13] K. F. Wiedenheft, H. A. Guo, X. Qu, J. B. Boreyko, F. Liu, K. Zhang, F. Eid, A. Choudhury, Z. Li, and C.-H. Chen. “Hotspot cooling with jumping-drop vapor chambers”. In: *Applied Physics Letters* 110.14 (2017), p. 141601.
- [14] K.-Y. Law and H. Zhao. *Surface wetting: characterization, contact angle, and fundamentals*. Basel, Switzerland: Springer, 2016.
- [15] R. N. Wenzel. “Resistance of solid surfaces to wetting by water”. In: *Industrial & Engineering Chemistry* 28.8 (1936), pp. 988–994.
- [16] A. Cassie and S Baxter. “Large contact angles of plant and animal surfaces”. In: *Nature* 155.3923 (1945), p. 21.
- [17] A. Carlson, M. Do-Quang, and G. Amberg. “Modeling of dynamic wetting far from equilibrium”. In: *Physics of Fluids* 21.12 (2009), p. 121701.
- [18] P. Yue, C. Zhou, and J. J. Feng. “Sharp-interface limit of the Cahn-Hilliard model for moving contact lines”. In: *Journal of Fluid Mechanics* 645 (2010), p. 279.
- [19] U. Thiele, L. Brusch, M. Bestehorn, and M. Bär. “Modelling thin-film dewetting on structured substrates and templates: Bifurcation analysis and numerical simulations”. In: *The European Physical Journal E* 11.3 (2003), pp. 255–271.
- [20] Y Wu, J. Fowlkes, N. A. Roberts, J. Diez, L Kondic, A. González, and P. Rack. “Competing liquid phase instabilities during pulsed laser induced self-assembly of copper rings into ordered nanoparticle arrays on SiO₂”. In: *Langmuir* 27.21 (2011), pp. 13314–13323.
- [21] D. Jacqmin. “Calculation of two-phase Navier–Stokes flows using phase-field modeling”. In: *Journal of Computational Physics* 155.1 (1999), pp. 96–127.
- [22] D. Bonn, J. Eggers, J. Indekeu, J. Meunier, and E. Rolley. “Wetting and spreading”. In: *Reviews of Modern Physics* 81.2 (2009), p. 739.
- [23] S.-D. Poisson. *Nouvelle théorie de l’action capillaire*. Paris, France: Bachelier père et fils, 1831.
- [24] V. Baidakov and G. S. Boltachev. “Extended version of the van der Waals capillarity theory”. In: *The Journal of Chemical Physics* 121.17 (2004), pp. 8594–8601.
- [25] T. Young. “III. An essay on the cohesion of fluids”. In: *Philosophical Transactions of the Royal Society of London* 95 (1805), pp. 65–87.
- [26] P. Laplace. *Mécanique celeste 10, Supplement to the tenth edition*. Boston, USA: Hillard, Gray, Little, and Wilkins, 1806.
- [27] L. M. Siqueland and S. M. Skjæveland. “Derivations of the Young-Laplace equation”. In: *Unpublished research*. <https://doi.org/10.13140/RG.2.4485.5768> (2014).
- [28] P. W. Voorhees. “The theory of Ostwald ripening”. In: *Journal of Statistical Physics* 38.1 (1985), pp. 231–252.

- [29] Y. Zheng, H. Bai, Z. Huang, X. Tian, F.-Q. Nie, Y. Zhao, J. Zhai, and L. Jiang. “Directional water collection on wetted spider silk”. In: *Nature* 463.7281 (2010), pp. 640–643.
- [30] H. Chen, P. Zhang, L. Zhang, H. Liu, Y. Jiang, D. Zhang, Z. Han, and L. Jiang. “Continuous directional water transport on the peristome surface of *Nepenthes alata*”. In: *Nature* 532.7597 (2016), pp. 85–89.
- [31] K.-C. Park, P. Kim, A. Grinthal, N. He, D. Fox, J. C. Weaver, and J. Aizenberg. “Condensation on slippery asymmetric bumps”. In: *Nature* 531.7592 (2016), pp. 78–82.
- [32] C Duprat, S Protiere, A. Beebe, and H. A. Stone. “Wetting of flexible fibre arrays”. In: *Nature* 482.7386 (2012), pp. 510–513.
- [33] A. T. Bradley, F. Box, I. J. Hewitt, and D. Vella. “Wettability-independent droplet transport by Bendotaxis”. In: *Physical Review Letters* 122.7 (2019), p. 074503.
- [34] L. Wu, Z. Dong, F. Li, and Y. Song. “Designing laplace pressure pattern for microdroplet manipulation”. In: *Langmuir* 34.2 (2018), pp. 639–645.
- [35] Y. Chen, K. Li, S. Zhang, L. Qin, S. Deng, L. Ge, L.-P. Xu, L. Ma, S. Wang, and X. Zhang. “Bioinspired superwetable microspine chips with directional droplet transportation for biosensing”. In: *ACS Nano* 14.4 (2020), pp. 4654–4661.
- [36] A. Marmur and E. Bittoun. “When Wenzel and Cassie are right: reconciling local and global considerations”. In: *Langmuir* 25.3 (2009), pp. 1277–1281.
- [37] A. Cassie and S Baxter. “Wettability of porous surfaces”. In: *Transactions of the Faraday Society* 40 (1944), pp. 546–551.
- [38] A. Cassie. “Contact angles”. In: *Discussions of the Faraday Society* 3 (1948), pp. 11–16.
- [39] P. Lenz and R. Lipowsky. “Morphological transitions of wetting layers on structured surfaces”. In: *Physical Review Letters* 80.9 (1998), p. 1920.
- [40] A. A. Darhuber, S. M. Troian, S. M. Miller, and S. Wagner. “Morphology of liquid microstructures on chemically patterned surfaces”. In: *Journal of Applied Physics* 87.11 (2000), pp. 7768–7775.
- [41] R. Konnur, K. Kargupta, and A. Sharma. “Instability and morphology of thin liquid films on chemically heterogeneous substrates”. In: *Physical Review Letters* 84.5 (2000), p. 931.
- [42] M. Brinkmann and R. Lipowsky. “Wetting morphologies on substrates with striped surface domains”. In: *Journal of Applied Physics* 92.8 (2002), pp. 4296–4306.
- [43] X.-M. Li, D. Reinhoudt, and M. Crego-Calama. “What do we need for a superhydrophobic surface? A review on the recent progress in the preparation of superhydrophobic surfaces”. In: *Chemical Society Reviews* 36.8 (2007), pp. 1350–1368.
- [44] H Kusumaatmaja and J. Yeomans. “Modeling contact angle hysteresis on chemically patterned and superhydrophobic surfaces”. In: *Langmuir* 23.11 (2007), pp. 6019–6032.

- [45] J. Carmeliet, L. Chen, Q. Kang, and D. Derome. “Beyond-cassie mode of wetting and local contact angles of droplets on checkboard-patterned surfaces”. In: *Langmuir* 33.24 (2017), pp. 6192–6200.
- [46] Y. Wang, M. Jian, H. Liu, and X. Zhang. “Anisotropic wetting of droplets on stripe-patterned chemically heterogeneous surfaces: effect of length ratio and deposition position”. In: *Langmuir* 35.12 (2018), pp. 4387–4396.
- [47] D. Quéré. “Wetting and roughness”. In: *Annual Review of Materials Research* 38 (2008), pp. 71–99.
- [48] A. P. Mouat, C. E. Wood, J. E. Pye, and J. C. Burton. “Tuning contact line dynamics and deposition patterns in volatile liquid mixtures”. In: *Physical Review Letters* 124.6 (2020), p. 064502.
- [49] F. Boyer and C. Lapuerta. “Study of a three component Cahn-Hilliard flow model”. In: *ESAIM: Mathematical Modelling and Numerical Analysis* 40.4 (2006), pp. 653–687.
- [50] S. Dong. “Wall-bounded multiphase flows of N immiscible incompressible fluids: Consistency and contact-angle boundary condition”. In: *Journal of Computational Physics* 338 (2017), pp. 21–67.
- [51] J. Kim. “Phase-field models for multi-component fluid flows”. In: *Communications in Computational Physics* 12.3 (2012), pp. 613–661.
- [52] M. Ben Said, M. Selzer, B. Nestler, D. Braun, C. Greiner, and H. Garcke. “A phase-field approach for wetting phenomena of multiphase droplets on solid surfaces”. In: *Langmuir* 30.14 (2014), pp. 4033–4039.
- [53] C.-Y. Zhang, H. Ding, P. Gao, and Y.-L. Wu. “Diffuse interface simulation of ternary fluids in contact with solid”. In: *Journal of Computational Physics* 309 (2016), pp. 37–51.
- [54] C. Semperebon, T. Krüger, and H. Kusumaatmaja. “Ternary free-energy lattice Boltzmann model with tunable surface tensions and contact angles”. In: *Physical Review E* 93.3 (2016), p. 033305.
- [55] M. Wöhrwag, C. Semperebon, A. M. Moqaddam, I. Karlin, and H. Kusumaatmaja. “Ternary free-energy entropic lattice Boltzmann model with a high density ratio”. In: *Physical Review Letters* 120.23 (2018), p. 234501.
- [56] R. H. H. Abadi, M. H. Rahimian, and A. Fakhari. “Conservative phase-field lattice-Boltzmann model for ternary fluids”. In: *Journal of Computational Physics* 374 (2018), pp. 668–691.
- [57] N. Bala, M. Pepona, I. Karlin, H. Kusumaatmaja, and C. Semperebon. “Wetting boundaries for a ternary high-density-ratio lattice Boltzmann method”. In: *Physical Review E* 100.1 (2019), p. 013308.
- [58] B. Merriman, J. K. Bence, and S. J. Osher. “Motion of multiple junctions: A level set approach”. In: *Journal of Computational Physics* 112.2 (1994), pp. 334–363.
- [59] K. A. Smith, F. J. Solis, and D. Chopp. “A projection method for motion of triple junctions by level sets”. In: *Interfaces and Free Boundaries* 4.3 (2002), pp. 263–276.

- [60] J. A. Sethian and P. Smereka. “Level set methods for fluid interfaces”. In: *Annual Review of Fluid Mechanics* 35.1 (2003), pp. 341–372.
- [61] R.-H. Chen and C.-T. Chen. “Collision between immiscible drops with large surface tension difference: diesel oil and water”. In: *Experiments in Fluids* 41.3 (2006), pp. 453–461.
- [62] O. Ramírez-Soto, V. Sanjay, D. Lohse, J. T. Pham, and D. Vollmer. “Lifting a sessile oil drop from a superamphiphobic surface with an impacting one”. In: *Science Advances* 6.34 (2020), eaba4330.
- [63] Y. Li, C. Diddens, P. Lv, H. Wijshoff, M. Versluis, and D. Lohse. “Gravitational effect in evaporating binary microdroplets”. In: *Physical Review Letters* 122.11 (2019), p. 114501.
- [64] D. Lohse and X. Zhang. “Physicochemical hydrodynamics of droplets out of equilibrium”. In: *Nature Reviews Physics* 2.8 (2020), pp. 426–443.
- [65] V. Ogarev, T. Timonina, V. Arslanov, and A. Trapeznikov. “Spreading of polydimethylsiloxane drops on solid horizontal surfaces”. In: *The Journal of Adhesion* 6.4 (1974), pp. 337–355.
- [66] O. Voinov. “Hydrodynamics of wetting”. In: *Fluid Dynamics* 11.5 (1976), pp. 714–721.
- [67] L. Tanner. “The spreading of silicone oil drops on horizontal surfaces”. In: *Journal of Physics D: Applied Physics* 12.9 (1979), p. 1473.
- [68] R. Cox. “The dynamics of the spreading of liquids on a solid surface. Part 1. Viscous flow”. In: *Journal of Fluid Mechanics* 168 (1986), pp. 169–194.
- [69] P. De Gennes, X Hua, and P Levinson. “Dynamics of wetting: local contact angles”. In: *Journal of Fluid Mechanics* 212 (1990), pp. 55–63.
- [70] A. E. Seaver and J. C. Berg. “Spreading of a droplet on a solid surface”. In: *Journal of Applied Polymer Science* 52.3 (1994), pp. 431–435.
- [71] A. Cazabat and M. C. Stuart. “Dynamics of wetting: effects of surface roughness”. In: *The Journal of Physical Chemistry* 90.22 (1986), pp. 5845–5849.
- [72] A. Oron, S. H. Davis, and S. G. Bankoff. “Long-scale evolution of thin liquid films”. In: *Reviews of Modern Physics* 69.3 (1997), p. 931.
- [73] G. McHale, M. Newton, S. Rowan, and M Banerjee. “The spreading of small viscous stripes of oil”. In: *Journal of Physics D: Applied Physics* 28.9 (1995), p. 1925.
- [74] H. P. Kavehpour, B. Ovrzyn, and G. H. McKinley. “Microscopic and macroscopic structure of the precursor layer in spreading viscous drops”. In: *Physical Review Letters* 91.19 (2003), p. 196104.
- [75] A. Marmur. “Equilibrium and spreading of liquids on solid surfaces”. In: *Advances in Colloid and Interface Science* 19.1-2 (1983), pp. 75–102.
- [76] F. T. Dodge. “The spreading of liquid droplets on solid surfaces”. In: *Journal of Colloid and interface Science* 121.1 (1988), pp. 154–160.

- [77] M. J. De Ruijter, J. De Coninck, and G. Oshanin. “Droplet spreading: partial wetting regime revisited”. In: *Langmuir* 15.6 (1999), pp. 2209–2216.
- [78] H. E. Huppert. “The propagation of two-dimensional and axisymmetric viscous gravity currents over a rigid horizontal surface”. In: *Journal of Fluid Mechanics* 121 (1982), pp. 43–58.
- [79] A.-L. Biance, C. Clanet, and D. Quéré. “First steps in the spreading of a liquid droplet”. In: *Physical Review E* 69.1 (2004), p. 016301.
- [80] J. C. Bird, S. Mandre, and H. A. Stone. “Short-time dynamics of partial wetting”. In: *Physical Review Letters* 100.23 (2008), p. 234501.
- [81] S. Varagnolo, D. Ferraro, P. Fantinel, M. Pierno, G. Mistura, G. Amati, L. Biferale, and M. Sbragaglia. “Stick-slip sliding of water drops on chemically heterogeneous surfaces”. In: *Physical Review Letters* 111.6 (2013), p. 066101.
- [82] N. Savva, G. A. Pavliotis, and S. Kalliadasis. “Contact lines over random topographical substrates. Part 2. Dynamics”. In: *Journal of Fluid Mechanics* 672 (2011), pp. 384–410.
- [83] R. Vellingiri, N. Savva, and S. Kalliadasis. “Droplet spreading on chemically heterogeneous substrates”. In: *Physical Review E* 84.3 (2011), p. 036305.
- [84] N. Savva and S. Kalliadasis. “Droplet motion on inclined heterogeneous substrates”. In: *Journal of Fluid Mechanics* 725 (2013), pp. 462–491.
- [85] N. Savva, D. Groves, and S. Kalliadasis. “Droplet dynamics on chemically heterogeneous substrates”. In: *Journal of Fluid Mechanics* 859 (2019), pp. 321–361.
- [86] L. W. Schwartz. “Hysteretic effects in droplet motions on heterogeneous substrates: direct numerical simulation”. In: *Langmuir* 14.12 (1998), pp. 3440–3453.
- [87] C. Y. Lim and Y. C. Lam. “Phase-field simulation of impingement and spreading of micro-sized droplet on heterogeneous surface”. In: *Microfluidics and nanofluidics* 17.1 (2014), pp. 131–148.
- [88] X. Wang, D.-L. Sun, X.-D. Wang, and W.-M. Yan. “Dynamics of droplets impacting hydrophilic surfaces decorated with a hydrophobic strip”. In: *International Journal of Heat and Mass Transfer* 135 (2019), pp. 235–246.
- [89] N. A. Malvadkar, M. J. Hancock, K. Sekeroglu, W. J. Dressick, and M. C. Demirel. “An engineered anisotropic nanofilm with unidirectional wetting properties”. In: *Nature Materials* 9.12 (2010), pp. 1023–1028.
- [90] X. Chen, R. Ma, J. Li, C. Hao, W. Guo, B. L. Luk, S. C. Li, S. Yao, and Z. Wang. “Evaporation of droplets on superhydrophobic surfaces: Surface roughness and small droplet size effects”. In: *Physical Review Letters* 109.11 (2012), p. 116101.
- [91] R. Raj, S. Adera, R. Enright, and E. N. Wang. “High-resolution liquid patterns via three-dimensional droplet shape control”. In: *Nature Communications* 5.1 (2014), pp. 1–8.

- [92] J. Li, X. Zhou, J. Li, L. Che, J. Yao, G. McHale, M. K. Chaudhury, and Z. Wang. “Topological liquid diode”. In: *Science Advances* 3.10 (2017), eaao3530.
- [93] M. Lee, Y. S. Chang, and H.-Y. Kim. “Drop impact on microwetting patterned surfaces”. In: *Physics of Fluids* 22.7 (2010), p. 072101.
- [94] W. Miao, S. Zheng, J. Zhou, B. Zhang, R. Fang, D. Hao, L. Sun, D. Wang, Z. Zhu, X. Jin, et al. “Microchannel and nanofiber array morphology enhanced rapid superspreading on animals’ corneas”. In: *Advanced Materials* 33.23 (2021), p. 2007152.
- [95] B. Derby. “Inkjet printing of functional and structural materials: fluid property requirements, feature stability, and resolution”. In: *Annual Review of Materials Research* 40 (2010), pp. 395–414.
- [96] S. Peng, D. Lohse, and X. Zhang. “Spontaneous pattern formation of surface nanodroplets from competitive growth”. In: *ACS Nano* 9.12 (2015), pp. 11916–11923.
- [97] L. Fisher and A. Golovin. “Nonlinear stability analysis of a two-layer thin liquid film: Dewetting and autophobic behavior”. In: *Journal of Colloid and Interface Science* 291.2 (2005), pp. 515–528.
- [98] U. Thiele, M. Mertig, and W. Pompe. “Dewetting of an evaporating thin liquid film: Heterogeneous nucleation and surface instability”. In: *Physical Review Letters* 80.13 (1998), p. 2869.
- [99] R. V. Craster and O. K. Matar. “Dynamics and stability of thin liquid films”. In: *Reviews of Modern Physics* 81.3 (2009), p. 1131.
- [100] G. Reiter. “Dewetting of thin polymer films”. In: *Physical Review Letters* 68.1 (1992), p. 75.
- [101] R. Xie, A. Karim, J. F. Douglas, C. C. Han, and R. A. Weiss. “Spinodal dewetting of thin polymer films”. In: *Physical Review Letters* 81.6 (1998), p. 1251.
- [102] J. Becker, G. Grün, R. Seemann, H. Mantz, K. Jacobs, K. R. Mecke, and R. Blossey. “Complex dewetting scenarios captured by thin-film models”. In: *Nature Materials* 2.1 (2003), pp. 59–63.
- [103] G. Reiter. “Dewetting of highly elastic thin polymer films”. In: *Physical Review Letters* 87.18 (2001), p. 186101.
- [104] A. M. Telford, S. C. Thickett, and C. Neto. “Functional patterned coatings by thin polymer film dewetting”. In: *Journal of Colloid and Interface Science* 507 (2017), pp. 453–469.
- [105] D. Peschka, S. Haefner, L. Marquant, K. Jacobs, A. Münch, and B. Wagner. “Signatures of slip in dewetting polymer films”. In: *Proceedings of the National Academy of Sciences* 116.19 (2019), pp. 9275–9284.
- [106] C. V. Thompson. “Solid-state dewetting of thin films”. In: *Annual Review of Materials Research* 42 (2012), pp. 399–434.
- [107] J. Lian, L. Wang, X. Sun, Q. Yu, and R. C. Ewing. “Patterning metallic nanostructures by ion-beam-induced dewetting and Rayleigh instability”. In: *Nano Letters* 6.5 (2006), pp. 1047–1052.

- [108] J. Ye and C. V. Thompson. “Regular pattern formation through the retraction and pinch-off of edges during solid-state dewetting of patterned single crystal films”. In: *Physical Review B* 82.19 (2010), p. 193408.
- [109] O. Reynolds. “IV. On the theory of lubrication and its application to Mr. Beauchamp tower’s experiments, including an experimental determination of the viscosity of olive oil”. In: *Philosophical Transactions of the Royal Society of London* 177 (1886), pp. 157–234.
- [110] A. A. Pahlavan, L. Cueto-Felgueroso, G. H. McKinley, and R. Juanes. “Thin films in partial wetting: internal selection of contact-line dynamics”. In: *Physical Review Letters* 115.3 (2015), p. 034502.
- [111] A Sharma and E Ruckenstein. “Mechanism of tear film rupture and formation of dry spots on cornea”. In: *Journal of Colloid and Interface Science* 106.1 (1985), pp. 12–27.
- [112] J. B. Grotberg. “Respiratory fluid mechanics and transport processes”. In: *Annual Review of Biomedical Engineering* 3.1 (2001), pp. 421–457.
- [113] R. W. Griffiths. “The dynamics of lava flows”. In: *Annual Review of Fluid Mechanics* 32.1 (2000), pp. 477–518.
- [114] L. Kondic, A. G. González, J. A. Diez, J. D. Fowlkes, and P. Rack. “Liquid-state dewetting of pulsed-laser-heated nanoscale metal films and other geometries”. In: *Annual Review of Fluid Mechanics* 52 (2020), pp. 235–262.
- [115] F. Girard, M. Antoni, S. Faure, and A. Steinchen. “Influence of heating temperature and relative humidity in the evaporation of pinned droplets”. In: *Colloids and Surfaces A: Physicochemical and Engineering Aspects* 323.1-3 (2008), pp. 36–49.
- [116] F Girard, M Antoni, and K Sefiane. “On the effect of Marangoni flow on evaporation rates of heated water drops”. In: *Langmuir* 24.17 (2008), pp. 9207–9210.
- [117] S. Semenov, V. Starov, M. Velarde, and R. Rubio. “Droplets evaporation: Problems and solutions”. In: *The European Physical Journal Special Topics* 197.1 (2011), pp. 265–278.
- [118] S. Semenov, V. Starov, R. Rubio, and M. Velarde. “Instantaneous distribution of fluxes in the course of evaporation of sessile liquid droplets: computer simulations”. In: *Colloids and Surfaces A: Physicochemical and Engineering Aspects* 372.1-3 (2010), pp. 127–134.
- [119] H. Hu and R. G. Larson. “Marangoni effect reverses coffee-ring depositions”. In: *The Journal of Physical Chemistry B* 110.14 (2006), pp. 7090–7094.
- [120] J. Fournier and A. Cazabat. “Tears of wine”. In: *EPL (Europhysics Letters)* 20.6 (1992), p. 517.
- [121] L. Keiser, H. Bense, P. Colinet, J Bico, and E. Reyssat. “Marangoni bursting: evaporation-induced emulsification of binary mixtures on a liquid layer”. In: *Physical Review Letters* 118.7 (2017), p. 074504.

- [122] G. Durey, H. Kwon, Q. Magdelaine, M. Casiulis, J. Mazet, L. Keiser, H. Bense, P. Colinet, J. Bico, and E. Reyssat. “Marangoni bursting: Evaporation-induced emulsification of a two-component droplet”. In: *Physical Review Fluids* 3.10 (2018), p. 100501.
- [123] L.-Q. Chen. “Phase-field models for microstructure evolution”. In: *Annual Review of Materials Research* 32.1 (2002), pp. 113–140.
- [124] J. D. van der Waals. “The thermodynamic theory of capillarity under the hypothesis of a continuous variation of density”. In: *Journal of Statistical Physics* 20.2 (1979), pp. 200–244.
- [125] P. Yue, J. J. Feng, C. Liu, and J. Shen. “A diffuse-interface method for simulating two-phase flows of complex fluids”. In: *Journal of Fluid Mechanics* 515 (2004), p. 293.
- [126] J. W. Cahn and J. E. Hilliard. “Free energy of a nonuniform system. I. Interfacial free energy”. In: *The Journal of Chemical Physics* 28.2 (1958), pp. 258–267.
- [127] J. W. Cahn. “On spinodal decomposition”. In: *Acta Metallurgica* 9.9 (1961), pp. 795–801.
- [128] J. Cahn and S. Allen. “A microscopic theory for domain wall motion and its experimental verification in Fe-Al alloy domain growth kinetics”. In: *Le Journal de Physique Colloques* 38.C7 (1977), pp. C7–51.
- [129] S. M. Allen and J. W. Cahn. “A microscopic theory for antiphase boundary motion and its application to antiphase domain coarsening”. In: *Acta Metallurgica* 27.6 (1979), pp. 1085–1095.
- [130] C. Liu and J. Shen. “A phase field model for the mixture of two incompressible fluids and its approximation by a Fourier-spectral method”. In: *Physica D: Nonlinear Phenomena* 179.3-4 (2003), pp. 211–228.
- [131] T. W. Heo and L.-Q. Chen. “Phase-field modeling of nucleation in solid-state phase transformations”. In: *Journal of The Minerals* 66.8 (2014), pp. 1520–1528.
- [132] K. Deckelnick, G. Dziuk, and C. M. Elliott. “Computation of geometric partial differential equations and mean curvature flow”. In: *Acta Numerica* 14 (2005), p. 139.
- [133] J. Rubinstein and P. Sternberg. “Nonlocal reaction—diffusion equations and nucleation”. In: *IMA Journal of Applied Mathematics* 48.3 (1992), pp. 249–264.
- [134] X. Yang, J. J. Feng, C. Liu, and J. Shen. “Numerical simulations of jet pinching-off and drop formation using an energetic variational phase-field method”. In: *Journal of Computational Physics* 218.1 (2006), pp. 417–428.
- [135] E. Bretin and M. Brassel. “A modified phase field approximation for mean curvature flow with conservation of the volume”. In: *Mathematical Methods in the Applied Sciences* 34 (2011), pp. 1157–1180.
- [136] Y. Li, E. Jung, W. Lee, H. G. Lee, and J. Kim. “Volume preserving immersed boundary methods for two-phase fluid flows”. In: *International Journal for Numerical Methods in Fluids* 69.4 (2012), pp. 842–858.

- [137] J. Kim, S. Lee, and Y. Choi. “A conservative Allen–Cahn equation with a space–time dependent Lagrange multiplier”. In: *International Journal of Engineering Science* 84 (2014), pp. 11–17.
- [138] S. Zhai, Z. Weng, and X. Feng. “Investigations on several numerical methods for the non-local Allen–Cahn equation”. In: *International Journal of Heat and Mass Transfer* 87 (2015), pp. 111–118.
- [139] D. Jeong and J. Kim. “Conservative Allen–Cahn–Navier–Stokes system for incompressible two-phase fluid flows”. In: *Computers & Fluids* 156 (2017), pp. 239–246.
- [140] J. Yang, Y. Li, C. Lee, and J. Kim. “Conservative Allen–Cahn equation with a nonstandard variable mobility”. In: *Acta Mechanica* 231.2 (2020), pp. 561–576.
- [141] B. Nestler, F. Wendler, M. Selzer, B. Stinner, and H. Garcke. “Phase-field model for multiphase systems with preserved volume fractions”. In: *Physical Review E* 78.1 (2008), p. 011604.
- [142] H. Garcke, B. Nestler, B. Stinner, and F. Wendler. “Allen–Cahn systems with volume constraints”. In: *Mathematical Models and Methods in Applied Sciences* 18.08 (2008), pp. 1347–1381.
- [143] H. Garcke, B. Nestler, and B. Stoth. “A multiphase field concept: numerical simulations of moving phase boundaries and multiple junctions”. In: *SIAM Journal on Applied Mathematics* 60.1 (1999), pp. 295–315.
- [144] B. Nestler, H. Garcke, and B. Stinner. “Multicomponent alloy solidification: phase-field modeling and simulations”. In: *Physical Review E* 71.4 (2005), p. 041609.
- [145] J. Berry, C. P. Brangwynne, and M. Haataja. “Physical principles of intracellular organization via active and passive phase transitions”. In: *Reports on Progress in Physics* 81.4 (2018), p. 046601.
- [146] P. C. Hohenberg and B. I. Halperin. “Theory of dynamic critical phenomena”. In: *Reviews of Modern Physics* 49.3 (1977), p. 435.
- [147] D. M. Anderson, G. B. McFadden, and A. A. Wheeler. “Diffuse-interface methods in fluid mechanics”. In: *Annual Review of Fluid Mechanics* 30.1 (1998), pp. 139–165.
- [148] T. Qian, X.-P. Wang, and P. Sheng. “Power-law slip profile of the moving contact line in two-phase immiscible flows”. In: *Physical Review Letters* 93.9 (2004), p. 094501.
- [149] H. Ding and P. D. Spelt. “Wetting condition in diffuse interface simulations of contact line motion”. In: *Physical Review E* 75.4 (2007), p. 046708.
- [150] W. Ren and E. Weinan. “Derivation of continuum models for the moving contact line problem based on thermodynamic principles”. In: *Communications in Mathematical Sciences* 9.2 (2011), pp. 597–606.
- [151] D. N. Sibley, A. Nold, N. Savva, and S. Kalliadasis. “The contact line behaviour of solid-liquid-gas diffuse-interface models”. In: *Physics of Fluids* 25.9 (2013), p. 092111.

-
- [152] J. Shen, X. Yang, and H. Yu. “Efficient energy stable numerical schemes for a phase field moving contact line model”. In: *Journal of Computational Physics* 284 (2015), pp. 617–630.
- [153] A. Fakhari and D. Bolster. “Diffuse interface modeling of three-phase contact line dynamics on curved boundaries: A lattice Boltzmann model for large density and viscosity ratios”. In: *Journal of Computational Physics* 334 (2017), pp. 620–638.
- [154] J. Hoyt. “The continuum theory of nucleation in multicomponent systems”. In: *Acta Metallurgica et Materialia* 38.8 (1990), pp. 1405–1412.
- [155] S. Mao, D. Kuldinow, M. P. Haataja, and A. Košmrlj. “Phase behavior and morphology of multicomponent liquid mixtures”. In: *Soft Matter* 15.6 (2019), pp. 1297–1311.
- [156] L. K. Antanovskii. “A phase field model of capillarity”. In: *Physics of Fluids* 7.4 (1995), pp. 747–753.
- [157] L. Espath, A. Sarmiento, P. Vignal, B. Varga, A. Cortes, L. Dalcin, and V. M. Calo. “Energy exchange analysis in droplet dynamics via the Navier–Stokes–Cahn–Hilliard model”. In: *Journal of Fluid Mechanics* 797 (2016), pp. 389–430.
- [158] A Tiribocchi, A Montessori, S Aime, M Milani, M Lauricella, S Succi, and D Weitz. “Novel nonequilibrium steady states in multiple emulsions”. In: *Physics of Fluids* 32.1 (2020), p. 017102.
- [159] J. Shen and X. Yang. “A phase-field model and its numerical approximation for two-phase incompressible flows with different densities and viscosities”. In: *SIAM Journal on Scientific Computing* 32.3 (2010), pp. 1159–1179.
- [160] S. Mao, M. S. Chakraverti-Wuerthwein, H. Gaudio, and A. Košmrlj. “Designing the Morphology of Separated Phases in Multicomponent Liquid Mixtures”. In: *Physical Review Letters* 125.21 (2020), p. 218003.
- [161] F Wang, A Choudhury, M Selzer, R Mukherjee, and B Nestler. “Effect of solutal Marangoni convection on motion, coarsening, and coalescence of droplets in a monotectic system”. In: *Physical Review E* 86.6 (2012), p. 066318.
- [162] F. Wang and B. Nestler. “Wetting transition and phase separation on flat substrates and in porous structures”. In: *The Journal of Chemical Physics* 154.9 (2021), p. 094704.
- [163] G. Muñoz. “Lagrangian field theories and energy-momentum tensors”. In: *American Journal of Physics* 64.9 (1996), pp. 1153–1157.
- [164] H. Bonart, C. Kahle, and J.-U. Repke. “Comparison of energy stable simulation of moving contact line problems using a thermodynamically consistent Cahn–Hilliard Navier–Stokes model”. In: *Journal of Computational Physics* 399 (2019), p. 108959.
- [165] Y. Wu, F. Wang, M. Selzer, and B. Nestler. “Investigation of equilibrium droplet shapes on chemically striped patterned surfaces using phase-field method”. In: *Langmuir* 35.25 (2019), pp. 8500–8516.

- [166] J. Hötzer, O. Tschukin, M. B. Said, M. Berghoff, M. Jainta, G. Barthelemy, N. Smorchkov, D. Schneider, M. Selzer, and B. Nestler. “Calibration of a multi-phase field model with quantitative angle measurement”. In: *Journal of Materials Science* 51.4 (2016), pp. 1788–1797.
- [167] F. Wang, A. Reiter, M. Kellner, J. Brillo, M. Selzer, and B. Nestler. “Phase-field modeling of reactive wetting and growth of the intermetallic Al₂Au phase in the Al-Au system”. In: *Acta Materialia* 146 (2018), pp. 106–118.
- [168] B. Lavi and A. Marmur. “The exponential power law: partial wetting kinetics and dynamic contact angles”. In: *Colloids and Surfaces A: Physicochemical and Engineering Aspects* 250.1-3 (2004), pp. 409–414.
- [169] R. A. Meric and H. Y. Erbil. “Evaporation of sessile drops on solid surfaces: Pseudospherical cap geometry”. In: *Langmuir* 14.7 (1998), pp. 1915–1920.
- [170] H. P. Jansen, K. Sotthewes, C. Ganser, C. Teichert, H. J. Zandvliet, and E. S. Kooij. “Tuning kinetics to control droplet shapes on chemically striped patterned surfaces”. In: *Langmuir* 28.37 (2012), pp. 13137–13142.
- [171] H. P. Jansen, K. Sotthewes, J. van Swigchem, H. J. Zandvliet, and E. S. Kooij. “Lattice Boltzmann modeling of directional wetting: Comparing simulations to experiments”. In: *Physical Review E* 88.1 (2013), p. 013008.
- [172] Y Yu, Q Li, C. Q. Zhou, P Zhou, and H. Yan. “Investigation of droplet evaporation on heterogeneous surfaces using a three-dimensional thermal multiphase lattice Boltzmann model”. In: *Applied Thermal Engineering* 127 (2017), pp. 1346–1354.
- [173] J Leopoldes, A Dupuis, D. Bucknall, and J. Yeomans. “Jetting micron-scale droplets onto chemically heterogeneous surfaces”. In: *Langmuir* 19.23 (2003), pp. 9818–9822.
- [174] A Dupuis and J. M. Yeomans. “Lattice Boltzmann modelling of droplets on chemically heterogeneous surfaces”. In: *Future Generation Computer Systems* 20.6 (2004), pp. 993–1001.
- [175] H Kusumaatmaja and J. Yeomans. “Modeling contact angle hysteresis on chemically patterned and superhydrophobic surfaces”. In: *Langmuir* 23.11 (2007), pp. 6019–6032.
- [176] M. A. Cabrerizo-Vilchez. “Wetting on chemically heterogeneous surfaces: Pseudo-spherical approximation for sessile drops”. In: *Contact Angle, Wettability and Adhesion* 4 (2006), p. 183.
- [177] O Bliznyuk, E Vereshchagina, E. S. Kooij, and B. Poelsema. “Scaling of anisotropic droplet shapes on chemically stripe-patterned surfaces”. In: *Physical Review E* 79.4 (2009), p. 041601.
- [178] H. P. Jansen, O. Bliznyuk, E. S. Kooij, B. Poelsema, and H. J. Zandvliet. “Simulating anisotropic droplet shapes on chemically striped patterned surfaces”. In: *Langmuir* 28.1 (2012), pp. 499–505.
- [179] R. David and A. W. Neumann. “Anisotropic drop shapes on chemically striped surfaces”. In: *Colloids and Surfaces A: Physicochemical and Engineering Aspects* 393 (2012), pp. 32–36.

- [180] Y. V. Kalinin, V. Berejnov, and R. E. Thorne. “Contact line pinning by microfabricated patterns: effects of microscale topography”. In: *Langmuir* 25.9 (2009), pp. 5391–5397.
- [181] H Kusumaatmaja, R. Vrancken, C. Bastiaansen, and J. Yeomans. “Anisotropic drop morphologies on corrugated surfaces”. In: *Langmuir* 24.14 (2008), pp. 7299–7308.
- [182] C. Semprebon, C. Herrmann, B.-Y. Liu, R. Seemann, and M. Brinkmann. “Shape evolution of droplets growing on linear microgrooves”. In: *Langmuir* 34.36 (2018), pp. 10498–10511.
- [183] Y. Wu, F. Wang, M. Selzer, and B. Nestler. “Droplets on chemically patterned surface: A local free-energy minima analysis”. In: *Physical Review E* 100.4 (2019), p. 041102.
- [184] Y. Wu, F. Wang, S. Ma, M. Selzer, and B. Nestler. “How do chemical patterns affect equilibrium droplet shapes?” In: *Soft Matter* 16.26 (2020), pp. 6115–6127.
- [185] W. Feng, L. Li, E. Ueda, J. Li, S. Heißler, A. Welle, O. Trapp, and P. A. Levkin. “Surface patterning via thiol-yne click chemistry: an extremely fast and versatile approach to superhydrophilic-superhydrophobic micropatterns”. In: *Advanced Materials Interfaces* 1.7 (2014), p. 1400269.
- [186] Y. Wu, M. Kuzina, F. Wang, M. Reischl, M. Selzer, B. Nestler, and P. A. Levkin. “Equilibrium droplet shapes on chemically patterned surfaces: theoretical calculation, phase-field simulation, and experiments”. In: *Journal of Colloid and Interface Science* 606 (2022), pp. 1077–1086.
- [187] W. Feng, L. Li, X. Du, A. Welle, and P. A. Levkin. “Single-Step Fabrication of High-Density Microdroplet Arrays of Low-Surface-Tension Liquids”. In: *Advanced Materials* 28.16 (2016), pp. 3202–3208.
- [188] T. M. Schutzius, G. Graeber, M. Elsharkawy, J. Oreluk, and C. M. Megaridis. “Morphing and vectoring impacting droplets by means of wettability-engineered surfaces”. In: *Scientific Reports* 4.1 (2014), pp. 1–7.
- [189] A. Russo, M. Icardi, M. Elsharkawy, D. Ceglia, P. Asinari, and C. M. Megaridis. “Numerical simulation of droplet impact on wettability-patterned surfaces”. In: *Physical Review Fluids* 5.7 (2020), p. 074002.
- [190] S. Brandon, N. Haimovich, E. Yeger, and A. Marmur. “Partial wetting of chemically patterned surfaces: The effect of drop size”. In: *Journal of Colloid and Interface Science* 263.1 (2003), pp. 237–243.
- [191] P. Kant, A. L. Hazel, M. Dowling, A. B. Thompson, and A. Juel. “Sequential deposition of microdroplets on patterned surfaces”. In: *Soft Matter* 14.43 (2018), pp. 8709–8716.
- [192] M. Hartmann and S. Hardt. “Stability of evaporating droplets on chemically patterned surfaces”. In: *Langmuir* 35.14 (2019), pp. 4868–4875.
- [193] S. Ramos, J. Dias, and B. Canut. “Drop evaporation on superhydrophobic PTFE surfaces driven by contact line dynamics”. In: *Journal of Colloid and Interface Science* 440 (2015), pp. 133–139.

- [194] J. Zhang, F. Müller-Plathe, and F. Leroy. “Pinning of the contact line during evaporation on heterogeneous surfaces: slowdown or temporary immobilization? Insights from a nanoscale study”. In: *Langmuir* 31.27 (2015), pp. 7544–7552.
- [195] M. Wörner, N. Samkhaniani, X. Cai, Y. Wu, A. Majumdar, H. Marschall, B. Frohnäpfel, and O. Deutschmann. “Spreading and rebound dynamics of sub-millimetre urea-water-solution droplets impinging on substrates of varying wettability”. In: *Applied Mathematical Modelling* 95 (2021), pp. 53–73.
- [196] W. Lei, P. Krolla, T. Schwartz, and P. A. Levkin. “Controlling geometry and flow through bacterial bridges on patterned lubricant-infused surfaces (pLIS)”. In: *Small* 16.52 (2020), p. 2004575.
- [197] J. M. Scheiger, M. A. Kuzina, M. Eigenbrod, Y. Wu, F. Wang, S. Heißler, S. Hardt, B. Nestler, and P. A. Levkin. “Liquid wells as self-healing, functional analogues to solid vessels”. In: *Advanced Materials* 33.23 (2021), p. 2100117.
- [198] H. Sobol, J. Garfias, and J. Keller. “Effect on the water/air surface tension of air diffusion and interface structuring”. In: *The Journal of Physical Chemistry* 80.17 (1976), pp. 1941–1948.
- [199] D Villers and J. Platten. “Temperature dependence of the interfacial tension between water and long-chain alcohols”. In: *The Journal of Physical Chemistry* 92.14 (1988), pp. 4023–4024.
- [200] A Estrada-Baltazar, J. d. l. S. López-Lázaro, G. Iglesias-Silva, and J Barajas-Fernandez. “Density and surface tension of binary mixture of 1-Nonanol+ n-Octane,+ n-Nonane, and+ n-Decane from (293.15 to 323.15) K at P= 0.1 MPa”. In: *The Journal of Chemical Thermodynamics* 150 (2020), p. 106225.
- [201] A. H. Demond and A. S. Lindner. “Estimation of interfacial tension between organic liquids and water”. In: *Environmental Science & Technology* 27.12 (1993), pp. 2318–2331.
- [202] R. Stephenson and J. Stuart. “Mutual binary solubilities: water-alcohols and water-esters”. In: *Journal of Chemical and Engineering Data* 31.1 (1986), pp. 56–70.
- [203] Y.-C. Lee, Y.-B. Liou, R. Miller, H.-S. Liu, and S.-Y. Lin. “Adsorption Kinetics of Nonanol at the Air- Water Interface: Considering Molecular Interaction or Aggregation within Surface Layer”. In: *Langmuir* 18.7 (2002), pp. 2686–2692.
- [204] UMCS. *Adsorption at the solid/gas interface*. 2020. URL: <http://www.zzm.umcs.lublin.pl/Wyklad/FGF-Ang/3A.F.G.F.Adsorp.L-G.Interface.pdf> (visited on 04/13/2021).
- [205] J. Leutz. “Numerische Untersuchungen von Tropfenbenetzungen auf verschiedenen strukturierten Oberflächen unter dem Einfluss von Strömung”. BA thesis. Institute of Applied Materials–Computational Materials Science, Karlsruhe Institute of Technology. 2018.
- [206] D. Baratian, A. Cavalli, D Van Den Ende, and F Mugele. “On the shape of a droplet in a wedge: new insight from electrowetting”. In: *Soft Matter* 11.39 (2015), pp. 7717–7721.

- [207] P. Chantelot, A. M. Moqaddam, A. Gauthier, S. S. Chikatamarla, C. Clanet, I. V. Karlin, and D. Quéré. “Water ring-bouncing on repellent singularities”. In: *Soft Matter* 14.12 (2018), pp. 2227–2233.
- [208] D. Song, B. Song, H. Hu, X. Du, and F. Zhou. “Selectively splitting a droplet using superhydrophobic stripes on hydrophilic surfaces”. In: *Physical Chemistry Chemical Physics* 17.21 (2015), pp. 13800–13803.
- [209] T. Wang. “Numerical simulation of droplet wetting on chemically patterned surfaces”. MA thesis. Institute of Applied Materials–Computational Materials Science, Karlsruhe Institute of Technology, 2020.
- [210] H. Li, W. Fang, Y. Li, Q. Yang, M. Li, Q. Li, X.-Q. Feng, and Y. Song. “Spontaneous droplets gyrating via asymmetric self-splitting on heterogeneous surfaces”. In: *Nature Communications* 10.1 (2019), pp. 1–6.
- [211] W.-Z. Yuan and L.-Z. Zhang. “Lattice Boltzmann simulation of droplets impacting on superhydrophobic surfaces with randomly distributed rough structures”. In: *Langmuir* 33.3 (2017), pp. 820–829.
- [212] Y. Kwon, N. Patankar, J. Choi, and J. Lee. “Design of surface hierarchy for extreme hydrophobicity”. In: *Langmuir* 25.11 (2009), pp. 6129–6136.
- [213] W. Zhang, D. Wang, Z. Sun, J. Song, and X. Deng. “Robust superhydrophobicity: mechanisms and strategies”. In: *Chemical Society Reviews* 50 (2021), pp. 4031–4061.
- [214] J. C. Bird, R. Dhiman, H.-M. Kwon, and K. K. Varanasi. “Reducing the contact time of a bouncing drop”. In: *Nature* 503.7476 (2013), pp. 385–388.
- [215] D. A. Burzynski, I. V. Roisman, and S. E. Bansmer. “On the splashing of high-speed drops impacting a dry surface”. In: *Journal of Fluid Mechanics* 892 (2020), A2.
- [216] W. Ristenpart, P. McCalla, R. Roy, and H. Stone. “Coalescence of spreading droplets on a wettable substrate”. In: *Physical Review Letters* 97.6 (2006), p. 064501.
- [217] J. B. Boreyko and C.-H. Chen. “Self-propelled dropwise condensate on superhydrophobic surfaces”. In: *Physical Review Letters* 103.18 (2009), p. 184501.
- [218] M. A. Hack, W. Tewes, Q. Xie, C. Datt, K. Harth, J. Harting, and J. H. Snoeijer. “Self-similar liquid lens coalescence”. In: *Physical Review Letters* 124.19 (2020), p. 194502.
- [219] J. G. Leidenfrost. *De aquae communis nonnullis qualitatibus tractatus*. Duisburg, Germany: Ovenius, 1756.
- [220] M. Shirota, M. A. van Limbeek, C. Sun, A. Prosperetti, and D. Lohse. “Dynamic Leidenfrost effect: Relevant time and length scales”. In: *Physical Review Letters* 116.6 (2016), p. 064501.
- [221] D. V. Zaitsev, D. P. Kirichenko, V. S. Ajaev, and O. A. Kabov. “Levitation and self-organization of liquid microdroplets over dry heated substrates”. In: *Physical Review Letters* 119.9 (2017), p. 094503.

- [222] X. Man and M. Doi. “Vapor-induced motion of liquid droplets on an inert substrate”. In: *Physical Review Letters* 119.4 (2017), p. 044502.
- [223] N. J. Cira, A. Benusiglio, and M. Prakash. “Vapour-mediated sensing and motility in two-component droplets”. In: *Nature* 519.7544 (2015), pp. 446–450.
- [224] R. D. Deegan, O. Bakajin, T. F. Dupont, G. Huber, S. R. Nagel, and T. A. Witten. “Capillary flow as the cause of ring stains from dried liquid drops”. In: *Nature* 389.6653 (1997), pp. 827–829.
- [225] X. Cai, H. Marschall, M. Wörner, and O. Deutschmann. “Numerical simulation of wetting phenomena with a phase-field method using openFOAM®”. In: *Chemical Engineering & Technology* 38.11 (2015), pp. 1985–1992.